Current-Induced Spin Polarization and Dynamic Nuclear Polarization: Generation and Manipulation of Electron and Nuclear Spin Polarization in Gallium Arsenide

by

Joseph Rocco Iafrate

A dissertation submitted in partial fulfillment
of the requirements for the degree of
Doctor of Philosophy
(Applied Physics)
in The University of Michigan
2020

Doctoral Committee:

Professor Vanessa Sih, Chair
Professor Pallab K. Bhattacharya
Professor Çağlıyan Kurdak
Professor Theodore B. Norris
Professor Duncan G. Steel

Joseph R. Iafrate

iafratej@umich.edu

ORCID iD: 0000-0002-2749-873X

DEDICATION

This dissertation is dedicated to four individuals whose support enabled me to persevere and complete my doctoral studies:

To George and Mary Lindquist, who opened their home to me and other tired, hungry graduate students every week for a home-cooked meal, and more importantly, a feeling of home away from home;

To Dr. Ryan Hayes, who throughout our time together at Michigan has looked out for me in every way, providing me with food and friendship when needed and well-timed puns (which are always needed);

And to Dr. Deanna Montgomery, whose knack for helping me to think more clearly and focus my own thoughts is unrivaled, and without whom this dissertation would never have reached completion.

ACKNOWLEDGEMENTS

Like most advances in science, this story is the story of more than one person. If I were to list every single person who was a part of my physics journey, there would be far more names than equations and figures in this dissertation. That said, certain people and organizations made an outsized impact and deserve special recognition.

First and foremost, I am grateful to the members of my research group, especially my advisor, Dr. Vanessa Sih. I have not always been a fast learner nor known the most productive questions to ask, but Vanessa's patience and willingness to chat, through whatever research challenges I might be facing, created an environment in which I could thrive as a researcher.

I was introduced to the world of spin research by Aneesh Venugopal during my first summer in the group. I was fortunate enough to receive a second introduction from Dr. Marta Luengo-Kovac, who brought me up to speed on the optical setup featured in this dissertation. Working with Dr. Michael Macmahon allowed me to improve our data collection even further through his programming ingenuity. These colleagues laid the groundwork for my experimental abilities, and so this dissertation would not have been possible without them. Though I never met him, Caleb Zerger was responsible for building the MATLAB program that enabled my CISP studies, and so he deserves special mention as well.

I worked closely with Dr. Michael Macmahon and Michael Dominguez on the project in dynamic nuclear polarization (DNP). From start to finish, this has truly been a team effort. While I took lead on the experimental end, they took lead on the computational aspects of this project, so the fits and simulations shown in this dissertation appear thanks to them. Together, we have observed and explained magnetic-field-sweep-direction-dependent dynamic nuclear polarization, and I am excited to see where Michael D. takes the project next.

Along the way, discussions with Dr. Xinlin Song, Spencer Batalden, and Howard Hsu have refined my own knowledge of spin physics and our experimental methods. Mentoring Rachel Woo and Mayank Goyal contributed likewise. While their names do not explicitly appear in any of these chapters, they were also key to my success.

Writing a dissertation is a form of science communication. As both a participant and facilitator of the RELATE summer workshop, I have had the opportunity to think through the best practices for communication with the incredibly bright and committed RELATE coordinator team. Along the way, I have refined my communication skills, and I hope these skills have shone through in this text!

Overall, this story begins and ends with Applied Physics. After all, the motivation for this dissertation is application. The Applied Physics program has gone above and beyond in supporting me and creating an environment for thriving in grad school. When we call AP a family, we mean it. Thank you to Çağlıyan, Cyndi, Lauren, Keith, and Laci, for your open doors and willingness to help in any way possible. The AP office is a special place that I will miss dearly, not for the furniture but for the warmth inside. To the AP community, thank you for a fantastic six years.

During my first two years in graduate school, I was supported by the Applied Physics program and the Center for Photonic and Multiscale Nanomaterials (CPHOM), a National Science Foundation Materials Research Science and Engineering Center. From 2016 through 2019, I was supported by the Department of Defense through the National Defense Science and Engineering Graduate Fellowship (NDSEG) program. Following my NDSEG tenure, I was supported by Rackham Graduate School through the Rackham Predoctoral Fellowship.

The work on current-induced spin polarization (CISP) in Chapter 5 was supported in part by the U.S. Department of Energy, Office of Basic Energy Sciences, Division of Materials Sciences and Engineering, Award DE-SC0016206. The InGaAs sample under study was provided by the research group of Dr. Rachel Goldman. Dr. Goldman and Dr. Simon Huang were supported in part by the National Science Foundation, Grant No. DMR 1410282, while Dr. Davide Del Gaudio was supported in part by the National Science Foundation, Grant No. EECS 1610362.

The work on DNP in Chapters 6 and 7 was supported in part by the National Science Foundation under Grant No. DMR-1607779.

Sample fabrication for both projects was performed in part at the University of Michigan Lurie Nanofabrication Facility.

TABLE OF CONTENTS

CHAPTER

LIST OF FIGURES

Figure

LIST OF TABLES

Table

LIST OF APPENDICES

Appendix

ABSTRACT

Spintronics would utilize the spin of the electron for information processing and storage, leading to devices that may be smaller, faster, and more energy-efficient than their electronic counterparts. Before these spin-based devices can be fully realized, we must answer the following questions: How do we effectively generate electron spin polarization? What factors impact the ability of the spins to stay polarized? How do we effectively detect spin polarization? In our materials of interest, gallium arsenide (GaAs) and its alloy indium gallium arsenide (InGaAs), the detection method is optical, via Faraday or Kerr rotation. This dissertation focuses on the electrical generation of electron spin polarization (current-induced spin polarization, or CISP) and dynamic nuclear polarization (DNP) generated by periodic optical electron spin pumping, which will impact the electron spin system.

First, we modify an electrical technique for generating CISP in InGaAs to extend the voltage range of our experiments. In previous studies, current heating limited the magnitude of the applied voltage, leading to uncertainty regarding the relationship between the voltage and the spin polarization generation rate. We modify a bipolar square wave to reduce the time spent at nonzero voltage, and by generating CISP via modified waveforms with increasing off/on ratios, we reduce heating by up to an order of magnitude on the range of 1 to 7 V applied. At off/on ratios of 5 and above, we recover the expected linear relationship between generation rate and applied voltage.

Then, we investigate DNP in GaAs under periodic optical excitation in the regime of resonant spin amplification (RSA). The measured Kerr rotation exhibits warped RSA peaks, shifted from their expected positions depending on the direction in which the external magnetic field is incremented, or swept. This points to a DNP accumulated along the external field direction, perpendicular to the direction of optical spin generation, altering electron spin precession through a sweep-direction-dependent Overhauser field, with nuclear T_1 times on the order of tens of seconds. After establishing a physical framework based upon RSA and the optical Stark effect, we identify a set of experimental parameters to characterize the DNP: laser wavelength, pump power, time elapsed, and external field history. We present data exploring each of these parameter spaces, comparing to numerical simulations for the wavelength and elapsed time cases. Finally, we discuss the origin of the sweep-direction dependence.

We focus on the external field history of DNP through the steep sweep experiments, in which a field sweep is paused for two minutes to allow for DNP buildup. Certain steep fields result in post-steep RSA peaks that mimic the steeping behavior, showcasing a minutes-long precise memory of the electron-nuclear system's magnetic field history, the steep echo. We examine the steep sweeps through the lens of nuclear-induced frequency focusing, a conceptual framework for the buildup of DNP complementing our physical model. To explain the steep echo, we propose a modification to our physical picture that would involve a distribution of electron-nuclear interactions, with preliminary simulations showing promising correspondence to our measurements.

Taken together, these studies elucidate considerations that can arise in and compromise optical spintronic experiments. Proper mitigation (for current heating) and understanding (for DNP) will aid in the future research necessary to bring about semiconductor spintronic devices.

CHAPTER 1

A New Spin on Electronics

1.1 Introduction

Technology is incredible! Over the past fifty years, computers have been reduced in size by orders of magnitude, from the size of a room to the palm of a hand. The transistor has been instrumental to this progression. Through a network of transistors, devices can carry out advanced logical computations towards data processing and storage. This dissertation was written with the aid of a computer that relies on transistors to process information. The equipment used in collecting the data shown rely on transistors as well. The reader is most likely using an electronic device to view these words right now.

The electronics industry has been driven to innovation by Moore's Law [1], a principle that suggests that every one to two years, the number of transistors that can fit onto a computer chip doubles. Adherence to Moore's Law is one factor that spurs the improvement of electronic devices. However, there are challenges to further miniaturization. At microscopic scales, quantum effects will become significant. Furthermore, the smaller the devices become, the more difficult it will be to effectively dissipate heat generated by currents. Overheating can be detrimental to performance. It is accepted that Moore's Law will one day fail, but there is no consensus on when that will be.

While many alternatives have been suggested for continuing innovation in electronics, we focus on a particular field of research that has already allowed for advances in data storage applications: *spintronics*. While today's electronic devices utilize the charge of the electron as the carrier of information for storage and processing, future devices could instead rely on spin. These spintronic devices would have the potential to be smaller, faster, and more energy-efficient than their electronic counterparts [2]. Spintronics has already enabled the high-density magnetic hard disk drives of the late 1990's and 2000's and holds great promise for applications in data processing as well [3, 4].

1.2 Spin and Spin Polarization

In order to understand spintronics, we must first understand spin. Spin is intrinsic angular momentum. In this dissertation, we often think of spin as a magnetic dipole moment. This framework will aid in understanding our magneto-optical experiments. Classically, a magnetic dipole is related to its angular momentum $\vec{L}$ through the gyromagnetic ratio γ: $\vec{m} = \gamma \vec{L}$. For the electron, we instead replace $\vec{L}$ with spin $\vec{S}$. The gyromagnetic ratio for the electron is $\gamma = -\frac{g\mu_B}{\hbar}$, where g is the electron g factor, μ_B is the Bohr magneton, and $\hbar$ is the reduced Planck's constant.

Spin is a fundamentally quantum property, in that measurements of the electron spin can yield only one of two outcomes: spin up, with value $\frac{\hbar}{2}$, or spin down, with value $-\frac{\hbar}{2}$. When we measure spin, we measure with respect to some axis of quantization, which tells us how "up" and "down" are oriented in space. Changing this axis does not allow us to obtain a third outcome for electrons, though it may change the probability of the outcomes.

When an electron is placed in an external magnetic field, the energy of the electron changes based on its spin. The Hamiltonian for a spin in a magnetic field is given by

$$\hat{H} = -\hat{\vec{m}} \cdot \vec{B}, \tag{1.1}$$

where $\hat{\vec{m}}$ is the magnetic dipole operator and $\vec{B}$ is the external magnetic field [5]. We neglect any additional terms due to the motion of the electron or any potentials. The dipole operator looks just like the classical magnetic dipole, such that $\hat{\vec{m}} = -\frac{g\mu_B B_0}{\hbar}\hat{\vec{S}}$. The spin operator can be further defined in terms of the Pauli spin matrices: $\hat{\vec{S}} = \frac{\hbar}{2}\hat{\vec{\sigma}}$. We set the magnetic field $\vec{B} = B_0\hat{z}$ and choose $\hat{z}$ as our axis of quantization. The Hamiltonian is then

$$\begin{aligned}
\hat{H} &= -\hat{\vec{m}} \cdot \vec{B} \\
&= \frac{g\mu_B}{\hbar}\hat{\vec{S}} \cdot \vec{B} \\
&= \frac{g\mu_B}{\hbar}\hat{\vec{S}} \cdot B_0\hat{z} \\
&= \frac{g\mu_B}{\hbar}\hat{S}_z B_0 \\
&= \frac{g\mu_B B_0}{\hbar}\frac{\hbar}{2}\hat{\sigma}_z \\
&= \frac{g\mu_B B_0}{\hbar}\frac{\hbar}{2}\begin{pmatrix} 1 & 0 \\ 0 & -1 \end{pmatrix} \\
&= \frac{g\mu_B B_0}{2}\begin{pmatrix} 1 & 0 \\ 0 & -1 \end{pmatrix}.
\end{aligned}$$

The energy of our two spin states is then given by

$$\begin{aligned}
\hat{H}\left|\uparrow_z\right\rangle &= \frac{g\mu_B B_0}{2}\left|\uparrow_z\right\rangle \\
&= \Omega\frac{\hbar}{2}\left|\uparrow_z\right\rangle, \\
\hat{H}\left|\downarrow_z\right\rangle &= -\frac{g\mu_B B_0}{2}\left|\downarrow_z\right\rangle \\
&= -\Omega\frac{\hbar}{2}\left|\downarrow_z\right\rangle.
\end{aligned}$$

The presence of the external magnetic field breaks the energy degeneracy of the two spin states, which were otherwise identical. This spin splitting, the energy difference $\hbar\Omega = g\mu_B B_0$, is called *Zeeman splitting*. Spin up aligns with the external field, while spin down anti-aligns with the external field. Which spin state has higher energy depends on the sign of the electron g factor.

So far we have considered a single electron, but we do not deal with single electrons in our work. We are dealing with a number of electrons on the order of 10^{16} or more, which requires the concept of spin polarization. The spin polarization of a system is a measure of the net spin of the system. Mathematically, spin polarization P is defined as

$$P = \frac{n_\uparrow - n_\downarrow}{n_\uparrow + n_\downarrow}, \tag{1.2}$$

where $n_\uparrow$ and $n_\downarrow$ are the numbers of spin-up and spin-down electrons, respectively, corresponding to the chosen axis of quantization. Each spin up balances a spin down, so we have a nonzero spin polarization only when there is an imbalance between them.

1.3 Generation, Manipulation, and Detection

In order to facilitate the replacement of today's electronic devices with spin-based alternatives, a great deal of research focuses on using the same materials that industry has already adapted for electronics: semiconductors [6]. For a brief overview of advances in semiconductor spintronics and the considerations specific to this field, see Ref. [7]. For each material that we consider, we must answer three important questions about the polarization, or alignment, of spins [8]:

1. How do we effectively generate spin polarization?
2. What factors impact the ability of the spins to stay polarized?
3. How do we effectively detect spin polarization?

Only by identifying answers to all three questions can the field of spintronics move forward. Each answer is material-specific; a method that generates spin polarization in one material may not work in another. For example, optical orientation is our chosen method for generating electron spin polarization in gallium arsenide, a historically vital platform for studying electron spin dynamics. This method fails in silicon, the most commonly used semiconductor in modern-day electronics. Data processing applications require the encoding of information into a population of electrons whose spins will stay polarized long enough to carry out the necessary logical operations. Thus, understanding electron spin dynamics in a material is necessary before devices can be fabricated.

1.4 Dissertation Outline

In this dissertation, we first address the questions of electron spin polarization generation, manipulation, and detection in gallium arsenide. This serves as necessary background for understanding our experimental techniques. Once we have established our methods and optical setup, we present two main areas of focus, current-induced spin polarization (CISP) and dynamic nuclear polarization (DNP).

In Chapter 2, we introduce two methods for generating electron spin polarization in gallium arsenide, optical orientation and CISP. We then present an overview of the factors that affect electron spin polarization, using the Bloch equation for spin dynamics to guide our discussion. The chapter culminates in a derivation of spin polarization in the regime of resonant spin amplification.

In Chapter 3, we explain how we measure spin polarization in our materials. After a brief section on Faraday/Kerr rotation, we describe our experimental setup. This is accompanied by a discussion of lock-in measurement techniques.

Chapter 4 is a compilation of all of the experimental techniques that were used in collecting the results shown in this dissertation. For each technique, a schematic is presented alongside example data and the relevant fit equations.

Chapter 5 describes the use of modified voltage waveforms for CISP measurements. This modification to our standard CISP generation technique enables experiments at larger applied currents while reducing current heating. Removing ambiguity due to heating effects will prove useful for future fundamental studies of CISP. This work has been previously published in AIP Advances [9].

Chapter 6 introduces a novel interaction between electron and nuclear spin systems in which field-resolved Kerr rotation measurements display a magnetic-field-sweep-direction-dependence. That is, increasing the external field yields different results than decreasing the external field over the same field range, as first reported in Physical Review B [10]. We present a physical model for understanding this DNP, previously published in Physical Review B [11]. We devote the bulk of the chapter to our experimental findings, interpreting them in light of the model.

In Chapter 7, we approach our DNP discussion from the perspective of nuclear-induced frequency focusing (NIFF), lending greater insight into our studies. We then examine a novel class of field sweeps that debuted in Ref. [10] and use them to propose alterations to our model intended to better represent our physical system. This work is currently in preparation for publication.

Future outlook on these and other projects is presented in Chapter 8.

Two appendices are included. Appendix A contains full derivations for resonant spin amplification, with and without the influence of the optical Stark effect (featured in Chapters 2 and 6, respectively). Appendix B presents an extended derivation of Faraday rotation and an analogous derivation for Kerr rotation.

CHAPTER 2

Generation and Manipulation of Electron Spin Polarization

2.1 Motivation

The key to making spintronic devices a reality is to identify a material platform in which a spin polarization can be generated and manipulated. Whether the eventual application is data storage or processing, the venture cannot even begin if there is no spin polarization. While a ferromagnet may feature a spin polarization without any positive action on our part, most materials of interest are not spin-polarized at equilibrium. Thus, we must utilize techniques to generate a non-equilibrium spin polarization.

Most applications then require some way to interact with that spin polarization. Even if we are content to just generate a spin polarization and then detect it, we need to know what is happening to the spin polarization between those two steps. We present an overview of the factors that affect spin polarization in our material, culminating in the Bloch equation. From there, we derive an expression for the expected spin polarization in our material under periodic optical pumping.

2.2 Generation of Electron Spin Polarization

There exist multiple approaches to generating electron spin polarization, reflecting the multiple disciplines within condensed matter physics. Each approach will be better suited to certain materials and applications. For example, researchers working with magnetic materials may prefer to utilize the spin-polarized carriers that are already present. Researchers looking to integrate spintronics with existing solid-state technologies might prefer an electrical-based approach. We consider one such mechanism, current-induced spin polarization.

However, the future of electronics may lie in communication via light. In this scheme, spin generation by light may be ideal. Optical orientation is the primary method used in our research group. To understand why these two methods generate a spin polarization, we must take a closer look at the material that will provide the context for the rest of this dissertation: gallium arsenide (GaAs).

2.2.1 Concept: Optical Orientation

Optical orientation, or optical spin pumping, is the use of light to generate a spin polarization [8]. In addition to electrons, holes or quasiparticles such as excitons can also be the target of optical orientation. The term *orientation* refers to previously unpolarized electrons having their spins oriented along a particular direction. At its simplest, optical orientation is the application of two fundamental laws of physics, conservation of energy and conservation of momentum. It is the transfer of energy and angular momentum from incident light to electrons, resulting in spin polarization.

More specifically, optical orientation is the exploitation of optical selection rules in a material such that certain transitions are favored. When the transitions result in an uneven number of spin-up and spin-down electrons, a spin polarization is formed. The details are heavily dependent on the material under study, and so this optical method may not be valid in some materials. Specifically, this method is used in semiconductor materials with a direct band gap. We restrict our attention to GaAs, a III-V semiconductor in the zincblende crystal structure. This analysis will cover the alloy InGaAs as well.

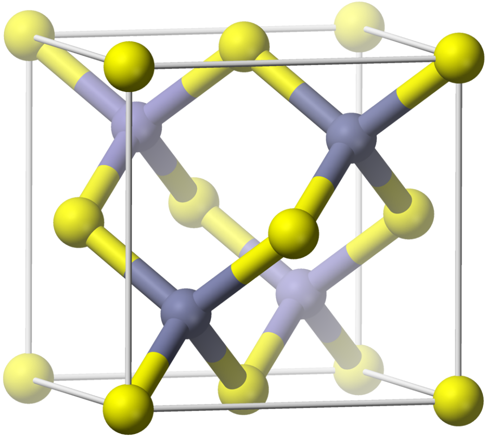

Figure 2.1: Cartoon representation of the crystal structure of GaAs, the zincblende structure. Yellow (gray) spheres represent the gallium (arsenic) atoms. Image generated by Wikimedia user benjah-bmm27.

2.2.2 Example: Optical Orientation in Zincblende (GaAs)

Gallium arsenide (GaAs) is a binary compound consisting of the group III element gallium and the group V element arsenic. The atoms form a zincblende crystal structure, as shown in Fig. 2.1. The yellow (gray) spheres indicate gallium (arsenic) atoms. Notably, the zincblende structure lacks an inversion center, meaning there is no point such that the lattice looks the same in all directions. More specifically, if the crystal were inverted (right becomes left, for example), the difference would be noticeable. This bulk inversion asymmetry is a key factor when considering spin-orbit fields, which we briefly discuss later in this chapter.

Electrons in a crystal lattice behave differently than free electrons. They behave like a particle with an effective mass m^* rather than the standard electron mass m_0. Similarly, the correspondence between the spin of the electron and its magnetic moment is modified by the g factor. This will become important when it comes to spin precession. The electron momentum becomes quantized as crystal momentum k, and the atomic lattice determines the energy states available to electrons in the crystal. There are a myriad of energy bands

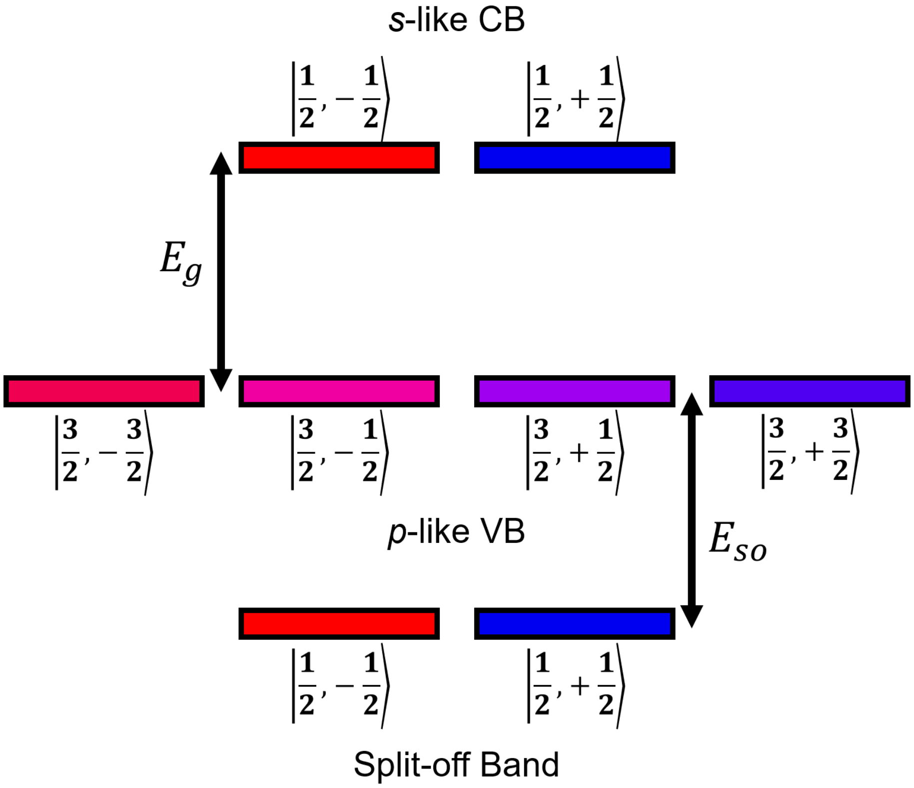

Figure 2.2: Available electron states at the Γ point in GaAs. The conduction band states are separated from the heavy hole and light hole states by the band gap energy E_g. The split-off band is separated further by E_{so}. Level separations are not to scale.

with varying relations between the crystal momentum and the energy E. In pure GaAs, all energy bands are filled up through a particular band known as the valence band (VB). The next energy band, which is empty, is the conduction band (CB). The energy difference between the VB and CB is the band gap E_g. Mathematical methods allow us to compute these bands as a function of electron crystal momentum, with particular details (like the band gap energy) determined by the particular atoms involved. For a thorough treatment of crystal structure and the ramifications on the states of the electrons in a crystal, see any graduate condensed matter textbook, such as that by Ashcroft and Mermin [12].

GaAs has a direct band gap, so the minimum of the conduction band occurs at the same crystal momentum as the maximum of the valence band. These occur at the Γ point, with crystal momentum of zero. This is the point of interest for us for optical orientation, where no phonons are required to elicit a transition from the VB to the CB.

The VB is really three distinct bands, separated in energy by a much smaller margin than the band gap. The two higher-energy bands are known as the *heavy hole* and *light hole* bands based on their curvature. They are degenerate at the Γ point and separate for nonzero crystal momentum. The split-off band is literally split off from the two other valence bands by an energy E_{so}.

Knowing the band structure at the Γ point informs us of the available electron states, which we can represent by the total angular momentum J, a combination of orbital momentum L and spin angular momentum S. The axis of quantization for spin is the optical axis, determined by the propagation of the light. An in-depth description of the system would be framed in terms of the symmetry properties of the bands [13]. Here, however, we will assume the results of the band structure calculation and apply the conservation laws of energy and momentum.

At the Γ point, the conduction band states are s-like. That is, they are like electron states with orbital angular momentum $l = 0$. Their total angular momentum is just their spin angular momentum. The valence bands are instead p-like. The p-orbitals are combinations of $l = 1$ orbital angular momentum eigenstates, so the total angular momentum is obtained by mixing $s = 1/2$ and $l = 1$. This results in six potential electron states, two with total angular momentum $J = 1/2$ and four with total angular momentum $J = 3/2$. These are shown in Fig. 2.2.

The $J = 1/2$ states require a different energy than the other states to be excited to the conduction band, $E_g + E_{so}$. These split-off band states have the same total momentum as the conduction band states, so no additional momentum is required to effect the transition. Light with zero angular momentum evenly excites both spin-up and spin-down electrons from the split-off band to the conduction band, resulting in zero net spin polarization.

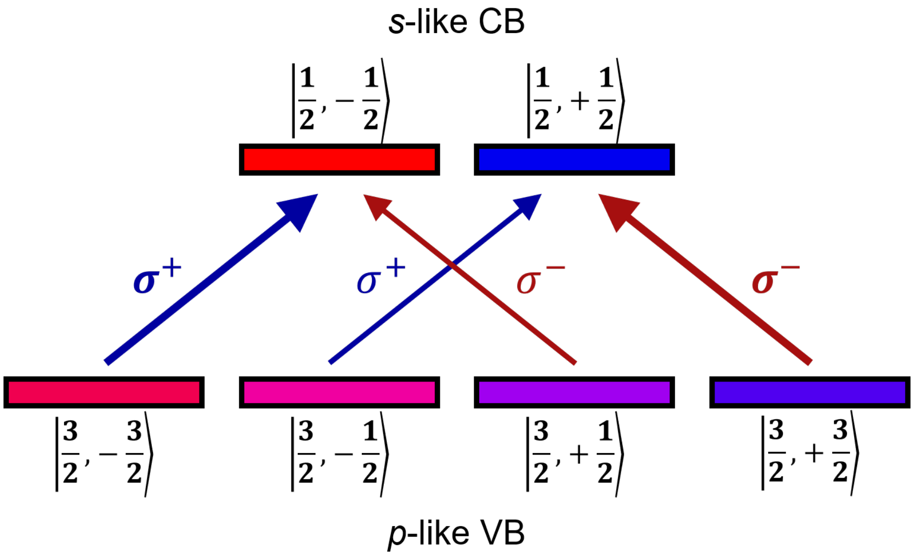

Figure 2.3: Allowed optical transitions in GaAs between the valence band and conduction band linked by σ^+ and σ^- light. The relative strengths of the transitions are 3:1 heavy-hole to light-hole, as described in the text.

Instead, we consider the $J = 3/2$ states corresponding to the heavy hole ($m_j = \pm 3/2$) and light hole ($m_j = \pm 1/2$) states. They are degenerate in energy, so we need light at the band gap energy to excite the transitions. The total momenta of these states do not match the conduction band states, so we require angular momentum transfer from light. While electrons are spin-1/2, photons are spin-1. There are three possible angular momentum states for light: $-\hbar$ (denoted σ^-), 0 (sometimes denoted π), and $+\hbar$ (denoted σ^+). The σ^+ and σ^- photons are circular polarization. The exact correspondence to right-hand and left-hand polarization is based on convention; we elect not to decide one way or the other, using only the σ notation for simplicity.

Because the total electron momentum is also given in units of $\hbar$, circularly polarized light can connect valence and conduction band states with m_j that differ by ± 1. Thus, σ^+ light can excite electrons from the $m_j = -3/2$ and the $m_j = -1/2$ valence band states to the $m_j = -1/2$ and $m_j = +1/2$ conduction band states, respectively. Similarly, σ^- enables transitions from the $m_j = +1/2$ and $m_j = +3/2$ states. This fact would have no use if each transition were excited with equal probability. Fortunately, these transitions feature different probabilities, or oscillator strengths. Calculations with the states themselves yield a 3:1 ratio between the heavy hole and light hole states. Put another way, σ^+ light excites three times as many electrons from the $m_j = -3/2$ state as the $m_j = -1/2$ state. This means our conduction band will have three times as many spin-down electrons ($3n_0$) as spin-up electrons (n_0). This is a 50% spin polarization:

$$\begin{aligned} P &= \frac{n_\uparrow - n_\downarrow}{n_\uparrow + n_\downarrow} \\ &= \frac{n_0 - 3n_0}{n_0 + 3n_0} = -\frac{2n_0}{4n_0} = -\frac{1}{2}. \end{aligned} \tag{2.1}$$

Rather, it is a −50% spin polarization. The transitions are outlined in Fig. 2.3.

In practice, we do not usually measure 50%. Each optically oriented spin-polarized electron leaves a hole with the opposite spin. They will want to recombine, returning the electron to the valence band. Pure GaAs has an empty conduction band at equilibrium, so all of the excited electrons will return to the valence band. We will lose the spin polarization on the timescale of the optical recombination time, which in GaAs is on the order of a few hundred picoseconds. As we will discuss shortly, spin polarization does not persist indefinitely, but even if it did, we would lose it to electron-hole recombination. Hence, we work with doped materials. The GaAs considered in this dissertation is n-doped with doping density on the order of 10^{16} cm^{-3}. At equilibrium (and depending on temperature), we will have a large number of electrons already in the conduction band. Now consider optical orientation again, but with the 50% spin-polarized electrons added to a pool of unpolarized conduction band electrons. The holes in the valence band are effectively p-states. This is a different orbital angular momentum from the s-states, and the spin-orbit interaction plays a role in spin relaxation. The stronger spin-orbit coupling leads to stronger relaxation, so the hole spin polarization does not last as long as the electron spin polarization in the conduction band.

In fact, we expect the hole spins to become depolarized in hundreds of picoseconds. This leaves us with polarized electrons and unpolarized holes, along with all the extra unpolarized electrons already in our conduction band. The holes will recombine, but not exclusively with the polarized electrons. Our electron spin polarization will persist, albeit at less than 50%.

We stress again that this method only holds for the zincblende crystal structure. Though this is by no means universal, it is a useful mnemonic to remember that the valence band states with triple the momentum projection m_j result in triple the conduction band electrons.

2.2.3 Example: Optical Orientation of Donor-Bound Excitons

The inclusion of dopant atoms allows for new electron states to emerge. High enough doping levels can lead to a doping density past the metal-insulator transition, causing our material to function more closely to a metal than an insulator. For GaAs, the critical doping density is 2×10^{16} cm^{-3}, and the doping level has ramifications for the dominant spin relaxation mechanisms present [14].

In n-GaAs, silicon donor atoms replace gallium atoms. Being in group IV, silicon atoms possess an additional electron. At high temperatures, thermal energy is enough to ionize most of these donors, leading to a higher density of free carriers. As temperature drops, more electrons remain localized to their donors. This allows for a new electron state, the donor-bound exciton (represented notationally as $\mathrm{D}^0\mathrm{X}$). In lower-dimensional systems, this state is known as the charged trion. Rather than promoting an electron directly from the valence band to the conduction band, which can form, with a hole, a free exciton (notationally X), the exciton can bind to a donor electron. This creates a new state consisting of two electrons and one hole. The electrons have opposite spin, so the trion spin is determined by the hole. The overall charge of the three particles matches the electron charge, hence the “charged” trion. When accounting for the donor atom, the system has no net charge. The excitation

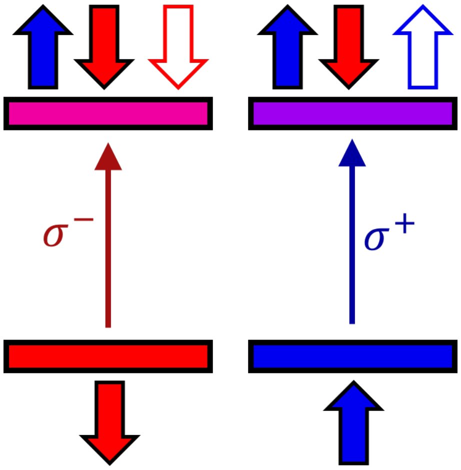

Figure 2.4: Allowed optical transitions between donor-bound electrons and the donor-bound exciton ("charged trion") linked by σ^+ and σ^- light.

energy for this state is slightly lower than that needed for the free exciton.

With new electron states come new optical selection rules. Instead of bands, the donor-bound exciton is best described as a two-level system, with each level separated into its two spin states. A full quantum-mechanical treatment of this system can be found in Ref. [15]. Here, we present the outcome of the calculations, shown graphically in Fig. 2.4. Unlike the bulk system, each of the spin-split excited states is only accessible through one excitation polarization.

The electron pair is in a singlet state, so they do not precess in an external magnetic field (more on precession later in this chapter). The hole here is a heavy hole. We still expect that hole spin lifetime is shorter than electron spin lifetime. The holes in these donor-bound excitons will depolarize first; then the holes will recombine with one of the electrons. For example, based on the selection rules, σ^+ light will excite spin-up donor-bound excitons from spin-up electrons. The spin-down donor-bound electrons remain unaffected. The depolarization of the holes leads to depolarization of the donor-bound excitons, returning donor-bound electrons having no net spin polarization. However, this results in an imbalance after all, since we converted a number of spin-up donor-bound electrons to spin-down electrons through depolarization and recombination. Thus we obtain an overall electron spin polarization, with the D^0X state as a pathway to get there. The overall sign of this polarization will match the sign for polarization generated by σ^+ in bulk. See Refs. [16] and [17] for further elaboration. This state will be key to understanding nuclear spin polarization in Chapter 6.

2.2.4 Concept: Current-Induced Spin Polarization

For certain materials, application of an external electric field forces the generation of an electron spin polarization. This effect is innately tied to the crystal structure of the material. The crystal direction along which the electric field is applied determines the axis along which the electron spins will orient. When we utilize this method to generate spin polarization, we choose a crystal direction for the current such that the induced spin polarization is in-plane, perpendicular to that crystal direction. For GaAs and its alloy InGaAs, the crystal directions of interest are [110] and $[1\bar{1}0]$. See Fig. 2.5 for a simple schematic. Contrast this with the spin polarization generated by optical orientation, where the axis of quantization is along the optical axis. For our experimental geometries, these two methods would generate spin polarization along orthogonal directions. Our laboratory has exploited this fact to generate nuclear polarization along the CISP direction, which can be measured through its effect on the optically generated electron spin polarization [18].

While we know how to generate CISP in the laboratory, the precise mechanisms that lead to the spin polarization are still under study. Multiple effects are thought to play a role, from spin-orbit fields (discussed below) to the spin Hall effect [19]. Our laboratory has previously investigated how the induced polarization varies based on material parameters such as spin-orbit fields, doping density, and strain [20]. It has been shown that structural inversion asymmetry may be necessary, as GaAs epilayers like the one studied in Chap-

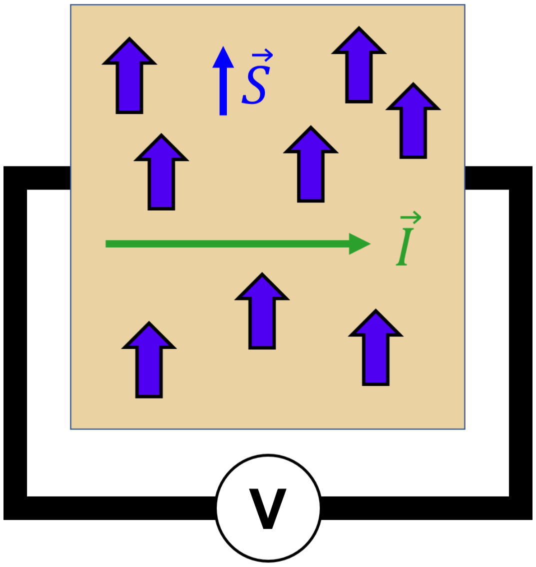

Figure 2.5: Cartoon representation of current-induced spin polarization. A voltage is applied across a material, generating a current through it (green thin arrow) that orients the electron spins (blue thick arrows). We choose the direction of the current to polarize the electrons in-plane, perpendicular to the direction of current.

ter 6 did not yield appreciable CISP, in contrast to InGaAs epilayers like the one studied in Chapter 5 which feature uniaxial strain along the growth direction due to alloying. We demonstrate a modified experimental technique in Chapter 5 to aid future research into CISP.

2.3 Manipulation of Electron Spin Polarization

Once we have generated an electron spin polarization, any steps toward information storage or processing would occur next. These can be electrical or optical in nature, with the time required based on the specific operation. For more details on some of these goals and methods, see Ref. [8].

However, the spin polarization will not persist indefinitely. There are mechanisms at work in our material that will return the electron spin polarization to its equilibrium value, which will usually be zero. Thus, a key component of manipulation is understanding how long spin polarization will last. More specifically, we want to understand the time evolution of our spin polarization.

2.3.1 Concept: The Bloch Equation

In 1946, Felix Bloch proposed a phenomenological equation to describe the time dynamics of a magnetization in an external magnetic field [21]. The eponymous Bloch equation was written for a classical magnetization and intended for application to nuclear magnetic resonance (NMR) imaging. Electron spin polarization, like nuclear spin polarization, can be treated as a macroscopic magnetization, so the equation holds for our purposes as well, remarkably. Even though individual electrons have a defined spin with respect to the axis of quantization when measured, we can write spin polarization as the classical pseudovector $\vec{S}$. We determine the components of this vector along the coordinate axes S_x, S_y, and S_z separately or simultaneously, which would not be possible at the quantum level.

The Bloch equation for our system can be written as

$$\frac{\partial \vec{S}}{\partial t} - \vec{\Omega} \times \vec{S} + \vec{\Gamma} \cdot \vec{S} - \Gamma_{\text{eff}} \vec{S}_{\text{eq}} = \vec{\gamma}, \tag{2.2}$$

where $\vec{\Gamma}$ is here the *spin relaxation tensor*, $\vec{\Omega}$ is the axis of *spin precession* with *Larmor precession frequency* Ω, Γ_{eff} describes relaxation to the *equilibrium spin polarization* $\vec{S}_{\text{eq}}$, and $\vec{\gamma}$ describes *spin polarization generation* [22]. An extension by Torrey incorporates a term describing spin diffusion, yielding a version of the equation referred to as the Bloch-Torrey equation [23]. Spin diffusion can play a large role in some systems, but in our GaAs epilayers we are safe to ignore it.

While the initial formalism was classical in nature, spin density matrix formalism results in a "microscopic" quantum version of the Bloch equation that is then extended to the macroscopic scale [17].

Before we solve this equation, we consider each term and what it means for our electron spin system. For optical orientation, this generation term is a delta function in time, with the spin polarization formed at $t = 0$. We will solve the equation for all subsequent times, letting us set $\vec{\gamma} = 0$. For CISP, this is a constant vector quantity so long as the current is applied. In the next few sections, we will walk through the remaining terms in the Bloch equation, describing the underlying physics and connecting the phenomenological to the quantum principles. Then we can solve the Bloch equation and know what to expect when we carry out our measurements.

2.3.2 Concept: Electron Spin Precession

The first term we consider in the Bloch equation is the term describing electron spin precession in the presence of a magnetic field:

$$\vec{\Omega} \times \vec{S}.$$

Remember that spin is an intrinsic angular momentum. In classical mechanics, a rotating body has an axis of rotation with an angular velocity. Precession is the change in the orientation of this axis in time. Thus, precession is a change in the orientation of the spin pseudovector.

Classical physics can grant us greater insight. A magnetic moment $\vec{m}$ placed in an external magnetic field $\vec{B}$ will change in time following the equation

$$\frac{d\vec{m}}{dt} = \gamma \vec{m} \times \vec{B},$$

where γ is the gyromagnetic ratio connecting the moment to angular momentum. This classical equation describes the precession of a magnetic moment in an external field, known as Larmor precession. If we run with the analogy that spin polarization is a magnetic

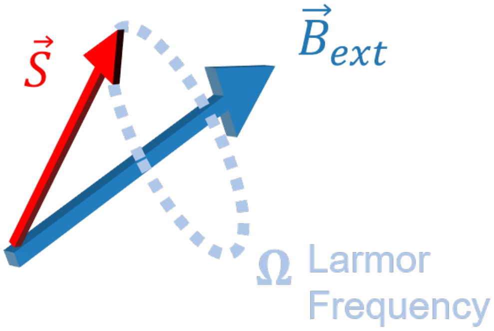

Figure 2.6: Cartoon representation of a spin polarization $\vec{S}$ precessing about an external field $\vec{B}_{\mathbf{ext}}$. The angular velocity of precession is the Larmor precession frequency Ω.

moment, we can rewrite this equation for spin. Replacing $\vec{m}$ with $\vec{S}$,

$$\begin{aligned}\frac{d\vec{S}}{dt} &= \vec{S} \times \left(-\frac{g\mu_B}{\hbar}\vec{B}\right) \\ &= \frac{g\mu_B}{\hbar}\vec{B} \times \vec{S} \\ &= \vec{\Omega} \times \vec{S},\end{aligned} \tag{2.3}$$

where we have defined the Larmor precession frequency Ω as $g\mu_B B/\hbar$. This term is often designated ω_L in the literature. Thus, spin polarization will precess about the external field with angular velocity Ω (Fig. 2.6).

The experiments described in this dissertation require the presence of a magnetic field external to the material under study. The external field will reorient the direction of the spin polarization, moving it in a direction transverse to the direction of the field itself. Components of the spin polarization along the external field direction will be unaffected.

This classical analogy holds at the microscopic level as well. If we were to measure the spin of a single electron, our measurement would still only produce either $-\frac{\hbar}{2}$ or $\frac{\hbar}{2}$. Precession does not change this fact, but it does change the probability of these outcomes, and that is essentially what we are measuring when we measure spin polarization. We will take a short detour into quantum mechanics to show that precession does emerge at the level of a single spin.

Our definitions and derivation are based on Ref. [5]. For a transverse magnetic field applied along $\hat{x}$, our Hamiltonian takes the form:

$$\begin{aligned}
\hat{H} &= -\hat{\vec{m}} \cdot \vec{B} \\
&= \frac{g\mu_B}{\hbar}\hat{\vec{S}} \cdot \vec{B} \\
&= \frac{g\mu_B}{\hbar}\hat{\vec{S}} \cdot B_0\hat{x} \\
&= \frac{g\mu_B}{\hbar}\hat{S}_x B_0 \\
&= \Omega\hat{S}_x.
\end{aligned}$$

We are interested in the dynamics, so we must incorporate time-dependence. The field, and thus the Hamiltonian, do not change in time. There are two potential paths forward. One is to adopt the Schrödinger picture, in which the quantum states evolve in time. We will instead prefer the Heisenberg picture. In this rendering of quantum mechanics, quantum states remain fixed in time and the operators evolve. We compute the time-dependence of our measurement, the spin component along $\hat{z}$, by computing the time-dependence of the operator S_z:

$$\begin{aligned}
\frac{d\hat{S}_z}{dt} &= \frac{i}{\hbar}\left[\hat{H}, \hat{S}_z\right] \\
&= \frac{i}{\hbar}\left[\frac{g\mu_B}{\hbar}\hat{\vec{S}} \cdot \vec{B}, \hat{S}_z\right] \\
&= \frac{i}{\hbar}\frac{g\mu_B}{\hbar}\left[\vec{S}_x B_x + \vec{S}_y B_y + \vec{S}_z B_z, \hat{S}_z\right] \\
&= \frac{i}{\hbar}\frac{g\mu_B}{\hbar}\left(B_x\left[\vec{S}_x, \hat{S}_z\right] + B_y\left[\vec{S}_y, \hat{S}_z\right] + B_z\left[\vec{S}_z, \hat{S}_z\right]\right) \\
&= \frac{i}{\hbar}\frac{g\mu_B}{\hbar}\left(-i\hbar B_x\vec{S}_y + i\hbar B_y\vec{S}_x\right) \\
&= \frac{g\mu_B B_x}{\hbar}\vec{S}_y - \frac{g\mu_B B_y}{\hbar}\vec{S}_x \\
&= \Omega_x\vec{S}_y - \Omega_y\vec{S}_x \\
&= \epsilon_{zjk}\Omega_j\vec{S}_k.
\end{aligned}$$

In the last line, we wrote the equation in Einstein notation using the Levi-Civita symbol. The time evolution of our S_z measurements is then obtained by taking the expectation value of both sides. The move to Einstein notation reveals that this equation is the z-component of a cross-product. We can easily move to the time-dependence of the full vector operator $\hat{\vec{S}}$:

$$\begin{aligned}\left(\frac{d\hat{\vec{S}}}{dt}\right)_i &= \epsilon_{ijk}\Omega_j\vec{S}_k \\ \frac{d\hat{\vec{S}}}{dt} &= \vec{\Omega} \times \hat{\vec{S}}. \end{aligned} \tag{2.4}$$

We can obtain the expected value of our measurements by taking the expectation value of both sides. Using a quantum picture, we obtain an expression for spin precession matching the classical outcome, just with the spin pseudovector replaced by spin operators. This result gives us confidence in applying the classical reasoning to our quantum system.

2.3.3 Aside: Spin-Orbit Fields

External magnetic fields are not the only source of magnetic fields in our material. Electrons moving through the crystal lattice will experience Coulomb interactions with the atoms that compose the material. These interactions depend on the direction and momentum with which the electrons are traveling, or more properly, on their crystal momentum k. When electrons begin to approach relativistic speeds, a purely electric field in our inertial reference frame may appear as a magnetic field in theirs [24]. Thus, electrons traveling through the crystal will experience effective magnetic fields. These fields play a substantial role in loss of electron spin polarization.

The spin-orbit fields can be explicitly written in terms of the crystal momentum of the electron, proceeding from an effective Hamiltonian. We omit the details but present the main ideas behind two types of spin-orbit splitting. For materials like GaAs that lack bulk inversion symmetry, the effective magnetic fields due to spin-orbit coupling are proportional to the cubed crystal momentum: k^3. Technically, it is proportional to a product of three components of $\vec{k}$, such as $k_y k_x^2$. This is the Dresselhaus spin-orbit splitting [25]. Another type of symmetry is structural inversion symmetry. This symmetry is broken along the growth direction in heterostructures. It is also naturally broken in wurtzite crystal structures, as those feature a potential gradient along the [001] direction due to the arrangement of the atoms. An external applied electric field would have the same effect. In crystals with structural inversion asymmetry, a different spin-orbit splitting emerges that is linear in k, Rashba splitting [26, 27]. We expect Rashba splitting in InGaAs due to the strain of alloying but not in bulk GaAs.

Usually, we presume that we are working with electrons at the Γ point, or that we are averaging over the various crystal momenta. Individual electrons experience spin-orbit fields, but we would not usually expect to see them manifest as magnetic fields in our experiments. By applying an external electric field, or voltage, to our material, we can cause the electrons to move with a particular crystal momentum. Measuring this electron spin packet as it moves through the crystal, we can detect the spin-orbit fields through magneto-optical means. The *spin drag* experimental technique measures the change in precession frequency of the electron spin packet due to spin-orbit fields oriented both parallel and perpendicular to an external magnetic field. While this experiment did not factor directly into our study of CISP in Chapter 5, the details of spin drag are provided for reference in Chapter 4.

Our samples are processed with electrical contacts that allow for voltage to be applied in either the [110] or [$1\bar{1}0$] crystal directions. These special crystal directions are selected because both the Dresselhaus and Rashba spin-orbit fields are oriented perpendicular to the crystal axes. That is, the spin-orbit fields are perpendicular to the motion of the spin packet. These are also the crystal directions that allow for CISP oriented in the plane of the sample.

For a more detailed treatment of spin-orbit fields and the considerations that go into these experiments, see Refs. [22, 28].

2.3.4 Concept: Spin Lifetime

A key concern for any spintronic application is spin *relaxation* or *decay.* This is a natural loss of spin polarization independent of any actions we take. Spin polarization naturally decays to its equilibrium value, which is usually zero in our materials of interest like GaAs. This decay tends to be exponential, but it shows up in the Bloch equation as the term

$$\vec{\Gamma} \cdot \vec{S}.$$

Here, $\vec{\Gamma}$ is a tensor, allowing for relaxation to differ for each spatial direction. The elements of the tensor Γ_{ij} are the spin decay rates. While each of these elements can in principle be nonzero, we can choose crystal axes such that the tensor is diagonalized. This is the case in GaAs for the basis formed by the crystal directions [110], $[1\bar{1}0]$, and [001]. By this point, we have emphasized three times in this chapter why these axes are of special interest to researchers. Rather than talk about relaxation rates, we would prefer to talk in terms of characteristic timescales.

In addition to the Bloch equation, we will also borrow terminology from the NMR community to describe the various timescales for spin relaxation. These times are all defined with respect to the application of an external magnetic field and apply to any type of spin polarization, not just electrons. The three main timescales for spin relaxation and a simple

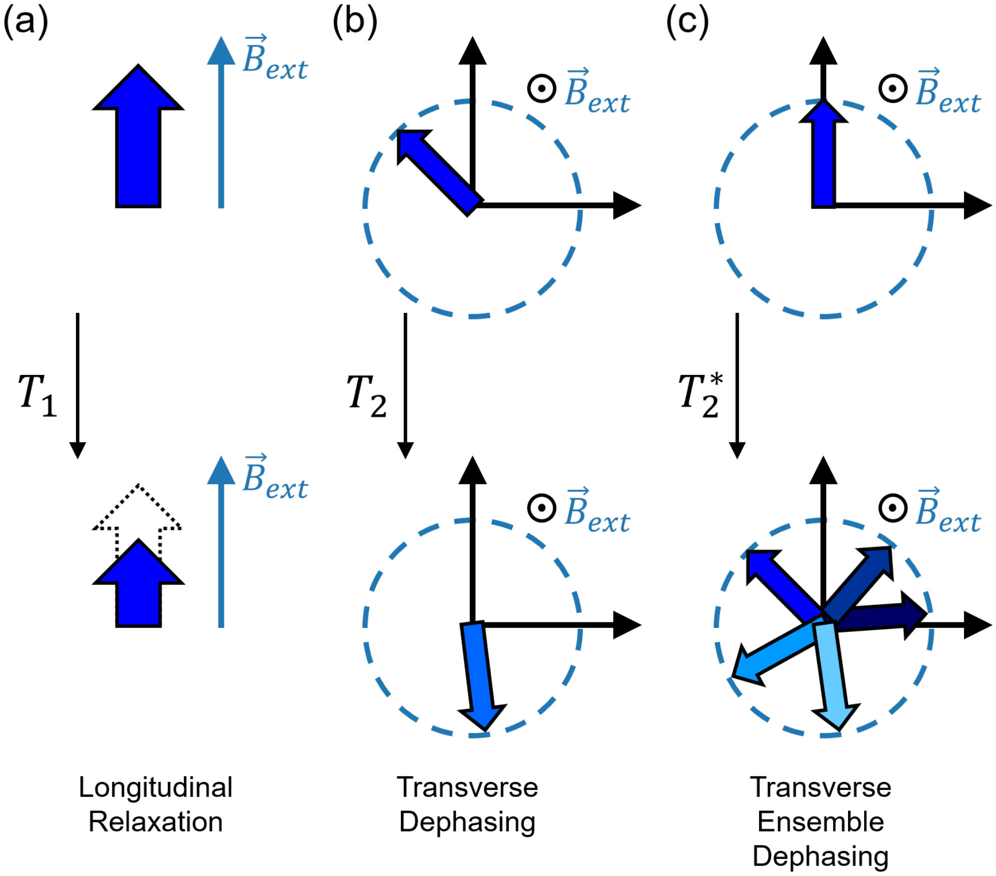

Figure 2.7: Cartoon representation of the three timescales for spin relaxation. (a) Longitudinal relaxation is represented by time T_1 and describes the reduction in spin polarization magnitude parallel to an applied magnetic field. (b) Transverse dephasing is represented by time T_2 and describes the loss of spin coherence in a direction perpendicular to an applied magnetic field. (c) Transverse ensemble dephasing is a reversible effect represented by time T_2^* and describes the loss of coherence among an ensemble of electrons each precessing with a slightly different frequency.

interpretation for each are

1. T_1: longitudinal relaxation
2. T_2: transverse dephasing (homogeneous)
3. T_2^*: transverse ensemble dephasing (inhomogeneous)

The timescales and interpretations are represented graphically in Fig. 2.7.

The longitudinal relaxation time T_1 describes the exponential decay time for spin polarization aligned along the external magnetic field direction. We can think of this as the polarization simply shrinking in size towards its equilibrium value. It is worth acknowledging that a single electron can only have spin up or down along the magnetic field direction (no fractional spins). This relaxation is caused by spin flips which reduce the imbalance of spin-up and spin-down electrons.

The transverse dephasing time T_2 describes relaxation in a direction perpendicular to the external magnetic field. Rather than shrinking, this is the irreversible loss of phase information. Put another way, this is the time it takes for the spin to lose the relationship between its current orientation and its original orientation. There can be distinct T_2 times for each perpendicular direction. This is a homogeneous dephasing time because it can affect even a single spin.

The transverse ensemble dephasing time T_2^* is unique in that it only emerges when there are multiple spins present. The spins all start out with definite phase relationships, but through local fluctuations, this relative phase information is lost. For example, spatially separated electrons may feel slightly different effective magnetic fields due to spin-orbit coupling. Alternatively, electrons in different locations in the crystal structure may have slight variations in g factor. Either way, the electrons will precess at slightly different Larmor precession frequencies. Very quickly, the spins will no longer be aligned, resulting in an overall loss of spin polarization. This dephasing time is inhomogeneous because it relies on some factor that causes spins to react differently to the application of an external field. In general, we expect that our measurements for transverse spin dephasing yield the ensemble dephasing time, which should never exceed the homogeneous dephasing time, $T_2^* \leq T_2$. In contrast to T_2, this dephasing is technically reversible. Spin-echo experiments can “undo” inhomogeneous dephasing, allowing us to measure T_2 instead [29, 30].

In summary, we make a distinction between longitudinal and transverse spin decay. Most properly, longitudinal decay is “relaxation” and transverse decay is “dephasing”, but we tend to use these terms interchangeably with “decay” in our experiments. In isotropic systems, $T_1 = T_2$, and these terms really do refer to the same timescale. Going forward, we consider spin systems with transverse magnetic fields, and we will use T_2^* or even the more general τ to stand in for the spin relaxation time, which we will at last term the *spin lifetime.* This measure gives us an idea of long our spin polarization will last.

For an isotropic system with an external magnetic field applied along $\hat{x}$, the spin relaxation tensor will take the form

$$\vec{\Gamma} = \begin{pmatrix} \frac{1}{T_1} & 0 & 0 \\ 0 & \frac{1}{T_2^*} & 0 \\ 0 & 0 & \frac{1}{T_2^*} \end{pmatrix},$$

where we have distinguished between T_1 and T_2^* to drive home the distinction in application.

Formulas for spin relaxation times can be derived based on the physical mechanism under consideration [8], but for our part we will treat these as phenomenological constants that cover all of the potential microscopic mechanisms. That said, it is worth briefly mentioning two main mechanisms that affect conduction band electrons, the D’yakonov-Perel’ and Elliott-Yafet mechanisms. They are represented graphically in Fig. 2.8.

We consider the relation between these mechanisms and electron scattering time. This is the average time that an electron can travel in the crystal before a scattering event, which will send the electron off with a new crystal momentum.

As an electron moves through the lattice, it will experience an effective magnetic field due to spin-orbit coupling. Suddenly, it scatters off a nucleus, emerging with a new crystal momentum. When it emerges from a scattering event, its new momentum will result in a different spin-orbit magnetic field and a new precession frequency. Each scattering event resets the precession axis and frequency for each electron. When we described ensemble spin dephasing, we noted that electrons experiencing different effective magnetic fields would

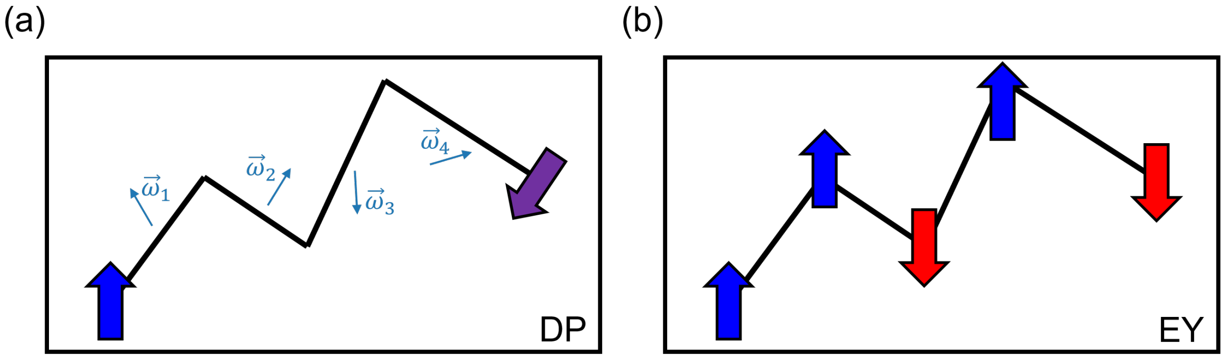

Figure 2.8: Cartoon representation of the D'yakonov-Perel' (DP) and Elliott-Yafet (EY) spin relaxation mechanisms. (a) The DP mechanism results from the effective magnetic fields experienced by individual electrons in the crystal, which depend on the electron's crystal momentum. When an electron scatters, it emerges with a new crystal momentum and experiences a different effective magnetic field than before the collision. These changes in individual electron precession frequencies and axes result in ensemble dephasing. (b) The EY mechanism results from scattering events that do not preserve the electron spin state. At each collision, the electron might flip to the other spin state. Eventually, this leads to spin relaxation. Figure adapted from Ref. [31].

dephase due to slight differences in Larmor precession frequency. If those frequencies remained fixed, the spins could eventually come back into alignment (a beating effect in the sum of two sinusoids). These scattering events randomize the individual electron precession frequencies, destroying the ability to re-phase the ensemble. This is the D'yakonov-Perel' relaxation mechanism (Fig. 2.8a) [32]. As a result, the relaxation time due to this mechanism is inversely proportional to scattering time.

The Elliott-Yafet spin relaxation mechanism can best be characterized as spin-flip transitions [33, 34]. When spin-orbit coupling is added to our Hamiltonian, energy eigenstates are no longer single spin states. That is, the lattice states mix spin-up and spin-down electron states. Individual electrons no longer conserve spin upon scattering, so every event is an opportunity to alter the spin polarization of the system. Scattering that results in the change of the electron spin state is a spin-flip transition (Fig. 2.8b). In contrast to the D'yakonov-Perel' mechanism, the Elliott-Yafet relaxation time is proportional to momentum scattering time. The more events, the more potential spin-flips.

Overall, spin relaxation mechanisms depend on a host of material and experimental parameters. For an in-depth study of spin lifetime in n-doped GaAs, see Ref. [14]. We turn our attention here to temperature.

Both D'yakonov-Perel' and Elliott-Yafet relaxation depend on temperature, especially as it affects momentum scattering. We must also be concerned about the thermal energy in the crystal. If this energy is comparable or exceeds the spin-splitting energy, spins can flip simply due to being hot enough. Now, this glosses over the difference between electron temperature and lattice temperature. Nevertheless, it is a general rule of thumb that spin polarization will persist for longer times at lower temperatures. As a result, we carry out our experiments at cryogenic temperatures. The measurements shown in this dissertation were obtained at either 10 K or 30 K. To achieve such low temperatures, we must use liquid helium and vacuum-pumped cryostats.

Working at low temperatures leads to a different set of considerations. For GaAs, we must account for nuclear spin polarization, the effects of which are present at 30 K and below. We introduce the concept of dynamic nuclear polarization at the conclusion of this chapter and present experimental studies in Chapters 6 and 7.

2.3.5 Example: Solving the Bloch Equation

We are now ready to solve the Bloch equation. We assume optical orientation, yielding a spin polarization S_0 initially generated along $\hat{z}$ at time $t = 0$, with no generation for all times thereafter. As is the case for GaAs, we assume no equilibrium spin polarization. We apply a transverse external magnetic field along $\hat{x}$. Lastly, for simplicity, we proceed with an isotropic relaxation tensor. This is perhaps the most egregious assumption we will make, and will fail when considering certain nanostructures that differ significantly along one of their axes. As it turns out, the eventual solution will not differ in form, and for bulk GaAs, this is close enough. Thus we seek a solution to the set of differential equations

$$\begin{aligned}
\frac{\partial \vec{S}}{\partial t} - \vec{\Omega} \times \vec{S} + \vec{\Gamma} \cdot \vec{S} &= 0, \\
\frac{\partial \vec{S}}{\partial t} - \Omega \hat{x} \times \vec{S} + \frac{1}{T_2^*} \vec{S} &= 0,
\end{aligned}$$

or in component form,

$$\frac{\partial S_x}{\partial t} + \frac{1}{T_2^*} S_x = 0, \tag{2.5a}$$

$$\frac{\partial S_y}{\partial t} + \Omega S_z + \frac{1}{T_2^*} S_y = 0, \tag{2.5b}$$

$$\frac{\partial S_z}{\partial t} - \Omega S_y + \frac{1}{T_2^*} S_z = 0. \tag{2.5c}$$

The x-component of the Bloch equation can be easily solved:

$$S_x\left(t, B_{\text{ext}}\right) = S_{0x} e^{-t/T_2^*}, \tag{2.6}$$

where S_{0x} is any initial spin polarization along $\hat{x}$. This spin polarization along the external field direction will simply decay exponentially without precession. For optical orientation, $S_{0x} = 0$, so $S_x = 0$ for all time. In Chapter 6, we will examine a situation where we do accumulate spin polarization along this direction.

The y- and z- components are coupled differential equations. Some algebraic manipulation allows us to decouple them:

$$\begin{aligned}
\ddot{S}_y + \frac{2}{T_2^*} \dot{S}_y + \left(\Omega^2 + \frac{1}{T_2^{*2}}\right) S_y &= 0, \\
\ddot{S}_z + \frac{2}{T_2^*} \dot{S}_z + \left(\Omega^2 + \frac{1}{T_2^{*2}}\right) S_z &= 0.
\end{aligned}$$

The solutions for both S_y and S_z will be decaying sinusoids. Specifying the initial condition that $S_z = S_0$ and $S_y = 0$ allow us to set the phases. All together, we arrive at the

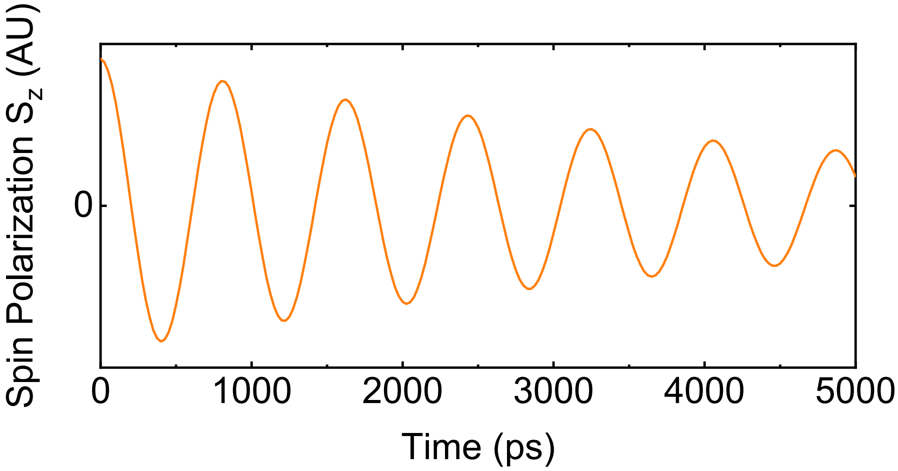

Figure 2.9: Time-dependent spin polarization component S_z as a function of time since spin generation. The Larmor precession frequency corresponds to that of a material with $g = -0.44$ (matching GaAs) in an external magnetic field of 200 mT. The spin lifetime is chosen to be 5 ns to show appreciable decay over this time range.

solutions to the Bloch equation:

$$S_x\left(t, B_{\text{ext}}\right) = 0, \tag{2.7a}$$

$$S_y\left(t, B_{\text{ext}}\right) = -S_0\, e^{-t/T_2^*} \sin\left(\Omega t\right), \tag{2.7b}$$

$$S_z\left(t, B_{\text{ext}}\right) = S_0\, e^{-t/T_2^*} \cos\left(\Omega t\right). \tag{2.7c}$$

Our spin polarization decays exponentially in time as it precesses in the yz-plane. Our measurements will exclusively measure S_z; thus we expect to measure a decaying sinusoid in time. The above equation for S_z is plotted in Fig. 2.9. This expression describes our measurements exceptionally well. In our experimental contexts, the time t takes on the interpretation of delay time between the generation event (the pump) and the detection event (the probe). For this reason, we often refer to these measurements as *delay scans*. We can alternatively measure as a function of applied magnetic field, which will be a sinusoid with amplitude determined by the time that has passed since the spin polarization was generated. We refer to magnetic-field-dependent measurements as *field sweeps*.

We close with a few notes on these solutions. Each of these terms features an implicit Heaviside theta function $\Theta\left(t\right)$. After all, spin polarization cannot exist before it has been generated. Alternatively, we can restrict the domain of our solution to times $t > 0$. In a pulsed system, we are repetitively generating and measuring spin polarization. We can adjust the pump-probe delay time to be negative, which really means we are measuring the spin polarization generated by a previous pulse. For this reason, it is often expedient to talk about negative delay. Of course, in this system, we must think about the effect that multiple pulses has on existing spin polarization; this is the subject of the next section.

In situations with anisotropic dephasing, the exponential decay time will essentially become the average of the decay times along $\hat{y}$ and $\hat{z}$ [22]. The sinusoid oscillation frequency will also be modified slightly from the expected Larmor precession frequency with a term dependent on these decay times. An anisotropic g factor further muddles the picture. However, the solutions will retain the character of a decaying sinusoid.

Finally, we note that the choice of $-S_0$ as opposed to S_0 for the pre-factor in S_y is determined by the component form of the Bloch differential equation. A spin polarization with a positive g factor will precess counter-clockwise about an external field along $\hat{x}$. However, GaAs has a negative g factor, so it will actually precess in the opposite, clockwise, direction. The sign conventions used in this dissertation are consistent with the experimental outcomes presented here, but we recommend that the interested reader pay attention to their assumptions when comparing our figures and equations to their physical system.

2.3.6 Concept: Resonant Spin Amplification

The decaying cosine we just derived is the time evolution of a single spin polarization pseudovector in a transverse external magnetic field without any further spin generation. The pulsed laser has enabled the study of the ultrafast spin relaxation dynamics present in our systems. These devices output a train of identical pulses, each with pulse duration τ_p and time between pulses T_R. In order to observe spin dynamics of a single-pulse-generated spin polarization, we would have to block all pulses after the first. The Mira-900 Ti:Sapph laser used for this dissertation puts out picosecond-duration pulses every 13.16 ns. Imagine standing with an index card to let the first pulse go by but block all the rest! This is not to say that the period between pulses cannot be extended, as electronic "pulse pickers" can block a subset of output pulses, picking every nth pulse for use in the experiment. We do not have one of these devices in our laboratory. Thus, billions of pulses go by every second, so we should be prepared to understand the effect this may have on our electron spin polarization.

First, we must compare the spin lifetime T_2^* to the repetition period T_R. If the lifetime is much shorter than this period, then by the time the next pulse has arrived, the initial spin polarization will have essentially decayed away. In that case, we can use the solution to the Bloch equation for a single pulse. As soon as T_2^* is comparable to T_R, the possibility exists for there to be leftover spin polarization when the second pulse arrives. This is the situation we consider.

When the next pulse arrives, it will generate a new spin polarization identical to the first, but the first has changed since its generation. It has decayed, with decay factor e^{-T_R/T_2^*}. More importantly, it has precessed about the external magnetic field for a time T_R. The rotation angle of precession is ΩT_R, where Ω is the Larmor precession frequency $g\mu_B B_{\text{ext}}/\hbar$. The repetition period is fixed for our laser, so the only free quantity in this rotation angle is B_{ext}. The external field will determine where in its precession the first spin polarization falls when the second spin polarization is generated. It could be anywhere from aligned with the new spin polarization, yielding constructive interference, to directly opposing the new polarization, yielding destructive interference, to anywhere in between.

The vector sum of these two spin polarizations precesses for the next T_R until the third pulse arrives and generates another spin polarization. The vector sum will not necessarily point along the direction that the first polarization was pointing when the second pulse arrived. There may be constructive or destructive interference. The new spin polarization superposition is formed, and this process continues every 13.16 ns. A graphical accompaniment to this description is shown in Fig. 2.10.

Consider the special case where the first spin polarization has aligned itself perfectly with the newly formed second spin polarization. The vector sum of these two will result in a spin polarization larger than that due to a single pulse. Further, it will precess through the same rotation angle in T_R, lining up with the third spin polarization, and so on. The spin polarization will be amplified, so this phenomenon is known as *resonant spin amplification* [35]. The term “resonant” refers to this phenomenon occurring for external fields such that the existing spin polarization has completed an integer number of full precessions about the external field. We obtain this resonance condition by setting the argument of the cosine in the Bloch solution equal to an integer multiple of 2π:

$$\begin{aligned} \Omega T_R &= 2\pi k, \quad k \in \mathbb{Z} \\ \frac{g\mu_B}{\hbar} B_{\text{ext}} T_R &= 2\pi k \\ B_{\text{ext}} &= 2\pi \frac{\hbar}{g\mu_B T_R} k. \end{aligned} \tag{2.8}$$

This resonance condition is tied to the laser through the repetition period T_R and the material under study through the g factor. For GaAs, $g = -0.44$, so in our measurements,

$$B_{\text{ext}} \approx 12.3\ k\ \text{mT}. \tag{2.9}$$

In Chapter 6, we find this quantity to be closer to 12.2 mT (corresponding to $g = -0.444$). At these external fields, the spin polarization will be amplified. We can express this condition in terms of the Larmor precession frequency of the electrons instead:

$$\begin{aligned} \Omega T_R &= 2\pi k, \quad k \in \mathbb{Z} \\ \Omega &= 2\pi \frac{1}{T_R} k. \end{aligned} \tag{2.10}$$

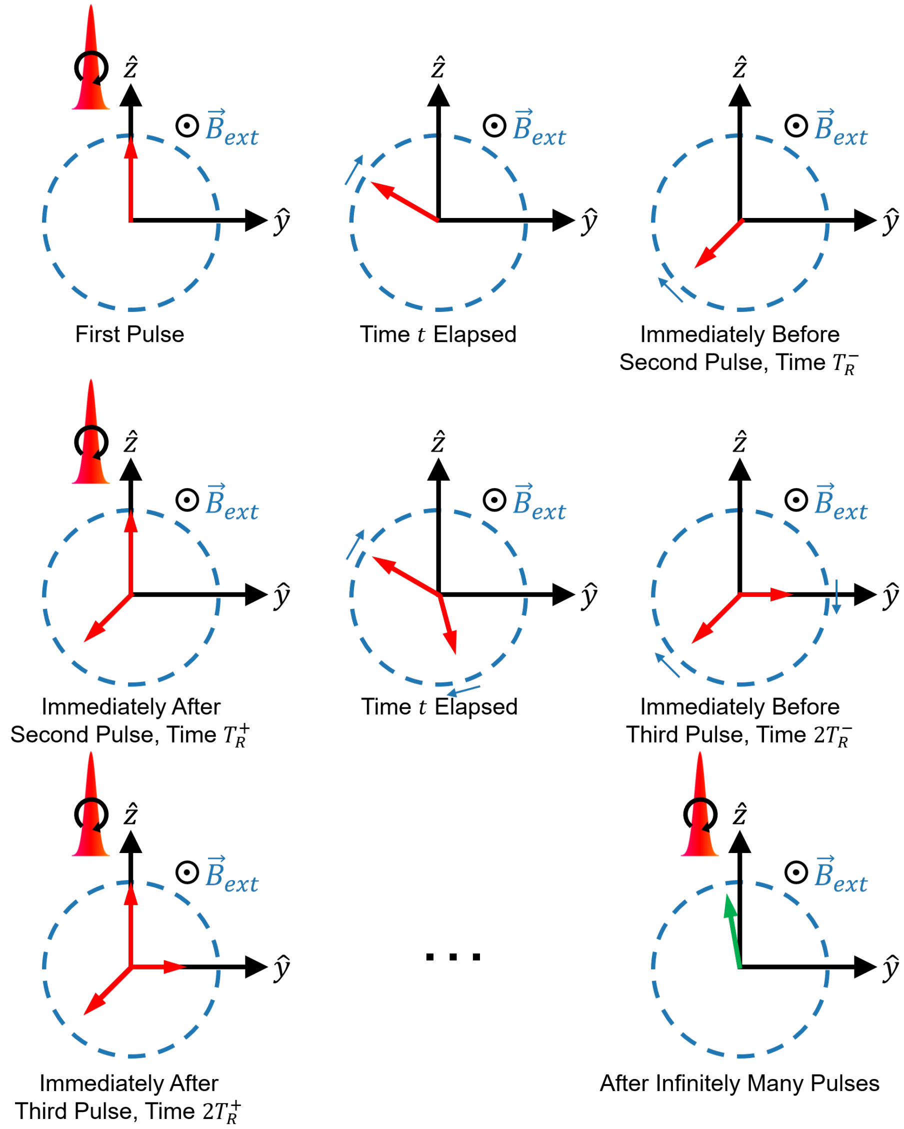

Figure 2.10: Schematic for resonant spin amplification (RSA). This figure considers spin polarization generated along $+\hat{z}$ (red arrow) and precessing in the clockwise direction ($g < 0$) about $\hat{x}$. The top row represents the time period T_R after the arrival of the first laser pulse at $t = 0$. At the end of this period, immediately before the next pulse arrives, the initial spin polarization will have decayed and will point in a direction dependent on the external field. When the second pulse arrives (middle row), an additional spin polarization is formed along $\hat{z}$. The two polarizations will decay and precess during the next time interval T_R. Generation of electron spin polarization and precession for periods of T_R continue indefinitely. The contributions of an infinite number of pulses can be represented as a single spin polarization, the green arrow in the bottom-right panel.

This is known as the phase synchronization condition (PSC) and is independent of the material system. For our laser,

$$\Omega \approx 477\ k\ \text{kHz}. \tag{2.11}$$

This version of the condition is not as practical for everyday usage in our laboratory, but it will be key when exploring nuclear-induced frequency focusing (NIFF) in Chapter 7.

At the resonance condition, the spin polarization will be amplified; away from the condition, the spin polarization will fall off. Three cases for three slightly different precession frequencies are shown in Fig. 2.11. The contribution from multiple pulses may not be apparent when viewing spin polarization as a function of time. However, fixing time and changing the external field will sweep the spin polarization through these resonance conditions. A single spin polarization plotted as a function of external field will simply be a sinusoid. The contribution from multiple pulses becomes clear in this view, as we will no longer have this sinusoidal shape.

If T_2^* is not much longer than T_R, then we can fit our data to the sum of just a few spin polarization vectors. For longer lifetimes, though, we do not want to be adding a billion terms together in order to accurately fit our data. We want to describe the action of all of these pulses in a single, closed-form expression, which we will refer to as the RSA equation. Rather than count the number of pulses that have been emitted since we turned on our laser, we presume that there have been an infinite number of prior pulses. A finite spin lifetime ensures that most of those infinitely long ago pulses are negligible.

Conventionally, we take the solution to the Bloch equation and sum up infinite copies of it. This is the sum of the projections of the spin pseudovector along a particular axis, here $\hat{z}$. This yields the sum

$$S_z\left(t, B_{\text{ext}}\right) = S_0 \sum_{n=0}^{\infty} \Theta\left(t + nT_R\right)\, e^{-(t+nT_R)/\tau} \cos\left(\Omega\left(t + nT_R\right)\right), \tag{2.12}$$

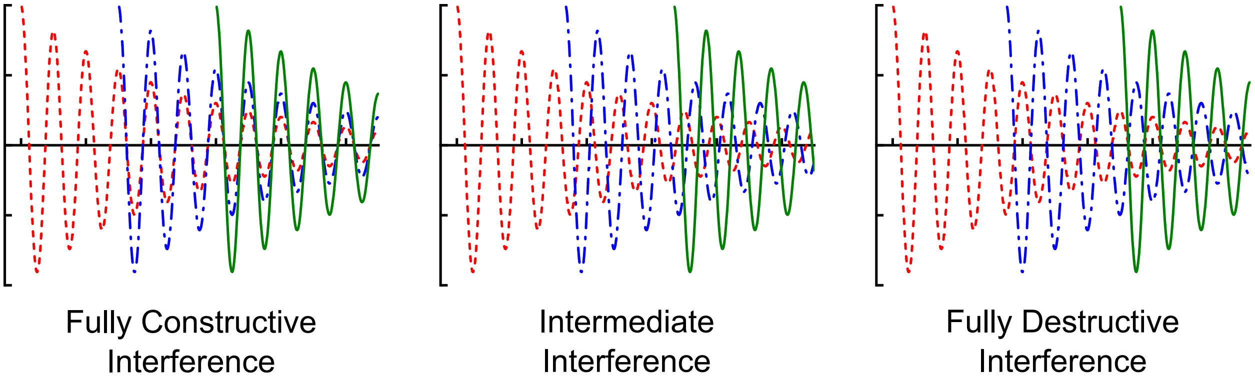

Figure 2.11: Schematic demonstrating interference of precessing spin polarizations as a function of time. When spin polarizations are in phase with the remainder of the previous polarization, they constructively interfere, and we obtain RSA. These polarizations can also destructively interfere, resulting in reduced overall spin polarization. The cases in between contribute to giving RSA its peaked appearance; see Fig. 2.12.

where we use τ to stand in for T_2^* for notational simplicity.

This is the expected projection of the spin pseduovector along $\hat{z}$ after an infinite number of pulses have been incident on the system. Evaluating this sum is made difficult by the presence of causality, so some derivations will omit the Heaviside functions and present an expression that is only valid for times after the final pulse has arrived. One such derivation views the sum as the real part of a sum of complex exponentials. This complex sum can be formed into a geometric series and evaluated. The resulting expression offers insight into the amplitude and phase modifications introduced by the train of pulses [36].

However, this expression and sum only work for S_z and only for initial spin polarization along $\hat{z}$. We present here a generalization of this sum that covers the full spin pseudovector and can be used in a wider array of experimental contexts. This approach is inspired by the Heisenberg picture of quantum mechanics, which we used earlier to derive spin precession. The S_z operator evolved in time while the spin state remained fixed. When we solved the Bloch equation, we treated the spin polarization S_z as the quantity changing in time. In analogy, we will re-imagine our solution to the Bloch equation as a time-dependent operator acting on a fixed initial spin polarization. This spin polarization matrix will incorporate the time-dependence of the problem, communicating to us the general principles of precession under the influence of a train of pulses.

Precession is a rotation of the spin pseudovector, so we represent rotation about an external field $B_{\text{ext}}\hat{z}$ with the rotation matrix

$$\hat{R}\left[\theta\right] = \begin{pmatrix} 1 & 0 & 0 \\ 0 & \cos\theta & -\sin\theta \\ 0 & \sin\theta & \cos\theta \end{pmatrix}, \tag{2.13}$$

where $\theta = \Omega t$ is the angle through which the pseudovector has precessed in time t.

At time $t = 0$, a spin polarization S_0 is generated along some direction. It will precess through an angle ΩT_R before the next pulse occurs. It will also decay exponentially during this time. The next pulse adds a new spin polarization S_0. For the next period T_R, the sum of these two spin polarizations will collectively precess through another angle ΩT_R and decay exponentially. A third pulse is incident, and the cycle continues. Refer back to Fig. 2.10. After an infinite number of pulses, the spin polarization pseudovector is given by

$$\vec{S}\left(t\right) = \left(\sum_{n=0}^{\infty} \hat{R}^{n}\left[\Omega T_R\right] e^{-nT_R/\tau}\right)\vec{S}_0. \tag{2.14}$$

The spin polarization at a time t after the arrival of the final pulse is given by

$$\vec{S} = \left(\sum_{n=0}^{\infty} \hat{R}\left[\Omega\left(t + nT_R\right)\right] e^{-(t+nT_R)/\tau}\right)\vec{S}_0.$$

When $\vec{S}_0 = S_0\hat{z}$, we can pull the initial spin polarization into the sum and simplify, yielding:

$$\vec{S}\left(t\right) = S_0 \sum_{n=0}^{\infty} \begin{pmatrix} 0 \\ -\sin\left(\Omega\left(t + nT_R\right)\right) \\ \cos\left(\Omega\left(t + nT_R\right)\right) \end{pmatrix} e^{-(t+nT_R)/\tau}. \tag{2.15}$$

Considering only the S_z component brings us back to the sum considered earlier.

We encapsulate all of the precession of the infinitely many pulses in the term in parentheses in Eq. 2.14. This is a geometric series, adding up the product of rotation matrices rather than scalar quantities. We can still compute the outcome, which we designate as $\hat{R}^{\infty}$:

$$\hat{R}^{\infty} = \begin{pmatrix} \frac{1}{1-e^{-T_R/\tau}} & 0 & 0 \\ 0 & r\cos\gamma & r\sin\gamma \\ 0 & -r\sin\gamma & r\cos\gamma \end{pmatrix}. \tag{2.16a}$$

where

$$r = \left(1 - 2e^{-T_R/\tau}\cos\left(\Omega T_R\right) + e^{-2T_R/\tau}\right)^{-1/2} \tag{2.16b}$$

is a magnetic-field-dependent effective spin polarization amplitude and

$$\gamma = -\arctan\left(\frac{e^{-T_R/\tau}\sin\left(\Omega T_R\right)}{1 - e^{-T_R/\tau}\cos\left(\Omega T_R\right)}\right) \tag{2.16c}$$

is a magnetic-field-dependent effective phase. These interpretations will be clear shortly.

An infinite number of precession and decays about the x-axis leads to the decay of any S_x polarization. The precession mixes S_y and S_z, with the degree of mixing determined by γ. Hence, there is a phase introduced that rotates the initial spin polarization by an angle γ in the yz-plane. The amplitude of these spin components is determined by r.

When we factor back in the precession over a time t after the arrival of the final pulse, we see that the spin polarization pseudovector is given by the matrix expression

$$\vec{S}\left(t\right) = e^{-t/\tau}\begin{pmatrix} \frac{1}{1-e^{-T_R/\tau}} & 0 & 0 \\ 0 & r\cos\left(\Omega t - \gamma\right) & -r\sin\left(\Omega t - \gamma\right) \\ 0 & r\sin\left(\Omega t - \gamma\right) & r\cos\left(\Omega t - \gamma\right) \end{pmatrix}\vec{S}_0. \tag{2.17}$$

Notice that γ is now properly a phase shift in the oscillatory terms.

This expression is true for any initial spin polarization and any external field magnitude, so long as the field is applied along $\hat{x}$. The full derivation is given in Appendix A and can be carried out for any external field configuration.

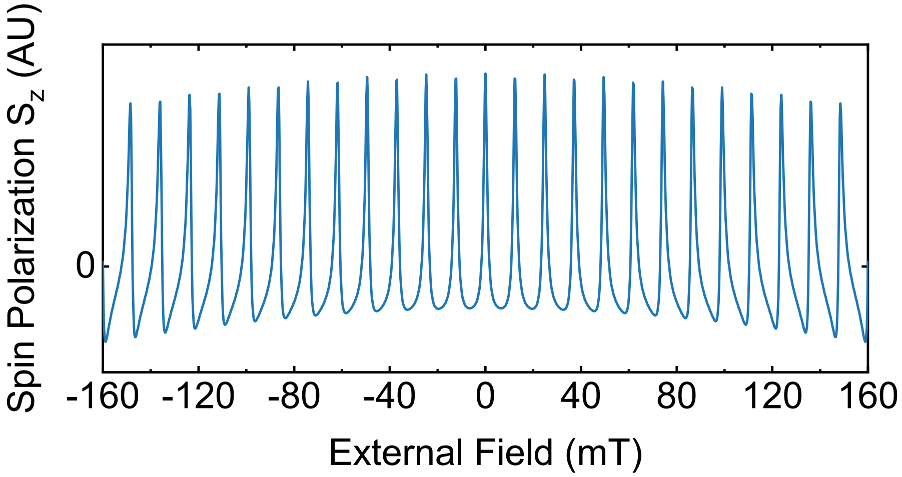

Figure 2.12: Field-dependent spin polarization component S_z in the RSA regime. For purposes of this example, the elapsed time, or pump-probe delay, is set to 13 ns to match the experiments shown in the rest of this dissertation. The parameter values $g = -0.44$ and $T_2^* = 30$ ns are chosen to match the GaAs considered in Chapter 6.

For optical orientation, we expect $\vec{S}_0 = S_0\hat{z}$. The vector expression for spin polarization is then

$$\vec{S}\,(t) = S_0 r\ e^{-t/\tau} \begin{pmatrix} 0 \\ -\sin\left(\Omega t - \gamma\right) \\ \cos\left(\Omega t - \gamma\right) \end{pmatrix}. \tag{2.18}$$

We plot S_z as a function of external field in Fig. 2.12, using a spin lifetime of $T_2^* = 30$ ns. A two-dimensional plot that factors in time-dependence is shown in Chapters 4 and 7. These equations will serve as a starting point in Chapter 6 when integrating the optical Stark effect into our picture of spin polarization.

Instead of a cosine, we now have a series of sharp peaks, spaced apart by the RSA period or PSC. We will often refer to these peaks as "RSA" peaks. Closer to zero field, the peaks are fairly symmetric about their maximum values and resemble Lorentzians. At larger fields, the peaks exhibit a natural asymmetry with the sign of the external field. The center peak at zero external field can be fit with an even Lorentzian to estimate the spin lifetime of the system, following the fitting procedure for a Hanle measurement (see Chapter 4):

$$\frac{1}{1+\left(\frac{g\mu_B}{\hbar}T_2^*\right)^2}. \tag{2.19}$$

This is particularly useful for systems with lifetimes so long that they do not show appreciable decay over the period T_R. As this equation implies, the longer the lifetime, the narrower the center peak. On the opposite extreme, for lifetimes shorter than T_R, S_z will resemble a cosine yet again and this method to obtain the lifetime becomes invalid.

There is one caveat to the equations discussed here: this approach holds only so long as the presence of a spin polarization does not impact the optical orientation of successive pulses. For example, as a spin system approaches saturation, the pump pulses will no longer be able to excite the same proportion of spin-up and spin-down electrons. In practice, we never approach saturation of our electron spin system, so we are free to adopt the model of independent spin polarizations corresponding to each pulse.

2.3.7 Concept: Dynamic Nuclear Polarization

Electron spin is the motivation for this entire dissertation, but we must also consider the spin of the atomic nuclei that make up our crystal lattice. We designate nuclear spin with I, as opposed to S for electrons. Whether a nucleus will have a nonzero spin depends on the number of constituent protons and neutrons. If the nucleus does have a spin, it will not necessarily be spin-1/2. For example, arsenic and the stable isotopes of gallium have spin-3/2. This changes some of the details (like the gyromagnetic ratios), but the ideas remain the same. Just like electron spin, nuclear spin can be polarized, presenting an intriguing alternative for spintronic applications. Already, nuclear spins have found widespread use in everyday life; NMR is the underlying concept behind magnetic resonance imaging (MRI), a key tool for radiologists in diagnosing a host of ailments.

One reason for interest in nuclear spin is a lifetime orders of magnitude longer than electron spin lifetime. While electrons may only stay polarized for nanoseconds, even at low temperatures, nuclei may stay polarized for tens to hundreds of seconds. We should take a moment to be careful with our terminology again. In the context of electron spins, we usually intend lifetime to mean ensemble dephasing time. In the context of nuclei, we actually intend lifetime to mean longitudinal relaxation time. The transverse dephasing time for nuclei is not particularly long, so we will not consider the precession of nuclei in a transverse magnetic field [8]. Instead, we will only encounter nuclei whose spins are polarized along an external magnetic field. These long relaxation times could enable the sorts of information processing and storage applications that we desire for electron spin polarization. Instead of asking how to keep electron spins polarized, perhaps we should ask how to effectively polarize nuclear spins in our materials of interest.

Our interest lies in all-optical experiments, but we don't have optical selection rules to directly polarize nuclei in GaAs. Instead, we must rely on the electron spin population as an intermediary. The electrons and nuclei are coupled through the Fermi contact interaction, sometimes referred to in less general terms as the hyperfine interaction [17]. The Hamiltonian roughly has the form of

$$\hat{H} \propto A\left(\hat{\vec{I}} \cdot \hat{\vec{S}}\right), \tag{2.20}$$

with $\hat{\vec{I}}$ and $\hat{\vec{S}}$ the nuclear and electron spin operators, respectively, and A the hyperfine coupling constant. This constant is given for the isotopes in GaAs in Chapter 6. This Hamiltonian represents an interaction between electrons and nuclei in which they can swap spin. For example, a spin-up electron can exchange its spin with a spin-down nucleus. It is energetically favorable for electrons to transfer their spin polarization to the nuclear lattice. This is actually a chief mechanism of spin relaxation in GaAs with low doping [14].

We can consider nuclear spins as magnetic moments as we did electron spins. An accumulated nuclear spin polarization will act on the electron spin system as an additional magnetic field, the Overhauser field [37]. Of course, this extra magnetic field will alter electron spin precession. This may impact the component of electron spin polarization along the external magnetic field, thereby impacting the electron spin polarization that polarized the nuclei in the first place. This becomes a feedback loop: the electrons polarize nuclei which alter the electron spin polarization.

The electron spins act back on the nuclear spin system with their own effective magnetic field, the Knight field [38]. With the advent of polarization modulation devices like photoelastic modulators (discussed in the next chapter), it has become possible to generate a Knight field oscillating at the NMR frequencies of nuclei under study, allowing for all-optical studies of NMR [39, 40]. In our experimental contexts, we do not consider the Knight field.

The interactions between the electron and nuclear spin systems are summarized graphically in Fig. 2.13. We omit the effect of microwave radiation usually found in NMR studies. Refer back to this figure when reading Chapter 6. It is clear that even if we are only interested in electron spin polarization, understanding the interaction between electron and nuclear spin is vital. The nuclei present yet another factor manipulating our electron spin, but with proper understanding we may be able to use it our advantage.

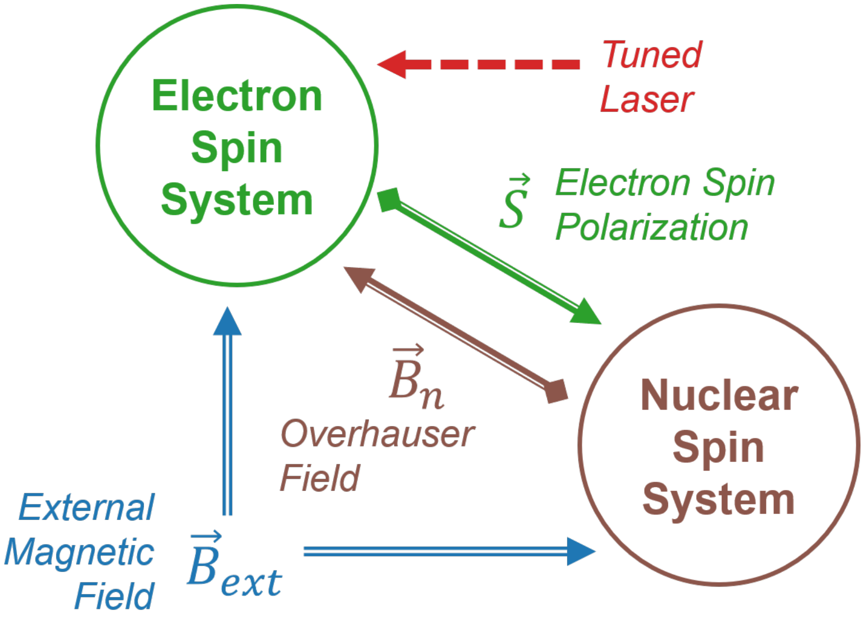

Figure 2.13: Diagram summarizing the coupled electron-nuclear spin systems. While only the electron spin system is addressed via laser, both spin systems are affected by the presence of an external magnetic field. The electron spins polarize the nuclei, which act as an additional magnetic field, the Overhauser field, on the electron spin system. This creates a feedback loop. Figure inspired by and adapted from Ref. [13].

CHAPTER 3

Detection of Electron Spin Polarization

3.1 Motivation

In the previous chapter, we described both how to generate an electron spin polarization in our materials of interest as well as the physical mechanisms that will modify that polarization, both within and outside our control. All of that is for naught if we do not have a reliable method for detecting, or measuring, spin polarization.

In our laboratory, we use an optical detection method, measuring Faraday/Kerr rotation. This technique converts the problem of measuring a spin polarization in our material into the problem of measuring a small change in polarization of light. While the term "polarization" is used for both spins and light, these are two fundamentally different concepts and this is not a trivial conversion. Throughout this chapter, we will be careful to make clear which polarization is intended in each situation.

Faraday/Kerr rotation is a means of encoding spin polarization information into another physical medium, here light. We must then find some means of reading out that information, or decoding the light polarization back into spin polarization. This is an abstract way of stating that we must have a way to measure the polarization of the light we use in our experiments. We describe how our optical setup measures Faraday/Kerr rotation, providing the final context for the experiments that form the bulk of this dissertation. The chapter ends with the role lock-in detection plays in noise suppression. Familiarity with lock-in detection will be necessary to follow the project described in Chapter 5.

3.2 Detection of Electron Spin Polarization

The realm of spintronics research encompasses all-electrical, all-optical, and mixed experiments. The suitability of a particular detection method relies on the system under consideration and the laboratory equipment available. In the previous chapter, we laid out the two generation mechanisms utilized in our laboratory, optical orientation and CISP. In both cases, we will use optical means to measure the generated spin polarization. While the pulsed lasers that enable our investigations are a relatively recent development, the technique we use has its foundations in the mid-1800s.

3.2.1 Concept: Faraday/Kerr Rotation

In 1845, Michael Faraday wrote in his diary about a discovery we now call the *Faraday effect* [41]. He sent polarized light through a glass while applying a magnetic field parallel to the propagation direction, observing that the polarization of the light was rotated when measured after the glass. The presence of the magnetization in the material resulted in circular birefringence: the two circular polarizations of light experienced slightly different dielectric responses as they propagated along the magnetization direction. Put another way, the two polarizations travel at different speeds through the material. Since the incoming linear polarization is a superposition of left- and right-handed circular polarization, this results in a phase difference between the two polarization components. When the light leaves the material, the phase difference manifests as a rotation of the linear polarization. This rotation angle is *Faraday rotation*.

It is not the presence of a magnetic field that rotates the polarization of light, but rather the magnetic field is necessary to magnetize the material. Faraday rotation is thus material-dependent. If a material cannot be magnetized or is only weakly magnetized, the Faraday effect may be negligible or absent. Furthermore, the rotation angle accumulates as light traverses the material, introducing a dependence on material thickness.

The *magneto-optic Kerr effect*, named for physicist John Kerr, is the reflection-geometry analogue of the Faraday effect. When linearly polarized light is reflected off of a magnetized surface, the polarization of the reflected light is rotated. This rotation angle is *Kerr rotation.* Practically, we use Faraday and Kerr rotation interchangeably, differentiating only by the geometry of the experiment. However, there is a subtle difference in the mathematics behind the rotation that results in a significant difference in wavelength-dependence; see Appendix B

Considering electron spins as magnetic moments, we can think of spin polarization as a magnetization. Thus, the presence of a spin polarization in a material will result in Faraday rotation. This can be shown classically. Assume that spin polarization is generated along the optical axis $\hat{z}$ as is the case for optical orientation. This is a uniaxial magnetization along $\hat{z}$, which modifies the dielectric tensor describing the optical properties of the material. Specifically, it introduces off-diagonal terms [42, 43], and as a result the eigenstates of propagation become σ^+ and σ^-. In the next section, we will work in terms of σ^+ and σ^- light due to optical selection rules, but here we see that choice being a more general consequence. Treating linear polarization as a superposition of circular polarizations, we can use the dielectric tensor to calculate the outgoing light, with the spectral form of the tensor depending on the physical details of the system. One approach is to adopt the Lorentz model for an electron moving in an electromagnetic field to derive a functional form for the dielectric tensor elements. This can be carried out for transmission geometry [42, 44] and reflection geometry [42, 43].

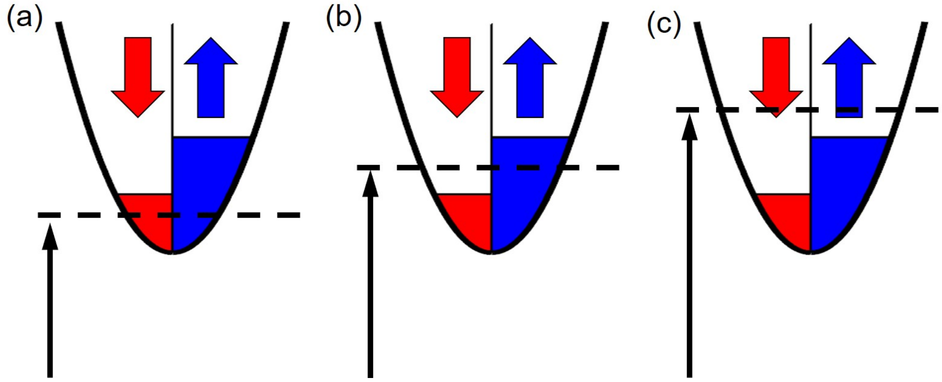

Figure 3.1: Available conduction band states for an excited electron based on the energy of excitation and the spin polarization of the material. For the excitation energy indicated by the black arrow, (a) no states, (b) only spin-down states, and (c) states of either spin are available.

In addition to a classical approach, there also exist fully quantum-mechanical approaches to the Faraday effect [44]. Here, however, we will proceed with a semiclassical avenue that is informed by the absorption properties of our material.

3.2.2 Concept: Absorption Model and the Faraday Spectrum

Assume that there is an existing spin polarization in our material. The mechanism of generation does not matter here. Rather than think of the spin polarization as a magnetization, we consider what the polarization means for the available energy states in the material. We represent the conduction band of our material as a parabola in crystal momentum k. In reality, there are two superimposed parabolas, one for spin-up electrons and one for spin-down. We represent this graphically by splitting the parabola down the middle, color-coding spin-up as blue and spin-down as red.

By definition, the presence of a spin polarization means that there are more electrons in our material with one spin than the other (with respect to a suitably defined axis of quantization, of course). Thus, more electron states must be occupied for one spin than the other. This is an imbalance in the density of states, as shown in Fig. 3.1.

What happens when we send in circularly polarized light depends on the energy. At too low of an energy (Fig. 3.1a), the electron states are fully filled, and we cannot excite any additional conduction band electrons. The light should just pass through without being absorbed. At too high of an energy (Fig. 3.1c), electron states are open for both spins, and both circular polarizations will be absorbed. Consider the intermediate case presented in Fig. 3.1b. At this energy, there are available spin-down states but no spin-up states. Light can excite spin-down conduction band electrons but not spin-up conduction band electrons. Based on the selection rules, one circular polarization will be more preferentially absorbed, as it is connecting to unfilled electron states. Near the band gap, then, absorption will differ for the two circular polarizations. Put another way, the absorption spectrum for σ^+ light will be shifted in energy with respect to the absorption spectrum for σ^- light. When linearly polarized light is incident on the system, the circular components of that light will be unevenly absorbed. However, we generally expect the difference in absorption to be negligibly small.

We started with a quantum description of our spin polarization in terms of available electron states and connected it to the absorption spectrum, which is a classical concept. From here, we will again work purely in terms of classical optics, ignoring the form of absorption (which should also depend on the original quantum picture we constructed).

In real materials, the index of refraction is a complex quantity $\widetilde{n}$ given by $\widetilde{n} = n + i\kappa$, where n is the commonly cited index of refraction and κ is the "extinction coefficient" related to the absorption coefficient α. As a consequence of causality, the real and imaginary parts of $\widetilde{n}$ are mathematically intertwined. Knowledge of either n or κ for all frequencies necessarily determines the other through the Kramers-Kronig relations. In analysis or signal processing contexts, these are known as Hilbert transforms. The relations for the complex index of refraction are [12]

$$n(\omega) - 1 = \frac{1}{\pi} P \int_{-\infty}^{\infty} \frac{\kappa(\omega')}{\omega' - \omega} \, d\omega', \tag{3.1a}$$

$$\kappa(\omega) = -\frac{1}{\pi} P \int_{-\infty}^{\infty} \frac{n(\omega') - 1}{\omega' - \omega} \, d\omega', \tag{3.1b}$$

where P denotes the principal value of the integral. This is a symmetric version of the relations that spans all frequencies, though for real systems they are often rewritten in terms of non-negative frequencies [24, 45]. Rather than relate n and κ, Eq. 3.1a is a Hilbert transform on $(n-1)$ and κ.

Note that experiments measure the absorption coefficient α rather than κ. These quantities are related by

$$\kappa(\omega) = \frac{c}{2\omega} \alpha(\omega) .$$

To determine the frequency dependence of the index n, we can substitute a known or expected absorption α for κ into the Kramers-Kronig relations.

Without yet assuming a form for absorption, we can still derive Faraday rotation. A full derivation is presented in Appendix B; we present the highlights here. In our experiments, we measure Faraday rotation with linearly polarized light, specifically s-polarized. This is vertical with respect to our laboratory frame and corresponds to $\hat{y}$ based on the coordinate axes used throughout this dissertation. We can rewrite this polarization as a superposition of σ^+ and σ^-:

$$\begin{aligned} \hat{y} &= \begin{pmatrix} 0 \\ 1 \end{pmatrix} \\ &= \frac{1}{\sqrt{2} i} \left[\hat{\sigma}^+ - \hat{\sigma}^- \right] . \end{aligned}$$

These two separate polarizations will acquire both amplitude and phase modifications as they travel into, through, and out of the material. In general, transmission, absorption, and propagation are polarization-dependent. For simplicity, we assume here that the transmitted amplitude and absorption are the same for both helicities, representing the change in field amplitude with the real quantity τ, and focus only on the phase difference due to propagation. We treat the full case in the appendix.

The electric field $\vec{E}_{\text{out}}$ transmitted through a spin-polarized material of depth d for an incident field $\vec{E}_{\text{in}}$ is given by

$$\begin{aligned}
\vec{E}_{\text{in}} &= E_0 \hat{y} \\
&= \frac{E_0}{\sqrt{2}i} \left(\hat{\sigma}^+ - \hat{\sigma}^- \right) \\
&\Rightarrow \\
\vec{E}_{\text{out}} &= \frac{E_0}{\sqrt{2}i} \left(\tau e^{in^+ \frac{\omega}{c} d} \hat{\sigma}^+ - \tau e^{in^- \frac{\omega}{c} d} \hat{\sigma}^- \right) \\
&= \frac{E_0 \tau}{\sqrt{2}i} \left(e^{in^+ \frac{\omega}{c} d} \hat{\sigma}^+ - e^{in^- \frac{\omega}{c} d} \hat{\sigma}^- \right) \\
&= \frac{E_0 \tau}{\sqrt{2}i} \left(e^{i\theta^+} \hat{\sigma}^+ - e^{i\theta^-} \hat{\sigma}^- \right),
\end{aligned}$$

where $\theta^{\pm}$ is shorthand for the phases acquired by $\sigma^{\pm}$ light. We define the phase difference

$$\begin{aligned}
\theta &= \frac{\theta^+ - \theta^-}{2} \\
&= \left(\frac{n^+ - n^-}{2} \right) \frac{\omega}{c} d, \qquad (3.2)
\end{aligned}$$

which will shortly end up being our Faraday rotation. We now rewrite the electric field in

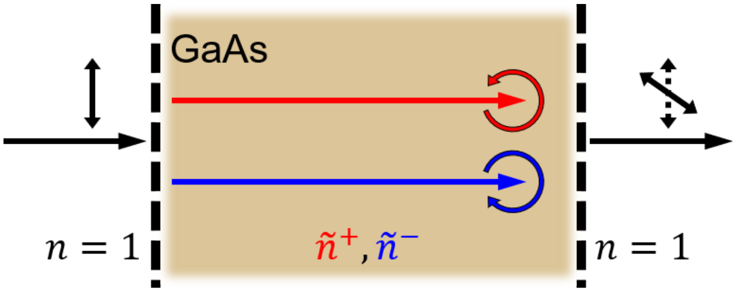

Figure 3.2: Simple schematic for Faraday rotation in GaAs. The incident light is linearly polarized. The transmitted light is also linearly polarized, though it has been rotated by the Faraday rotation angle. This rotation stems from the different optical responses of the material for σ^+ and σ^- light, depicted with different colors here.

terms of the linear polarization basis:

$$
\begin{aligned}
\vec{E}_{\text{out}} &= \frac{E_0\tau}{\sqrt{2}i}\left(e^{i\theta^+}\frac{1}{\sqrt{2}}\begin{pmatrix}1\\ i\end{pmatrix} - e^{i\theta^-}\frac{1}{\sqrt{2}}\begin{pmatrix}1\\ -i\end{pmatrix}\right)\\
&= \frac{E_0\tau}{2i}\begin{pmatrix}e^{i\theta^+} - e^{i\theta^-}\\ i\left(e^{i\theta^+} + e^{i\theta^-}\right)\end{pmatrix}\\
&= \frac{E_0\tau}{2i}e^{i\left(\frac{\theta^+ + \theta^-}{2}\right)}\begin{pmatrix}e^{i\theta} - e^{-i\theta}\\ i\left(e^{i\theta} + e^{-i\theta}\right)\end{pmatrix}\\
&= \frac{E_0\tau}{2i}e^{i\left(\frac{\theta^+ + \theta^-}{2}\right)}\begin{pmatrix}2i\sin\theta\\ i\left(2\cos\theta\right)\end{pmatrix}\\
&= E_0\tau e^{i\left(\frac{\theta^+ + \theta^-}{2}\right)}\begin{pmatrix}\sin\theta\\ \cos\theta\end{pmatrix} \qquad (3.3)\\
&= E_0\tau e^{i\left(\frac{\theta^+ + \theta^-}{2}\right)}\begin{pmatrix}\cos\theta & \sin\theta\\ -\sin\theta & \cos\theta\end{pmatrix}\begin{pmatrix}0\\ 1\end{pmatrix}. \qquad (3.4)
\end{aligned}
$$

We receive back our initial polarization, rotated by an angle θ. This rotation of the initial polarization is the Faraday rotation. See Fig. 3.2 for a simple schematic based on our calculation. The overall effective transmission coefficient $\tau e^{i\left(\frac{\theta^+ + \theta^-}{2}\right)}$ does not factor into the rotation itself.

While this model considered only transmission, the same physical principles are at work in reflection geometry. We still expect an electron spin polarization to rotate the polarization of reflected light. However, this does not emerge from a propagation term, leading to notable differences in frequency-dependence [17, 42, 46]. We treat this derivation in Appendix B.

The Faraday rotation angle is directly proportional to the distance traversed through the material as well as the frequency of the light used to measure it. However, the frequency dependence of Faraday rotation is made more complicated by the frequency dependence of the indices of refraction. We refer to this frequency- or wavelength-dependence as the Faraday spectrum. The spectrum is independent of the mechanism used to generate the spin polarization, so it is not fully sufficient for describing the frequency dependence of the experiments in which we optically pump the electron spin polarization. The frequency of optical orientation must also be factored into any analysis of optical pump-probe experiments. However, it is still useful to compute the Faraday spectrum to build intuition for our experiments. In Chapter 5, we mention the use of the Faraday spectrum to estimate the band gap of our InGaAs epilayer. In Chapter 6, we present the measured Kerr spectrum (the reflection analog) in GaAs and use it to help determine the cause of apparent "two-species behavior."

If we know the absorption spectrum of our material, we can use the Kramers-Kronig relations to obtain the (real) index of refraction. Shifting the absorption spectra for σ^+ and σ^- give us n^+ and n^- and thus $n^+ - n^-$.

Calculating the index of refraction analytically from an absorption spectrum is difficult for all but the simplest of cases. Instead, we proceed numerically. We will present the index difference, which is close enough to Faraday rotation for the small energy range close to the band gap under consideration.

3.2.3 Example: Faraday Spectrum for Bulk Semiconductor

In this dissertation, we work with bulk GaAs. Generally, the absorption spectrum of bulk semiconductors can be described by an expression that is proportional to the three-dimensional density of states:

$$\alpha\left(\hbar\omega\right) = \alpha_0 \frac{\left(\hbar\omega - E_g\right)^{1/2}}{\hbar\omega}, \tag{3.5}$$

where E_g is the band gap and α_0 is a constant specific to each material depending, among other things, on the effective mass and the oscillator strength of the transition under consideration. For GaAs, $\alpha_0 = 5.6 \times 10^4$ [45].

For energies below the band gap, this absorption is zero. This is not necessarily the case in real systems at nonzero temperatures. There is absorption occurring below the band gap that decays exponentially away from the band gap, smoothing the absorption edge. This additional absorption "tail" is known as the Urbach tail [47, 48]. Urbach tails are a fairly universal phenomenon in a wide variety of materials and have been attributed to disorder in a material [49]. Degeneracy in semiconductors will also lead to an exponential tail on the absorption edge known as bandtailing [45]. An example of the absorption edge of GaAs at room temperature is found in Ref. [50].

We implement the Hilbert transform in *Mathematica*, allowing us to calculate the index of refraction for this absorption profile. In Fig. 3.3, we show the computed index difference for both the idealized bulk absorption and the absorption modified with an Urbach tail. In both cases, the index difference is an asymmetric odd function about the band gap. The Urbach tail simply serves to smooth out the index difference. Regardless of the sign of the actual spin polarization, we expect our Faraday rotation to invert when crossing through the band gap. As we probe with energies further from the band gap, the index difference approaches zero on both sides, so we do not expect to measure Faraday rotation at these far-off energies

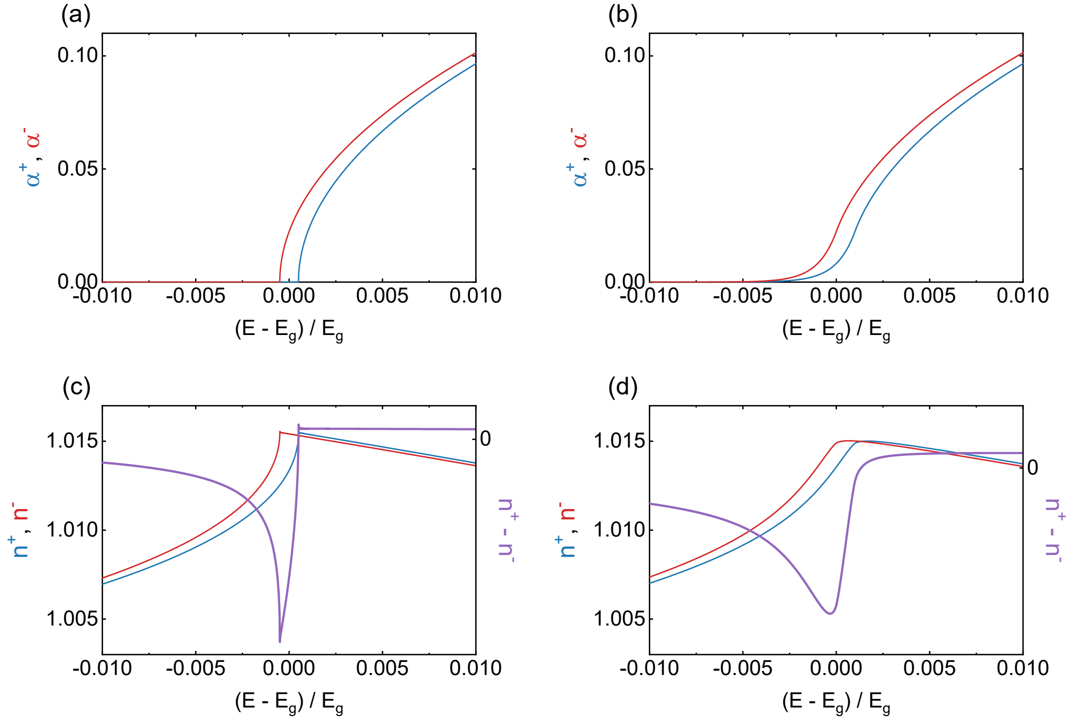

Figure 3.3: Absorption profile for a bulk semiconductor with calculated indices of refraction. Profiles are shown both (a) without and (b) with an Urbach tail. The spectrum is plotted as a function of energy normalized to the band gap. Due to the existence of a spin polarization in the material, the absorption profiles for σ^+ and σ^- light (blue and red, respectively) are shifted with respect to one another. The shift has been chosen for illustrative purposes rather than correspondence to a particular physical system. By the Kramers-Kronig relations, the absorption profiles (a) and (b) are transformed into indices of refraction in plots (c) and (d), respectively. The difference in index for σ^+ and σ^-, shown in purple, is proportional to Faraday rotation.

even when the polarization is still present. This Faraday spectrum has been reported by our laboratory in the past on InGaAs for both transmission and reflection experiments [22, 28].

The Faraday spectrum can also be computed for lower-dimensional systems, though the method of calculation may differ from the absorption method presented here. See Refs. [16, 17] for an example of the Faraday spectrum computed (and measured) for quantum wells based on excitonic lineshapes.

3.2.4 Concept: Choosing Faraday or Kerr Rotation

In practice, we consider Faraday and Kerr rotation to be interchangeable, with the only difference being the experimental geometry. We are often interested in temporal dynamics, which depend on the spin polarization itself, not whether we are measuring via transmission or reflection. However, these rotations emerge from different parts of the complex index of refraction. Above, we showed that Faraday rotation comes from a difference in indices of refraction for σ^+ and σ^- light resulting from propagation through a spin-polarized material. The light used for Kerr rotation measurements does not travel through the material, and thus the rotation must emerge elsewhere. As shown in Appendix B, Kerr rotation can instead be thought of as coming from the extinction coefficients. This should result in a different spectral shape for Faraday and Kerr rotation in the same material. Notably, if one is odd in energy, the other should be even. Based on our plot of the Faraday spectrum, we would then expect the Kerr spectrum to be even about the band gap. Recent work has acknowledged this to not be the case in bulk GaAs, but it is shown through dielectric function calculations that the discrepancy can be attributed to an energy-dependent optical recombination time [46].

Experimentally, our decision between measuring Faraday and Kerr rotation comes down to pragmatism. Some optical setups and cryostats are configured for only transmission or reflection geometries, in which case the question is settled. Some, like ours, can be reconfigured for either geometry. In that case, we decide based on the material under study. Faraday rotation scales with thickness, but so does the light intensity lost to absorption. For the samples used in our setup, thickness should not be a concern. If the material is grown or deposited on a substrate, we must consider the absorption profile of the substrate. If it is roughly transparent in the wavelength region of interest, then we can ignore the substrate, as we do in the Faraday rotation calculations above. However, if the substrate absorbs in the experiment wavelength range, transmission experiments are compromised and reflection geometry must be used.

As an example, consider the samples studied in Chapters 5 and 6. For our CISP studies, we measured an InGaAs epilayer grown on GaAs. Despite the small concentration of In, the band gap of the epilayer was shifted to lower energies than pure GaAs. We worked in the wavelength range of 830 to 840 nm, below the band gap of the substrate GaAs, allowing us to measure in transmission geometry. For our DNP studies, we measured a GaAs epilayer grown on an undoped GaAs substrate that was itself grown on AlGaAs. The undoped GaAs substrate absorbs in the 818 to 820 nm range we use for experiments, so transmission was not an option.

3.3 Experimental Detection of Electron Spin Polarization

Now that we have the physical foundations for generating, manipulating, and measuring electron spin polarization, we must realize it in our laboratory. This is achieved through a class of experiments known as *pump-probe spectroscopy.* We define this idea in greater detail in Chapter 4, in which we describe the various experimental techniques we employ in our laboratory.

Broadly, the *pump* effects some change in the properties of the system under study and the *probe* evaluates the results of that change. Specifically, the pump is our means of generating electron spin polarization, and the probe is our means of measuring it. By *spectroscopy*, we mean that we are interested in the response of our physical systems to light. Earlier in this chapter we discussed using light to measure spin polarization, encoding it as Faraday rotation. Thus, the probe in our experiments is light.

In this section, we introduce our optical setup, which is equipped to use ultrafast pulses

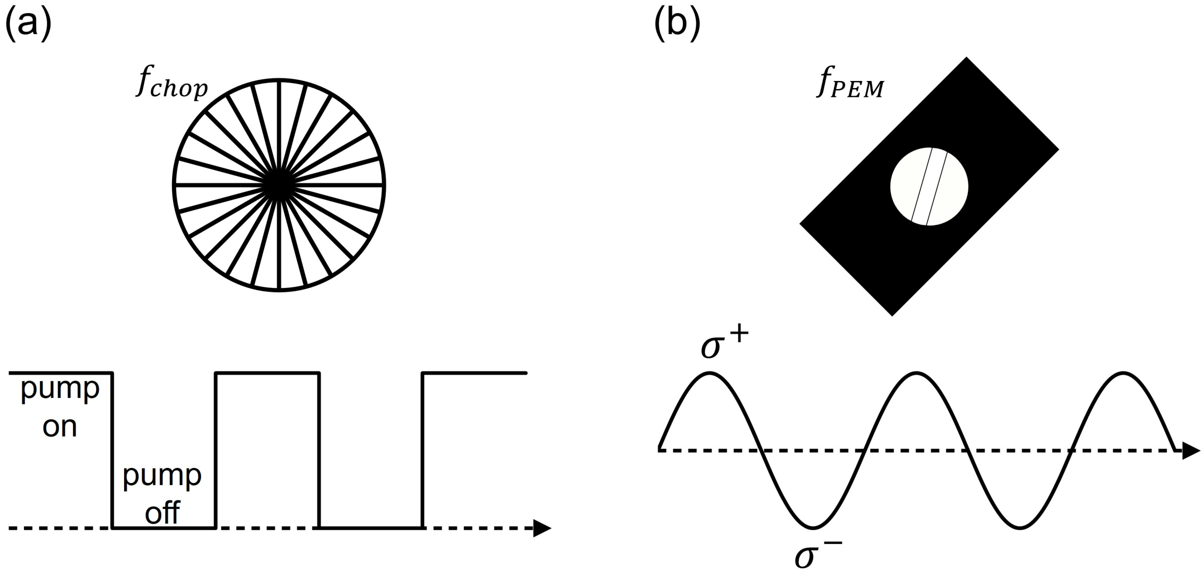

Figure 3.4: Cartoon representation of the pump modulation devices described in the text. (a) The optical chopper blocks and unblocks the pump, essentially turning it on and off. This is intensity modulation. (b) The PEM leaves the pump intensity unaffected but alters the polarization state. The pump oscillates between σ^+ and σ^-, with the dashed line representing the initial linear polarization. This is polarization modulation.

from a mode-locked laser to generate and detect spin polarization. It can also be converted to apply voltage for CISP measurements. We expect measured Faraday rotation to be very small, so we employ two experimental techniques in our measurements. First, a balanced photodiode bridge allows us to measure a small angle. Then, lock-in detection eliminates noise sources that would overwhelm this small signal. The lock-in translates our spin polarization information again into a voltage, and we present the mathematics needed to convert this final quantity into the desired spin polarization.

3.3.1 Concept: Modulation

When planning an experiment, we must have in mind what sort of measured quantities are expected. For spin polarization generated by optical orientation, we expect the measured Faraday rotation to be on the order of microradians. A linear polarizer and photodiode will not suffice for measuring such a small rotation. Even with a reliable method for measuring that rotation (the balanced photodiode bridge described below), our measurement could be jeopardized by stray light or other experimental noise that could overwhelm our small signal. As such, we employ a standard optical technique: modulation. Optical modulation will reduce experimental noise due to the environment while allowing us to isolate the small quantity of interest.

The end goal is to measure only the light that has interacted with a physical system that was impacted by the pump. Thus, we modulate the pump. One such way is to place an optical chopper in the pump path. The chopper simply blocks and unblocks the pump. The timescale of spin dynamics is nanoseconds, while a conventional optical chopper will block and unblock with a frequency in the range of kilohertz, so millions of pulses will make it through without interacting with the chopper wheel. When the pump is unblocked, spin polarization is generated and the probe will experience Faraday rotation. When the pump is blocked, spin polarization is not generated and the probe will not experience rotation. The frequency of the pump beam – on and off – is thus imprinted onto the probe beam as it rotates between Faraday rotation and no rotation. We send this signal to a lock-in amplifier, which can track this frequency and extract the amplitude of the oscillation. A graphical representation of this modulation method is shown in Fig. 3.4.

Rather than modulate the intensity of the pump in this way, we can instead employ polarization modulation. We use a photoelastic modulator (PEM), a crystal that changes its birefringence based on applied stress. The controller box applies periodic stress with frequency 50 kHz. By orienting the PEM at 45 degrees with respect to the polarization of our pump, the PEM acts to periodically modulate the polarization of the pump. The pump polarization oscillates from linear to σ^+ to linear to σ^- to linear, repeating the process. We will alternate exciting spin polarizations in opposite directions. Of course, the PEM period

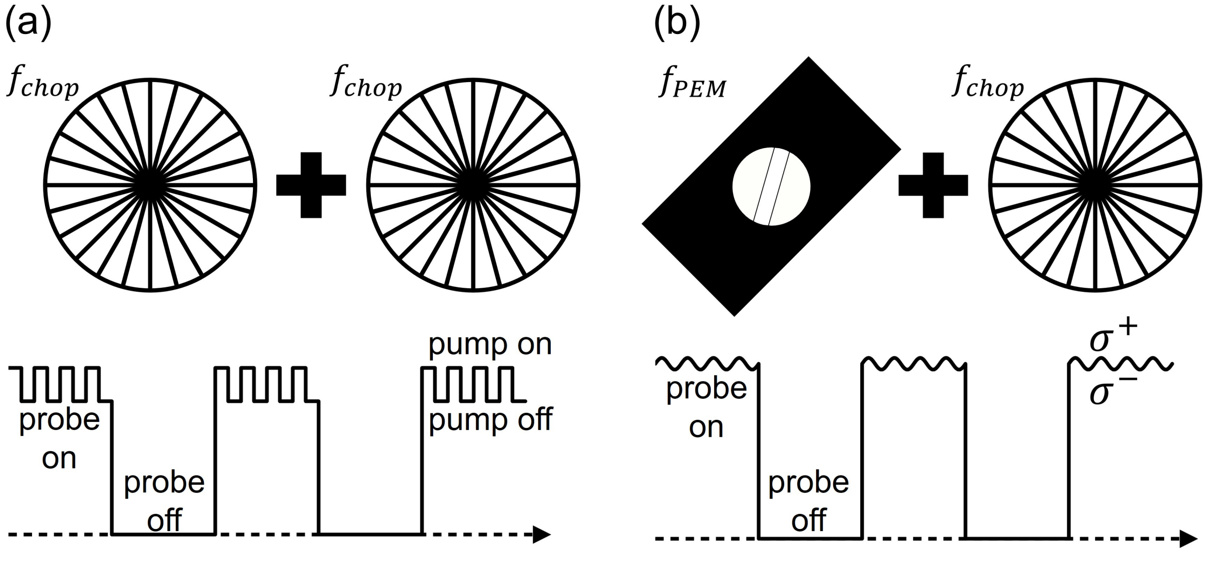

Figure 3.5: Cartoon representation of the double-modulation scheme employed in this dissertation. (a) The pump and the probe are chopped. The desired spin polarization is only measured when both pump and probe are unblocked. (b) The pump is modulated with a PEM and the probe is chopped. The desired spin polarization is only measured when the probe is unblocked. The lock-in follows the PEM frequency, picking out only the spin polarization due to a circularly polarized pump.

of 2 μs is far longer than the duration of each pump pulse, so we do not need to worry about polarization changing during a pump pulse or during the pump-probe delay. The lock-in amplifier can follow this oscillation as well and track the Faraday rotation. The PEM offers a benefit over the chopper in that the incident pump intensity on the sample is constant. This modulation method is represented graphically in Fig. 3.4.

Whichever method we choose, we modulate the pump, ensuring that we only measure changes in the probe due to the pump. This does not, however, account for stray pump light, which is also modulated at the pump frequency. The lock-in amplifier would not distinguish this noise source from the actual signal. Ideal optical alignment should preclude this possibility, but as an additional step, we can also modulate the probe. By chopping the probe beam, we add another frequency for the lock-in amplifier to follow. Chopping the probe and not modulating the pump would measure all probe light, regardless of whether the pump was present or not. Employing both modulations will pick out only the probe light that was affected by the pump. Demodulating twice will require two lock-in amplifiers, but this allows our experiments to be run with room lights on. See Fig. 3.5 for a cartoon depicting the modulation methods.

3.3.2 The Pump-Probe Setup

All of the measurements featured in this dissertation were acquired using the pump-probe optical setup in 1277 Randall Laboratory. A schematic is shown in Fig. 3.6.

At the beginning of our setup, ultrafast laser pulses are produced by an optically pumped mode-locked titanium-sapphire laser. The Verdi V10 is a continuous-wave diode laser that outputs 532 nm light at powers up to 10 W. The Mira-900 is a box of optical components built around a titanium-doped sapphire crystal. It focuses the green light from the Verdi into the crystal, producing red light in the range of 700 to 1000 nm. Through passive mode-locking, the Mira-900 forms the light into optical pulses, which it emits with a repetition rate of 76 MHz. That is equivalent to one pulse every 13.16 ns (the repetition period T_R). This time is determined by the optical path inside the Mira-900 box. The Mira can be configured to output either 2 ps pulses ("pico mode") or 150 fs ("femto mode"). While it might seem advantageous to use as short a pulse as possible for the best possible temporal resolution, shorter pulses come with a larger spectral width. This may make it more difficult to address particular optical transitions. The timescales we are interested in tend to be in the range of hundreds of picoseconds or longer, so we are content to carry out our experiments in pico mode. In almost every case, we are eventually interested in the polarization of these short laser pulses, which start out linearly polarized.

A 50:50 beamsplitter (BS) splits the train of pulses from the Mira-900, yielding pump and probe pulses from the same source. This is demonstrated in the setup schematic by a purple

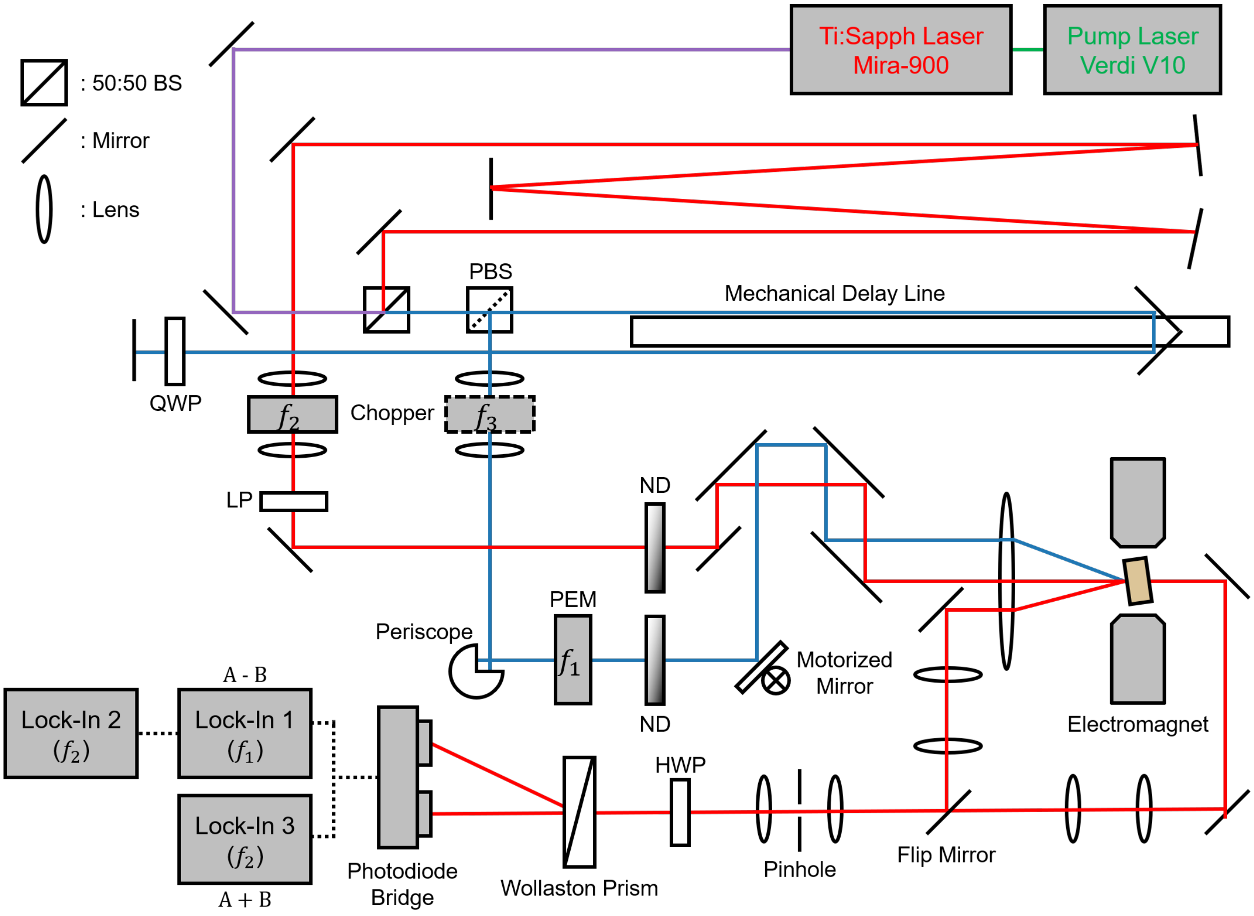

Figure 3.6: Schematic of the optical pump-probe setup in 1277 Randall, as viewed from above. Optics that appear throughout the setup are unlabeled; see the legend at top-left. The remaining optics or other equipment are labeled, with abbreviations defined in the text. Optics used for alignment (such as irises) or for coupling into other optical setups have been omitted from the figure. The optical elements are not to scale but are drawn roughly where they are placed in the real setup.

beam splitting into blue (pump) and red (probe) beams. We carefully control the physical distance traversed by the pump and probe beams so that we know the temporal relationship between them. That is, the difference in optical path lengths directly translates into a time delay between when split pump and probe pulses arrive at the sample. While pump-probe measurements do not necessarily need to incorporate timing data, this opens up the door to measuring ultrafast dynamics. An optical path length difference of a few feet can give us a temporal separation of nanoseconds, far shorter timescales than we could achieve through other means. We utilize a series of mirrors to effectively double the probe path back on itself to make the pump and probe paths nearly equal in extent.

To change the relative path length during an experiment (without having to pick up our mirrors off the table), we use a mechanical delay stage in our pump path. This stage is essentially a mirror on a cart that can be moved forwards and backwards. We translate the stage position into pump-probe delay. This particular delay line uses the double-pass geometry. The light travels down the line, is reflected back by the retroreflector on the stage (which displaces the light in space), and encounters at the other end a quarter-wave plate (QWP). This alters the polarization of the pump from linear to circular. The pump bounces back off a mirror, which reverses the helicity. The light proceeds back through the QWP, now assuming a linear polarization orthogonal to its initial state and travels the original path backwards. We place a polarizing beamsplitter (PBS) in the pump path to send this light into the rest of the setup. The double-pass geometry is more prone to alignment issues than a single-pass geometry, especially as it pertains to sending back-reflections to the Mira-900, which may disrupt mode-locking. However, the double-pass geometry allows us to achieve a delay nearly double that of the physical length of our line, and as a result, our stage can change the pump path by 7 nanoseconds (in terms of delay).

For most of this dissertation, we choose to work with pump-probe delays of -2 to $+5$ ns, though we can adjust this by altering the probe path length. Negative delay might sound counterintuitive, as we need the pump to arrive before the probe. However, since pulses are emitted from the Mira-900 every 13.16 ns, negative delay is measuring the impact of the previous pump pulse. The delay range under consideration is really modulo 13.16 ns, so we see both the end of one repetition period and the beginning of the next. This can be useful if one expects any transient behavior that would interfere with the signal at short pump-probe delays but not at longer delays. We have also found anecdotally that interpreting the results of field-dependent Faraday rotation experiments is simpler for pump-probe delays just shorter than the repetition period.

In order to generate spin polarization, the pump must be circularly polarized. The Mira-900 outputs linearly polarized pulses, which is ideal for the probe. We could use a QWP to polarize the pump, but instead we will use a photoelastic modulator, PEM-100 from Hinds Instruments. By orienting the PEM crystal at 45 degrees with respect to the pump polarization, we obtain a pump that oscillates between σ^+ and σ^- light, with frequency 50 kHz. The PEM also serves to modulate the pump for noise reduction through lock-in detection. We have space designated in our setup for an optical chopper for the pump line, should we desire this alternate means of modulation. This is marked in the figure with a dashed box. We adjust the height of the pump beam above the table with a periscope and can adjust the position of the pump on the sample through use of a motorized mirror.

The probe is sent through a New Focus Model 3501 Optical Chopper, chopping with frequency 1.37 kHz. This additional modulation will also assist with noise reduction. The probe is further sent through a linear polarizer (LP) to ensure it is still linear when it reaches the sample. Both pump and probe go through neutral density filter wheels (ND), allowing us to modify the power of each independently. We can apply filtering of up to OD 4.0. Finally, the two beams join paths again before the sample, though they are spatially separated. They are incident on a focusing lens with a fairly long focus (30 cm) immediately before the cryostat. The beams are focused onto the sample with spot sizes on the order of tens of microns.

To enable low-temperature measurements, the sample is mounted in one of our optical cryostats. The current setup is configured for using a Janis ST-300 transmission cryostat. The sample is mounted on a metal cold finger using silver paint as an adhesive. Silver paint ensures good thermal conductivity so the sample is held at the same temperature as the cold finger. The adhesion must be reliable, as the cryostat is mounted with the cold finger perpendicular to the ground. Gravity will attempt to pull the sample down. The cold finger is surrounded by a vacuum shroud with a window for optical access in the near-infrared wavelengths output by the Mira-900.

The low temperatures themselves are achieved with a continuous flow of liquid helium. We order 60 L dewars from Linde. One end of a cryogen transfer line is submerged into the dewar to build up pressures of 2-3 psi. This pressure forces helium through the vacuum-shrouded transfer line to the other end, which is carefully nestled into an inlet on the top of the cryostat. The helium cools the cold finger, in turn cooling the sample. Used helium gas is vented from an output on the cryostat, and we do not recover or re-use it. We can crudely control the temperature of the sample by adjusting a valve on the transfer line, limiting the amount of helium transferred. We can also adjust the pressure inside the helium dewar, but without an external pressure source, this is very difficult to control precisely.

Fine control of temperature is achieved with a heater located on the cold finger. We connect an electrical 10-pin connector from the cryostat to a Lakeshore Model 331 Cryogenic Temperature Controller. The controller monitors the current output of an AlGaAs diode on the cold finger and calculates the temperature using a calibration curve. The Lakeshore 331 acts to create a feedback loop between the heater and the temperature diode. We designate a setpoint temperature, and the controller continuously adjusts the heater power. While we could assume full control of this process and manually set the heater power, the feedback is fairly reliable, so long as the pressure in the dewar is roughly static. Using the controller, we can cool a sample from room temperature to 10 K in about an hour. This is a nonlinear process, with most time spent stabilizing the system at 10 K. A standard eight-hour data run will consume approximately 10 L of helium with our system, which roughly translates to some amount of startup usage and then 1 L per hour to maintain the temperature.

The ST-300 also features wiring posts on the cold finger that can connect wires at the sample with a ten-pin electrical connector on the exterior of the cryostat (distinct from that used for temperature control). Voltages are applied to the sample through this connector, such as for CISP measurements. Finally, the ST-300 is itself mounted on a set of Thorlabs motorized translation stages (LNR50 series). This stage can move the cryostat in all three spatial directions, giving us some additional flexibility in alignment.

The cold finger is nestled between two poles of a GMW Model 3470 45 mm electromagnet, which can achieve fields at the sample between -300 and $+300$ mT. The field at the sample is determined by the current flowing through the electromagnet. We can calibrate the electromagnet so that the relationship between current and field is known. Despite this, the calibration is sensitive to the increments by which the field is changing, which can complicate experiments with small field steps or nonstandard ordering of field points. We can account for the actual field by running our field steps again, replacing the cryostat with a gaussmeter. The Lakeshore Model 475 DSP Gaussmeter will measure the true magnetic field, giving us a new calibration that is valid only for that set of field points. For most experiments, the standard calibration is sufficient, but knowing the actual field is necessary when working with DNP. Because we were interested in Overhauser fields on the order of a few mT, it was imperative that we gaussmeter-correct our data. Thus, all of the data shown in Chapters 6 and 7 has been corrected with the actual field as measured by a gaussmeter.

For transmission experiments, light proceeds through the sample and out an optical access window on the rear of the vacuum shroud. This transmitted light is guided into a common collection path. For reflection experiments, the cryostat is tilted at a slight angle such that the reflected beam is spatially separated from the incident beam. A series of mirrors then guide the light into the collection path. These paths are shown together in the figure, though only one is ever in use thanks to a flip mirror. The collection path consists of a pinhole to filter out additional light, a half-wave plate (HWP), and a Wollaston prism. This prism is a type of linear polarizer that decomposes incident light into orthogonal polarizations and spatially separates them. The two beams are coupled into fibers which are sent to a photodiode bridge. The use of the HWP will be explained shortly. The photodiode bridge outputs a difference signal, a voltage, that is sent via BNC cable to a pair of lock-in amplifiers for demodulation.

3.3.3 Concept: Faraday Rotation and the Balanced Photodiode Bridge

In the spin systems we are considering, the rotation angle due to spin polarization is on the order of microradians. While our initial thought might be to use a linear polarizer and photodiode to measure the drop in intensity along the initial polarization direction, we know that $\cos\theta \approx 1$ when θ is very small. The light transmitted or reflected from our sample will be nearly unchanged. Furthermore, under usual experimental conditions, the reflected power from our samples is on the range of tens of microwatts. Thus, we would expect very little intensity along the orthogonal direction, which may challenge the sensitivity of our detector. It is worth noting that we do not need the absolute polarization angle of our transmitted/reflected light, only the angle relative to the incident probe. In principle, we could have used any linear polarization for our incident light. We only chose s-polarization for pragmatic reasons.

Thus, we desire a detection method that is sensitive to a microradian rotation of the axis of light polarization that is not easily compromised by room conditions. We use modulation and lock-in amplifiers to reduce external sources of noise. The lock-in amplifier is expecting an electrical signal, but that does not have to come from a single photodiode. Our detection solution is described simply as “two is better than one.” First, we employ two photodiodes in a bridge configuration that outputs a voltage proportional to the difference between the

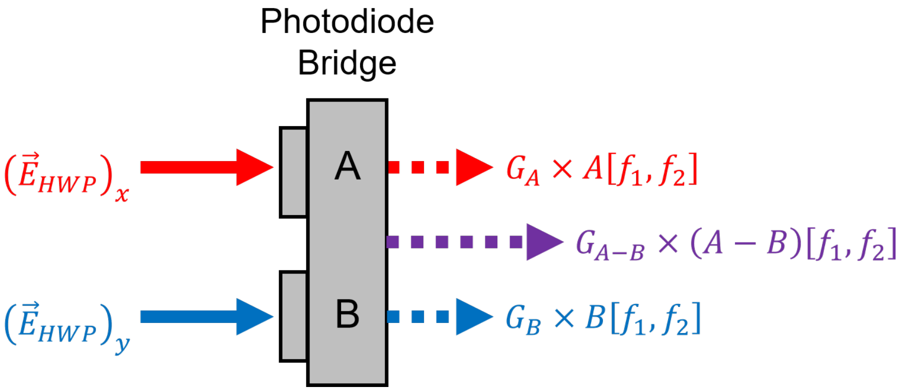

Figure 3.7: Cartoon representation of the balanced photodiode bridge. As described in the text, collected probe light is sent through a half-wave plate and a Wollaston prism, where it is split into two orthogonal components (solid arrows). These are coupled by fiber into the two photodiodes designated A and B. The bridge outputs three voltages (dashed arrows) via BNC cables to the lock-in amplifiers. The pump and probe are both modulated, so each voltage is modulated in time with frequencies f_1 (pump) and f_2 (probe). The gain factors G_i determine the conversion between incident light intensity and voltage. For the bridge used in this dissertation, the quantity G_A is unknown, but $G_B = -G_A$ and $G_{A-B} = 2G_A$.

individual signals. Second, we introduce a second rotation to our transmitted/reflected light that will allow us to measure the original rotation to a high degree of sensitivity.

We note here that a photodiode measures light intensity and converts it into electrical current. Our photodiode bridge takes two inputs, converts them into electric currents, and then calculates the difference current. These three currents are converted into voltages which are sent to the lock-in amplifier. The conversion between incident intensity and output voltage is determined by the circuitry inside the bridge and will depend on the frequency of the incident light. The difference signal may have a different conversion factor than the other outputs. Our bridge was constructed by previous students in our laboratory. For commercial boxes such as the Thorlabs PDB450A, this conversion may be available in the documentation. Either way, the conversion can be obtained by calibrating at frequencies of interest.

By convention, we refer to the two photodiode bridge inputs and their corresponding output voltages as A and B, respectively. See the cartoon in Fig. 3.7. The difference signal is denoted $A - B$. We have a single transmitted/reflected beam split into two beams using a Wollaston prism, which become our A and B. We identified the problems with trying to measure either the vertical or horizontal components of our collected light (basically all the light or basically none of the light, respectively). One can support these conclusions with calculations and show that subtracting one polarization component from the other fails to yield the rotation angle. However, the Wollaston prism is not tied to the frame of our experiment. In principle, it can be rotated in such a way that the light is split along a different set of orthogonal axes. For practical purposes, rather than rotate the prism, we introduce a half-wave plate, which can act to rotate the axis of linear polarization of light. Here is where the second angle becomes key.

Earlier, we considered a simplified calculation for Faraday rotation that ignored absorption and transmission coefficients. The transmitted light is of the form:

$$\vec{E}_{\text{out}} = E_0 \tau e^{i\left(\frac{\theta^+ + \theta^-}{2}\right)} \begin{pmatrix} \sin\theta \\ \cos\theta \end{pmatrix}.$$

The quantity of interest is θ. In what follows, we omit the amplitude and phase pre-factor for clarity, focusing only on the components.

We will assume that the Wollaston prism splits the collected light into horizontal (A) and vertical (B) components. We introduce a half-wave plate that rotates the linear polarization of the light by an angle $\phi \in [0, \pi)$:

$$\begin{aligned} \vec{E}_{\text{HWP}} &\propto \begin{pmatrix} \cos\phi & -\sin\phi \\ \sin\phi & \cos\phi \end{pmatrix} \begin{pmatrix} \sin\theta \\ \cos\theta \end{pmatrix} \\ &= \begin{pmatrix} \sin\theta\cos\phi - \cos\theta\sin\phi \\ \sin\theta\sin\phi + \cos\theta\cos\phi \end{pmatrix} \\ &= \begin{pmatrix} \sin(\theta - \phi) \\ \cos(\theta - \phi) \end{pmatrix}. \end{aligned}$$

The half-wave plate mixes the two orthogonal components of light, replacing the original angle θ with the new rotation angle $(\theta - \phi)$. The intensity in input A is still proportional to a squared sine, and the intensity in input B is still proportional to a squared cosine. Our photodiode bridge outputs $A - B$. In this calculation, we forego the final simplification into single sinusoids above, as it makes our final point much clearer:

$$\begin{aligned}
A - B &\propto (\sin\theta\cos\phi - \cos\theta\sin\phi)^2 - (\sin\theta\sin\phi + \cos\theta\cos\phi)^2 \\
&= \sin^2\theta\cos^2\phi + \cos^2\theta\sin^2\phi - 2\sin\theta\cos\theta\cos\phi\sin\phi \\
&- \left(\sin^2\theta\sin^2\phi + \cos^2\theta\cos^2\phi + 2\sin\theta\cos\theta\cos\phi\sin\phi\right) \\
&= \left(\sin^2\theta - \cos^2\theta\right)\left(\cos^2\phi - \sin^2\phi\right) - 4\sin\theta\cos\theta\cos\phi\sin\phi \\
&= -\cos 2\theta\cos 2\phi - \sin 2\theta\sin 2\phi.
\end{aligned}$$

We now choose ϕ with the goal of isolating θ. For very small θ, $\sin 2\theta \approx 2\theta$, so we choose ϕ to eliminate the cosine term. We set $\phi = \frac{\pi}{4}$, so $\cos 2\phi = 0$ and $\sin 2\phi = 1$. We are left with

$$\begin{aligned}
A - B &\propto -\sin 2\theta \\
&\approx -2\theta. \qquad (3.6)
\end{aligned}$$

Note that $\cos\frac{\pi}{4} = \sin\frac{\pi}{4} = \frac{1}{\sqrt{2}}$, so the second rotation served to distribute the intensity nearly evenly between the orthogonal polarizations. Hence, we refer to our photodiode bridge as “balanced.” Balanced detection is a key method for eliminating sources of noise by getting rid of the common signal in two inputs.

Knowing the general spectral shape expected for Faraday rotation is great for building intuition, but in real experiments, we cannot turn off the difference in transmission for the different helicities. If we want to calculate the expected outcome of a Faraday rotation experiment, we should work with the full electric field components, replacing the sine and cosine with the more general E_x and E_y. That is what we are actually doing in the laboratory.

These terms now incorporate the additional amplitude and phase factors, whether or not we assume that absorption differs noticeably for the handedness of light. The light coming out of the half-wave plate is now

$$\begin{aligned}\vec{E}_{\text{HWP}} &= \begin{pmatrix} \cos\frac{\pi}{4} & -\sin\frac{\pi}{4} \\ \sin\frac{\pi}{4} & \cos\frac{\pi}{4} \end{pmatrix} \begin{pmatrix} E_x \\ E_y \end{pmatrix} \\ &= \begin{pmatrix} E_x\cos\frac{\pi}{4} - E_y\sin\frac{\pi}{4} \\ E_x\sin\frac{\pi}{4} + E_y\cos\frac{\pi}{4} \end{pmatrix} \\ &= \frac{1}{\sqrt{2}} \begin{pmatrix} E_x - E_y \\ E_x + E_y \end{pmatrix} .\end{aligned}$$

We calculate $A - B$:

$$\begin{aligned} A - B &= \left| \frac{1}{\sqrt{2}} (E_x - E_y) \right|^2 - \left| \frac{1}{\sqrt{2}} (E_x + E_y) \right|^2 \\ &= \frac{1}{2}\left(|E_x|^2 + |E_y|^2 - E_x E_y^* - E_x^* E_y \right) - \frac{1}{2}\left(|E_x|^2 + |E_y|^2 + E_x E_y^* + E_x^* E_y \right) \\ &= -E_x E_y^* - E_x^* E_y \\ &= -2 \text{ Re}\left[E_x E_y^* \right] , \end{aligned} \tag{3.7}$$

where E_i^* is the complex conjugate of E_i. Only the cross-term remains, and this yields a signal proportional to Faraday rotation. In a sense, we are measuring the mixed intensity of the orthogonal polarizations. However, when comparing measurements for different experimental conditions, or even different materials, we must have a measurement that is independent of the transmitted light intensity. We want a normalization factor.

It is natural to normalize the signal by the total intensity of the transmitted light. This is obtained by the sum of the two inputs A and B, and is independent of the rotation due to the half-wave plate:

$$
\begin{aligned}
A+B &= \left|\frac{1}{\sqrt{2}}\left(E_x - E_y\right)\right|^2 + \left|\frac{1}{\sqrt{2}}\left(E_x + E_y\right)\right|^2 \\
&= \frac{1}{2}\left(\left|E_x\right|^2 + \left|E_y\right|^2 - E_x E_y^* - E_x^* E_y\right) + \frac{1}{2}\left(\left|E_x\right|^2 + \left|E_y\right|^2 + E_x E_y^* + E_x^* E_y\right) \\
&= \left|E_x\right|^2 + \left|E_y\right|^2 .
\end{aligned}
$$

Putting it all together, we obtain an expression for measuring Faraday rotation in terms of either the photodiode inputs A and B or the electric field components once rotated by the half-wave plate:

$$
\begin{aligned}
\sin 2\theta &= \frac{A-B}{A+B} \\
-2\theta &\approx \frac{A-B}{A+B} \\
\theta &\approx -\frac{1}{2}\left(\frac{A-B}{A+B}\right) \\
&= \frac{2 \text{ Re}\left[E_x E_y^*\right]}{\left|E_x\right|^2 + \left|E_y\right|^2}. \qquad (3.8)
\end{aligned}
$$

The negative sign here is a consequence of how we defined our angles and rotation matrices. It can be omitted, as the sign of our lock-in voltage is determined separately from the phase between the reference oscillation and the internal oscillator.

The output $A-B$ of our photodiode bridge is thus proportional to the quantity of interest. For most experimental situations, this is sufficient for extracting timescales of interest. In practice, $A+B$ remains close enough to constant over the course of a measurement, whether we are changing pump-probe delay time or external field magnitude. Thus our laboratory practice is to present $A-B$ as Faraday or Kerr rotation, rendered in arbitrary units (AU). Most of the data shown in this dissertation is either unnormalized or normalized up to a set of constants (elaborated on in the next section). Only when we are interested in measuring or comparing the magnitude of rotation do we need to proceed further. Extracting Faraday rotation was a key part of our CISP studies and the major exception to the practice stated here.

3.3.4 Concept: Decoding Lock-In Voltage

We utilize a lock-in detection scheme to measure small signals that might otherwise be drowned out by much larger backgrounds. Specifically, we use a number of Signal Recovery SR7265 lock-in amplifiers in our experiments, and we want to understand how they pull our signal out of the noise. Consider some hypothetical small voltage we want to measure, V_{signal}, that is collected alongside some noise V_{noise}. Assume the signal is orders of magnitude smaller than the noise, so we would not not be able to follow it with a single detector.

We solve this problem by modulating our signal by some periodic function $M\left(f_1 t\right)$. This new time-varying voltage is sent to the lock-in amplifier:

$$V_{\text{in}}\left(t\right) = V_{\text{signal}} M\left(f_1 t\right) + V_{\text{noise}}.$$

Now, there are two components to our voltage: one that oscillates with frequency f_1 and amplitude equal to our desired measurement, and one that is constant. Even though that constant is huge, a lock-in amplifier is designed to ignore it. We tell the lock-in amplifier what frequency to look for (usually by providing an external reference) and it only picks out the amplitude of oscillations at that frequency. This is called *demodulation*. If we give the lock-in amplifier the above input voltage and a reference sine with frequency f_1, it will successfully pick out V_{signal}.

There are two main steps implemented by the electronics inside the lock-in in the demodulation process. First, the lock-in mixes the input voltage with a sine wave voltage at the reference frequency. Then, it applies a low-pass filter. The filter used is determined by the *time constant* set by the user. Most simply, the time constant is how long the lock-in samples the input voltage before it outputs the demodulated signal. The time constant also determines the cutoff frequency of the low-pass filter. The low-pass filter is aiming to isolate the DC voltage component that results from the mixing.

Here is a simple example to demonstrate why this method works. We modulate our signal V_{signal} by a sine at frequency f_1:

$$V_{\text{signal}} \sin(2\pi f_1 t) + V_{\text{noise}}.$$

The lock-in mixes our entire input by a sine at this frequency, equivalent to multiplying the whole thing by a sine. We use trigonometry to simplify the expression:

$$\begin{aligned} V_{\text{mix}}(t) &= V_{\text{signal}} \sin(2\pi f_1 t) \sin(2\pi f_1 t) + V_{\text{noise}} \sin(2\pi f_1 t) \\ &= V_{\text{signal}} \sin^2(2\pi f_1 t) + V_{\text{noise}} \sin(2\pi f_1 t) \\ &= V_{\text{signal}} \frac{1}{2} (1 - \cos(2\pi (2f_1) t)) + V_{\text{noise}} \sin(2\pi f_1 t) \\ &= \frac{V_{\text{signal}}}{2} - \frac{V_{\text{signal}}}{2} \cos(2\pi (2f_1) t) + V_{\text{noise}} \sin(2\pi f_1 t). \end{aligned}$$

Three distinct frequencies have emerged: 0, f_1, and $2f_1$. These are the difference frequency, the original frequency, and the sum frequency, respectively. The DC term is proportional to our signal, so we want to keep that and get rid of the terms that are still oscillating. The low-pass filter, when chosen correctly, will do just that. Even if the background noise is also time-varying with frequency f_N, it will result in terms at frequencies $f_1 \pm f_N$, which will be filtered out. We note that a phase difference between the input signal and the reference could throw a wrench into this picture, introducing more oscillating terms. The SR7265 offers an auto-phasing feature that can eliminate any such phase difference.

This description of the lock-in is accurate, but conceptually, it may be more useful to think of the input signal in terms of a Fourier series. The lock-in amplifier acts to pick out the component of the Fourier sine series corresponding to the reference frequency. Put another way, the lock-in measures the first Fourier coefficient. In the example where we modulate by a sine, the Fourier coefficient of the sine is just 1. The lock-in should thus read the signal V_{signal}. For modulation $M(ft)$, the output of the lock-in will be $b_1 V_{\text{signal}}$, where b_1

is defined as the first Fourier sine coefficient

$$b_1 = \frac{1}{1/2} \int_0^1 M\left(ft\right) \sin\left(2\pi ft\right) d(ft). \tag{3.9}$$

Here, we have grouped frequency and time into a dimensionless quantity such that the "period" is 1. This is by no means necessary, but it does clean up the calculations for the modified waveforms we present in Chapter 5. Note that we could have taken $V_{\mathrm{mix}}\left(t\right)$ above and integrated that over one period (with proper normalization factor, of course).

As an example, consider modulation by a bipolar square wave. We modulate the applied voltage used for CISP in this way in Chapter 5. We define the square wave:

$$s_0\left(ft\right) = \begin{cases} 1, & ft \in \left[0, \frac{1}{2}\right) \\ -1, & ft \in \left(\frac{1}{2}, 1\right]. \end{cases} \tag{3.10}$$

The first Fourier sine coefficient is given by

$$\begin{aligned} b_1 &= \frac{1}{1/2} \int_0^1 M\left(ft\right) \sin\left(2\pi ft\right) d(ft) \\ b_1 &= \frac{1}{1/2} \int_0^1 s_0\left(ft\right) \sin\left(2\pi ft\right) d(ft) \\ &= 2 \int_0^{1/2} \sin\left(2\pi ft\right) d(ft) - 2 \int_{1/2}^1 \sin\left(2\pi ft\right) d(ft) \\ &= -2\frac{1}{2\pi} \cos\left(2\pi ft\right)\Big|_0^{1/2} + 2\frac{1}{2\pi} \cos\left(2\pi ft\right)\Big|_{1/2}^1 \\ &= -\frac{1}{\pi}\left(-1-1\right) + \frac{1}{\pi}\left(1+1\right) \\ &= \frac{2}{\pi} + \frac{2}{\pi} \\ &= \frac{4}{\pi}. \end{aligned}$$

Thus, if the signal of interest is V_{signal}, we would expect the lock-in to report the quantity $\frac{4}{\pi}V_{\mathrm{signal}}$. Numerically, $b_1 \approx 1.273$.

When an optical chopper is used in experiments, the modulating function is not a bipolar square wave, but a unipolar square wave that goes between 0 and 1. We define this function

u_0 in terms of s_0:

$$u_0\left(ft\right) = \frac{1}{2}\left(1 + s_0\left(ft\right)\right). \tag{3.11}$$

The first Fourier sine coefficient will be half of that for the bipolar square wave. Thus, demodulation by a unipolar square wave will report a value multiplied by $\frac{2}{\pi} \approx 0.6366$.

These conclusions are not *quite* correct yet. The amplifier actually reports a root-mean-square (RMS) voltage. The RMS value of a sinusoidal voltage is the amplitude of that sinusoid divided by $\sqrt{2}$. Thus, the actual output of the lock-in is $b_1 V_{\mathrm{signal}}/\sqrt{2}$.

Note that if we have signals $A - B$ and $A + B$ that proceed from the same experiment, the ratio will cancel these extra lock-in terms. As long as the gain factor for the signals are equivalent, then we can calculate Faraday rotation θ.

For the CISP experiments in Chapter 5, the $A + B$ measurement had not yet been implemented. Instead, because the probe beam is not chopped, A and B were measured directly from the photodiode bridge without demodulation through the lock-in's analog-to-digital converters. For the bridge used in this setup, the gain on output $A - B$ is twice that of the individual outputs. The Faraday rotation, measured in μrad, was thus calculated:

$$\theta_F = 10^6 \times \frac{1}{2} \times \frac{\sqrt{2}}{b_1} \times \frac{V_{A-B}}{2\left(V_A + V_B\right)}. \tag{3.12}$$

3.3.5 Concept: Cascaded Lock-Ins

The case for two modulations is trickier. In our experiments, we modulate the pump with a PEM at frequency f_1 and the probe with an optical chopper at frequency f_2. We send the double-modulated $A - B$ to a lock-in referenced to f_1. Rather than record the output of this lock-in, we send a partially demodulated signal to a second lock-in referenced to f_2.

The output of this second lock-in is our desired signal. We call this chaining of two lock-ins a *cascaded* lock-in setup.

We provide a schematic of this setup in Fig. 3.8 to assist with our explanation. In this picture, we represent each SR7265 with a simple cartoon. The two lock-ins are labeled "lock-in 1" and "lock-in 2", or ''LI1" and "LI2," for short. Each has two input ports intended for demodulating signals, designated A and $-B$. This is very unfortunate labeling, since these do NOT correspond to the A and B of our photodiode bridge. The input A demodulates the signal as is, while the input $-B$ demodulates the inverse of the signal. For now, we use a single input. Each lock-in also has two analog-to-digital converters (ADC), which are effectively voltmeters. The final input "Ref" takes in the reference frequency via BNC cable. The black arrows each represent a BNC cable, with the colored rectangles representing the colored zip ties we use to distinguish between cables in our laboratory. The demodulated output of each lock-in is displayed on its front panel. We group the constants acquired in the demodulation into the quantity Q_i. The SR7265 has a number of output ports, but we focus on only one, designated FASTX.

The FASTX port is an analog output proportional to the demodulated signal:

$$V_{\text{FASTX}} = (2.5\ V) \times \frac{V_X}{V_{\text{SENS}}},$$

where V_X is the partially demodulated signal and V_{SENS} is the sensitivity setting of that lock-in. We hesitate to equate V_X with V_{signal} because it is not clear to us whether the output voltage is RMS or if there is any additional gain applied. The sensitivity of the lock-in determines how large of a voltage the lock-in can demodulate and, at the same time, the resolution of the demodulated signal. It is generally best practice to set the sensitivity as low as possible such that the demodulated signal does not exceed the limit and overload the lock-in, lest the output not be reliable. The ratio V_X/V_{SENS} is also called the $X\%$, which can be displayed on the lock-in front panel. Surprisingly, this value can exceed 100%.

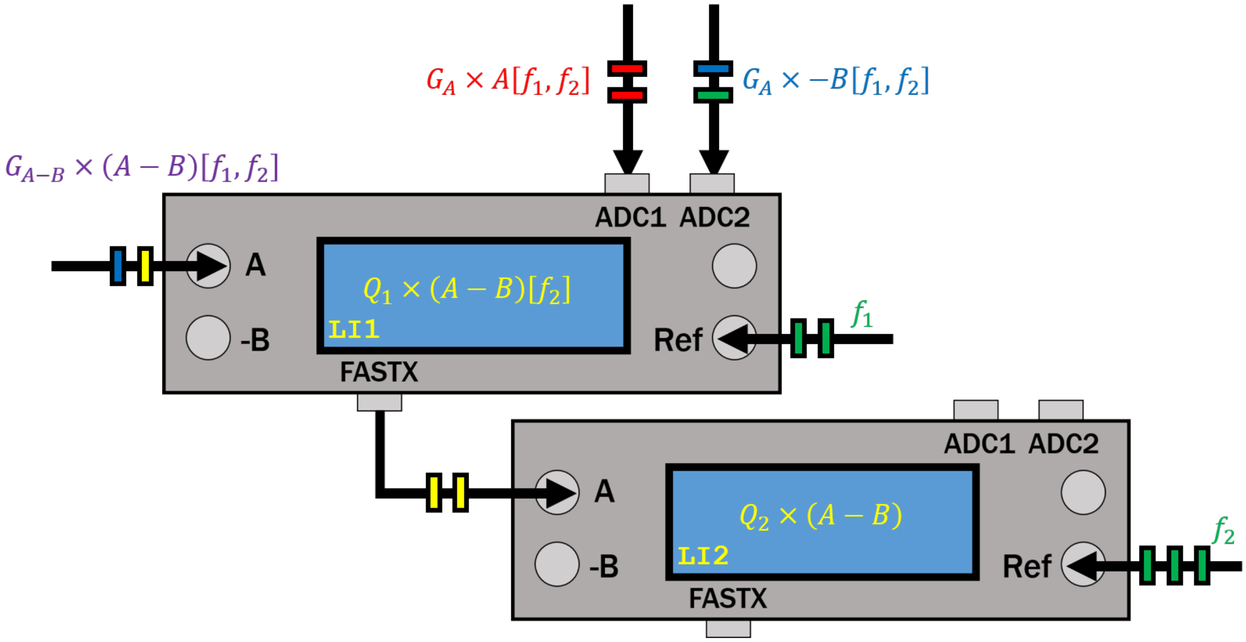

Figure 3.8: Cartoon representation of the cascaded lock-in setup utilized in this dissertation. The lock-ins are designated "LI1" and "LI2." The functions of the input ports A, $-B$, ADC1, ADC2, and Ref are described in the text. The only output port shown is FASTX. Each black arrow represents a BNC cable. In 1277 Randall, each cable is distinguished by a number of color-coded zip ties. The colored rectangles represent the zip ties in use at the time of this writing. The demodulated signals are displayed on the front panel of each lock-in. The signal in LI1 will still oscillate at the probe frequency f_2.

As a result, the FASTX output varies in time at the probe chopper frequency f_2, but the amplitude is no longer well-known. While we know how to correct the output of a single lock-in, we opt to leave the demodulated $A - B$ as is, in arbitrary units. Each data point is scaled by the same unknown factor Q_2, so we can still extract timescales and make other key observations from the data. Even so, experimentalists should still make sure to record the lock-in sensitivity of both lock-ins, among other experimental parameters, as that will give a sense for how data taken at different sensitivities will scale.

We specifically chose to demodulate by the pump frequency first. We noted during our initial description of the lock-in that, after mixing with the reference sine, the amplifier applies a low-pass filter. For now, we assume that each modulation is a sinusoid. The double-modulated signal is given by (omitting the noise term for now)

$$\begin{aligned} V_{\text{in}}\left(t\right) &= V_{\text{signal}}\sin\left(2\pi f_1 t\right)\sin\left(2\pi f_2 t\right) \\ &= \frac{V_{\text{signal}}}{2}\left(\cos\left(2\pi\left(f_1 - f_2\right)t\right) - \cos\left(2\pi\left(f_1 + f_2\right)t\right)\right). \end{aligned}$$

There are terms oscillating at both the sum and difference frequencies. When we mix in the reference sine at frequency f_1,

$$\begin{aligned} V_{\text{mix}}\left(t\right) &= \frac{V_{\text{signal}}}{2}\left(\cos\left(2\pi\left(f_1 - f_2\right)t\right) - \cos\left(2\pi\left(f_1 + f_2\right)t\right)\right)\sin\left(2\pi f_1 t\right) \\ &= \frac{V_{\text{signal}}}{2}\sin\left(2\pi f_2 t\right) + \frac{V_{\text{signal}}}{4}\left(\sin\left(2\pi\left(2f_1 - f_2\right)t\right) - \sin\left(2\pi\left(2f_1 + f_2\right)t\right)\right). \end{aligned}$$

We want the first term to make it through the filter so it can be demodulated by LI2. Therefore, we need f_2 to be much smaller than $2f_1 \pm f_2$, meaning we need $f_2 \ll f_1$. If the frequencies are comparable, we will keep a DC term that will be subsequently filtered out by LI2. Even if we choose the frequencies to be far apart, if we demodulate by the smaller frequency first, we will end up with three terms each at essentially the same frequency.

Fortunately for this method, the PEM oscillates at 50 kHz while optical choppers are on order of kHz. When using an optical chopper for the pump as well, we must be careful to choose as large a chopper frequency as possible. This may be accompanied by reducing the probe chopper frequency to maximize the ratio between them.

We must likewise select the time constant for LI1 to successfully filter out the unwanted higher-frequency terms while keeping the term oscillating at f_2. A general rule of thumb, from Ref. [51], is to select the time constant TC_1 such that $1/f_1 < \text{TC}_1 < 1/\left(4\pi f_2\right)$. In our experiments, we use $\text{TC}_1 = 160\ \mu\text{s}$ for PEM modulation and $\text{TC}_1 = 640\ \mu\text{s}$ for chopper modulation (of 6-7 kHz). We leave the time constant corresponding to the probe chopper at $\text{TC}_2 = 200$ ms.

All said, we do not at present have the means to calculate the magnitude of Faraday rotation obtained through a cascaded lock-in setup. We still elect to normalize the $A - B$

signal. In the past, this was accomplished by summing the raw V_A and V_B, as mentioned in the last section, measured through ADC1 and ADC2. However, when we chop the probe, V_A and V_B will reflect that chopping. Pointwise normalization will not work. Instead, we can infer from the series of recorded V_A and V_B what the unchopped amplitudes must have been and use those. Again, we must keep in mind any differences in gain when applying this normalization. This method will not account for drifts in laser power over the course of an experiment, though.

At present, we have employed the use of yet another lock-in to both make this normalization simpler for us and robust to laser power drift. “Lock-in 3”, or “LI3,” is represented in Fig. 3.9. Here, we do send photodiode bridge outputs A and B to the LI3 inputs A and $-B$. When both inputs are used simultaneously, the lock-in demodulates the sum of these inputs. The lock-in inverts our B, which is already inverted, so the demodulated signal works out to our $A + B$. The SR7265 does not have the ability to sum two modulated inputs, so we are fortunate that our photodiode bridge inverts B for us. Here, LI3 demodulates with the probe chopper frequency, so we measure the voltage due to the probe being unblocked. This method ignores the changes to the probe reflectivity due to the presence of the pump. We obtain $A+B$ for every point in our experiment, so we can apply the normalization point-wise. Because this is a single lock-in measurement, we can apply the correction factors from the previous section as well, but we do not do so for the measurements presented in this dissertation. If future researchers determine the correction factors for the cascaded lock-in setup, we have in hand a known normalization and can at last determine the magnitude of the measured Faraday rotation. Until then, we will proceed with this pointwise normalization.

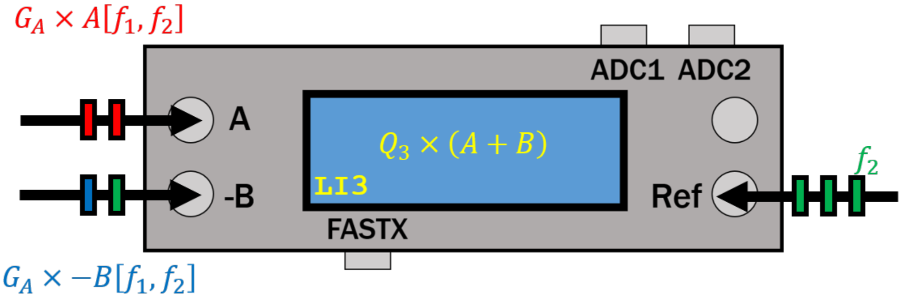

Figure 3.9: Cartoon representation of lock-in "LI3" used for normalizing the Faraday/Kerr rotation measurements in this dissertation. The functions of the input ports A, $-B$, ADC1, ADC2, and Ref are described in the text. The only output port shown is FASTX. Each black arrow represents a BNC cable. In 1277 Randall, each cable is distinguished by a number of color-coded zip ties. The colored rectangles represent the zip ties in use at the time of this writing. The demodulated signals are displayed on the front panel of each lock-in.

CHAPTER 4

Survey of Experimental Techniques

4.1 Motivation

In this chapter, we list each of the experimental techniques employed during the acquisition of the data shown in this dissertation. With the exception of photoluminescence, the techniques described here are examples of pump-probe spectroscopy. In most cases, the pump and probe are both optical pulses generated by our Ti:Sapph laser, though electrical pumping is used for current-induced spin polarization.

For each technique, a simple experimental schematic (adapted from Ref. [10]) is provided alongside the fit equation and sample data, primarily from one of the materials considered later in this dissertation. The schematics and equations are color-coded to make clear which experimental parameters are changed, with fixed parameters remaining in black. With the exception of time- and field-resolved Faraday and Kerr rotation, the experimental schematics are drawn for reflection geometry only. After a description of the implementation of each experiment, we give a short description of the usage. For ease of reference, technique names are bolded in this chapter. Two of these techniques do not show up explicitly elsewhere in this dissertation but were key to its completion.

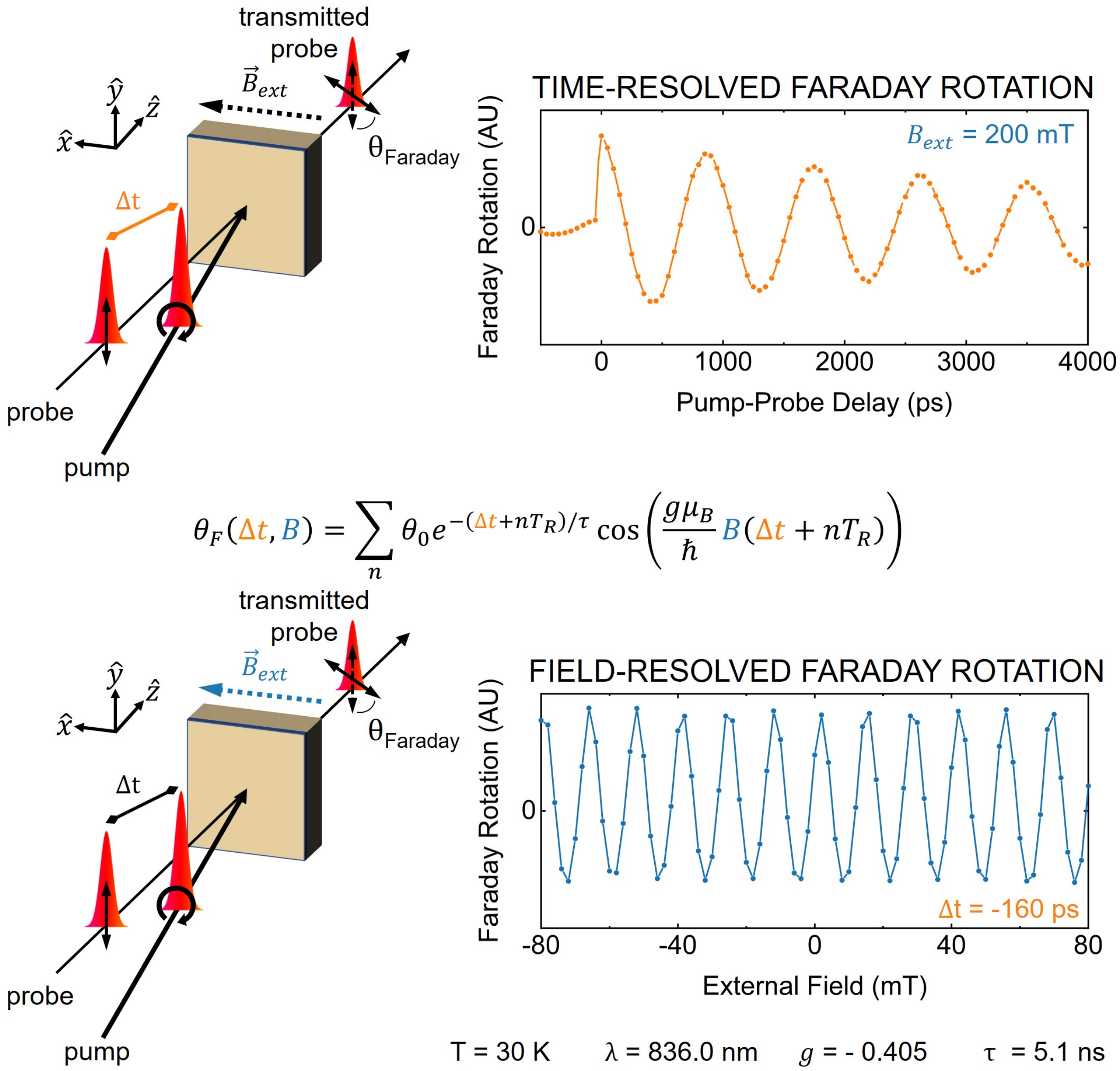

$$\theta_F(\Delta t, B) = \sum_n \theta_0 e^{-(\Delta t + nT_R)/\tau} \cos\left(\frac{g\mu_B}{\hbar} B(\Delta t + nT_R)\right)$$

Figure 4.1: Schematic and example experimental data for Time-Resolved and Field-Resolved Faraday Rotation. Both experiments are modeled with the same equation (shown center). In Time-Resolved Faraday Rotation (TRFR), the external field is fixed and the pump-probe time delay is incremented. Here, the external field is set to 200 mT and the pump-probe delay is scanned from −500 to +5000 ps in 25 ps increments (the delay range +4000 to +5000 ps is omitted for clarity, as are every other delay step). In Field-Resolved Faraday Rotation (FRFR), the pump-probe time delay is fixed and the external field is incremented. Here, the pump-probe delay is set to −160 ps, equivalent to 13 ns after the previous pulse, and the external magnetic field is swept from −200 to +200 mT in 2 mT steps (only −80 to +80 mT is shown). Both measurements were carried out on sample RMBE1130-K (Chapter 5) at temperature 30 K with laser wavelength 836.0 nm. For this material, the electron g factor is −0.405 and the spin lifetime is 5.1 ns.

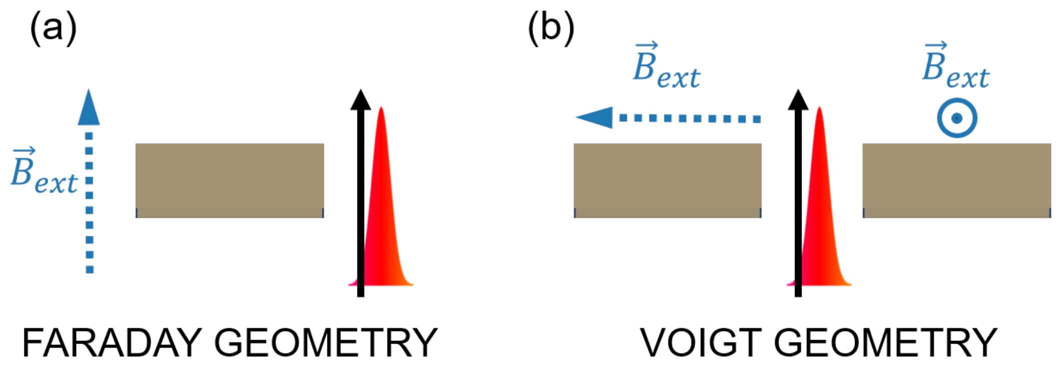

Figure 4.2: Faraday and Voigt experimental geometries for magneto-optical experiments. The sample is viewed from above, in contrast to the other schematics in this chapter. In the (a) Faraday geometry, the external field is parallel or anti-parallel to the optical axis (represented by a pulse). In the (b) Voigt geometry, the external field is perpendicular to the optical axis; two such possibilities are shown.

4.2 Time-Resolved Faraday/Kerr Rotation (Delay Scans)

Time-Resolved Faraday Rotation (TRFR) is a pump-probe measurement using ultrafast laser pulses split from the same source as pump and probe. The generation mechanism is optical orientation, generating an electron spin polarization along the optical axis $\hat{z}$. The experimental geometry is defined in Fig. 4.1. We transmit a linearly polarized probe pulse through the material to measure Faraday rotation, which is proportional to the spin polarization along the optical axis. If desired, a constant external magnetic field may be applied to the system. The experiment is in *Faraday geometry* when the applied field is parallel to the optical axis and in *Voigt geometry* when the applied field is transverse to the optical axis; see Fig. 4.2. In Voigt geometry, the electron spin polarization will precess about the external field.

This experiment is "time-resolved" because Faraday rotation is measured at each step of a series of pump-probe delays. In the absence of a transverse magnetic field, Faraday rotation will decay exponentially with increasing pump-probe delay. We can extract the spin lifetime from these measurements. In the presence of a transverse magnetic field, the spin polarization will precess as it decays. Faraday rotation will take the form of a decaying sinusoid, and we can extract both the spin lifetime and the electron g factor. Example data and the fit equation for Voigt geometry are shown in Fig. 4.1.

Time-Resolved Kerr Rotation (TRKR) is an analogous experiment performed in the reflection geometry, as shown in Fig. 4.3. The expected shape of the resulting data is expected to be the same as for Faraday rotation, yielding the same extracted lifetime and g factor. However, the spectral response to the wavelength of the probe should be different, as mentioned in Chapter 3. In Fig. 4.3, we demonstrate Kerr rotation measured in the absence of a magnetic field. The same governing fit equation applies.

The temporal dynamics accessed through these methods are limited only by the laser and the mechanical delay line. We cannot measure dynamics shorter than our optical pulse duration (of about 2 ps). The mechanical delay line sets the resolution of our experiments otherwise, and its length (here approximately 7 ns) determines the full delay range we can view. Since pump-probe delay is the changing experimental parameter, we refer to these experiments as **delay scans**.

4.3 Field-Resolved Faraday/Kerr Rotation (Field Scans)

Field-Resolved Faraday Rotation (FRFR) is a pump-probe measurement using ultrafast laser pulses split from the same source as pump and probe. The generation mechanism is optical orientation, generating an electron spin polarization along the optical axis $\hat{z}$. The experimental geometry is defined in Fig. 4.1. We transmit a linearly polarized probe pulse through the material to measure Faraday rotation, which is proportional to the spin polarization along the optical axis. In contrast to TRFR, pump-probe delay is fixed. This choice of delay is arbitrary but affects the measurements. An external magnetic field is applied,

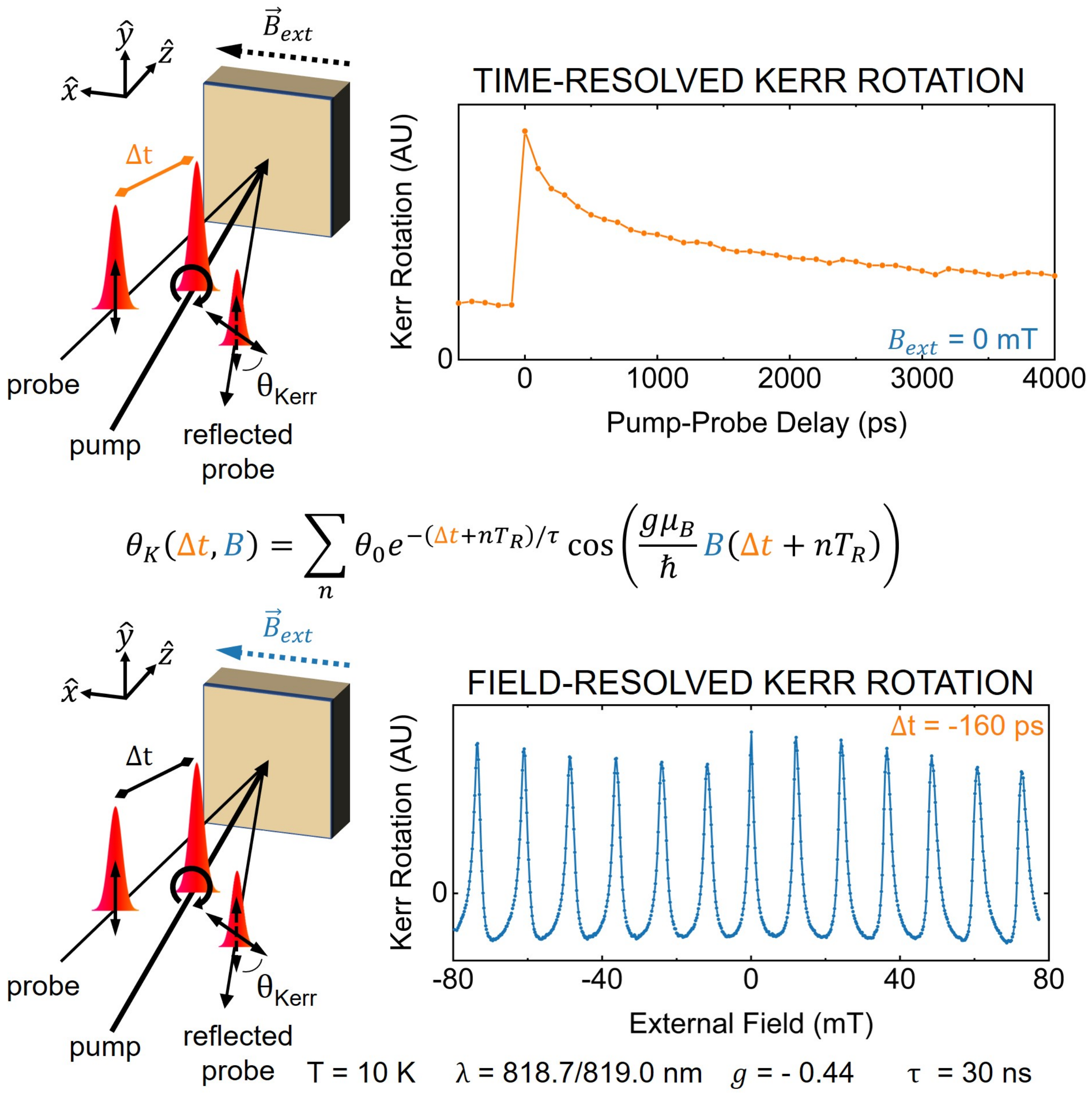

Figure 4.3: Schematic and example experimental data for Time-Resolved and Field-Resolved Kerr Rotation. Both experiments are modeled with the same equation (shown center). In Time-Resolved Kerr Rotation (TRKR), the external field is fixed and the pump-probe time delay is incremented. Here, the external field is turned off and the pump-probe delay is scanned from -500 to $+7000$ ps in 100 ps increments (the delay range $+4000$ to $+7000$ ps is omitted for clarity). In Field-Resolved Kerr Rotation (FRKR), the pump-probe time delay is fixed and the external field is incremented. Here, the pump-probe delay is set to -160 ps, equivalent to 13 ns after the previous pulse, and the external magnetic field is swept from -80 to $+80$ mT in 0.25 mT steps. Both measurements were carried out on sample 033XT-A5 (Chapter 6) at temperature 10 K with laser wavelength 818.7 nm (TRKR) and 819.0 nm (FRKR). For this material, the electron g factor is -0.44 and the spin lifetime is 30 ns.

and this is the quantity that is incremented. We operate exclusively in the Voigt geometry. As before, Field-Resolved Kerr Rotation (FRKR) denotes the version of this experiment performed in the reflection geometry. This experimental geometry is shown in Fig. 4.3. In analogy to delay scans, we refer to field-resolved scans as **field scans**. Alternatively, we use the term **field sweeps**.

As described in Chapter 2, spin polarization generated by successive laser pulses may constructively or destructively interfere (RSA). For spin lifetimes shorter than the period between pulses, the existing spin polarization will have mostly decayed in this period, and we can treat the Faraday rotation as essentially a single decaying cosine. When plotted as a function of external field as in Fig. 4.1, we observe a cosine. For longer lifetimes, that interference will lead to the buildup of spin polarization at certain external fields B_{ext} (the RSA period Eq. 2.9). The cosine becomes a series of Lorentzian-like peaks, as seen in Fig. 4.3. We derived an expression for the spin polarization after an infinite number of prior pulses, but we show the sum of pulses for clarity here. By default, we use a pump-probe delay of -160 ps, corresponding to 13 ns between pump and probe. At this delay, the overall envelope on Kerr rotation is relatively flat over the fields we consider.

Field-resolved measurements are key for any situation when an additional field component may be expected, such as spin-orbit fields or an Overhauser field. Because we know the magnitude of the applied external field, we can fit FRFR to determine the additional fields present. FRKR has been key to our understanding of the coupled-electron nuclear spin system in GaAs. FRKR has also been used to study anisotropic spin dephasing [52].

Given that the sharpness of the peaks scales inversely with spin lifetime, field-resolved measurements can be used to measure electron spin lifetimes that are much longer than T_R. The time-resolved experiments may not show appreciable decay over 13.16 ns, but the peaks in FRFR and FRKR can be fit. It is good practice, then, to carry out both time- and field-resolved measurements on a sample to check for consistency in lifetime fits.

In experiments where the temporal relationship between pump and probe is not defined (such as when using a continuous-wave pump), field scans still offer information on the spin lifetime of the system. Spin polarization is continuously generated and continuously decays, reaching a steady state. When an external magnetic field is applied, the generated spin polarization will precess, leading to accelerated dephasing and smaller steady-state spin polarization. The steady-state spin polarization is the integral of the solution to the Bloch equation over all time, where γ_{op} is the optical generation rate:

$$\begin{aligned} S_z &= \int_0^\infty \gamma_{op} e^{-t/\tau} \cos\left(\frac{g\mu_B}{\hbar} Bt\right) dt \\ &= \gamma_{op}\tau \frac{1}{1+(\Omega\tau)^2}. \end{aligned} \tag{4.1}$$

The Faraday rotation is proportional to S_z, so the FRFR will be an even Lorentzian. This is known as the Hanle curve, acquired via a **Hanle measurement** [53]. Extracting the width of the curve yields the coupled quantity $g\tau$, so if the g factor is known, the spin lifetime can be determined.

4.4 TRKR-RSA / Snapshot TRKR

TRKR-RSA and **Snapshot TRKR** are pump-probe measurements that combine both delay scans and field scans. Strictly speaking, we are not performing both types of scans simultaneously, as if we alternated delay steps and field steps. Instead, we carry out a scan of one parameter for a series of fixed values of the other parameter. We use reflection terminology, but these can be performed in transmission geometry as well. Here, TRKR-RSA refers to a series of delay scans carried out at a series of fixed external fields. For example, we might carry out a delay scan for each external field in the range 120 to 140 mT, in 1 mT steps. On the other hand, Snapshot TRKR is a series of field scans carried out at a series

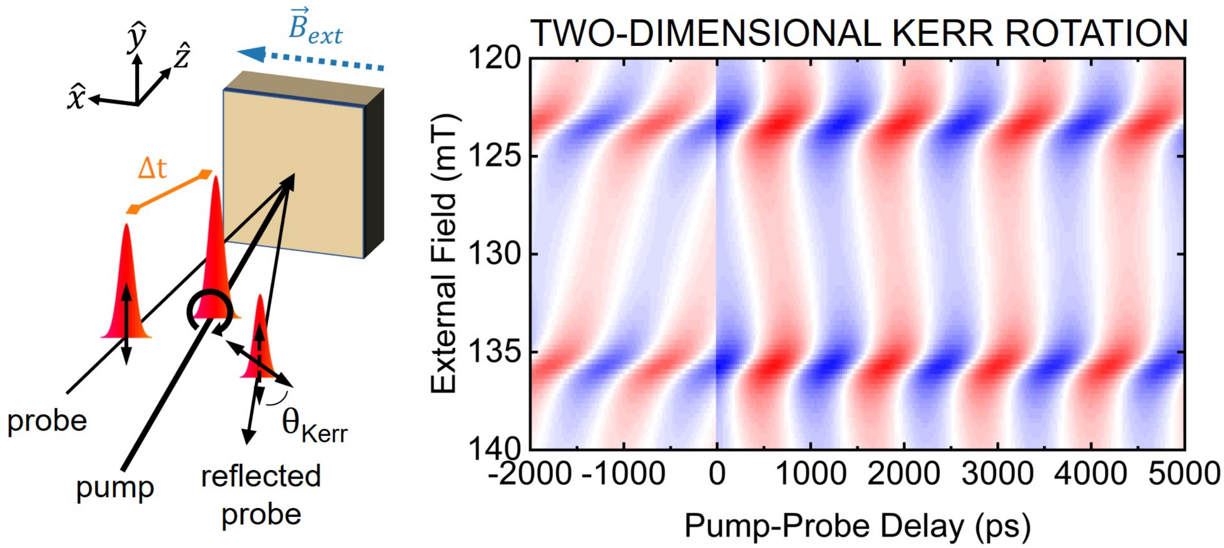

$$\theta_K(\Delta t, B) = \sum_n \theta_0 e^{-(\Delta t + nT_R)/\tau} \cos\left(\frac{g\mu_B}{\hbar} B(\Delta t + nT_R)\right)$$

(simulated) g = - 0.44 τ = 30 ns

Figure 4.4: Schematic and plotted fit equation for TRKR-RSA. The external field is fixed and the pump-probe time delay is incremented from −2000 to +5000 ps in 100 ps increments. The external field is then incremented by 1 mT from 120 to 140 mT. The two-dimensional data will follow the same equation for delay scans and field scans. The model here sums ten pulses, with parameters closely matched to sample 033XT-A5 (Chapter 6). Color scale omitted for clarity.

of pump-probe delays in the range −1920 to +1920 ps, in 160 ps steps. The difference in naming convention hints at a fundamentally different usage for these two seemingly identical methods.

In Chapter 3, we discussed RSA and the phase term γ that emerges from the influence of previous pulses. This phase was initially observed through TRKR-RSA experiments [36]. Modeled TRKR-RSA is presented alongside the experimental schematic in Fig. 4.4. This technique has found usage in experiments where the Larmor precession frequency is expected to change in a nonlinear way with external field, such as in hybrid semiconductor-ferromagnetic structures where this change follows a certain functional form [54]. In this dissertation, we consider instead the context of dynamic nuclear polarization (DNP) studies.

We can observe the Larmor precession frequency in our system change as the external field is changed through the delay scans. We present TRKR-RSA data on GaAs in Chapter 7 under the influence of nuclear-induced frequency focusing. Rather than the example TRKR-RSA shown here, those measurements revealed field ranges over which the precession frequency was roughly constant.

Snapshot TRKR was conceived for measuring the history-dependent DNP in Chapter 6. We take a series of identical field scans at a series of pump-probe delays in order to measure the Larmor precession frequency corresponding to each field step of the field scans. The extraction process is shown in Fig. 4.5. We compile all of the field scans (in blue) into a 2D array, Kerr rotation as a function of both external field and pump-probe delay. We then take a perpendicular slice of the data (in orange). This is the set of all identical field points, one at each delay step in the experiment. When plotted against pump-probe delay, these data points form an effective delay scan. This effective TRKR can be fit for precession frequency. In practice, fitting with a sinusoid (omitting the decaying exponential) is sufficient to extract this frequency. Ref. [55] instead recommends fitting to the entire 2D array.

That may seem like a fair amount of effort for a quantity that is usually available via a single delay scan. However, it presents a subtle but key advantage. In our DNP experiments, the accumulated Overhauser field depends in a nonlinear way on the external field history of the system. In a conventional delay scan, every delay point has a different temporal relationship with the external field. Further, in a TRKR-RSA experiment, every single data point will have a unique history based on the external field value and time duration. In Snapshot TRKR, the same field values are queried in the same order. The only difference from scan to scan is the pump-probe delay. The accumulated DNP at a given field point will be equivalent for every field scan. In this way, from delay to delay, each field point will have the same magnetic field history. The effective delay scans will then consist of

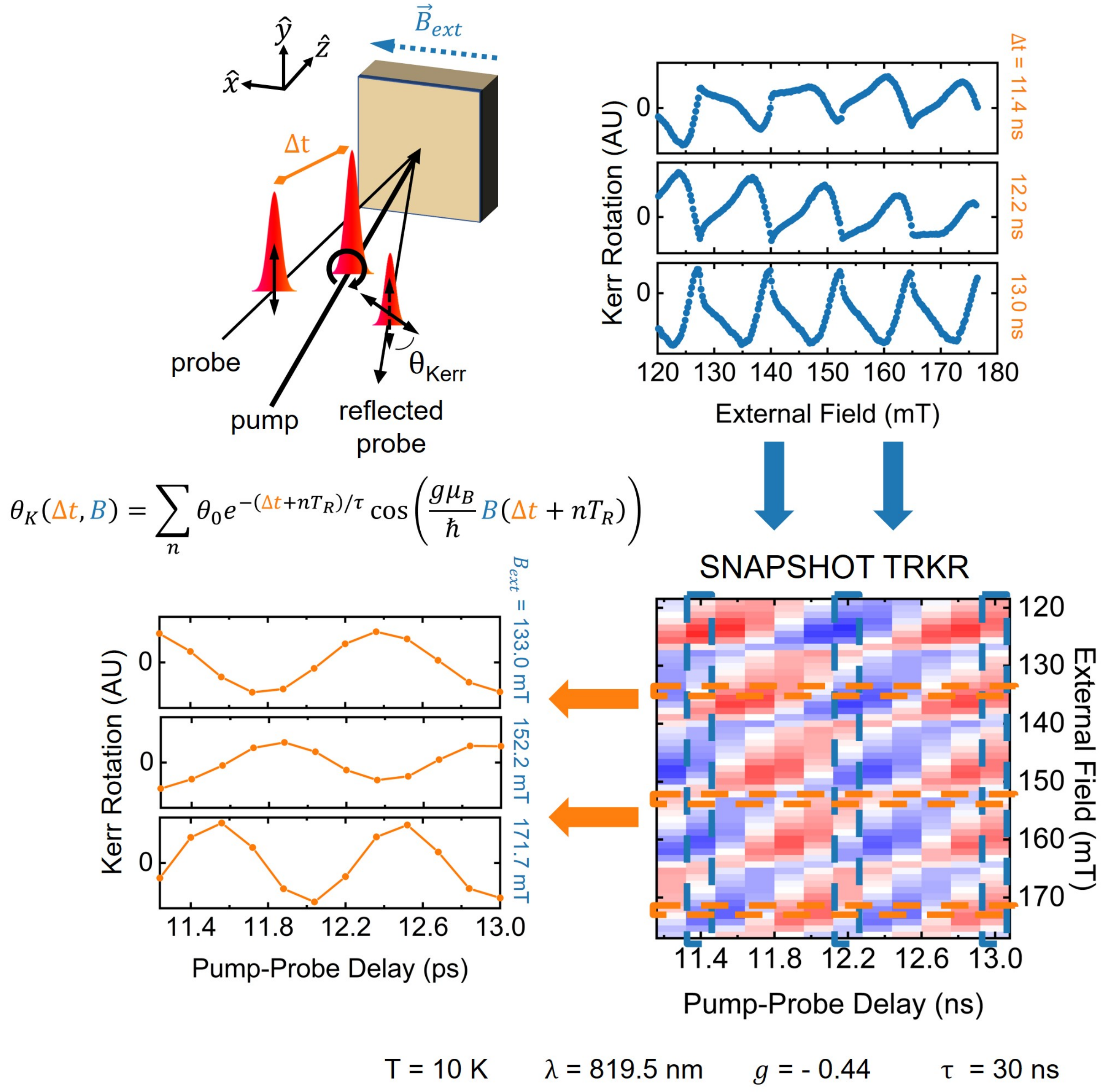

$$\theta_K(\Delta t, B) = \sum_n \theta_0 e^{-(\Delta t + nT_R)/\tau} \cos\left(\frac{g\mu_B}{\hbar} B(\Delta t + nT_R)\right)$$

Figure 4.5: Schematic and example experimental data for Snapshot TRKR. The pump-probe delay is fixed and the external field is incremented from 120 to 180 mT in 0.25 mT increments. This series of field steps is repeated for pump-probe delays from −1920 to −160 ps in 160 ps increments, with the field reset between delays. The field scans are compiled (blue arrows and boxes) into a two-dimensional array of Kerr rotation data. This two-dimensional array will follow the same equation for delay scans and field scans, though this particular example features the presence of an Overhauser field. As described in the text, effective delay scans can be constructed from the data (orange arrows and boxes) from which the Larmor precession frequency can be fit. The extracted Overhauser field is shown in Fig. 6.12c. Measurements were carried out on sample 033XT-A5 (Chapter 6) at temperature 10 K with laser wavelength 819.5 nm. For this material, the electron g factor is −0.44 and the spin lifetime is 30 ns. Color scale omitted for clarity. Figure inspired by Dr. Michael Macmahon [55].

data points with the same field history. The precession frequency extracted from this data will represent the external field experienced by the electron spin system at that particular moment in time, a snapshot of the system in its time evolution (hence the name). We can then extract the Overhauser field as a function of field step, giving us a deeper insight into the buildup of nuclear polarization. Overhauser fields acquired through this method are shown in Chapter 6.

For an additional discussion of the details (and challenges) of extracting the Overhauser field from Snapshot TRKR, see Ref. [55].

4.5 Spatially-Resolved Kerr Rotation (Mirror Scans)

Spatially-Resolved Kerr Rotation is a derivative experiment of TRKR. It is still a pump-probe measurement using ultrafast laser pulses split from the same source as pump and probe. The generation mechanism is still optical orientation, and we still reflect a linearly polarized probe pulse off the material to measure Kerr rotation. However, we are now interested in the spatial distribution of the generated spin polarization. Real laser pulses have a spatial extent, and the intensity of the pulses varies over this area. Under the assumption that the frequency of the pulse does not vary appreciably across the pump pulse, we expect spin polarization to be generated in proportion to the incident power. That is, the spatial spin distribution will reflect the spatial intensity distribution of the laser pulse. By moving the pump and probe beams relative to one another, we can map out this spatial distribution.

Of course, the probe beam also has a spatial extent. If the probe spot on the material under study does not overlap the pump spot, we would not expect to measure any spin polarization, barring some reason for the spin carriers to move (applied electric field, diffusion,

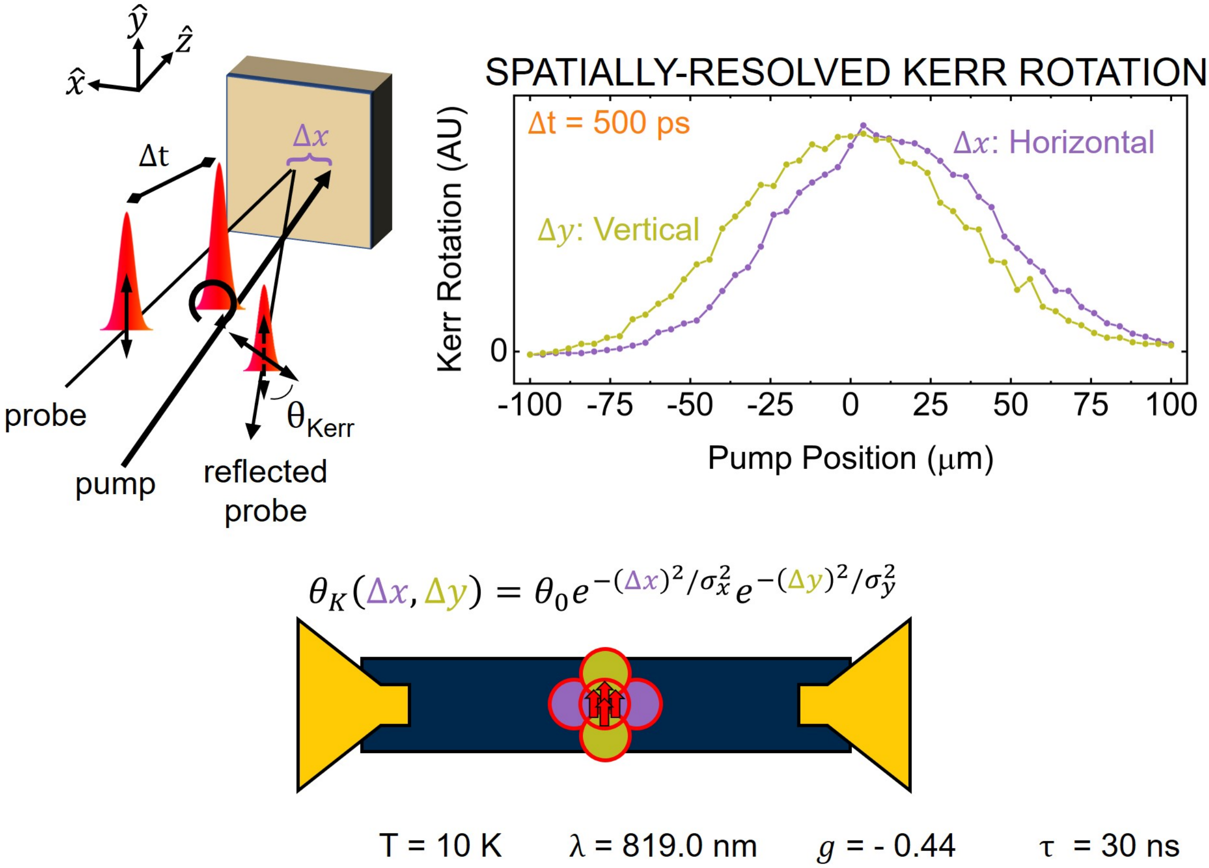

Figure 4.6: Schematic and example experimental data for Spatially-Resolved Kerr Rotation. The pump-probe time delay and probe position are fixed and a motorized mirror is used to move the pump in either the horizontal ($\hat{x}$) or vertical ($\hat{y}$) direction. The example data was carried out at a pump-probe delay of 500 ps. A magnetic field is not applied. The pump position is incremented from -100 to $+100$ μm along either $\hat{x}$ or $\hat{y}$, where 0 μm is the previous position corresponding to maximal pump-probe overlap. While one direction is scanned, the other is fixed to its own zero. The expected pulse shape is Gaussian in both directions, so the fit equation is Gaussian, with the width parameters related to the widths of the beams. In the example data, the center of the horizontal Gaussian is shifted over 10 μm from the expected zero position; this implies that the experimental system has experienced some spatial shift since the previous experiment, which is not unexpected from day to day. The example measurement was carried out on sample 033XT-A5 (Chapter 6) at temperature 10 K with laser wavelength 819.0 nm. Figure inspired by Dr. Marta Luengo-Kovac.

etc.). The overlap between pump and probe determines the Kerr rotation measured. For this reason, it may be prudent to use a pump beam appreciably larger than the probe to ensure pump-probe overlap. As long as the distance traversed by the beams is smaller than the material area, Kerr rotation measured as a function of beam position informs us about the shape of our laser beams. More specifically, the Kerr rotation follows the convolution of both the pump and probe beams. When both beams are Gaussian along both horizontal and vertical directions, the expected Kerr rotation will also be Gaussian, with a width depending on the width of the two composing Gaussian beams.

An experimental schematic along with example data is shown in Fig. 4.6. For purposes of measuring spin polarization, one can move the pump beam, the probe beam, or both. Practically, fixing the position of the probe beam allows us to leave our collection optics fixed, so we opt to move the pump beam. We do so with a motorized mirror, so these experiments are usually called **mirror scans**.

Mirror scans are often used as a tool for achieving maximal pump-probe overlap. Approximate overlap can be achieved through the use of well-placed irises, but a misalignment of tens of microns can significantly reduce the measured Kerr rotation. The motorized mirrors used in our experiments have sufficiently small resolution such that we can move beams on the scale of microns. Though mirror scans do not explicitly appear in the remainder of this dissertation, each session of data acquisition began with one such scan for both spatial directions perpendicular to the optical axis. For very long experimental sessions, mirror scans were run periodically to correct for any mirror drift. Since many of our setups are equipped with motors to move the position of the sample as well, alignment procedures include a combination of translation stage scans and mirror scans for repeatability over the course of an experimental run. Mirror scans can also be used to diagnose beam issues such as clipping.

Pump-probe delay is fixed for each mirror scan. In situations where lifetime cannot be easily extracted from a delay scan, mirror scans can be taken at a succession of delays. The change in amplitude for increasing delays can be used to determine the spin lifetime in the material. For example, this technique was used for determining spin lifetime in the transition metal dichalcogenide WSe_2 [56]. Application of an external magnetic field rotates the spin polarization and complicates the analysis, so mirror scans are performed in the absence of an external field.

4.6 Spin Drag

Spin Drag is a derivative experiment of FRKR under the application of a DC external voltage. It is used only in very specific scenarios where the desired outcome is a better understanding of spin-orbit fields. When an external electric field is applied to certain semiconductors, the electrons experience spin-orbit fields, effective magnetic fields that are tied to the geometry of the system. In zincblende structures like GaAs and its alloys, we can choose the orientation of our applied electric field in such a way that the spin-orbit fields are oriented perpendicular to the field.

We apply an external magnetic field (in the Voigt geometry) and record the FRKR. Returning to the Bloch equation, we treat the spin-orbit fields as additional components of the external field and solve for the spin polarization as a result of this "off-axis" field [28]. The spin-orbit field perpendicular to the external field serves to reduce the amplitude of the peak centered at zero external field. The spin-orbit field parallel to the external field in turn shifts the expected position of that zero-field peak. Scanning the external field, we can fit the FRKR to extract both spin-orbit fields.

Now, we optically pump electron spins in one spot on our sample, but due to the applied electrical potential, they may have moved outside the radius of our probe beam by the time it arrives. Knowing the mobility of our sample, we can estimate how far the spins will move during the pump-probe delay, which we still prefer to keep at 13 ns.

It is easier in practice to move the pump beam and allow the probe collection optics to remain fixed, so we fix the location of our probe and scan our pump along the direction of the applied electric field. For a given voltage, we estimate how far the electron spins will move

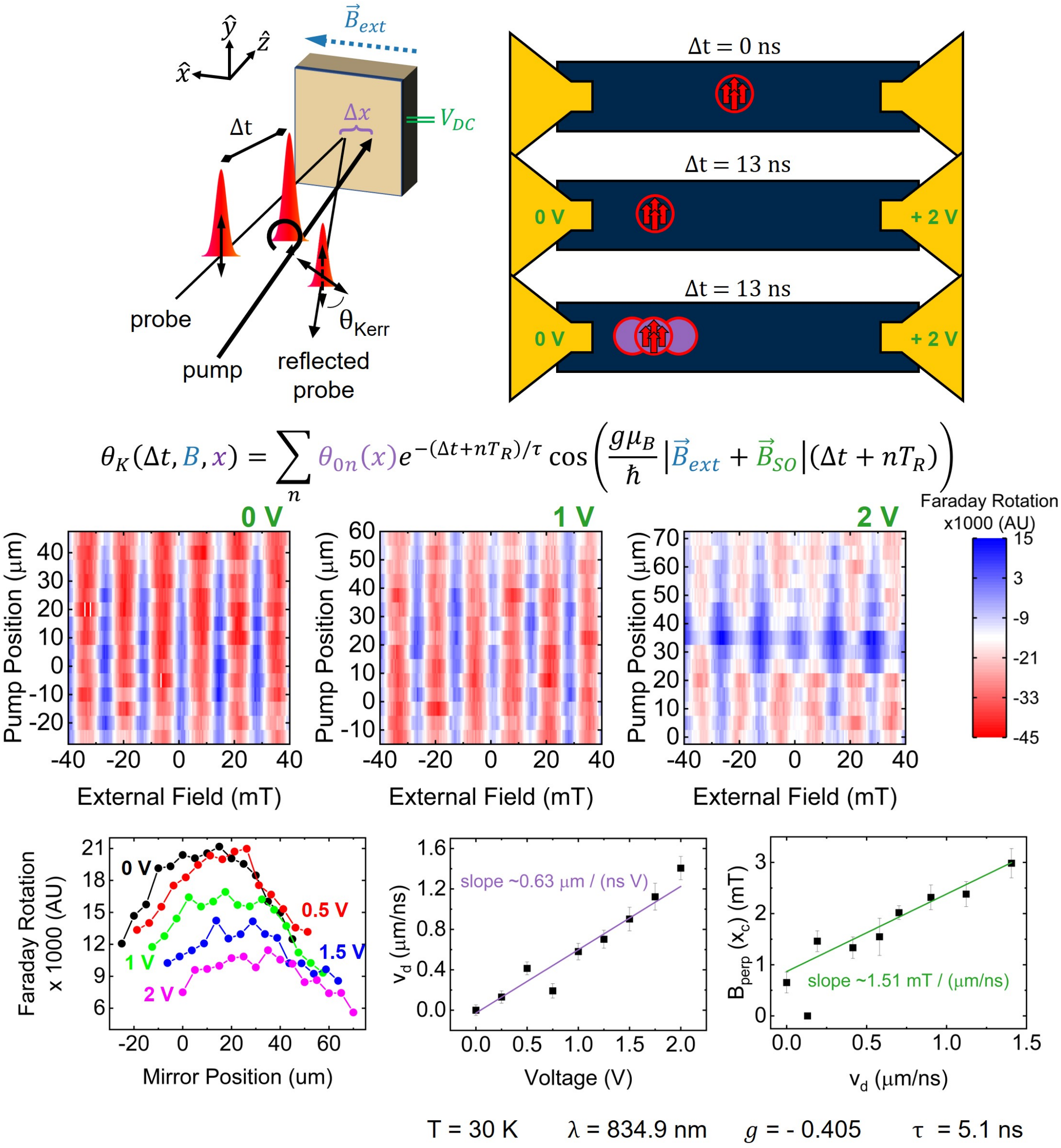

Figure 4.7: Schematic and example experimental data for Spin Drag. Voltage is applied along the $[1\bar{1}0]$ crystal direction, which is oriented parallel to an external magnetic field. The pump-probe delay is set to 13 ns. Measurements were carried out in transmission geometry on sample RMBE1130-K (Chapter 5) at temperature 30 K with laser wavelength 834.9 nm. (Top row) Experimental schematic, fit equation, and cartoon of spin packet drift. The pump is shown fixed at the center of the channel while the probe is moved, in contrast to the implementation described in the text. (Middle row) Field scans from -40 to $+40$ mT in steps of 0.5 mT for pump positions over a range of 70 μm in steps of 5 μm, taken at three applied voltages. The center of the spin packets can be identified. (Bottom row) Faraday rotation as a function of pump position for a range of applied voltages from 0 V to 2 V. The voltages were incremented in steps of 0.25 V, but only steps of 0.5 V are shown. The spin packet moves with voltage. From this data, drift velocity can be calculated as a function of voltage, and finally the perpendicular spin-orbit field B_{perp} can be determined. Figure inspired by Dr. Marta Luengo-Kovac.

in 13 ns; for our samples, this is usually on the order of tens of microns. Using our motorized pump steering mirror, we move the pump spot that distance away along the direction of the applied field and measure FRKR. To establish the shape and center of the spin packet, we repeat the measurement for a range of pump spot positions about the expected packet center. Overall, we acquire a set of FRKR measurements taken at a range of pump beam positions, each taken at a different applied voltage. The experimental schematic is shown in the top row of Fig. 4.7.

At each voltage, we generate a plot of Kerr rotation as a function of external field and mirror position. Fitting the amplitude of the FRKR allows us to map out the spatial shape of the spin packet. The number of pulse terms needed to accurately fit the data depends on the spin lifetime. We convert applied voltage into drift velocity, the rate at which the center of the packet moves. The end goal is to extract the spin-orbit fields as a function of drift velocity, allowing us to compare them across materials with different resistivities. We expect this relationship in our materials to be linear, with the proportionality constant, denoted κ, serving as a single parameter describing the strength of the spin-orbit coupling in that material. For more details on the spin drag experiment, see Ref. [28].

4.7 Current-Induced Spin Polarization

Current-Induced Spin Polarization is a method of generating spin polarization in certain materials. The eponymous experimental technique, also designated as **CISP**, combines the generation method with optical detection of Faraday or Kerr rotation. Thus, CISP is still a pump-probe measurement. An applied electric field acts as the pump while the probe is the familiar ultrafast laser pulse. The applied field generates an in-plane spin polarization. We choose to apply the field along particular crystal axes (such as $[1\bar{1}0]$) such that

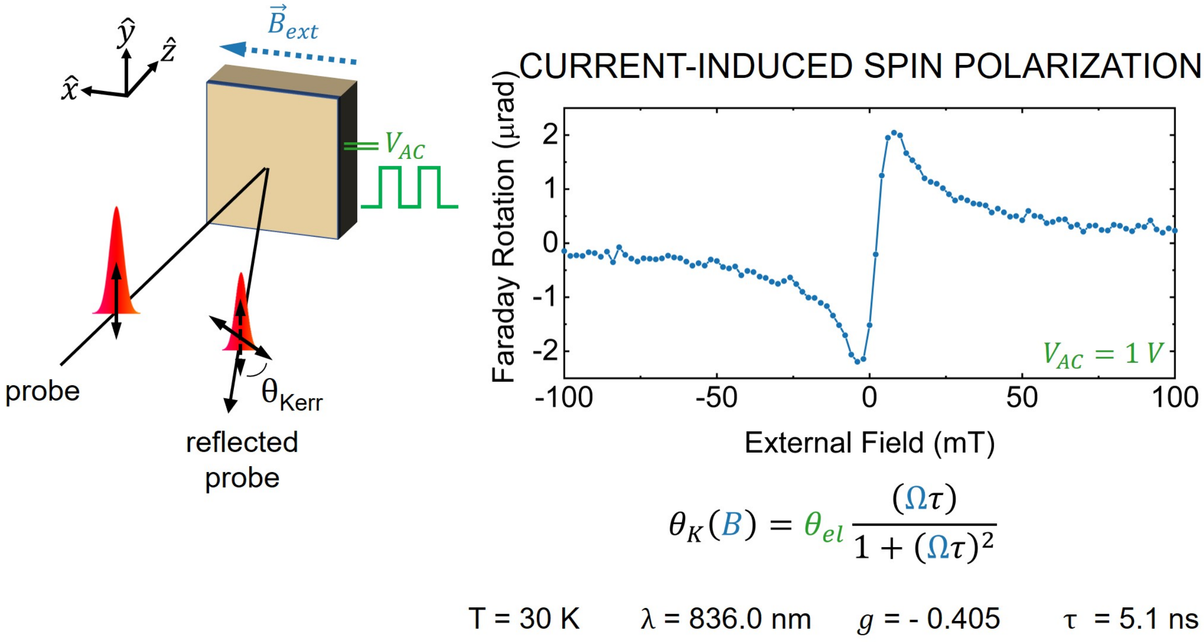

Figure 4.8: Schematic and example experimental data for current-induced spin polarization. A voltage waveform following a standard bipolar square wave with frequency 1.167 kHz and peak voltage 1 V is applied. The external magnetic field is incremented from −100 to +100 mT in steps of 2 mT. There is no optical pump. The measurement was carried out in transmission geometry on sample RMBE1130-K (Chapter 5) at temperature 30 K with laser wavelength 836.0 nm.

the generated spin polarization is along the laboratory axis $\hat{y}$. We must apply a transverse external magnetic field to rotate the spin polarization pseudovector to have a $\hat{z}$ component measurable by Faraday or Kerr rotation.

CISP experiments can be configured with voltage pulses for generating spin polarization. Electrical triggering can be implemented to establish a defined temporal relationship between spin generation and detection. In this case, a constant external magnetic field can be applied and the delay between voltage and optical pulses can be incremented to acquire data reminiscent of TRKR [57]. The sinusoid will be a sine rather than a cosine:

$$S_z\left(\Delta t, B\right) = \gamma e^{-\Delta t/\tau} \sin\left(\frac{g\mu_B}{\hbar} B \Delta t\right), \tag{4.2}$$

where γ is the electrical spin generation rate, sometimes denoted γ_{el}.

Instead, we opt for a steady-state experiment. We apply a voltage to generate CISP and probe without a defined time relationship. In analogy to the Hanle measurement described above, we scan the external field. Instead of an even Lorentzian, we acquire an odd Lorentzian:

$$\begin{aligned} S_z &= \int_0^\infty \gamma e^{-t/\tau} \sin\left(\frac{g\mu_B}{\hbar} Bt\right) dt \\ &= \gamma\tau \frac{\Omega\tau}{1 + (\Omega\tau)^2}. \end{aligned} \tag{4.3}$$

We alternatively define γ as Faraday rotation per unit time. In that case, we can rewrite the amplitude of the measured Lorentzian $\gamma\tau$ as θ_{el}.

The functional form of the data is shown alongside the experimental schematic in Fig. 4.8. Notice that at zero applied field, the measured rotation is zero. The odd Lorentzian can be fit to extract the coupled quantity $g\tau$ (from $\Omega\tau$), where τ is the spin lifetime. The material g factor must be known from other measurements. The CISP curve has maxima at $B_{\text{ext}} = \pm\hbar/g\mu_B\tau$.

In optical pump-probe measurements, we modulate the pump for lock-in detection. We can do the same for an electrical pump. Rather than apply a DC voltage, we apply an AC voltage waveform. Usually, this is the standard bipolar square wave s_0 as defined in Chapter 3. The applied voltage will cause electrons to drift in the material. However, we expect to polarize electron spins throughout the whole channel where we are applying an external electric field. Thus, we do not mind drift, as the spin-polarized electrons will be replaced by similarly polarized electrons as they drift. The AC voltage will mitigate this drift somewhat by reversing the direction of drift. Again, we are measuring limiting behavior.

To prepare for CISP experiments, it is useful to first perform delay and field scans. Determination of the g factor is necessary for eventually extracting the spin lifetime. Spin drag is often performed to experimentally determine the drift velocity for the material, for comparison of CISP spin generation rates γ between samples. Because we focus on a single

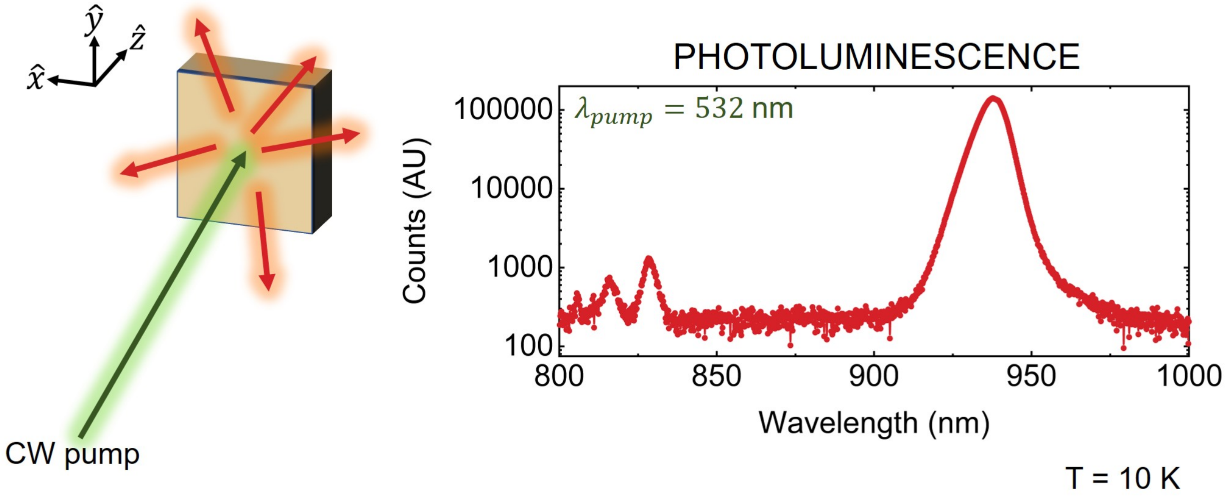

Figure 4.9: Schematic and example experimental data for photoluminescense. The example photoluminescence (PL) is emitted from sample 030512C, a single $\mathrm{In}_{0.2}\mathrm{Ga}_{0.8}\mathrm{As}$/GaAs quantum well at 10 K. Light from a 532 nm continuous-wave laser diode is focused onto the sample through a 100× microscope objective. The incident power is 400 μW. Reflected and emitted light are collected through the same objective lens and filtered through a longpass filter (FEL0550) to remove the diode light. The remaining light is sent into a spectrometer. Here, the 150 G grating is used to disperse the light onto the cooled CCD, which collects light for 1 second.

sample in Chapter 5, we leave γ in terms of applied voltage. Not every sample will show appreciable CISP. Uniaxial strain is needed, such as is present in InGaAs alloys but absent from GaAs epilayers [20]. The precise dependence of CISP on material parameters is an area of ongoing study [19].

4.8 Photoluminescence

Photoluminescence (PL) experiments differ from the other measurements presented in this chapter in that they are not pump-probe experiments. We still provide an optical pump, but the measured quantity is light emitted from radiative processes occurring in our material. The pump, at an energy much higher than that corresponding to the physical processes of interest, excites the material. As the material relaxes, it emits light corresponding to radiative processes that occur at lower energies than the pump, and this light is sent into a spectrometer, allowing us to see the relative intensities of the wavelength components of the light. We use a charge-coupled device (CCD) to record these intensities for most wavelengths.

We primarily use PL to identify the location of features in our material such as the band edge. Relative feature intensities can also be acquired. In order to observe these features, the pump energy must be significantly higher than the expected emitted light to excite the necessary physical processes. It is often instructive to view PL counts on a logarithmic scale, as shown in Fig. 4.9. Other quantitative investigations must take into account the spectral response of the measurement device (like the CCD) as well as potential noise sources. The reference data shown here is from a quantum well sample that our laboratory group has used for many years for PL alignment.

We usually collect PL at experiment temperatures. Other than cooling down, minimal preparation is required. Our PL setup, maintained separately from the pump-probe setup featured in Chapter 3, collects the reflected pump light as a proxy for emitted light, using a longpass filter to remove the pump light near the spectrometer. This is a practical reason for using a pump separated in energy from the expected features by an appreciable amount. Variations on this setup may be sensitive to the polarization of either the pump laser or the luminescence. A pulsed pump may be substituted for a CW pump, and when combined with a streak camera or similar device, time-resolved measurements can be made. This is a useful method for measuring radiative lifetimes in systems of interest. Combining time- and polarization-resolved measurements are an alternative window into spin dynamics. For example, see Ref. [58]. For a deeper discussion of PL, consult a textbook reference such as [59].

CHAPTER 5

Modified Periodic Waveforms for Study of Current-Induced Spin Polarization

5.1 Motivation

As alluded to in previous chapters of this dissertation, there is interest in the field of spintronics in understanding the electrical generation, manipulation, and detection of spin-polarized carriers, towards the goal of an all-electrical spin-based device [6, 7]. One way forward is to make use of current-induced spin polarization (CISP), introduced in Chapter 2, a phenomenon in which an electrical current generates a bulk, homogeneous, steady-state electron spin polarization [60]. CISP has been observed in various materials [20, 61, 62, 63, 64, 65, 66, 67, 68], with both electrical generation and manipulation achieved in an n-InGaAs heterostructure [57]. Recent theoretical work has produced a model that qualitatively agrees with the measured dependence of CISP on sample parameters [19, 20].

A majority of previous work has observed that CISP increases linearly with applied electric field [60, 63, 64, 66, 67]. However, previous investigations have also reported being limited to using smaller electric fields to avoid signal degradation due to heating [64]. Hernandez *et al.* also attributed a decrease in observed Kerr rotation at higher electric field to heating [68]. Our laboratory has previously found the CISP spin generation rate to deviate slightly from linear behavior as electric field was increased [20]. Naturally, we question whether this deviation is the result of heating or a new regime in which the physics changes. To settle the matter, we adjust our CISP measurement method, replacing the standard bipolar square wave voltage modulation with a modified square wave that reduces the amount of time a nonzero voltage is applied. This change reduces current heating, and by doing so we can confirm the expected linear dependence on electric field (here, voltage).

This chapter was originally published in AIP Advances [9]: J. R. Iafrate, S. Huang, D. Del Gaudio, R. S. Goldman, and V. Sih, Effect of modified periodic waveforms on current-induced spin polarization measurements, AIP Advances **8**, 065113 (2018). It is reproduced here with the permission of AIP Publishing. The following account is minimally modified, and with the exception of Figs. 5.1 and 5.4, each figure is adapted from the original publication.

5.2 Measuring CISP in InGaAs

The sample under study is a 500 nm $\mathrm{In_{0.026}Ga_{0.974}As}$ epilayer grown via molecular beam epitaxy on a (001) GaAs substrate, doped with silicon to achieve a doping density n = 1.55 $\times 10^{17}$ cm^{-3} (same wafer as Sample B studied by Luengo-Kovac *et al.*) [20]. The geometry is shown in Fig. 5.1. Designated sample RMBE1130-K, the sample is one piece of the larger wafer RMBE1130 grown by Dr. Simon Huang and Dr. Davide Del Gaudio during their doctoral studies in the lab of Dr. Rachel Goldman. Optical lithography and wet etching were used to pattern a cross-shaped channel onto the sample with arms along the [110] and [$1\bar{1}0$] crystal axes, following Norman *et al.* [67]. The channel arms are 500 μm in length and 270 μm in width. We apply a voltage to ohmic Au/Ge/Ni contacts to generate a current along the [$1\bar{1}0$] direction. The resistance of the 500-μm channel is on the order of hundreds of ohms. At 30 K, the temperature at which all measurements were performed, the channel resistance is approximately 500 Ω.

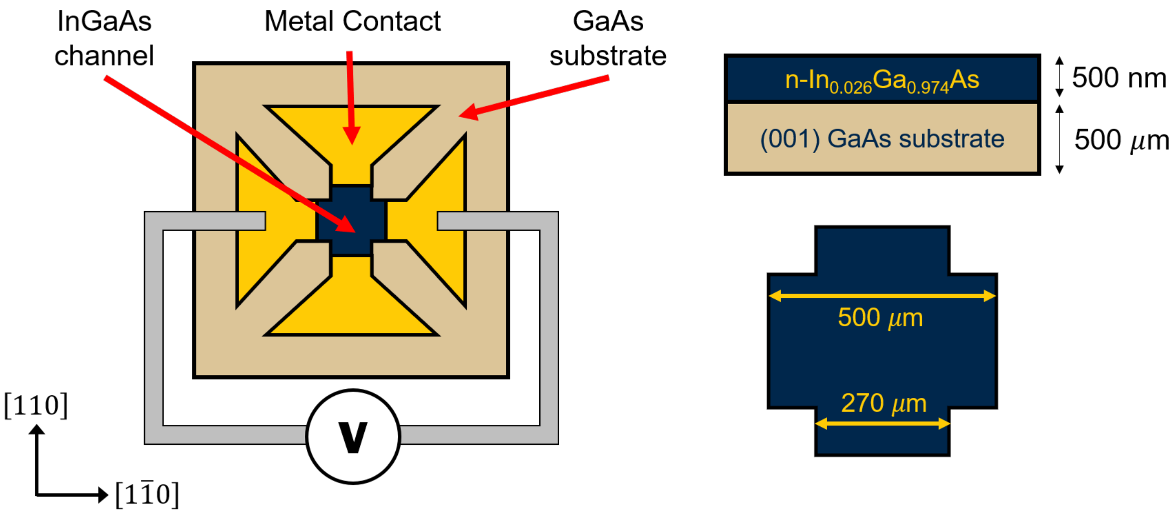

Figure 5.1: Schematic of the sample under study, RMBE1130-K.

The electrical current generates a homogeneous electron spin polarization in the plane of the sample. For current along $[1\bar{1}0]$, the spin polarization is perpendicular to the current direction [60, 67]. These directions correspond to the $\hat{x}$ and $\hat{y}$ directions used elsewhere in this dissertation. We apply an external magnetic field along the current direction ($\hat{x}$), causing the spin polarization to precess. We tune the Ti:Sapph laser to 836 nm and optically detect the out-of-plane spin polarization in transmission geometry. This Faraday rotation θ_F is related to the applied magnetic field by

$$\theta_F = \theta_{el}\frac{\Omega\tau}{1+(\Omega\tau)^2}, \tag{5.1}$$

where θ_{el} is the electrically-induced Faraday rotation, τ is the transverse spin lifetime, and Ω is the Larmor precession frequency corresponding to the applied field B_{ext} [60]. For this sample, the g factor was determined via time-resolved Faraday rotation to be -0.405; this measurement is shown in Fig. 4.1. Here, we are interested in the quantity $\gamma \equiv \theta_{el}/\tau$, which we will refer to as the *spin generation rate*, with units of (Faraday) rotation per unit time. Our definition for γ differs slightly from elsewhere in the literature. It is proportional to the density of spins oriented per unit time, but in contrast to Kato *et al.*, we omit

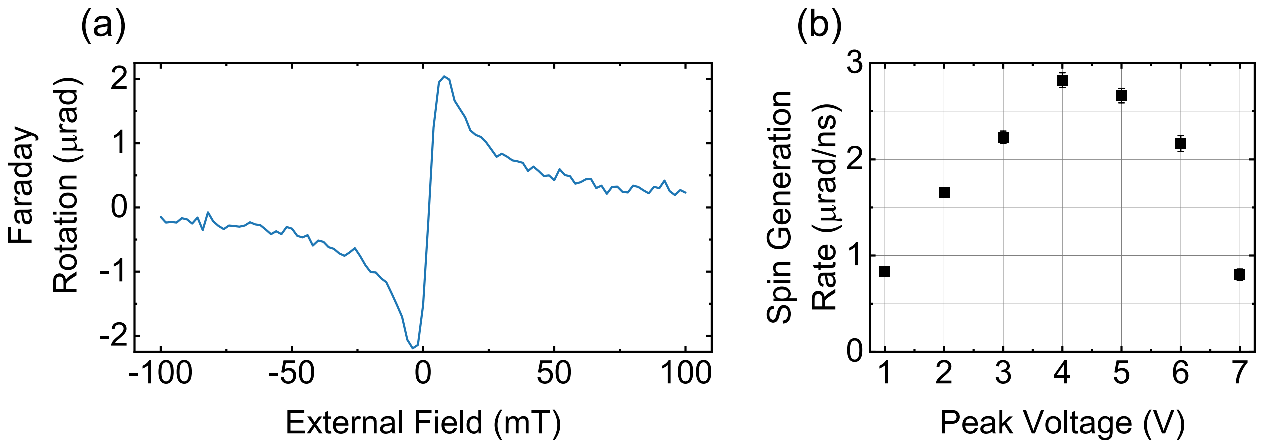

Figure 5.2: Current-induced spin polarization measured under application of bipolar square wave voltages. (a) Current-induced spin polarization measured under application of a bipolar 1 V peak square wave. (b) Extracted spin generation rate γ for CISP measured under application of bipolar square waves with peak voltage ranging from 1 V to 7 V. A linear relationship between γ and peak voltage is not observed.

the corresponding proportionality factor of spin density per (Faraday) rotation angle [60]. Previous studies have determined this factor to be 1.42 μm^{-3} μrad^{-1} for our material [20].

To make use of lock-in detection, as described in Chapter 3, the applied voltage is modulated as a bipolar square wave with frequency 1.167 kHz. By scanning the applied magnetic field, we obtain data such as that in Fig. 5.2a. We measure CISP at increasing applied voltages and fit to Eq. 5.1, extracting θ_{el} and τ and thus γ, our quantity of interest. We plot γ as a function of voltage in Fig. 5.2b. See that γ reaches a maximum at $V_{\text{pk}} = 4$ V before decreasing at higher applied voltages. This is a clear deviation from the expected nearly-linear dependence on voltage. We need a method for ascertaining whether current heating is responsible.

5.3 Modified Periodic Waveforms

Rather than utilize a standard bipolar square wave, we modify the applied voltage waveform by reducing the amount of time the voltage is nonzero. The standard bipolar square

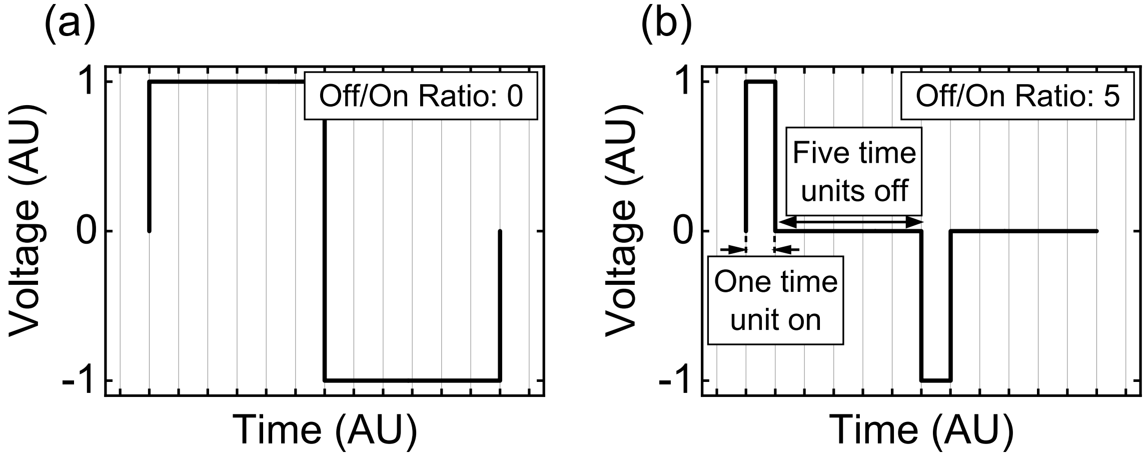

Figure 5.3: Example bipolar and modified square wave voltage waveforms for peak voltage 1 V. (a) Example bipolar square wave voltage waveform for peak voltage 1 V. (b) Example modified waveform used to generate CISP. The peak voltage and waveform frequency are fixed while the amount of time the voltage is on is reduced. A square wave with nonzero voltage for one time unit and zero voltage for n time units has off/on ratio n. The waveform presented here has off/on ratio 5.

wave, with frequency f and unit height, is defined over a single period as

$$s_0\left(ft\right) = \begin{cases} 1, & ft \in \left[0, \dfrac{1}{2}\right) \\ -1, & ft \in \left(\dfrac{1}{2}, 1\right] \end{cases}, \tag{5.2}$$

where we elect not to define the value at $ft = \frac{1}{2}$. The *off/on ratio* for a square wave is the ratio of time spent at zero voltage to the amount of time spent at peak voltage. With this idea in mind, we can generalize Eq. 5.2 as

$$s_n\left(ft\right) = \begin{cases} 1, & ft \in \left[0, \dfrac{1}{2\left(n+1\right)}\right) \\ -1, & ft \in \left(\dfrac{1}{2}, \dfrac{n+2}{2\left(n+1\right)}\right) \\ 0, & ft \in \left(\dfrac{1}{2\left(n+1\right)}, \dfrac{1}{2}\right), \left(\dfrac{n+2}{2\left(n+1\right)}, 1\right] \end{cases}, \tag{5.3}$$

where n is the off/on ratio. We compare the standard bipolar square wave to an example waveform with off/on ratio 5 in Fig. 5.3.

As the off/on ratio is increased, the overlap of the square wave with a sine at the same frequency is reduced. That is, the Fourier sine coefficient decreases as off/on ratio increases.

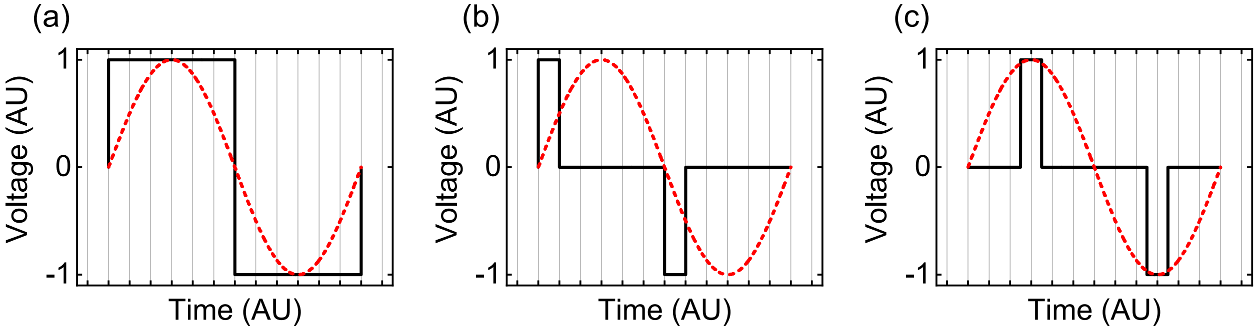

Figure 5.4: Visual comparisons of input voltage waveforms with 1 V peak voltage (solid black line) and a reference sine wave of the same frequency (dashed red line). (a) The peaks of the standard bipolar square wave naturally align with the peaks of the reference sine. (b) As off/on ratio increases, the peaks of the modified waveform no longer align with the reference sine. Fourier sine coefficients measured for this waveform will underestimate the actual measured coefficients. The relative phase of the waveforms must be shifted for optimal lock-in detection. (c) The waveform can be shifted in time (and the formula rewritten) to ensure maximal phasing. The first Fourier sine coefficients necessary to correct the measured CISP data are calculated using this version of the waveform.

Therefore, for a constant CISP amplitude, the lock-in amplifier will measure a smaller signal with increasing off/on ratio. To compensate for this drop-off in measured Faraday rotation due to measurement technique, we apply a correction factor to each of our data sets, normalizing by the Fourier coefficients. This processing step allows us to recover the actual Faraday rotation.

We must be careful in calculating Fourier coefficients. If we were to simply calculate the Fourier coefficient of Eq. 5.3, we would find it to become vanishingly small, even for modest n. This is the overlap graphically described in Fig. 5.4b. Instead, we must follow the lead of the lock-in amplifier and "auto-phase" the waveform. The amplifier aligns the peak of the reference waveform with the peak of the input signal, achieving maximum overlap. This is graphically described in Fig. 5.4c. We too must align the peak of the sine with the center of the square wave maximum. This occurs at a different phase for each n. While the lock-in amplifier shifts the sine wave to match the reference signal, it is notationally simpler to fix the sine wave and rewrite the square wave. Shifting Eq. 5.3 to align the center of the maximum with the sine wave maximum at $ft = \frac{1}{4}$ yields

$$s_n(ft) = \begin{cases} 1, & ft \in \left(\frac{1}{4} - \frac{1}{4(n+1)}, \frac{1}{4} + \frac{1}{4(n+1)}\right) \\ -1, & ft \in \left(\frac{3}{4} - \frac{1}{4(n+1)}, \frac{3}{4} + \frac{1}{4(n+1)}\right) \\ 0, & \text{else.} \end{cases} \tag{5.4}$$

We can now calculate the first Fourier sine coefficient b_1 as a function of off/on ratio:

$$\begin{aligned} b_1 &= \frac{1}{1/2}\int_0^1 s_n(ft)\sin(2\pi ft)\,d(ft) \\ &= 2\int_0^1 s_n(ft)\sin(2\pi ft)\,d(ft) \\ &= 2\int_{\frac{1}{4}-\frac{1}{4(n+1)}}^{\frac{1}{4}+\frac{1}{4(n+1)}} \sin(2\pi ft)\,d(ft) - 2\int_{\frac{3}{4}-\frac{1}{4(n+1)}}^{\frac{3}{4}+\frac{1}{4(n+1)}} \sin(2\pi ft)\,d(ft) \\ &= 2\int_{-\frac{1}{4(n+1)}}^{\frac{1}{4(n+1)}} \sin\left(2\pi u + \frac{\pi}{2}\right)du - 2\int_{-\frac{1}{4(n+1)}}^{\frac{1}{4(n+1)}} \sin\left(2\pi u + \frac{3\pi}{2}\right)du \\ &= 2\int_{-\frac{1}{4(n+1)}}^{\frac{1}{4(n+1)}} \cos(2\pi u)\,du + 2\int_{-\frac{1}{4(n+1)}}^{\frac{1}{4(n+1)}} \cos(2\pi u)\,du \\ &= 4\int_{-\frac{1}{4(n+1)}}^{\frac{1}{4(n+1)}} \cos(2\pi u)\,du \\ &= 4\frac{1}{2\pi}\sin(2\pi u)\Big|_{-\frac{1}{4(n+1)}}^{\frac{1}{4(n+1)}} \\ &= \frac{2}{\pi}\left(\sin\left(\frac{\pi}{2}\frac{1}{n+1}\right) - \sin\left(-\frac{\pi}{2}\frac{1}{n+1}\right)\right) \\ &= \frac{4}{\pi}\sin\left(\frac{\pi}{2}\frac{1}{n+1}\right). \end{aligned} \tag{5.5}$$

This is just the Fourier coefficient for the standard bipolar square wave $\frac{4}{\pi}$ modified by a sinusoidal function of $\frac{1}{n+1}$.

The point of introducing voltage off-time is to preserve the peak voltage V_{pk} while reducing

Table 5.1: Computed Fourier coefficient correction factors for a sampling of off/on ratios used in this chapter.

Off/On Ratio	0	1	5	10	20
Fourier Coefficient	1.27324	0.900316	0.329539	0.181201	0.0951493

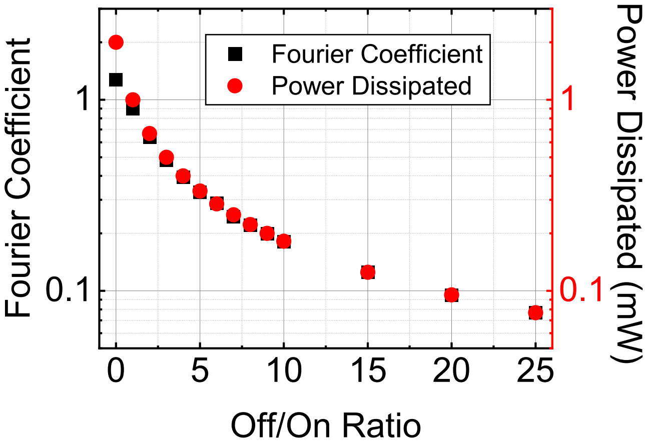

Figure 5.5: Calculated Fourier sine coefficients and power dissipated for a 1 V peak modified square wave on a 500 Ω channel as a function of off/on ratio. As off/on ratio increases, the Fourier sine coefficient corresponding to the fundamental frequency decreases, as does the power dissipated, following the Ohmic relation $P = V_{\mathrm{RMS}}^2/R$.

the root-mean-square voltage V_{RMS}. This is vital, as the power dissipated through resistive heating by a time-varying voltage is given by [69]

$$P_{\mathrm{diss}} = \frac{V_{\mathrm{RMS}}^2}{R}. \tag{5.6}$$

Reducing V_{RMS} reduces the dissipated heat. Our time-varying voltage is $V_{\mathrm{pk}}\ s_n(ft)$, so the RMS value, which is averaged over one period, is given by

$$\begin{aligned} s_{\mathrm{RMS}} &= \sqrt{\int_0^1 \left[s_n\left(ft\right)\right]^2 d(ft)} \\ &= \sqrt{\int_{\frac{1}{4}-\frac{1}{4(n+1)}}^{\frac{1}{4}+\frac{1}{4(n+1)}} \left[1\right]^2 d(ft) + \int_{\frac{3}{4}-\frac{1}{4(n+1)}}^{\frac{3}{4}+\frac{1}{4(n+1)}} \left[-1\right]^2 d(ft)} \\ &= \sqrt{\begin{aligned}&\left(\left(\tfrac{1}{4}+\tfrac{1}{4(n+1)}\right)-\left(\tfrac{1}{4}-\tfrac{1}{4(n+1)}\right)\right) \\ &\quad + \left(\left(\tfrac{3}{4}+\tfrac{1}{4(n+1)}\right)-\left(\tfrac{3}{4}-\tfrac{1}{4(n+1)}\right)\right)\end{aligned}} \\ &= \sqrt{\frac{1}{2\left(n+1\right)}+\frac{1}{2\left(n+1\right)}} \\ &= \frac{1}{\sqrt{n+1}}, \end{aligned} \tag{5.7}$$

and then

$$V_{\mathrm{RMS}} = \frac{V_{\mathrm{pk}}}{\sqrt{n+1}}. \tag{5.8}$$

The function $\frac{1}{n+1}$ appears again, this time in the power dissipated:

$$P_{\mathrm{diss}} = \frac{V_{\mathrm{pk}}^2}{R}\frac{1}{n+1}. \tag{5.9}$$

Following our formula for V_{RMS}, larger off/on ratios will reduce the amount of sample heating, as shown for a square wave with $V_{\mathrm{pk}} = 1$ V in Fig. 5.5. While we only considered integer n, Eq. 5.5 holds for arbitrary n. Calculated Fourier coefficients and power dissipated for a square wave with V_{pk} are shown for a range of off/on ratios in Fig. 5.5. A selection of coefficients are represented numerically in Table 5.1.

We demonstrate the effect of this processing in Fig. 5.6. Each curve corresponds to 1 V peak voltage. Note, however, that signal noise is also adjusted, preserving the signal-to-noise ratio. Measurements taken using square waves with larger off/on ratios should then yield the same data with decreased signal-to-noise ratio.

5.4 Relationship Between γ and Off/On Ratio

Measurements taken using square waves with larger off/on ratios *should* yield the same data with decreased signal-to-noise ratio, but this is not observed for larger voltages. We repeat our earlier experiments to extract γ using square waves with nonzero off/on ratios. Only V_{RMS} changes while all other experimental parameters remain the same. Data is shown for five ratios in Fig. 5.7. As off/on ratio is increased, the functional dependence of CISP on applied voltage becomes linear, as initially expected. The extracted values for γ are far more sensitive to off/on ratio at larger voltages. This latter point is shown in Fig. 5.8, in which we plot γ values as a function of off/on ratio for three selected applied voltages. At 1 V applied, γ does not appreciably change with off/on ratio.

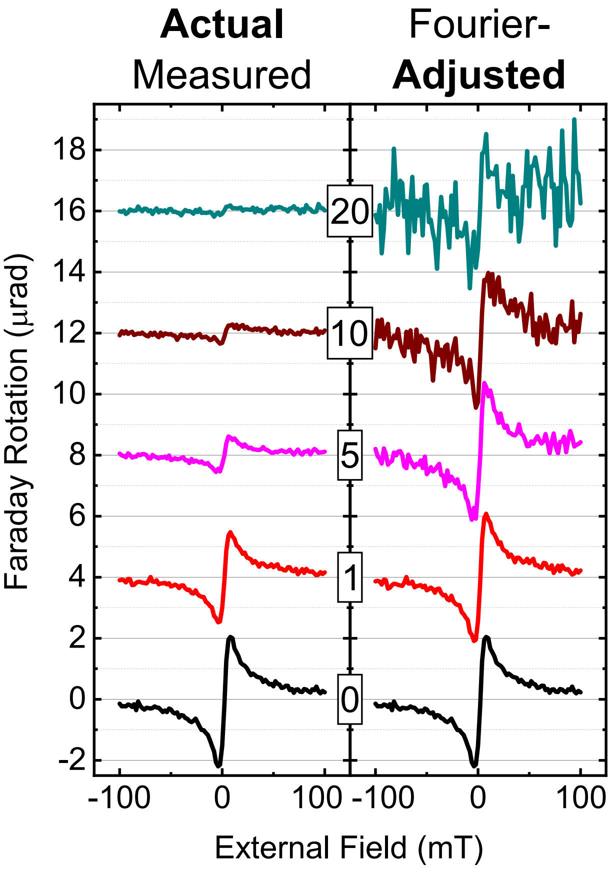

Figure 5.6: Current-induced spin polarization measured under application of a 1 V peak square wave for off/on ratios 0, 1, 5, 10, and 20. A vertical offset between curves has been added for clarity. (Left) This data has not been corrected for decreasing Fourier coefficient with increasing off/on ratio. As the ratio increases, the magnitude of the signal decreases. (Right) When rescaled by the Fourier coefficient, the signal magnitude of the data is consistent while the signal-to-noise ratio decreases with off/on ratio.

Ideally then we would choose an arbitrarily large off/on ratio to eliminate heating altogether. However, increasing the off/on ratio decreases the signal-to-noise ratio, compromising the ability to obtain accurate values of γ at off/on ratios of 25 and above. Furthermore, the voltage is supplied by an Agilent 33210A function generator that utilizes a finite number of points (8000) to represent the waveform. For sufficiently large ratios, it will no longer be possible to form a square wave with sharp rising and falling edges. Referring back to Fig. 5.8, γ appears to approach a constant value as off/on ratio is increased. The ideal ratio yields a γ close to the asymptotic value while preserving as large a signal-to-noise ratio as possible. For this sample, an off/on ratio between 5 and 10 (corresponding to linear behavior

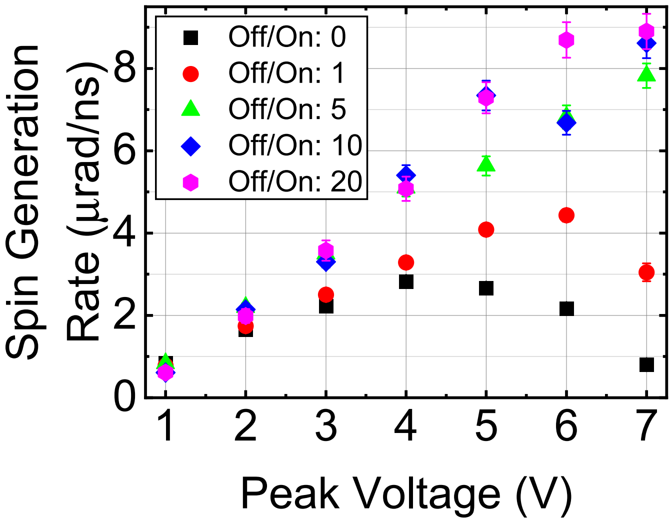

Figure 5.7: Spin generation rate γ as a function of applied voltage for off/on ratios 0, 1, 5, 10, and 20. As off/on ratio increases, γ approaches a linear dependence on voltage. Original measurement data is processed as described in the text, with error bars derived from the fit.

in Fig. 5.7) is ideal.

Thus far we have assumed that CISP depends on V_{pk}, but in previous measurements using standard bipolar square waves, V_{pk} and V_{RMS} are identical. We consider the possibility that γ actually depends on V_{RMS} rather than V_{pk} by recasting the measurements of Fig. 5.8 as a function of V_{RMS} in Fig. 5.9. A given V_{RMS} can be achieved with multiple combinations of V_{pk} and off/on ratios, so we are interested in whether two similar V_{RMS} based on different V_{pk} have the same γ. Instead, we observe three curves corresponding to the three peak voltages. For a given V_{RMS}, the measured γ are distinguished by V_{pk}, implying that the latter quantity sets the asymptotic γ while V_{RMS} determines the deviation from that ideal value. Because dissipated power is proportional to V_{RMS}^2, we attribute this dependence on V_{RMS} to heating effects.

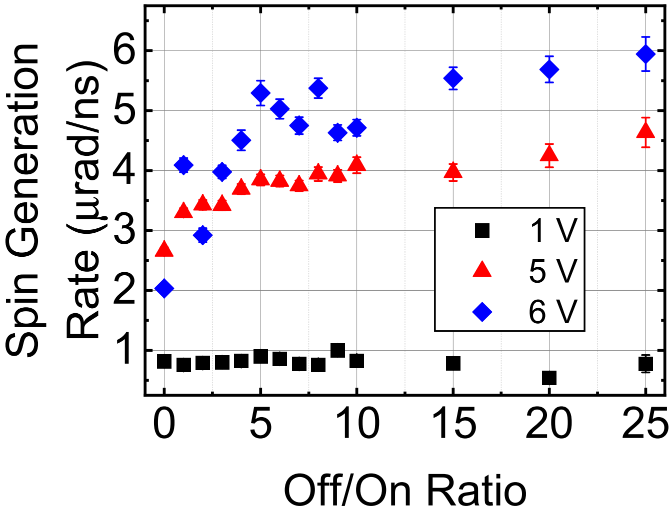

Figure 5.8: Spin generation rate γ measured as a function of off/on ratio for $V_{\mathbf{pk}} = 1$ V, 5 V, and 6 V. Original measurement data is processed as described in the text, with error bars derived from the fit. The data for each peak voltage approaches an asymptotic value with increasing off/on ratio.

5.5 Understanding the Influence of Heat Dissipation

In order to understand these results, we appeal back to dissipated power in Fig. 5.5. That plot displays the power for a waveform with $V_{\text{pk}} = 1$. For other applied peak voltages, one must scale the dissipated power by V_{pk}^2. For example, applying 6 V via a standard bipolar square wave should dissipate 72 mW, an order of magnitude difference from 2 mW in the 1 V case. As expected, application of a 6 V standard bipolar square wave noticeably affects the behavior of our cryostat's temperature controller. When peak voltages above 2 V are applied, we observe a drop in the amount of power required by the cryostat heater to maintain a 30 K temperature, sometimes by as much as 30%. This implies that the voltage is creating a temperature gradient, small enough to not heat the cryostat cold finger above 30 K but large enough to affect the sample. Predictably, then, the greater the expected dissipated power, the greater the deviation from linear dependence of γ. The temperature controller heater power is less affected when larger off/on ratios are used. Future experiments should measure heater power as a function of voltage to provide a quantitative side to this

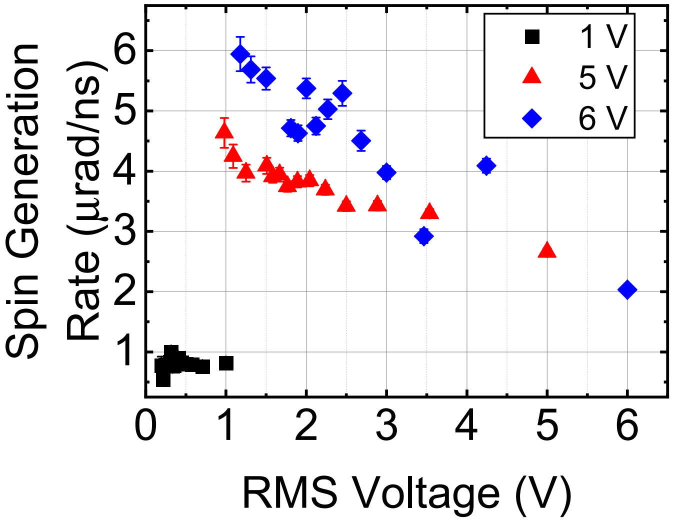

Figure 5.9: Spin generation rate γ measured as a function of V_{RMS} for $V_{\mathrm{pk}} = 1$ V, 5 V, and 6 V. Original measurement data is processed as described in the text, with error bars derived from the fit. Measurements corresponding to different V_{pk} do not lie along the same curve, indicating that V_{RMS} does not solely determine γ. However, as V_{RMS} increases, γ decreases.

qualitative observation.

Sample heating changes the temperature of our material, changing with it optical and electronic properties that can impact our measured spin generation rate [45]. For example, carrier concentration and mobility are electronic properties that can change with temperature, and CISP has been observed to depend on both of them [20]. Furthermore, if sample heating changes the momentum scattering time, the spin relaxation time and consequently the spin generation rate will be affected as well.

Sample heating will also change the optical absorption profile of the sample and shift the wavelength at which maximum Faraday rotation occurs. To verify this, we measured γ as a function of laser wavelength. For all-optical measurements in which a second laser pulse is used to generate a spin polarization instead of an applied voltage, the maximum Faraday rotation occurs around 836 nm. We measured CISP as a function of laser wavelength under application of both 1 V and 6 V standard bipolar square waves. For 1 V, both Faraday rotation and γ are maximized around 836 nm as well. For 6 V, we observe the peak wavelength redshift to approximately 838 nm. This implies that sample heating detunes our laser from the peak Faraday rotation wavelength by altering the absorption profile of our sample. For pure GaAs, this shift in the absorption edge is roughly equivalent to a temperature increase of 20 K [45]. This will reduce the magnitude of the signal we measure, even when the magnitude of the electrically-generated spin polarization is unaffected.

Thus we have demonstrated that observed deviations from linear CISP behavior are attributable to heating and can be reduced in an $In_{0.026}Ga_{0.974}As$ epilayer by utilizing a modified square wave voltage and applying a Fourier correction factor to the measurement data. Selecting the proper off/on ratio must balance the magnitude of heating with the desired signal-to-noise ratio. Future CISP studies can utilize this technique to reduce or eliminate heating effects, removing the limitations of experiments performed at large applied electric fields.

CHAPTER 6

History-Dependent Dynamic Nuclear Polarization in Gallium Arsenide

6.1 Motivation

A complete picture of electron spin dynamics cannot neglect the interplay between the electron and nuclear spin systems. On their own, nuclear spin dynamics hold great interest themselves for data processing and storage applications [70, 71, 72]. Work to manipulate nuclear polarization could lead to hyperpolarization, which would be a boon for data storage as well as other everyday applications such as nuclear magnetic resonance imaging [73]. For our part, we are interested in the role nuclear spins play in the context of electron spin dynamics. At best, control of nuclear spin polarization could allow experimentalists to extend the electron spin lifetime [70, 71, 72]. At worst, nuclear spin polarization can compromise the reliable measurement of electron spin polarization, obfuscating the proper interpretation of the acquired data. Should we understand the means by which this dynamic nuclear polarization (DNP) accumulates, we may be able to use it to our advantage.

We can learn about the electron-nuclear spin interactions via all-optical means. The presence of the nuclear polarization is felt by the electrons as a magnetic field, known as the Overhauser field. Magneto-optical techniques like Kerr rotation can thus give us a window into the action of the nuclei on electron spins. Indeed, DNP has been studied in a host of material systems, from bulk semiconductors [39, 40, 74, 75, 76] to quantum wells [40, 77] to quantum dots [78, 79]. We have particular interest in work carried out by researchers primarily at the Technische Univerität Dortmund who have produced a number of these studies over the past decade and contributed significantly to our understanding of the relevant physics. While their studies have spanned a wide range of materials, even including bulk GaAs, the subject of our own investigations, recently they have focused primarily on fluorine-doped ZnSe. Their papers showing the optical Stark effect as the mechanism for DNP [76, 80] have served both as an inspiration to us as well as an intriguing counterpoint, given the difference in observed nuclear behavior in their system. They also use time-resolved Kerr rotation for studying the nuclear spin system in the regime of resonant spin amplification, so their work is quite relevant to the studies presented here.

With that context in mind, we present in Fig. 6.1 a field-resolved Kerr rotation measurement in GaAs at 10 K that is emblematic of the worst-case scenario in which DNP severely affects the electron spin polarization [10]. The laser was tuned to 819.5 nm with pump-probe delay set to −160 ps. The external magnetic field was swept from −160 to +160 mT in 0.25 mT steps at a rate of one step every 1.1 s (upsweep, solid blue line). The field was then decremented with the same step size and timing from −160 to +160 mT (downsweep, dashed orange line). The RSA equation derived in Chapter 2 lacked any dependence on the sweep direction of the external field. Yet here we see a marked difference in character for Kerr rotation based on the field sweep direction. The RSA peaks are shifted with respect to one another, and notably with respect to the peak positions we may have expected. Furthermore, the peaks are warped into an asymmetric shape. Somehow, the electron spin polarization has acquired a dependence on the external field history of the system.

As the introduction to this chapter suggests, this behavior results from a DNP that depends not just on the current external field but also the prior external fields. This observation of magnetic-field-sweep-direction-dependent dynamic nuclear polarization became the driv-

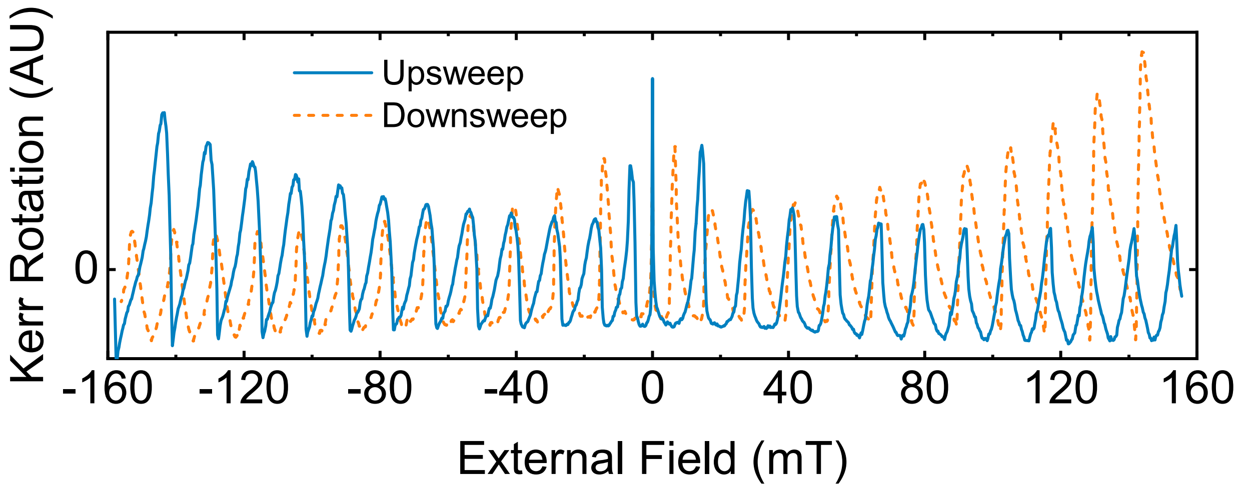

Figure 6.1: Field-sweep-direction-dependent Kerr rotation measured on bulk GaAs. Field-resolved Kerr rotation measured as a function of external magnetic field for a fixed pump-probe delay of 13 ns at laser wavelength 819.5 nm. The field is swept from −160 to +160 mT (upsweep, solid blue line) and then from +160 to −160 mT (downsweep, dashed orange line). With the exception of the zero-peak, upsweep peaks are shifted with respect to downsweep peaks, and all peaks assume an asymmetric form. Data originally published in Ref. [10].

ing force behind this investigation. We establish a model based on the optical Stark effect as the mechanism for generating nuclear spin polarization to explain our observations. We then discuss our experimental data through the lens of this model, verifying it at key points by comparison to simulated S_z. With the model in hand, we devote the next chapter to a new class of field sweeps, the steep sweeps, which lend new insights into the timescales of our system and serve to complete the picture we begin sketching here.

The model and a selection of data presented in this chapter were previously published in Physical Review B (© American Physical Society) [10, 11]: M. Macmahon, J. R. Iafrate, M. J. Dominguez, and V. Sih, Observation of magnetic field sweep direction dependent dynamic nuclear polarization under periodic optical electron spin pumping, Physical Review B **99**, 075201 (2019); and M. J. Dominguez, J. R. Iafrate, and V. Sih, Dynamic nuclear polarization by optical Stark effect in periodically pumped gallium arsenide, Physical Review B **101**, 205203 (2020). An additional manuscript, primarily consisting of material featured in the next chapter, is currently in preparation. All simulations and fits of spin polarization are provided by and appear courtesy of Dr. Michael Macmahon and Michael Dominguez.

6.2 Dynamic Nuclear Polarization and the Optical Stark Effect

6.2.1 Excitons in Gallium Arsenide

To establish a model for DNP, we need to understand the physics of GaAs, particularly at low temperatures. The sample under study is a piece of wafer 033XT, a 2-μm-thick Si-doped GaAs epilayer (doping density $n = 3 \times 10^{16}$ cm^{-3}) from IQE, Inc. The epilayer was grown on a 1-μm-thick undoped AlGaAs epilayer, which was grown on an undoped (001) GaAs substrate. Both epilayers were deposited by molecular-beam epitaxy. Sample geometry for the piece under consideration, 033XT-A5, is shown in Fig. 6.2. Optical lithography and wet etching were used to etch away the epilayers, leaving a cross-shaped channel with arms along the [110] and $[1\bar{1}0]$ crystal axes, just as was the case for the InGaAs sample considered in Chapter 5. The channel arms are 500 μm in length and 270 μm in width. Ohmic Au/Ge/Ni contacts were deposited on the sample for potential use in electrical experiments, but they were not utilized here. Sample processing was performed by a previous student. Unless otherwise stated, all measurements were performed at 10 K.

Further characterization is provided by photoluminescence measurements. Measured PL for an unprocessed piece of wafer 033XT at 10 K is shown in Fig. 6.3. We observe two features. The lower-energy peak observed in this wavelength range is attributed to donor-acceptor transitions, denoted DA. This is sufficiently far from the wavelengths used in these experiments, so we will ignore this feature going forward.

In relatively pure semiconductors, optically created electron-hole pairs can bind together through the Coulomb interaction into excitons (symbolically denoted as X), which can then move freely throughout the material. For an accessible treatment of excitons, see [59]. The binding energy of excitons in GaAs is fairly small, at 4.2 meV [59]. This would suggest that

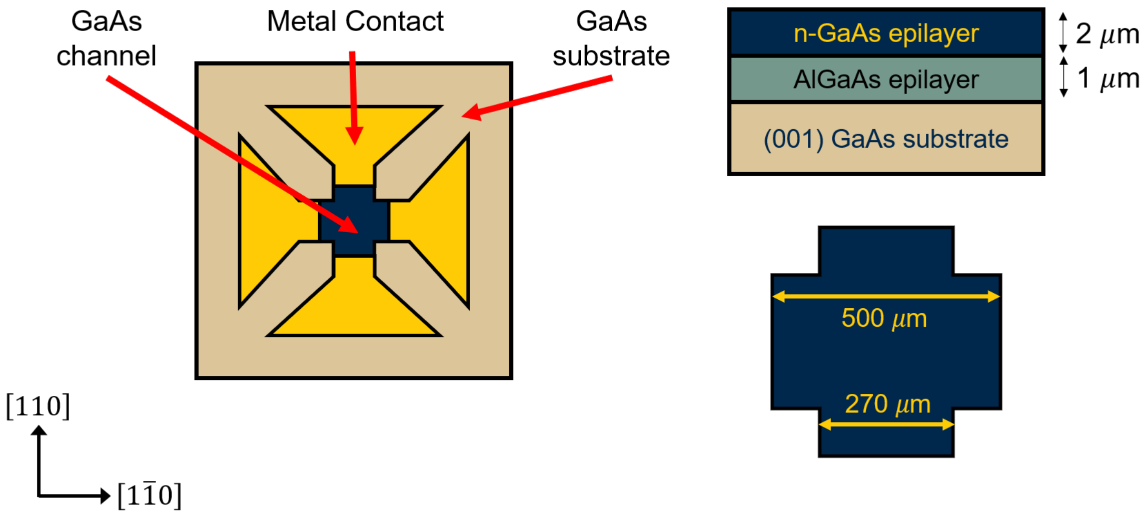

Figure 6.2: Schematic of the sample under study in this and the following chapter, 033XT-A5. The metal contacts were deposited for use in other experiments and do not factor into this study.

even fairly low temperatures would produce enough thermal energy to dissociate excitons; however, we should instead consider the temperature properties of the phonons that lead to the dissociation. With this consideration, we might expect excitons to persist to fairly high temperatures. This is the reality, as can be observed in absorption spectra for GaAs for temperatures as high as 185 K [81]. We would expect free excitons to show up in the PL spectrum for GaAs at energies just below the band gap.

An additional consequence of low-temperature measurements lies with the donors. At 10 K, there are a number of donors that have failed to ionize. This creates a population of electrons localized on donor sites. Excitons can form at lower energies by latching onto these localized electrons. Donor-bound excitons (often denoted D^0X) are composed of three particles: a free electron, a free hole, and a donor-bound electron, all bound together. This quasiparticle is often appropriately called a trion in lower-dimensional systems. Donor-bound excitons should also show up in the PL spectrum for GaAs at energies just below the band gap.

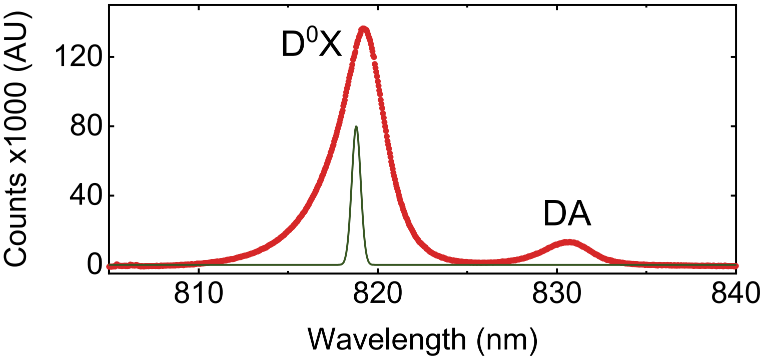

Figure 6.3: Photoluminescence measured at 10 K on an unprocessed piece of the wafer 033XT. The sample was excited with a 532 nm laser diode, with power 930 μW before a 100× microscope objective. The peak at approximately 819 nm has a full width at half maximum of about 3 nm. Identification of the donor-bound exciton peak (D^{0}X) and the donor-acceptor peak (labeled DA) follows Refs. [14] and [40]. The spectrum of the pump-probe pulses used in our Kerr rotation measurements is depicted as a dark green peak centered at wavelength 818.8 nm.

For materials with our doping level, PL features corresponding to the exciton and donor-bound excitons cannot be separately resolved. Our pump-probe experiments measure Kerr rotation using laser wavelengths in the range of 818.0 nm to 819.6 nm, right in the middle of this feature. As such, we cannot conclusively identify whether we are pumping solely one of these transitions or some combination of both. In fact, previous studies in lower-dimensional materials dealing with both an exciton and trion peak have observed the effects of both in spin polarization measurements even when pumping and probing at one of two well-defined transitions [16, 82]. That said, similar DNP studies have identified this feature in our PL with the donor-bound exciton, so we will do likewise.

For a comprehensive study of PL in GaAs for various doping levels and temperatures, see Ref. [83].

6.2.2 Spin Rotation via Optical Pulses

In Chapter 2, we considered the optical selection rules for donor-bound excitons, shown in Fig. 6.4a. We have a two-level system, with both the ground and excited states split into two states based on spin. The spin-up (-down) donor-bound exciton (spin determined by the hole spin) can only be excited from the spin-up (-down) donor-bound electron via σ^+ (σ^-) light.

But our setup uses a pulsed laser. These pulses are themselves time-varying electric fields. When a time-varying electric field is incident on a two-level system, the levels may be shifted in energy. This phenomenon is known as the optical Stark effect (OSE) [84, 85, 86]. It is alternatively referred to as the AC Stark effect. The magnitude of the shift is determined by the detuning of the field frequency from the transition frequency. Put another way, the detuning is proportional to the energy difference $E_{\text{pump}} - E_t$, where E_{pump} is the energy of the incoming field and E_t is the energy of the transition. We will define this detuning parameter shortly. When the incoming field is on resonance with the transition, there is no level shift. A negatively detuned field (red-shifted) will shift the levels away from each other, blue-shifting the transition; a positively detuned field (blue-shifted) will shift the levels toward one another, red-shifting the transition [87].

Polarization also factors into the shift. In the two-level system we are considering, circularly polarized light will also cause an energy shift. However, each helicity will only shift the transition that it couples. So σ^+ will only shift the spin-up transition (seen in Fig. 6.4 for negative detuning), leaving the spin-down transition at its resonance energy. Conversely, σ^- will only shift the spin-down transition. Thus, by using circularly polarized laser pulses, we induce a spin-dependent energy splitting in our donor-bound exciton transitions.

Spin-dependent energy splitting can also emerge in the presence of a magnetic field (Zeeman splitting). By analogy, we can attribute the spin-dependent energy splitting of the donor-bound exciton states by the OSE to an effective magnetic field. This field, aligned along the optical axis, persists only as long as the pulse is present. During that time, it will cause any components of electron spin polarization perpendicular to the optical axis to pre-

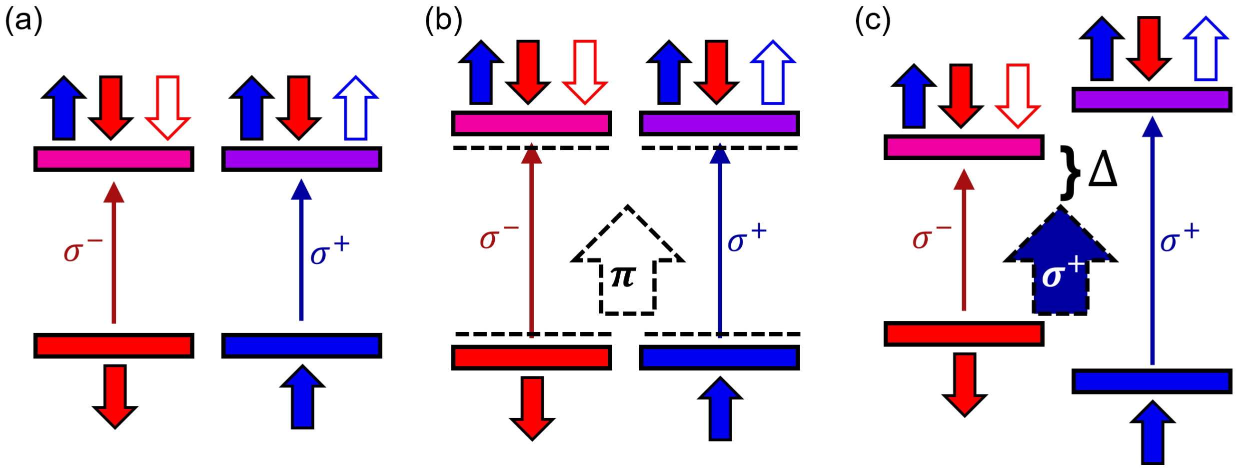

Figure 6.4: Cartoon representation of the optical Stark effect acting on the donor-bound exciton transition in GaAs. (a) In the absence of an AC field, the transition energy is independent of spin, though each transition couples to only one of σ^+ or σ^-. (b) In the presence of a linearly polarized AC field, the optical Stark effect shifts the energy levels of the two-level system. It shifts both transitions equally, so there is no energy difference between the two spin states. Case is shown for negative detuning. (c) In the presence of a circularly polarized AC field, only one of the two transitions is shifted in energy. This creates an energy splitting between the two spin states analogous to the effect of applying a longitudinal magnetic field. The dimensionless quantity Δ is a measure of the energy detuning from the usual transition energy. Figure inspired by and adapted from Ref. [87].

cess by some amount. We thus describe the OSE as a rotation of our spin polarization. Each pump pulse will both excite electron spins along $\hat{z}$ and cause any existing polarization to rotate. This calls for a modification of the RSA equation for the measured spin polarization S_z.

This rotation phenomenon has elsewhere been attributed to geometric phase [88, 89, 90]. It can also be described as an inverse Faraday effect, or a dynamic Zeeman effect [17, 91]. For our part, we do not distinguish between these attributions, following the lead of recent papers out of Dortmund.

Previous work has established a fully quantum formalism for understanding the donor-bound exciton or trion system under the effect of the OSE [15]. This has produced a series of relationships between the components of the spin pseudovector before and after the arrival of a pump pulse ($\vec{S}^-$ and $\vec{S}^+$, respectively). A number of considerations must go into this calculation, with some assumptions made to lead to an analytic solution (such as representing the optical pulses as Rosen and Zener pulses). We proceed from this point.

Yugova *et al.* have shown that, for σ^+ polarized pump pulses with duration much less than the laser repetition time ($\tau_p \ll T_R$),

$$S_x^+ = Q\cos\Phi S_x^- + Q\sin\Phi S_y^-, \tag{6.1a}$$

$$S_y^+ = Q\cos\Phi S_y^- - Q\sin\Phi S_x^-, \tag{6.1b}$$

$$S_z^+ = \frac{Q^2-1}{4} + \frac{Q^2+1}{2} S_z^-. \tag{6.1c}$$

The optical Stark rotation due to the pump pulse is characterized by the rotation angle Φ, measured in radians with respect to the y-axis:

$$\Phi = \arg\left(\frac{\Gamma^2\left(\frac{1}{2} - i\Delta\right)}{\Gamma\left(\frac{1}{2} - i\Delta - \frac{\theta}{2\pi}\right)\Gamma\left(\frac{1}{2} - i\Delta + \frac{\theta}{2\pi}\right)}\right); \tag{6.1d}$$

and the rotation amplitude Q:

$$Q = \left|\frac{\Gamma^2\left(\frac{1}{2} - i\Delta\right)}{\Gamma\left(\frac{1}{2} - i\Delta - \frac{\theta}{2\pi}\right)\Gamma\left(\frac{1}{2} - i\Delta + \frac{\theta}{2\pi}\right)}\right|. \tag{6.1e}$$

Both rotation angle and amplitude depend on the pump detuning from resonance and the pulse area. Detuning is a dimensionless quantity defined as $\Delta = (E_{\text{pump}} - E_t)\,\tau_p/2\pi\hbar$, where E_t is the energy of the donor-bound exciton transition, while the pulse area is defined as $\theta = \int 2\left|\langle d\rangle E(t)\right| dt/\hbar$.

We describe the OSE as a rotation about the optical axis, so we can construct a rotation matrix for it and modify our earlier derivation of the RSA equation:

$$\hat{R}_{\text{OSE}} = \begin{pmatrix} Q\cos\Phi & Q\sin\Phi & 0 \\ -Q\sin\Phi & Q\cos\Phi & 0 \\ 0 & 0 & \delta \end{pmatrix}. \tag{6.2}$$

Note that the direction of rotation is opposite to that of spin precession. This is not quite a rotation matrix in the traditional sense, as there is a rotation amplitude Q that varies with

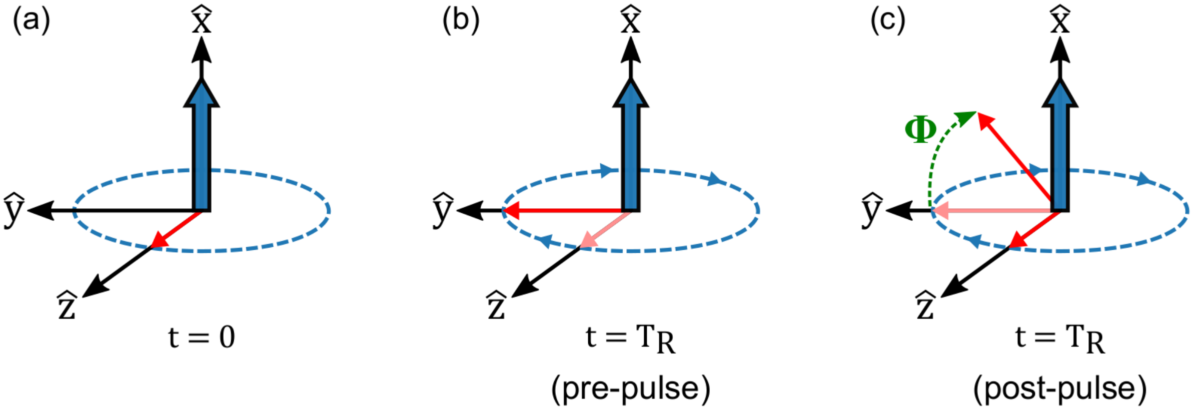

Figure 6.5: Schematic for spin polarization generation and precession under the influence of the optical Stark effect. This figure considers spin polarization generated along $+\hat{z}$ and precessing in the clockwise direction ($g < 0$) about $\hat{x}$. (a) At time $t = 0$, the first pump pulse arrives and an electron spin polarization (thin red arrow) is generated. An external magnetic field (thick blue arrow) is applied along the transverse direction $\hat{x}$. (b) The spin polarization precesses in the yz-plane until a time $t = T_R$ later, just before the next pump pulse arrives. (c) At this time $t = T_R$, the pulse arrives. By the optical Stark effect, its presence is experienced by the spin polarization as a magnetic field along the optical axis (not shown). The polarization rotates about the optical axis by angle Φ (green), resulting in a nonzero spin polarization along the external magnetic field direction $\hat{x}$. Simultaneously, spin polarization is generated along the optical axis, and the total polarization is the vector sum. This process repeats as pump pulses arrive at intervals of T_R. Refer back to Fig. 2.10 for the process of resonant spin amplification in the absence of the optical Stark effect. Figure adapted from Ref. [11].

detuning. Further, S_z does not remain unchanged by the action of the pump pulse. We have, for the first time in this dissertation, an expression for the spin polarization generated by a pump pulse in terms of the existing spin polarization. The zz-component of this "rotation" matrix represents the relationship between S_z before and after the pulse, $\left(Q^2 + 1\right)/2$. For simplicity of notation, we use the symbol δ to stand in for this term. The generated spin polarization $\vec{S}_0$ will have magnitude $\left(Q^2 - 1\right)/4$, but this does not factor into the rotation matrix.

Constructing the infinite sum is similar to before, but now the OSE also acts at every multiple of T_R. We proceed under the assumption that the pulse acts to simultaneously rotate the existing spin polarization along $\hat{x}$ and $\hat{y}$ while generating a new spin polarization S_0. A schematic of this physical process during the first period T_R is presented in Fig. 6.5.

Previously, we did not have to presume the optical axis to construct the sum. However, since the optical Stark rotation is about the optical axis, we are calculating an entire rotation matrix only to be able to use the z-column. That said, this result could find use in the case of a very small spin polarization along another axis (as a perturbation), but we do not consider this any further. Spin generation along any other axis will require a different optical Stark matrix, though the precession matrix is tied to the direction of the external magnetic field.

The spin pseudovector at a time t after a series of infinite pulses is given by

$$\vec{S} = \hat{R}\left[\Omega t\right]\, e^{-t/\tau} \left(\sum_{n=0}^{\infty} \left(\hat{R}_{\mathrm{OSE}} \hat{R}\left[\Omega T_R\right] \right)^n e^{-nT_R/\tau} \right) \vec{S}_0, \tag{6.3}$$

which is our earlier RSA expression, just with the precession rotation matrix replaced by the new total "rotation" matrix

$$\begin{aligned} \hat{R}_{\mathrm{rot}} &= \hat{R}_{\mathrm{OSE}} \hat{R}\left[\Omega T_R\right] \\ &= \begin{pmatrix} Q\cos\Phi & Q\sin\Phi & 0 \\ -Q\sin\Phi & Q\cos\Phi & 0 \\ 0 & 0 & \delta \end{pmatrix} \begin{pmatrix} 1 & 0 & 0 \\ 0 & \cos\left(\Omega T_R\right) & -\sin\left(\Omega T_R\right) \\ 0 & \sin\left(\Omega T_R\right) & \cos\left(\Omega T_R\right) \end{pmatrix} \\ &= \begin{pmatrix} Q\cos\Phi & Q\sin\Phi\cos\left(\Omega T_R\right) & -Q\sin\Phi\sin\left(\Omega T_R\right) \\ -Q\sin\Phi & Q\cos\Phi\cos\left(\Omega T_R\right) & -Q\cos\Phi\sin\left(\Omega T_R\right) \\ 0 & \delta\sin\left(\Omega T_R\right) & \delta\cos\left(\Omega T_R\right) \end{pmatrix}. \end{aligned} \tag{6.4}$$

Evaluation of the infinite sum is nontrivial and presented in Appendix A. We report here only the final expression for the spin pseudovector:

$$\vec{S} = S_0 r' e^{-t/\tau} \begin{pmatrix} -K\sin\left(\Omega T_R - \gamma\right) \\ -\sin\left(\Omega t - \gamma\right) \\ \cos\left(\Omega t - \gamma\right) \end{pmatrix}. \tag{6.5}$$

We have defined quantities as follows: K is the relative amplitude between the rotated

S_x and S_y components immediately following the action of a pump pulse, given by

$$K = \frac{Qe^{-T_R/\tau}\sin\Phi}{1 - Qe^{-T_R/\tau}\cos\Phi}; \tag{6.6a}$$

α is the amplitude change in S_y due to the pump pulse, given by

$$\alpha = Q\cos\Phi - KQ\sin\Phi; \tag{6.6b}$$

γ is a phase shift due to both external magnetic field and the actions of the pump pulse, analogous to the RSA phase shift derived previously and given here by

$$\gamma = -\arctan\left(\frac{\alpha e^{-T_R/\tau}\sin\left(\Omega T_R\right)}{1 - \alpha e^{-T_R/\tau}\cos\left(\Omega T_R\right)}\right); \tag{6.6c}$$

r, while not shown explicitly in the final expression, factors into the definition of γ and is analogous to the magnetic-field-dependent amplitude modification derived previously for RSA, given here by

$$r = \left(1 - 2\alpha e^{-T_R/\tau}\cos\left(\Omega T_R\right) + \alpha^2 e^{-2T_R/\tau}\right)^{-1/2}; \tag{6.6d}$$

and r' is defined as the magnetic-field-dependent amplitude modification following an infinite train of pulses, given by

$$r' = \left(\cos\gamma - \delta e^{-T_R/\tau}\cos\left(\Omega T_R - \gamma\right)\right)^{-1}. \tag{6.6e}$$

We also consider the total spin polarization after an infinite number of pulses $S_0^\infty = S_0 r'$. These equations were derived by Michael Dominguez for Ref. [11] through a method analogous to that used in Ref. [36], though our notation here differs slightly. Similarly, Ref. [92] derived a version of these expressions in the limit that the pump-probe delay goes to zero.

Before adding the effect of DNP into our model, we consider how each of the parameters that play a role in these equations vary with detuning and, where applicable, external

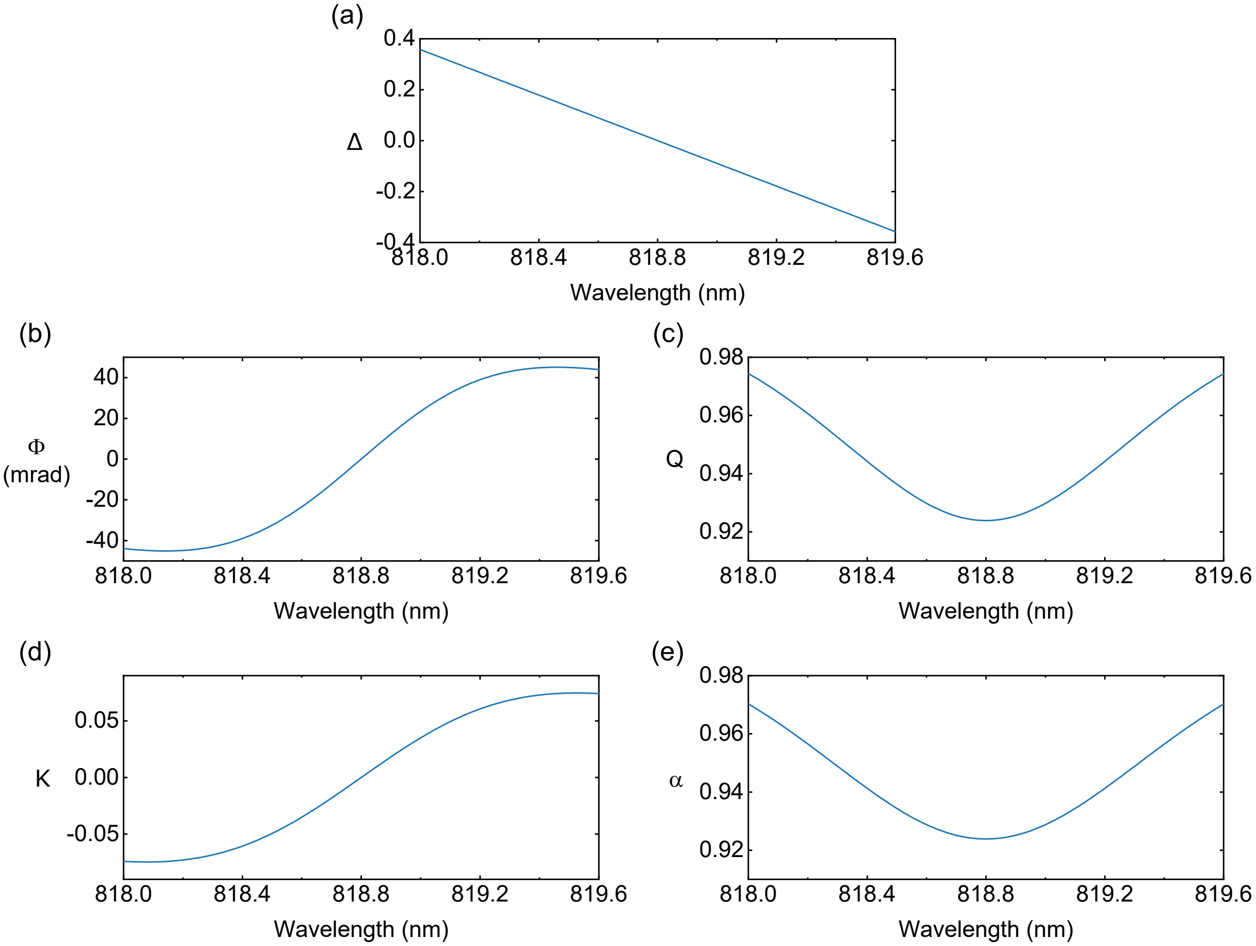

Figure 6.6: Optical Stark effect model parameters as a function of laser wavelength. (a) The correspondence between the detuning parameter Δ and wavelength is provided for reference. Calculations for (b) Φ (OSE rotation angle), (c) Q (OSE rotation amplitude), (d) K (relative amplitude between rotated S_x and S_y), and (e) α (change in S_y due to the pump pulse) assume pulse duration $\tau_p = 1$ ps and pulse area $\theta = \pi/4$.

magnetic field. To make the connection to our experiments clearer, we substitute the wavelengths of our measurements for detuning, under the assumption that the transition energy E_t corresponds to the wavelength 818.8 nm. Figure 6.6a shows the (linear) correspondence between detuning Δ and wavelength.

The remaining panels of Fig. 6.6 display the model parameters that depend on detuning but are independent of external magnetic field. Each of these parameters also depend on pulse width τ_p and area θ. We fix these quantities by finding the closest correspondence between simulated and measured Kerr rotation. In these and all future plots, we take $\tau_p = 1$ ps and $\theta = \pi/4$. See that the rotation angle Φ reverses sign with detuning, passing through zero at the resonance. This change will characterize the differences in detuning that are manifested in our Kerr rotation. Even at the edges of our wavelength range, the rotation angle is fairly small. Because K is proportional to $\sin\Phi$, it generally follows the same shape as Φ. The rotation amplitude Q can in principle vary from 0 to 1, but with our stipulated pulse parameters, it is close to 1 for all wavelengths. The S_y amplitude modification α is proportional to Q, so it generally follows Q here.

We consider the external-field-dependent parameters in Fig. 6.7. We select the field range -40 to $+40$ mT used for many of our experiments. The parameters γ (effective phase) and r (effective amplitude) are strongly field-dependent but appear fairly independent of detuning. This is reasonable to expect, given that both terms depend on detuning through α, which does not vary significantly over our wavelength range. See that r peaks at regularly-spaced field intervals. This is the RSA period of approximately 12.3 mT. In contrast, γ changes sign at the RSA period, going through zero. We do see a detuning-dependence in the total spin polarization S_0^∞ as well as behavior periodic with the RSA condition. It peaks at the RSA period (with negative sign) and at zero detuning. As detuning increases in either direction, this overall spin amplitude falls off. Away from the RSA period, the amplitude falls off as well. Note that we do not distinguish field sweep direction in these plots. These parameters are computed in the absence of the DNP that leads to the direction-dependence alluded to in the introduction to this chapter.

Finally, consider how the spin polarization itself changes under the influence of the optical Stark effect. We plot the components of the spin pseudovector $\vec{S}$ as a function of both wavelength and external field in Fig. 6.8. The plot for S_z bears a strong resemblance to the plot for S_0^∞, with S_z falling off away from the resonance wavelength and falling off even

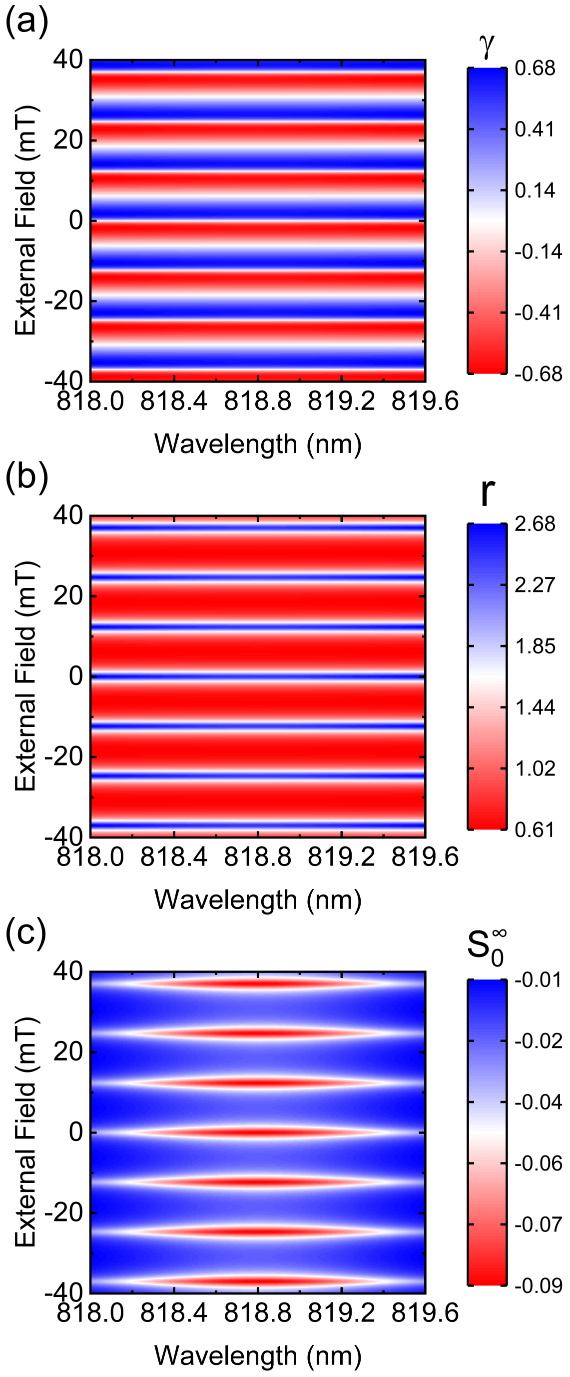

Figure 6.7: Optical Stark effect model parameters as a function of external magnetic field and laser wavelength. The parameters (a) γ (effective field-dependent phase), (b) r (effective field-dependent amplitude), and (c) S_0^∞ (spin polarization after infinite pulses) are plotted on different color scales. Calculations assume pulse duration $\tau_p = 1$ ps and pulse area $\theta = \pi/4$.

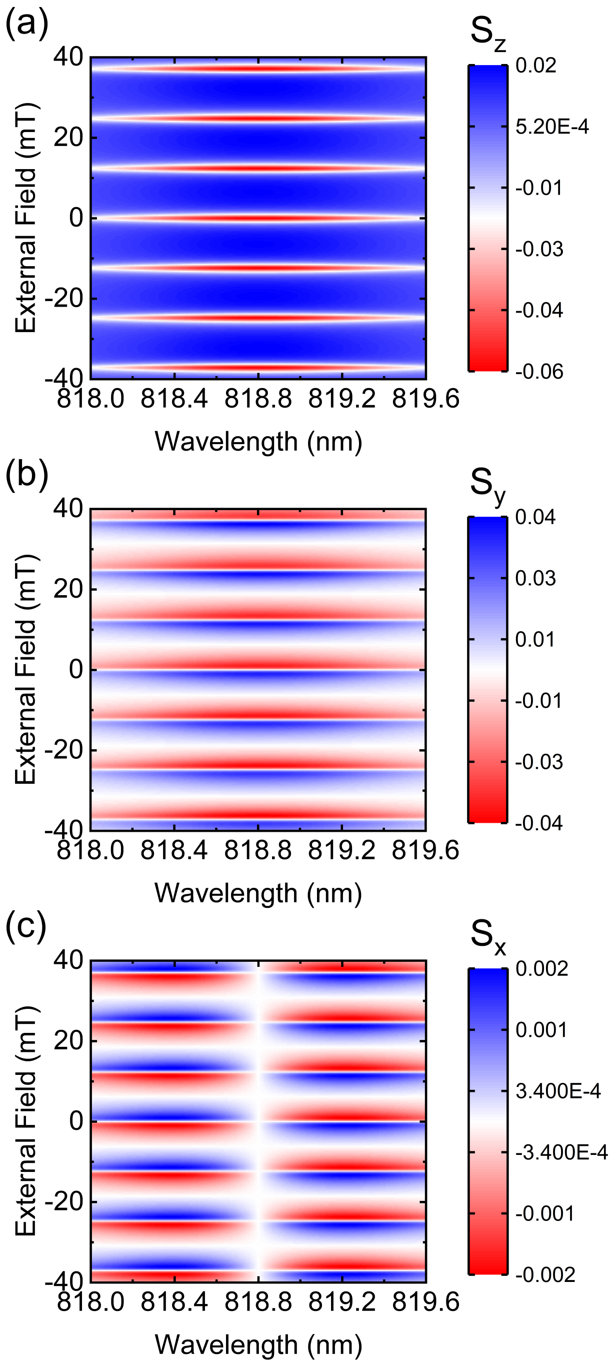

Figure 6.8: Calculated components of electron spin polarization under periodic optical excitation and the optical Stark effect in the absence of nuclear polarization, as a function of external magnetic field and laser wavelength. Unlike (a) S_z and (b) S_y, (c) S_x changes sign when optical detuning passes through zero and vanishes on resonance. Color scales are different for each panel. Calculations assume pump-probe delay 13 ns, spin lifetime $T_2^* = 30$ ns, pulse duration $\tau_p = 1$ ps, and pulse area $\theta = \pi/4$.

more strongly away from the RSA condition. The plot for S_y shows minimal dependence on wavelength but strong dependence on external field. Just as with γ, S_y changes sign when passing through the RSA condition. In contrast to these two, S_x displays a marked change with wavelength and field. At zero detuning, there is no S_x, as expected. For longer wavelengths (negative detuning), S_x mimics the field-dependence of S_y, just with different amplitude. However, when considering shorter wavelengths (positive detuning), the sign is flipped.

These features may be clearer by taking linecuts of the two-dimensional plots for particular choices of detuning. We compare positive and negative detuning cases to the no-detuning case in Fig. 6.9. In all three cases, S_z and S_y appear relatively unchanged. For nonzero detuning, the spin polarization acquires an S_x component, with the sign of this component tied to the detuning.

Before moving on, we note that for σ^- light, the effective magnetic field experienced by the electron spin polarization has the opposite sign, so the polarization is rotated in the opposite direction; the initial spin polarization S_0 is also reversed in direction [15]. These two sign flips conspire together such that S_x maintains the same sign for each detuning regardless of which polarization is exciting the system. Thus, we need not be concerned about using the PEM and alternating helicity in our experiments.

6.2.3 Dynamic Nuclear Polarization

By itself, the OSE would not cause any noticeable changes in our Kerr rotation measurements of S_z, and our measurement techniques do not lend themselves to measuring S_x. It is here that DNP enters the picture. Spin-polarized electrons transfer their spin polarization to the nuclear lattice via spin-flip hyperfine interactions. The only component of the nuclear spin that will play a role in our Kerr rotation measurements is along the external

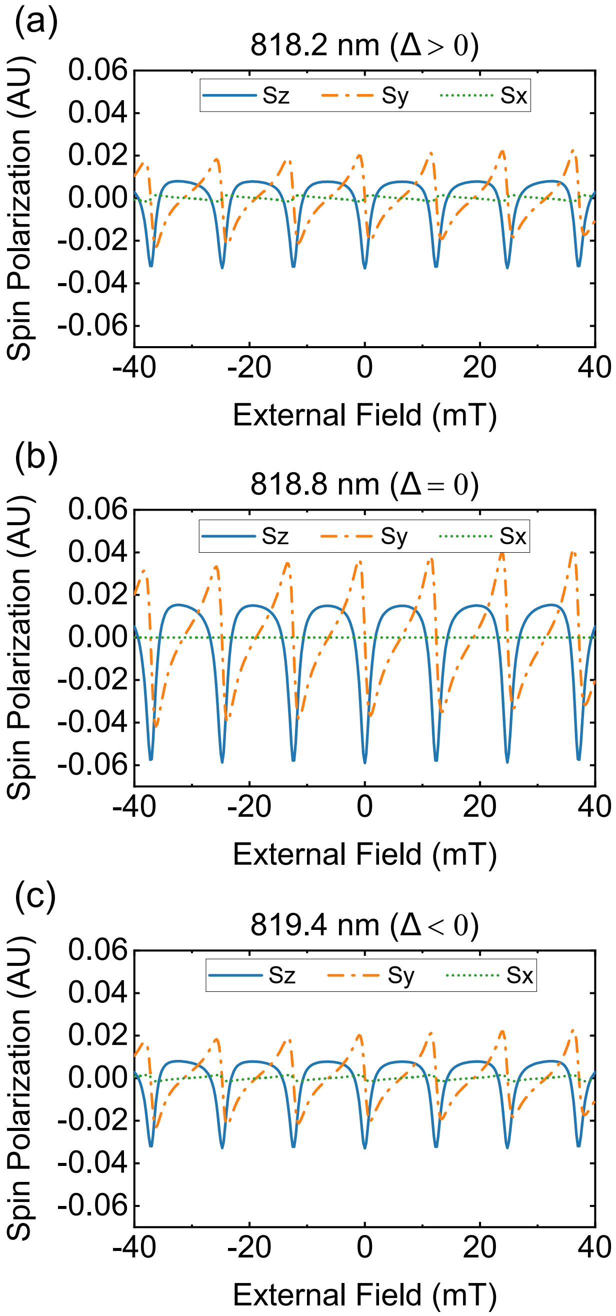

Figure 6.9: Calculated components of electron spin polarization under periodic optical excitation and the optical Stark effect in the absence of nuclear polarization, as a function of external magnetic field, for laser wavelengths (a) 818.2 nm (positive detuning), (b) 818.8 nm (resonance), and (c) 819.4 nm (negative detuning). Unlike S_z (solid blue line) and S_y (dot-dashed orange line), S_x (dotted green line) changes sign with the sign of optical detuning and vanishes on resonance. Calculations assume pump-probe delay 13 ns, spin lifetime $T_2^* = 30$ ns, pulse duration $\tau_p = 1$ ps, and pulse area $\theta = \pi/4$. Figure inspired by and adapted from Ref. [11].

field direction. The DNP will accumulate either parallel or antiparallel to the external field. Despite the fact that the gallium and arsenic atoms have spin 3/2 (as opposed to 1/2 like the electrons), we can still consider the nuclear spin pseudovector $\vec{I}$. It is possible to construct an analogous Bloch equation for the nuclear system, coupled to the electron system Bloch equation. However, we do not require this approach.

The nuclei and electrons operate on different timescales, so we should treat them differently. The electrons are polarized in the duration of a pump pulse by optical orientation; the nuclei are polarized over time by hyperfine interaction with electrons. The electron spin polarization relaxes on the order of nanoseconds, allowing polarization from subsequent pulses to accumulate but decaying away on any laboratory time scale; the nuclear spin polarization aligned along an external field persists for tens of seconds, allowing us to map out behavior on our time scales. From the perspective of the nuclei, the electron spin polarization changes far too quickly to follow. Instead, the nuclear spin polarization follows the time-averaged electron spin component along the field direction $\langle S_x \rangle$. Here, we mean time-averaged over a pulse period T_R, as at that point another pulse is incident. From the perspective of the electrons, the nuclei are frozen in time.

We are not measuring the contribution of individual nuclei, but the collective effect of the nuclei on the electron spin polarization. Thus, we are considering the average nuclear spin polarization I_{av}, a spatial average rather than a time average. That said, this is *dynamic* nuclear polarization, so we are interested in dynamics. The rate equation for the average nuclear spin polarization is given by

$$\frac{dI_{\mathrm{av}}}{dt} = -\frac{1}{T_{1e}} \left(I_{\mathrm{av}} - \frac{4}{3} I \left(I + 1 \right) \langle S_x \rangle \right) - \frac{I_{\mathrm{av}}}{T_{1n}}, \tag{6.7}$$

where T_{1e} is the nuclear polarization time from the hyperfine interaction, T_{1n} is the phenomenological nuclear spin relaxation time accounting for all relaxation processes, and I is the nuclear spin 3/2 [93, 94, 95]. We will frequently refer to Eq. 6.7 as the nuclear rate equation.

Note that the relaxation timescales for the nuclei are not T_2^*, the inhomogeneous dephasing timescale appropriate for electron spin dephasing in the Voigt geometry. Instead, we use T_1, as this is spin relaxation along the longitudinal direction (parallel to the external field). These timescales can vary significantly from material to material. In this chapter, our simulations use $T_{1e} = 180$ s and $T_{1n} = 20$ s, in line with values reported previously [13, 96, 97, 98].

The time-averaged $\langle S_x \rangle$ is here given by

$$\begin{aligned}
\langle S_x \rangle &= \frac{1}{T_R} \int_0^{T_R} \left(-S_0^\infty K \sin\left(\Omega T_R - \gamma\right) e^{-t/T_2^*} \right) dt \\
&= -\frac{1}{T_R} S_0^\infty K \sin\left(\Omega T_R - \gamma\right) \int_0^{T_R} e^{-t/T_2^*} dt \\
&= -\frac{1}{T_R} S_0^\infty K \sin\left(\Omega T_R - \gamma\right) \left(-T_2^* \left(e^{-T_R/T_2^*} - 1 \right) \right) \\
&= \frac{T_2^*}{T_R} \left(e^{-T_R/T_2^*} - 1 \right) S_0^\infty K \sin\left(\Omega T_R - \gamma\right). \qquad (6.8)
\end{aligned}$$

We plot $\langle S_x \rangle$ as a function of both wavelength and external field in Fig. 6.10, with linecuts plotted in Fig. 6.11. In each plot we are ignoring the effect of DNP. Notice that $\langle S_x \rangle$ is close in magnitude to S_x and shares the same general shape.

This differential equation does not fully capture how the electrons experience the presence of the nuclear spin polarization. Though it is not explicitly written, $\langle S_x \rangle$ is a function of magnetic field. This is not exclusively the external magnetic field, but includes the contribution from the nuclear spins. The Larmor frequency that enters into the equations derived for the OSE should really be an effective Larmor precession frequency:

$$\begin{aligned}
\Omega_{\text{eff}} &= \frac{g\mu_B}{\hbar} B_{\text{tot}} \\
&= \frac{g\mu_B}{\hbar} \left(B_{\text{ext}} + B_{\text{N}} \right), \qquad (6.9)
\end{aligned}$$

where B_{N} is the Overhauser field experienced by the electron spin polarization due to the

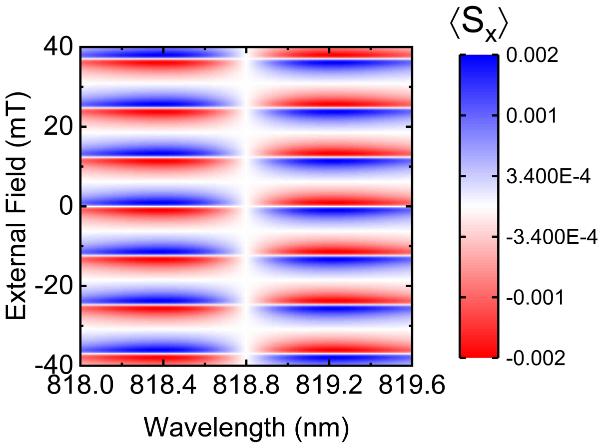

Figure 6.10: Calculated time-averaged component of electron spin polarization S_x under periodic optical excitation and the optical Stark effect in the absence of nuclear polarization, as a function of external magnetic field and laser wavelength. Calculations assume pump-probe delay 13 ns, spin lifetime $T_2^* = 30$ ns, pulse duration $\tau_p = 1$ ps, and pulse area $\theta = \pi/4$.

average nuclear spin polarization:

$$\vec{B}_{\mathrm{N}} = bn\ I_{\mathrm{av}}\left(t, \langle S_x \rangle \left(B_{\mathrm{tot}}\right)\right)\hat{x}, \tag{6.10}$$

with bn translating the nuclear spin polarization into a magnetic field:

$$bn = \sum_i \frac{A_i \chi_i}{g\mu_B}. \tag{6.11}$$

The sum is carried out over each nuclear species present in the material. Each term is the product of the hyperfine coupling constant A_i and the nuclear abundance χ_i. Hence, nuclear species with stronger nuclear-electron coupling will contribute more strongly to the Overhauser field. The contributions are weighted by the abundance of nuclei. The only stable isotope of arsenic is As_{75}, but we expect two isotopes of gallium to be present, Ga_{69} and Ga_{71}. The coupling constants and abundances are listed in Table 6.1.

Table 6.1: Hyperfine constants [40] and nuclear abundances [99] for the stable isotopes present in GaAs.

	Ga_{69}	Ga_{71}	As_{75}
$A\,(\mu\mathrm{eV})$	38.2	48.5	46
$\chi\,(\%)$	60.1	39.9	100

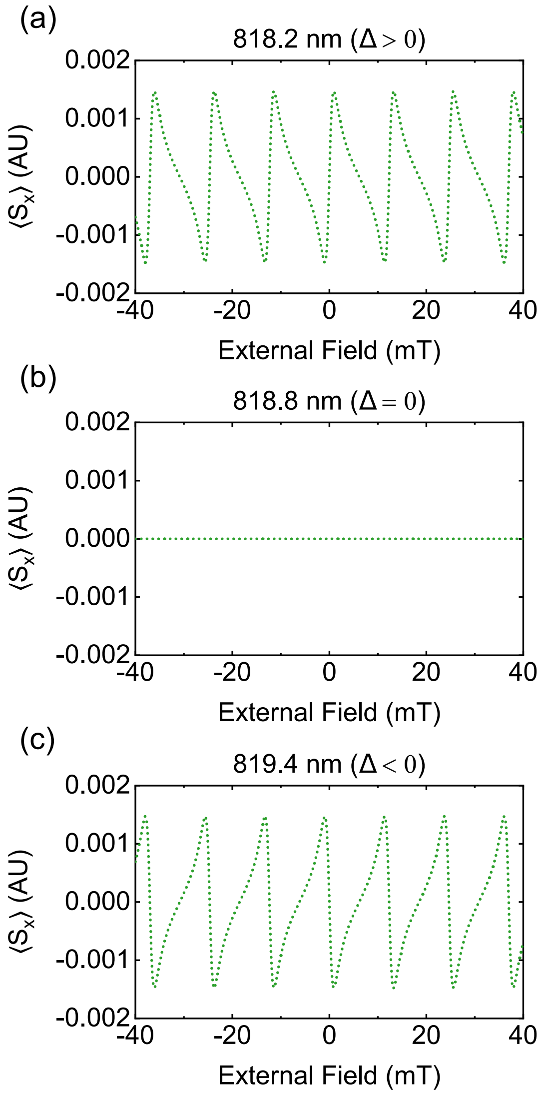

Figure 6.11: Calculated time-averaged component of electron spin polarization S_x under periodic optical excitation and the optical Stark effect in the absence of nuclear polarization, as a function of external magnetic field, for laser wavelengths (a) 818.2 nm (positive detuning), (b) 818.8 nm (resonance), and (c) 819.4 nm (negative detuning). Calculations assume pump-probe delay 13 ns, spin lifetime $T_2^* = 30$ ns, pulse duration $\tau_p = 1$ ps, and pulse area $\theta = \pi/4$.

When the external field vanishes, nuclear dipole-dipole couplings take over and depolarize the nuclear spins on a timescale much shorter than T_{1n}. Setting the external field to zero is a way of resetting the DNP in our material. The dipole-dipole couplings do not suddenly appear at zero field, but become more pronounced as the external field becomes smaller and smaller, approaching the local field B_L [13]. To account for this, we take the actual average nuclear polarization to be

$$I_{\mathrm{av}} = I_{\mathrm{av},0} \frac{B_{\mathrm{ext}}^2}{B_{\mathrm{ext}}^2 + \xi B_L^2}, \tag{6.12}$$

where $I_{\mathrm{av},0}$ is the average nuclear polarization in the absence of dipole-dipole effects. While B_L has been calculated to be 0.145 mT in GaAs [95], recent experiments have measured B_L as high as 0.6 mT [100]. We use 0.1 mT for our local field, and set the modeling constant $\xi = 1$.

Through the Overhauser field, $\langle S_x \rangle$ is a function of I_{av}, which through Eq. 6.7 is a function of $\langle S_x \rangle$. There is no simple solution to this equation. Our first impulse is to consider the steady-state, in which the nuclei reach a polarization such that $\langle S_x \rangle$ no longer changes, and thus the Overhauser field stays constant. Whether a steady-state can be reached and whether it will be reached in our experiments are two separate questions. To obtain the steady-state nuclear polarization, we can set the nuclear rate of change equal to zero and solve the nuclear rate equation numerically. This is the approach taken by Ref. [80] in describing the results of Ref. [76]. In their ZnSe system, the nuclear polarization timescales are orders of magnitude shorter than the timescales of their measurements [101], so they expect that at every external field, the system will reach its steady-state nuclear polarization before the data is recorded. They do not observe any history-dependent behavior.

Our expected nuclear timescales are very, very long in comparison. They are also long with respect to our 1.1 s experimental time steps. Thus, we cannot rely on the steady-state solution to the nuclear rate equation to describe the DNP we observe, though we will consider the steady-state solution in the next chapter. Our material also features an electron spin lifetime of 30 ns at 10 K, which is long enough to allow for RSA. Together, these effects will yield striking history-dependent behavior.

If we want to compare our experimental results to the model, we can simulate our laboratory experiments by numerically solving the differential equation. For a field scan, we generate a list of external field values identical to the field steps in our measurements. We assume that we start with no DNP. At each field step, we calculate B_{N}, which then allows us to calculate the electron spin polarization. The algorithm for these simulations, used by Michael Dominguez in Ref. [11], is as follows:

1. Set the effective magnetic field to the starting field B_{ext} for the experimental procedure, and set the nuclear spin polarization $I_{\mathrm{av}} = 0$.
2. Numerically integrate the nuclear differential equation over the time of laboratory measurement for I_{av}.
3. Calculate the Overhauser field B_{N} for the calculated I_{av}.
4. For the next experimental step, set the effective field to $B_{\mathrm{ext}} + B_{\mathrm{N}}$.
5. Repeat steps 2-4 until each measurement point of the experiment has been considered.

In what follows, we present Kerr rotation measurements on our GaAs sample that showcase the various dependences of the model on experimental parameters such as pump wavelength (detuning). For certain measurements, we present simulations produced using this algorithm. The correspondence between model and observation both confirm the veracity of our model and suggest areas of improvement. The simulations of spin polarization and the Overhauser field were provided by Michael Dominguez, while fits for the Overhauser field were provided by both Michael Dominguez and Dr. Michael Macmahon.

6.3 Experimental Verification of the OSE Model

While useful and interesting in its own right, the model was put together to solve the mystery posed by the field sweep data shown at the open of this chapter. Since our model points to the presence of DNP in our material, let us first examine the Overhauser field

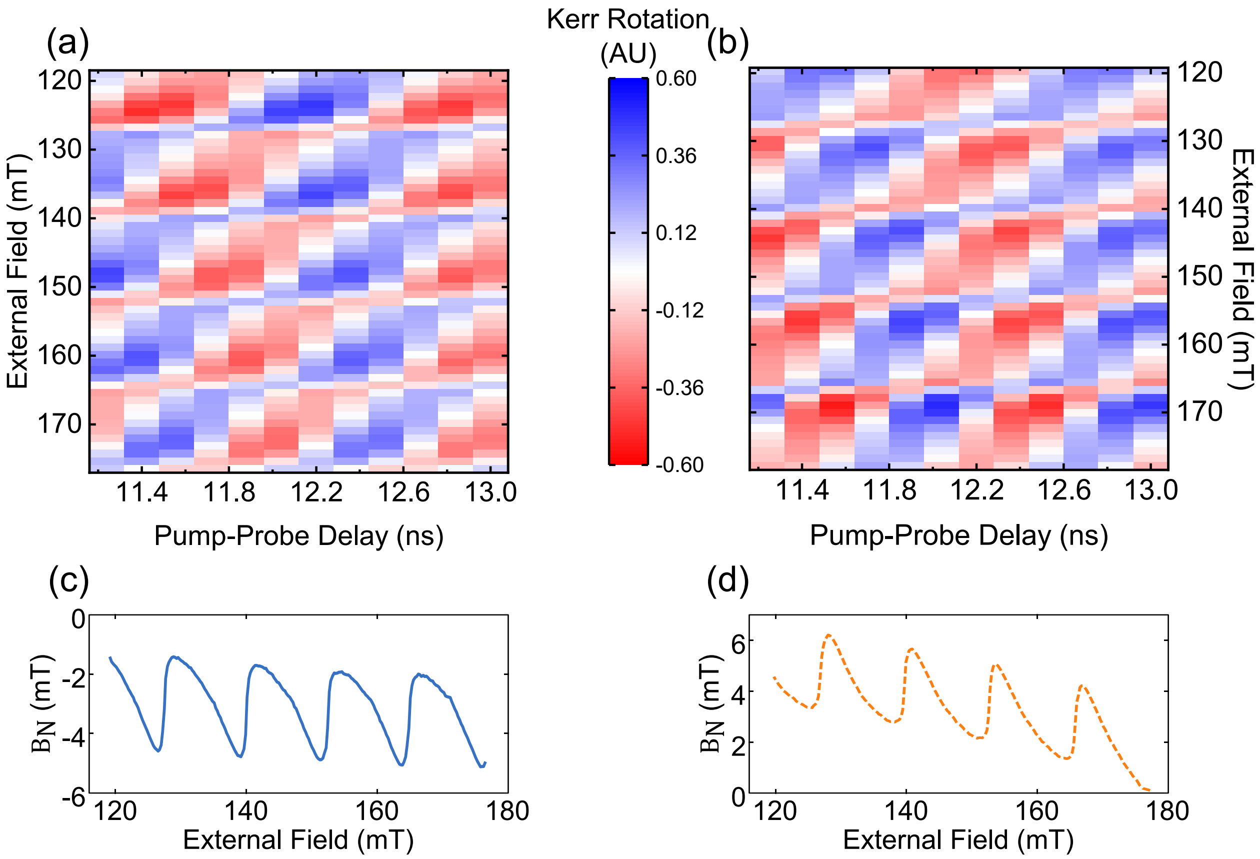

Figure 6.12: Field-sweep-direction-dependent Kerr rotation and extracted Overhauser field for upsweep and downsweep. Kerr rotation measured as a function of both external magnetic field and pump-probe delay at laser wavelength 819.5 nm on the field range 120 to 180 mT, with pump-probe delay incremented from −1920 to −160 ps in steps of 160 ps (Snapshot TRKR). The external field is set to zero between delays to reset the DNP. The (a) upsweep was measured with pump power 510 μW while the (b) downsweep was measured with pump power 540 μW. The extracted Overhauser field is shown for (c) upsweep and (d) downsweep, displaying a difference in sign based on sweep direction. Overhauser fits provided by Dr. Michael Macmahon. Data originally published in and fits reproduced from Ref. [10].

present for upsweeps and downsweeps. We use the Snapshot TRKR technique, measuring Kerr rotation for negative detuning (819.5 nm) on the external magnetic field range of 120 to 180 mT. Here, we repeat this field sweep at delays from −1920 to −160 ps, or +11240 to +13000 ps, and extract the Overhauser field from the resulting effective delay scans. It is clear from the two-dimensional Kerr rotation data in Figs. 6.12a and 6.12b that the peak locations differ based on field sweep direction. For the upsweep, the Overhauser field oscillates with external field, building to a maximum of almost −6 mT (Fig. 6.12c). For the downsweep, the Overhauser field also oscillates with external field, but it builds in the opposite direction, building to a maximum of almost +6 mT (Fig. 6.12d). In both cases, the Overhauser field accumulates to oppose the external field. The model must explain why field sweep direction reverses the sign of the Overhauser field in order to fulfill its initial objective.

At the same time, we want to understand how DNP resulting from the OSE manifests in not just this particular experiment, but in other field scans we might encounter in our laboratory. Thus, we explore the parameter space offered by the model, both to confirm its applicability to our system and to discover how DNP impacts the experiments we may want to run in the future.

Looking at its definition, the OSE rotation angle Φ is a function of two parameters, the detuning Δ and the pump area θ. We want to understand how our spin polarization changes as we vary those parameters. Experimentally, this translates into varying the laser wavelength (for detuning) and the pump power (for pump area). Technically, both Δ and θ incorporate the pump duration in their definitions, but we do not modify the pump pulse duration or shape in our experiments. We first explore these two parameter spaces. We show that the OSE model predicts a different character of warping for positive and negative detuning that is present in our measurements. Then, we present Kerr rotation measured for a series of pump powers. While we were unable to extract the Overhauser field from power-dependent measurements, we do observe that the peak warping increases with increasing power up to a point, past which it begins to decrease. This is consistent with the expectations of the model.

There is a third (and we will argue fourth) dependence to our observed spin polarization, timing. The OSE equations do not depend on time, but the nuclear rate equation does. The DNP here is not a transient effect. Instead, the Overhauser field builds as we wait longer at each experimental field step.

The fourth dependence is intertwined with time: history. It is not just how long we wait at a given external field value, but how long we waited at each field value before that. It is this history dependence that produces the direction-dependence introduced in the opening of this chapter. In the strongest confirmation of the history-dependence of our system, we carry out a field scan meant to destroy history, in which we take our usual experimental data points in a scrambled order. This wipes out our DNP. We close with a short discussion linking the nuclear rate equation to the observed history-dependence.

We will primarily present field scans, occasionally supplemented by delay scans. In this and the next chapter, the probe power in every case is approximately 100 μW. With the exception of the power-dependence measurements, incident pump power falls in the range of 500 to 700 μW. Unless otherwise stated, all field scans proceed in steps of 0.25 mT at intervals of 1.1 s for an effective field sweep rate of 0.23 mT/s.

Our field scans can be grouped into two main regimes: low magnetic field ($<$ 80 mT) and high magnetic field ($>$ 100 mT). These designations may seem absurd, as condensed matter experiments routinely involve fields on the order of Tesla, but there are very practical reasons for this distinction. At low fields, especially -40 to $+40$ mT where we carry out many experiments, the expected Overhauser field buildup (on the order of mT) is an appreciable percentage of the external field. Thus, the peak shifts and warping will be far more pronounced and easier to distinguish from the otherwise “normal” behavior. It is also worth noting that the shape of Kerr rotation in the RSA regime changes at higher external fields, somewhat obscuring the warping effects. Ideally, we would measure the Overhauser field in every experiment via Snapshot TRKR (though practically this would take many, many hours of experiment). In order to get an accurate fit for the effective magnetic field, we must collect enough data such that our effective delay scan constitutes at least a single oscillation within our delay range. As we use progressively smaller external fields, the delay range must increase to compensate. The repetition period of our laser is fixed at 13.16 ns, limiting us to a delay range of at most 13.16 ns for fitting the effective delay scans. This corresponds to an external field of roughly 30 mT. However, we are further limited by our experimental setup, which is not optimized for this purpose. Our current construction spans 7 ns of pump-probe delay, which revises our minimum external field to approximately 60 mT. There is merit, then, in measuring the Overhauser field at external fields large enough that fitting an entire oscillation is not a concern. We have adopted the range convention of 120 to 180 mT. Thus, low-field data is used to show peak warping effects while high-field data allows us to monitor the time evolution of the Overhauser field directly.

This section of the chapter is primarily intended to serve as confirmation of the OSE model. However, we also intend it as a demonstration of the effects that DNP can have on spin polarization measurements under a range of commonly adjusted experimental parameters. The genesis of this project was an unexpected peak warping that appeared when we were not looking for it. Thus, we hope that this data can be used as a comparison to unexpected effects observed in future experimental runs.

6.3.1 Wavelength Dependence

Perhaps the most obvious experimental knob to twist is the wavelength knob. Wavelength is a proxy for detuning in the plots we considered previously and in the data we consider now. To isolate the dependence of the measured spin polarization on detuning alone, we would ideally carry out a two-color pump-probe experiment in which the probe wavelength would remain fixed. Unfortunately, our setup is only configured for degenerate pump-probe measurements. As discussed in Chapter 3, for a given spin polarization, the amplitude and sign of the measured Kerr rotation will depend on the wavelength of the probe. We acknowledge

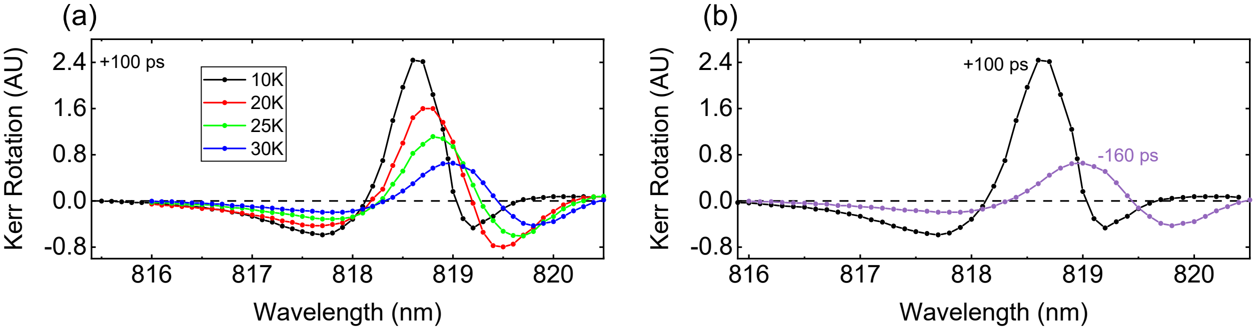

Figure 6.13: Kerr spectrum measured for 033XT-A5. Kerr rotation measured as a function of pump and probe wavelength in the absence of an external field, presented for (a) temperatures from 10 K to 30 K and (b) two pump-probe delays at 10 K. In contrast to the expected Faraday spectrum for bulk GaAs, this Kerr spectrum features three lobes. The spectrum redshifts with increasing temperature. It also shifts with pump-probe delay.

that when we compare our simulated spin polarization to our measured Kerr rotation, the amplitudes will not follow the same trend with detuning. The simulations, which actually present S_z, will only account for generation, not detection. The experimentally measured Kerr spectrum, which accounts for both generation and detection, is shown in Fig. 6.13.

To obtain the Kerr spectrum, we set our pump and probe wavelength and recorded both $A-B$ and $A+B$ from the lock-in amplifiers, plotting the ratio. The external field was turned off to avoid any DNP effects. Normalizing by $A+B$ reduces the impact of laser wavelength drift on the data, but measuring single points can in general be more prone to experimental fluctuations. When we completed the wavelength-dependent measurements, we plotted the amplitude of the field scan zero-peak and found the same Kerr spectrum shape. This gives us confidence in this data.

In Fig. 6.13a, we measure the Kerr spectrum at +100 ps for a series of temperatures. As we would expect, the spectrum redshifts with increasing temperature, and the maximum Kerr rotation decreases. Because our measurements will primarily focus on pump-probe delay -160 ps, we plot a spectrum taken at this delay for 10 K in Fig. 6.13b. We expect to see a difference in magnitude between the two delays, but the shift in the features is not expected. We will return to this in the next section. Despite the differences, the general shape of the Kerr spectrum is unchanged with delay.

In contrast to the Faraday or Kerr spectrum expected for bulk GaAs, the Kerr spectrum at the D^0X resonance has three lobes. The middle lobe, centered on the D^0X resonance, is of opposite sign compared to the lobes on either side. The overall sign is arbitrary due to lock-in demodulation, but the relative sign between lobes is a real effect. Note also that the lower-energy lobe is of smaller amplitude than the higher-energy lobe at 10 K and larger for other temperatures. This Kerr spectrum is neither odd nor even in wavelength. While we have not found a clear explanation for this shape in the literature, we expect, when considering the sum total of our data, that this shape results from measuring multiple subensembles of electrons [16]. In the future, we hope to replicate this spectrum in the same way that we plotted the Faraday spectrum for bulk GaAs in Chapter 3.

With that caveat in mind, we are interested in how Kerr rotation varies with the detuning of our pump and probe. We present in Fig. 6.14 both delay and field scans measured at nine wavelengths across nearly 2 nm. This covers the majority of the Kerr spectrum for non-negligible Kerr rotation. Each row of Fig. 6.14 features three plots. The left-most plot is a delay scan for delays from −2000 to +5000 ps in steps of 100 ps. The center plot is a field upsweep from +120 to +180 mT, the high-field range. The right-most plot is a −40 to +40 mT *zero-crossing*. This term designates a field scan in which we sweep from one field value through zero field to the field value with the opposite sign. In most cases, we immediately turn back, without resetting the field, scanning back down to the initial field value. Hence, these field scans cross zero. This type of scan was devised early in our studies to demonstrate the direction-dependence seen in Fig. 6.1. We acknowledge that the downsweep is not quite symmetric to the upsweep as the field history is different. However, we do not notice a qualitative difference when comparing a zero-crossing downsweep to a downsweep taken by

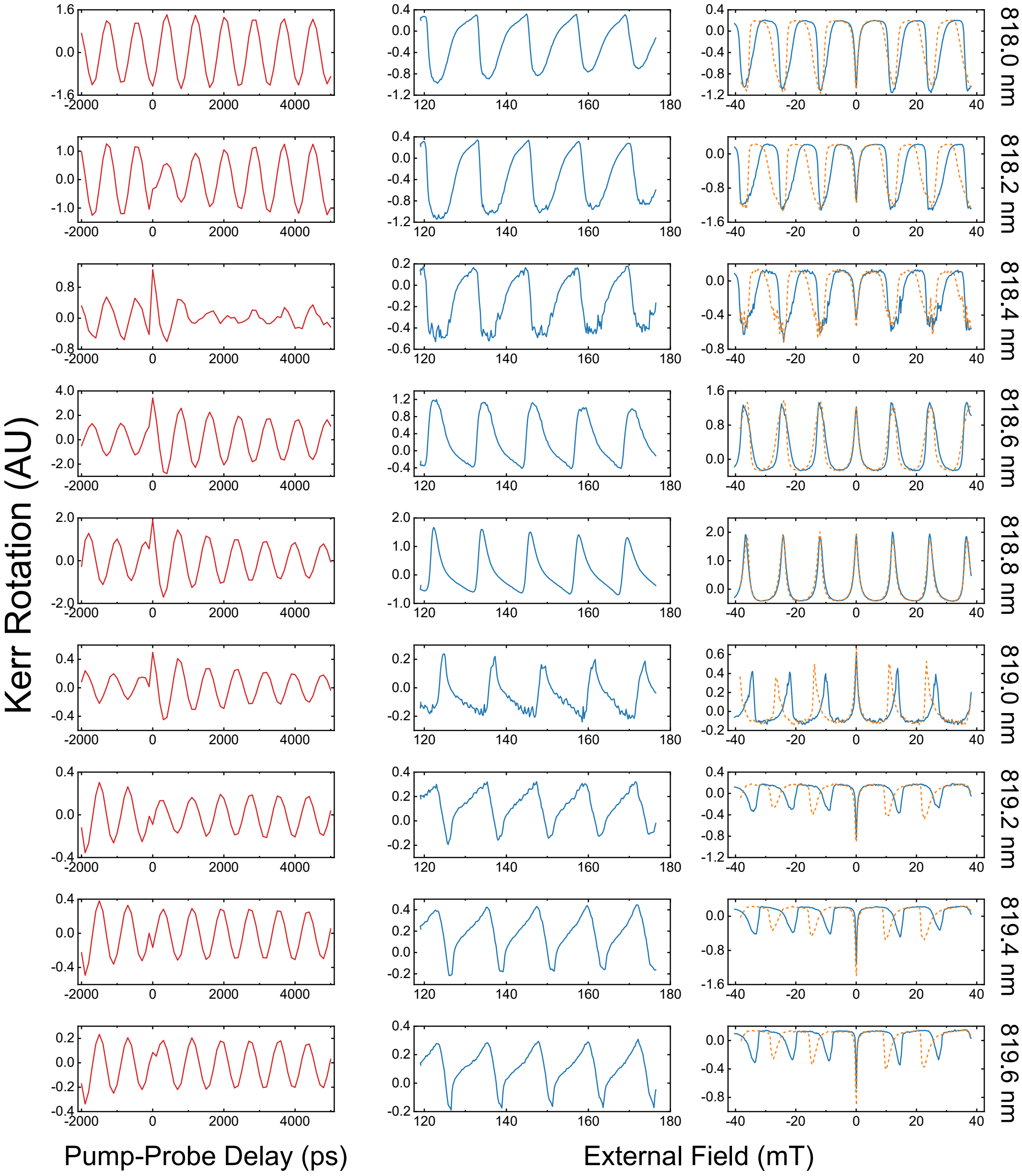

Figure 6.14: Delay scans, field scans, and zero-crossings for a series of laser wavelengths. Kerr rotation measured both as a function of pump-probe delay (for a fixed external magnetic field of 200 mT, left) and as a function of external magnetic field (for a fixed pump-probe delay of 13 ns, center and right). Wavelength is listed along the right column of the figure. The sign of the Kerr rotation has not been modified, showing the difference in sign due to optical detection. (Left) Pump-probe delay is incremented from −2000 to +5000 ps in steps of 100 ps. (Center) The field is swept from +120 to +180 mT. (Right) The field is swept from −40 to +40 mT (upsweep, solid blue line) and from +40 to −40 mT (downsweep, dashed orange line). The peak shifting and warping observed in Fig. 6.1 is observed in the field scans here as well. A portion of the zero-crossing data was originally published in Ref. [11].

itself. The field upsweep (-40 to $+40$ mT) is plotted with a solid blue line, while the field downsweep (-40 to $+40$ mT) is plotted with a dashed orange line.

We first consider the zero-crossings, as those clearly show the field-sweep- direction-dependence. Hearkening back to Fig. 6.6, we know that the OSE rotation angle Φ is odd in detuning about the resonance wavelength 818.8 nm. At this wavelength, we do not expect the OSE to rotate spin polarization, so we do not expect to see any effects due to DNP, such as peak warping or shifting. Indeed, the data taken at 818.8 nm resembles the expected field scan for RSA in the absence of DNP, and there is no noticeable field-sweep-direction-dependence.

As detuning crosses through zero, the sign of the OSE rotation angle reverses, so we expect that the DNP effects also reverse. This is indeed the case, seen when comparing data taken at other wavelengths to the resonant case. For negative detuning (wavelengths longer than 818.8 nm), such as was presented at the beginning of the chapter, the RSA peaks warp with a prolonged rising edge and a sharp falling edge. This gives a sawtooth-like shape. Positive detuning (wavelengths shorter than 818.8 nm) shows the opposite: the rising edge of peaks is shortened, while the falling edge is prolonged. There is a deeper insight here that we will examine in the next chapter.

Independent of the sign of the detuning, peaks shift in the direction of the field sweep. Upsweeps push peaks to more positive magnetic fields while downsweeps push peaks to more negative fields. Even though the character of the peak warping is tied to detuning, the peak shifts are tied to direction-dependence, and thus history.

Our general characterization of peak shape holds true for the high-field sweeps in the center plots. At 818.8 nm, the peaks resemble what we would expect for RSA in this field regime, which are not quite the Lorentzian-like shapes we observe at low fields. For nonzero detuning, the peaks are most deformed near the peak maxima (the phase synchronization condition, or PSC). The peak shifts are more difficult to discern in this range, given that the Overhauser field contributes about 5 mT, a small percentage of the total field. Thus, we elected to simulate the zero-crossings for comparison with our model.

Before we present those simulations, we must address the time-resolved Kerr rotation in the left-most plots. For nonzero detuning, we expect DNP to be accumulating, altering the Larmor precession frequency of the electron spin polarization as the scan progresses. We can see a difference in frequency simply by counting the number of oscillations at each wavelength. For example, the number of oscillations at negative delays increases with wavelength (from positive to negative detuning). Both positive and negative detuning show a very long spin lifetime, consistent with the sharp RSA peaks observed in field scans. However, the lifetime observed at resonance appears to be quite shorter, despite no evidence for this from the field scans. Furthermore, the TRKR for 818.4 nm stands out. While it looks like our laser may have lost mode-lock for this particular data run, this is a repeatable measurement. We seem to have a delay-dependent envelope on our decaying sinusoid. More specifically, the shape resembles a beating effect, implying the presence of more than one decaying spin polarization in our material. For this reason, we believe we are measuring two spin species simultaneously. This beating is also observed for 818.2 nm and 819.2 nm. In general, it appears near the zeroes of the Kerr spectrum. We elaborate briefly on this *two-species behavior* in the next section of this chapter.

To test the correspondence of our data to the model presented earlier in this chapter, we present a subset of our zero-crossings alongside model simulations in Fig. 6.15. To determine the appropriate electron spin lifetime T_2^* for the simulations, we compare our data at the resonance wavelength to the model output. The best correspondence occurs for $T_2^* = 30$ ns. We assume that the spin lifetime is essentially independent of pump wavelength and model the rest of the wavelengths with this value.

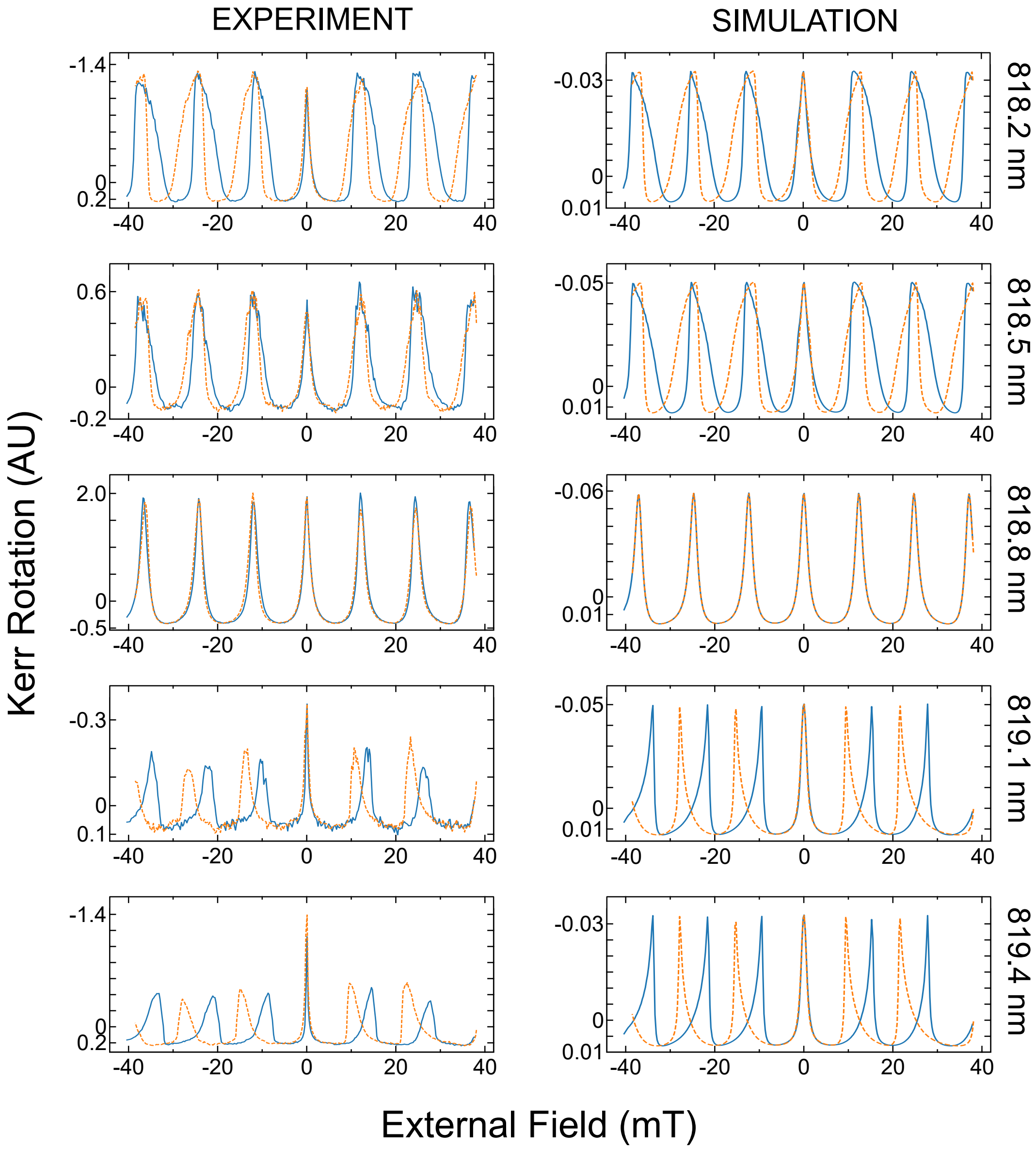

Figure 6.15: Comparison of measured and simulated zero-crossings for a selection of laser wavelengths. (Left) Measured Kerr rotation as a function of external magnetic field for a fixed pump-probe delay of 13 ns. Wavelength is listed along the right column of the figure. The field is swept from −40 to +40 mT (upsweep, solid blue line) and from +40 to −40 mT (downsweep, dashed orange line). (Right) Simulated spin polarization S_z as a function of external magnetic field for a fixed pump-probe delay of 13 ns, corresponding to the experimental data. Kerr rotation is directly proportional to S_z, so the experiments and simulations can be qualitatively compared. Because the sign of S_z does not change with wavelength, the axes of each data plot have been arranged such that the RSA peaks point upwards. Simulations assume $T_{1e} = 180$ s, $T_{1n} = 20$ s, spin lifetime $T_2^* = 30$ ns, pulse duration $\tau_p = 1$ ps, and pulse area $\theta = \pi/4$. Simulation provided by Michael Dominguez. Figure adapted from panels originally prepared with Michael Dominguez and published in Ref. [11].

With respect to peak warping and shifting, we observe good correspondence between our experimental data and the simulations. The degree of warping is more pronounced in our data, but the differences between positive and negative detuning are faithfully reproduced.

One curious detuning effect that is not reflected in our simulations is the difference in amplitude between the center peak near $B_{\text{ext}} = 0$ (the *zero-peak*) and the other peaks. At resonance, the zero-peak has the same amplitude as the others. This is not true in the case of spin-orbit fields, which can suppress the zero-peak, or for anisotropic spin dephasing, which can lead to a significantly enhanced zero-peak [52]. We do not expect either effect here. We observe a smaller zero-peak for positive detunings and a significantly larger zero-peak for negative detunings. Of course, it may be more proper to talk about the zero-peak maintaining a constant amplitude and the subsequent peaks either growing or shrinking, especially since the zero-peak occurs in the field range where the nuclear polarization is damped and DNP effects with it.

As a result of this dipole-dipole coupling, the zero-peak is not shifted away from $B_{\text{ext}} = 0$. However, the DNP is still sufficient to alter its width. We observe a noticeable narrowing of the zero-peaks when compared to resonance, particularly for negative detunings. This is not borne out in the simulation.

6.3.2 Aside: Two-Species Behavior

As an aside, we consider the strange two-species behavior observed for certain wavelengths. The two species we refer to would be two types of spin carrier with properties that result in different measured Kerr rotation as a function of pump-probe delay. While the species could in theory be anything from electrons to holes to excitons, we will assume here that we are dealing only with electron spin carriers. The beating effect manifests for wavelengths near the zeroes of the Kerr spectrum, where the measured Kerr rotation is relatively

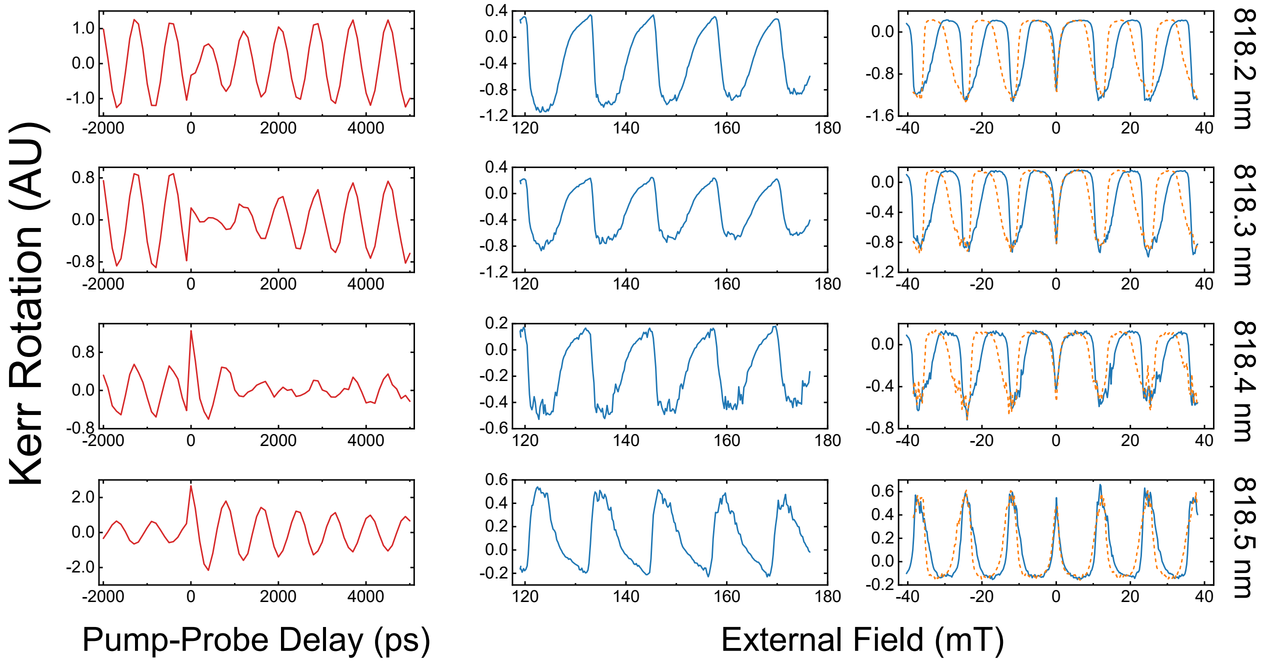

Figure 6.16: Delay scans, field scans, and zero-crossings for a series of laser wavelengths chosen to emphasize the observed two-species behavior near 818.4 nm. Kerr rotation measured both as a function of pump-probe delay (for a fixed external magnetic field of 200 mT, left) and as a function of external magnetic field (for a fixed pump-probe delay of 13 ns, center and right). Wavelength is listed along the right column of the figure. The sign of the Kerr rotation has not been modified, showing the difference in sign due to optical detection. (Left) Pump-probe delay is incremented from −2000 to +5000 ps in steps of 100 ps. (Center) The field is swept from +120 to +180 mT. (Right) The field is swept from −40 to +40 mT (upsweep, solid blue line) and from +40 to −40 mT (downsweep, dashed orange line). A portion of the zero-crossing data was originally published in Ref. [11].

small in magnitude. We zoom in on the positive-detuned and negative-detuned wavelengths in Figs. 6.16 and 6.17, respectively.

Measuring in steps of 0.1 nm rather than 0.2 nm, we uncover behavior at 819.1 nm similar to that at 818.4 nm. For positive detuning, we see a less severe beating at 818.2 and 818.3 nm. The delay scan shows no sign of beating at 818.5 nm. Similarly for negative detuning, we see minor beating effects near zero pump-probe delay for 819.2 nm and 819.3 nm, but the delay scan at 819.0 nm shows no such effect. To summarize, the wavelengths closest to resonance show no beating effects, while the beating continues to show up in a less severe form for wavelengths further from resonance.

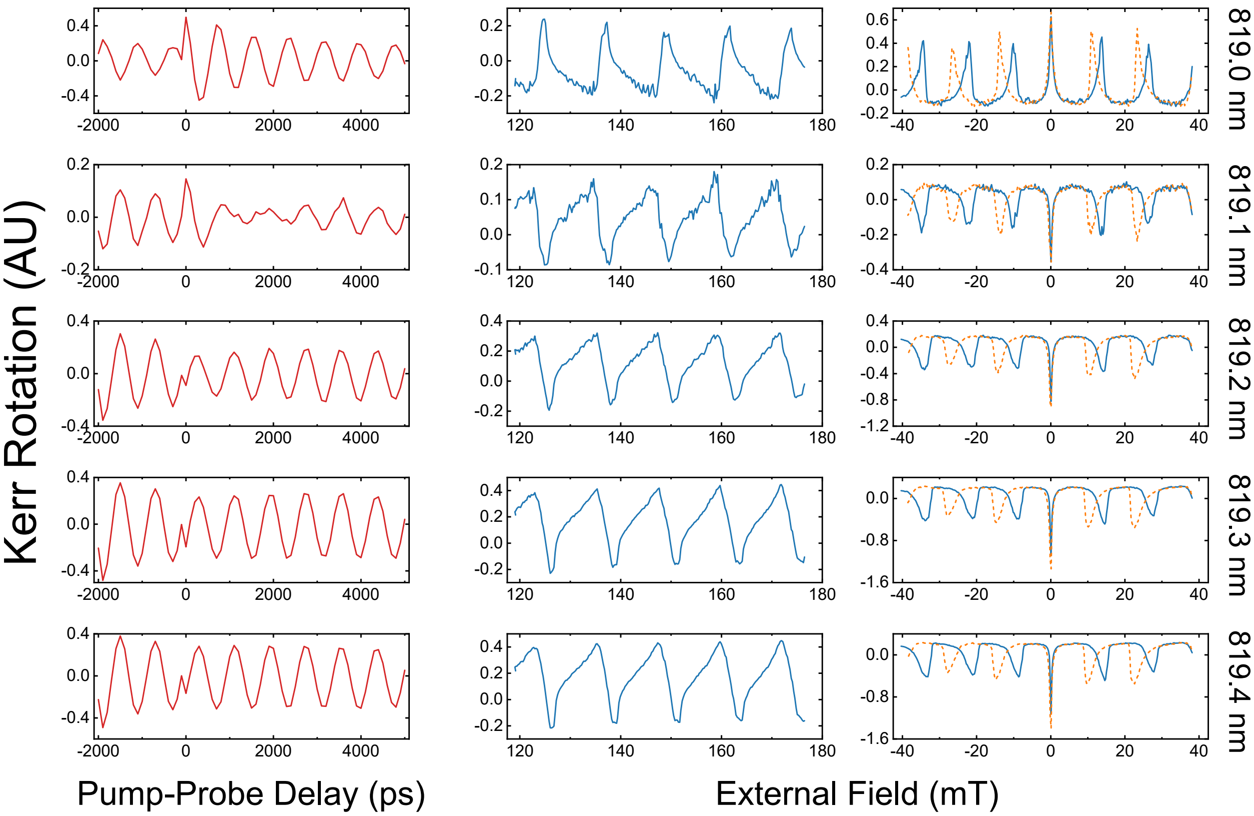

Figure 6.17: Delay scans, field scans, and zero-crossings for a series of laser wavelengths chosen to emphasize the observed two-species behavior near 819.1 nm. Kerr rotation measured both as a function of pump-probe delay (for a fixed external magnetic field of 200 mT, left) and as a function of external magnetic field (for a fixed pump-probe delay of 13 ns, center and right). Wavelength is listed along the right column of the figure. The sign of the Kerr rotation has not been modified, showing the difference in sign due to optical detection. (Left) Pump-probe delay is incremented from −2000 to +5000 ps in steps of 100 ps. (Center) The field is swept from +120 to +180 mT. (Right) The field is swept from −40 to +40 mT (upsweep, solid blue line) and from +40 to −40 mT (downsweep, dashed orange line). A portion of the zero-crossing data was originally published in Ref. [11].

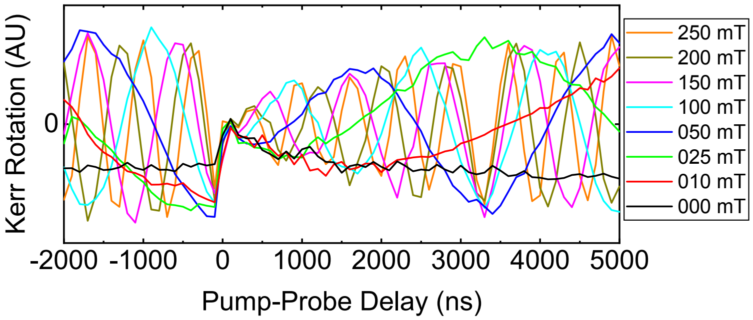

Figure 6.18: Delay scans for a variety of external magnetic fields chosen to show the two-species behavior. Kerr rotation measured as a function of pump-probe delay at laser wavelength 818.4 nm. The pump-probe delay is incremented from −2000 to +5000 ps in steps of 100 ps. The external field is reset before each delay scan to eliminate any DNP accumulated before the scan. The same delay-dependent envelope is present for each considered magnetic field.

Beating can result from the addition of two sinusoids with different precession frequencies. Two precession frequencies could correspond to either two effective magnetic fields (perhaps resulting from DNP effects) or two g factors. A time-varying envelope can also result from two sinusoids that decay at different rates. To identify which, if either, of these two descriptions fit our two-species behavior, we chose the wavelength 818.4 nm and carried out delay scans at various external magnetic fields. These scans are superimposed on one plot in Fig. 6.18.

The most striking conclusion of this plot is the magnetic-field-independence of the Kerr rotation envelope. If this were a DNP effect, we would expect to see some difference in where the beat occurs (in pump-probe delay), as the external fields were specifically chosen to not be multiples of the RSA period. That is not to say that DNP is not altering the precession frequency as the scan progresses, but it does imply that the beating effect is distinct. Further, if we had two spin species with separate g factors experiencing the same external field, we would certainly see a divergence in beating.

This beating effect can instead be described with two sinusoids of the same precession frequency but different lifetime. Specifically, these sinusoids must have opposite sign, and one must have a much shorter lifetime than the other to reproduce our data. That short lifetime would be on the order of nanoseconds.

Recall that the sign of Kerr rotation depends on both the sign of the generated spin polarization and the wavelength of the probe. We could conceivably excite two sets of spin carriers that have the same actual spin polarization but result in Kerr rotation of opposite sign. Alternatively, the wavelength-dependence of spin polarization generation may differ for the two species. Because the beating is only apparent near the zeroes of the Kerr spectrum, it may be that one of the species has a much smaller spin polarization or Kerr rotation amplitude across the entire spectrum. That is, the beating may not manifest for most wavelengths because the main species we measure dwarfs the second at all but a small range of wavelengths.

As for generating sets of carriers with different spin lifetimes, consider the spin lifetime observed on either side of the beating wavelengths. Near resonance, we observe shorter lifetimes than near the positive- and negative-detuned lobes of the Kerr spectrum. It is plausible, then, that we have the combination of the signals on either side of the Kerr spectrum zeroes.

We look to the literature for insight, in particular to the DNP studies out of Dortmund. Fokina *et al.* studied DNP in low-temperature InGaAs/GaAs quantum wells [16]. In their material, they can separately resolve trion and exciton peaks. They measured slightly different Faraday spectra for positive and negative pump-probe delays and concluded the presence of two subensembles of electrons. We observed similarly for our Kerr spectrum, in Fig. 6.13b. They attributed the negative-delay contributions to more strongly-localized electrons which have a longer spin lifetime. Less-localized electrons have shorter lifetime and contribute more at positive delays. The shorter lifetime is posited to result from exciton-electron scattering. These observations followed from a study in CdTe/(Cd,Mg)Te quantum wells [82], in which the longer lifetime is twice as long as the shorter lifetime.

Furthermore, at the exciton resonance, the authors of Ref. [16] were unable to fit field-resolved Faraday rotation with a single RSA equation. Instead, they added contributions from both the exciton and trion to replicate the observed data. This implies that both mechanisms of generating spin polarization are present at the exciton resonance. With this being the case in a system where the resonances are resolved, we operate in our system with the understanding that our Kerr rotation may also feature contributions from both donor-bound and free excitons. It may even be reasonable to expect two-species behavior, given these past studies.

However, we must be careful in interpreting this prior work. The authors of Ref. [16] observed beating in their measurements due to a spread of g factors in their quantum wells. Ref. [15] prescribes a distribution of g factors in an ensemble of quantum dots due both to inhomogeneities in the dots and the effect of DNP. Despite this, we do not expect to observe a distribution of g factors in our bulk GaAs, though we briefly consider this possibility in the next chapter.

As one final comment on previously observed behavior that might inform our understanding of two-species behavior, Ref. [98] studied nuclear spin relaxation in a GaAs spin valve. They observed "satellite peaks" in Hanle probe measurements that suggest the existence of two electron or nuclear species or regions of interaction, though they do not offer an explanation. This is yet another precedent for two-species behavior in our experiments.

We must be clear here that the presence of a short-lived second spin species will not appreciably impact the measurements in this chapter. Our individual field scans are always taken at -160, or $+13000$, ps, by which point any contribution from the second species should be negligible. Snapshot TRKR measurements also focus on long pump-probe delays near the repetition period T_R. Delay scans are only used in this chapter for wavelength dependence and will not factor into our discussion again. In the next chapter, we do show delay scans for a qualitative comparison, but the two-species behavior does not compromise this observation.

Our study of two-species behavior remains incomplete. After all, our delay scans only cover 7 ns. That is just over half of the pulse repetition period of 13.16 ns. Beating could conceivably occur for all wavelengths under consideration but fall outside of our observable range for most. For example, at the resonance wavelength 818.8 nm, we see a larger magnitude of Kerr rotation at negative delays than for the end of the scan at +5000 ps. The lifetime we expect from the delay scan seems shorter than what we would expect to produce the RSA observed in our field scans, so it is plausible that the reduced amplitude near the end of the scan could be due in part to the beginning of beating behavior that largely occurs outside of our range. As a counterpoint, DNP may be altering the Larmor precession frequency of the system, changing slightly the amplitude of Kerr rotation (even though we should be at resonance). Thus, it is difficult to disentangle DNP effects from the two-species behavior. A more thorough investigation would involve shifting our 7 ns range in increments to eventually cover an entire T_R of pump-probe delay.

6.3.3 Power Dependence

Pump power is the closest experimental knob we have to pump area. Generally, as pump power increases, so does the OSE angle Φ. We expect greater DNP effects with increasing power. However, this monotonic increase is only true for relatively small pump areas. Past a certain point, determined by detuning, the OSE angle changes discontinuously. Further, the rotation amplitude Q oscillates with pump area as well, complicating matters. While a full treatment of pump area dependence is outside the scope of this dissertation, the authors of Ref. [15] considered both Φ and Q as functions of a large range of detuning for a select number of pump areas. Experimentally, the authors of [76] demonstrated that DNP effects do not monotonically increase with pump power. In fact, they found that increasing the power

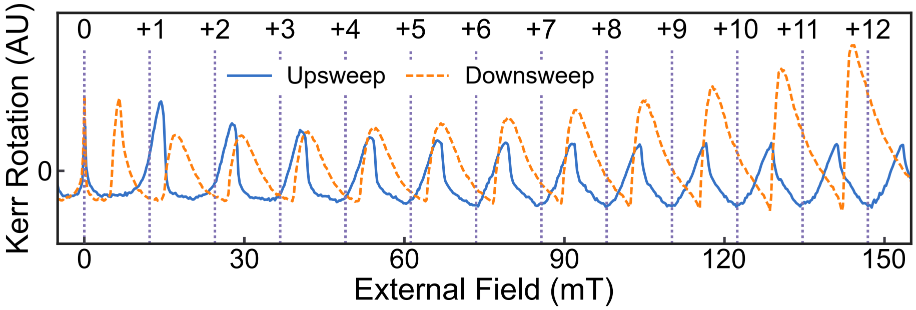

Figure 6.19: Positive-field upsweep and downsweep establishing peak indexing. Kerr rotation measured as a function of external magnetic field for a fixed pump-probe delay of 13 ns at laser wavelength 819.5 nm. The field is swept from −160 to +160 mT (upsweep, solid blue line) and from +160 to −160 mT (downsweep, dashed orange line), but only 0 to +160 mT is shown. Peak numbers are indexed to the zero-peak (0). The dotted purple lines are spaced apart by the RSA period 12.2 mT, corresponding to the expected RSA peak positions in the absence of DNP. The peak indexing used here appears throughout the remainder of this chapter. Figure adapted from panel originally prepared by Dr. Michael Macmahon and published in Ref. [10].

of their pump laser effected a change from positive-detuning behavior to negative-detuning behavior.

A study of pump-area-dependence would benefit from the ability to shape the pulse, though changing the pulse duration would also impact the detuning. By increasing pump power, we introduce the risk of heating our sample, compromising our measured Kerr rotation. Despite these shortcomings, we present pump-power-dependent Kerr rotation as a guide for future experiments.

The positive-external-field portion of a zero-crossing spanning −160 to +160 mT is shown for pump wavelength 819.5 nm (negative detuning) in Fig. 6.19. We establish here a system for peak numbering, indexed to the zero-peak. For example, peak +1 is the first RSA peak at positive external field. Put another way, peak +1 corresponds to the peak prescribed by Eq. 2.9 with $k = +1$. However, peak +1 is not centered at this field. For reference, the dotted purple lines mark the expected RSA peak positions in the absence of DNP, for k from 0 to +12. The difference between upsweep and downsweep is apparent. As the field sweep progresses, the peaks shift further from their expected positions and increasingly warp.

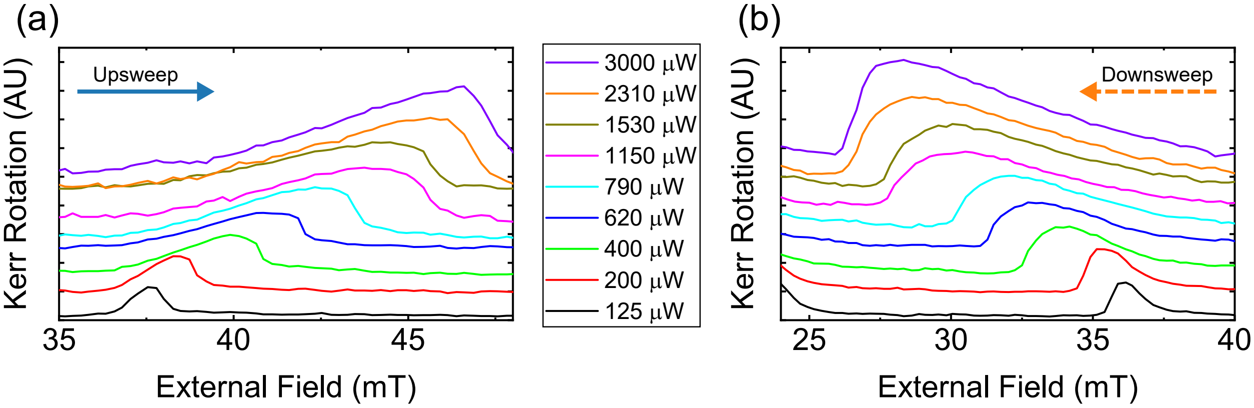

Figure 6.20: Pump-power-dependent upsweep and downsweep centering on peak +3. Kerr rotation measured as a function of external magnetic field for a fixed pump-probe delay of 13 ns at laser wavelength 819.5 nm, for several pump powers. The field range shown corresponds to peak +3 in Fig. 6.19. Field sweeps at different pump powers are offset vertically for clarity. As pump power increases, the peak increasingly deforms and shifts in the direction of the sweep. Both (a) upsweep and (b) downsweep are shown. A portion of this data was originally published in Ref. [10].

First, we examine the effect of pump power on the peak warping of an individual peak, peak +3, in Fig. 6.20. The upsweeps and downsweeps are displayed in separate panels, and data taken at subsequent powers is offset vertically for clarity. For both upsweep (Fig. 6.20a) and downsweep (Fig. 6.20b), we observe that peak warping becomes more pronounced with increasing pump power. Peak +3 shifts further in the direction of the sweep with pump power as well. This is consistent with the idea that increasing pump power leads to increased OSE angle and thus increased DNP effects.

Next, we consider the effect of pump power on peak shifts. In Ref. [10], we calculated the difference between actual and expected peak position for the sweeps in Fig. 6.19 and plotted this peak shift, shown in Fig. 6.21a. As is visually apparent, the peak shift increases as the scan progresses (increasing peak index for the upsweep and decreasing for the downsweep). This zero-crossing was carried out again for a much lower pump power of 125 μW, with the calculated peak shifts shown in Fig. 6.21b. At lower power, the peak shifts are much smaller, though they are by no means absent.

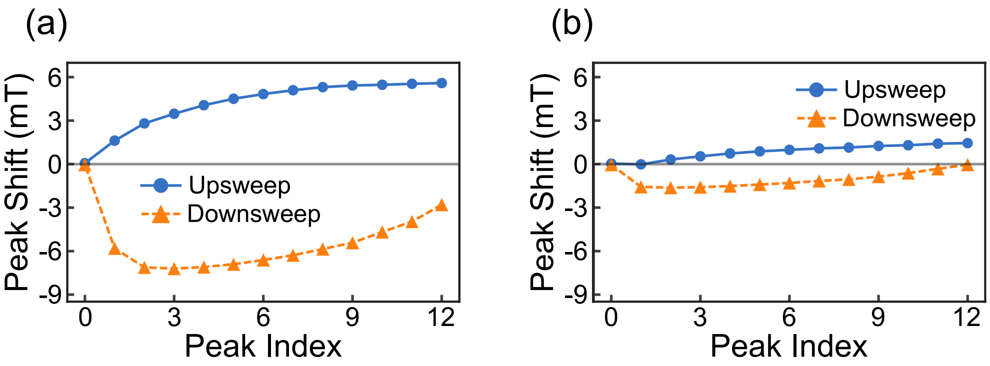

Figure 6.21: Peak shift as a function of peak index, compared for two pump powers. The sweeps from Fig. 6.19, with pump power (a) 630 μW, are compared with sweeps measured at the lower pump power (b) 125 μW. Peak shift serves as a proxy for the accumulated Overhauser field B_{N} and increases as the sweep progresses. The shifts are more significant for the higher pump power. Peak shifts calculated by Dr. Michael Macmahon. Figure adapted from panels originally prepared by Dr. Michael Macmahon and published in Ref. [10].

Finally, we show data indicative of the non-monotonic dependence of DNP on power, measured at higher pump powers than those shown in Fig. 6.20. We present a -40 to $+40$ mT zero-crossing for 819.3 nm (negative detuning) in Fig. 6.22. The upsweeps and downsweeps are displayed in separate panels (a and b, respectively), and data taken at subsequent powers is offset vertically for clarity. Up through 3500 μW, we see increasing peak warping and shifting with increasing pump power. For higher powers, though, we see the peaks "recollect" themselves with a reduction in both warping and shifting. While we do not see a reversal in detuning as reported by Ref. [76], we do see an increase and then decrease in DNP effects. The key takeaway is for those who desire to maximize the effect provided by the OSE: turning the pump power all the way up is not the answer.

Ideally, we would have followed these observations with a direct measurement of the Overhauser field through Snapshot TRKR. We attempted such a measurement at 819.5 nm for 1910 μW and 5100 μW, but we were not able to reliably fit the Overhauser field due to the fitting algorithm consistently over-estimating the nuclear contribution. Given the success of this method in lower-power instances, we must determine if a different range of field values or delays may be more conducive to measuring these larger Overhauser fields.

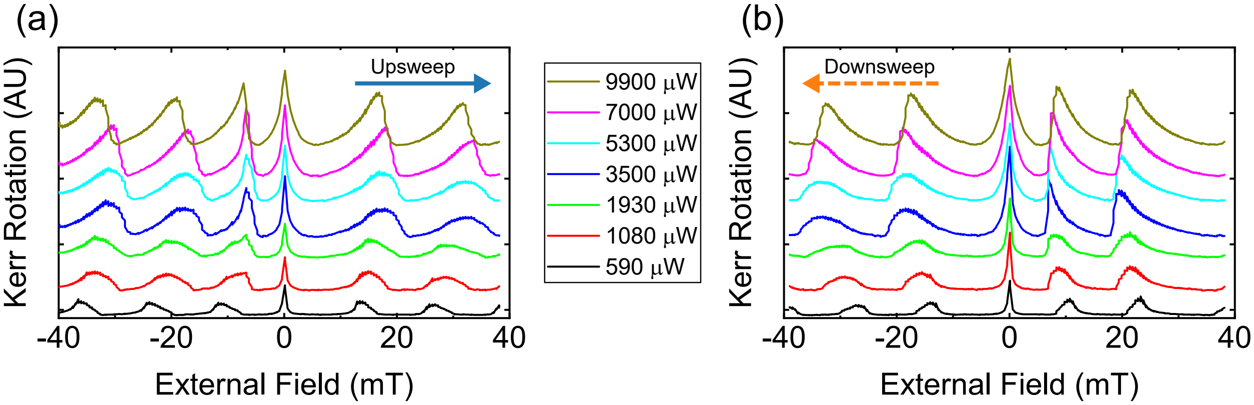

Figure 6.22: Pump-power-dependent zero-crossings. Kerr rotation measured as a function of external magnetic field for a fixed pump-probe delay of 13 ns at laser wavelength 819.3 nm. The field is swept from -40 to $+40$ mT for the (a) upsweeps and from $+40$ to -40 mT for the (b) downsweeps. Field sweeps at different pump powers are offset vertically for clarity. While the peak warping and shifting is present for each pump power used, the effects become more extreme at higher powers. The maximum shifting for both upsweep and downsweep is achieved for 3500 μW.

6.3.4 Time Dependence

We move from dependences inherent to the OSE to a purely nuclear dependence. We are interested in how the buildup of DNP depends on time. By time, we mean laboratory timescales rather than pump-probe delay. There are two aspects to time-dependence that we consider here. First, how does the Overhauser field accumulate over the course of a field sweep? Second, how does this accumulation differ as we change the duration of our field sweep? In both cases, we might expect that increased time for DNP buildup will lead to an increased buildup of DNP. While this might sound like a tautology, there is an important point here: the presence of DNP is not a transient effect encountered because we swept our external field too quickly. Of course, the particular peak warping and direction-dependence does result because we do not sweep our field slowly enough to reach steady-state behavior.

We return to the peak-indexed zero-crossing of Fig. 6.19. We have already considered how the peak shift increases as the field sweep progresses, but we approach it from an alternative

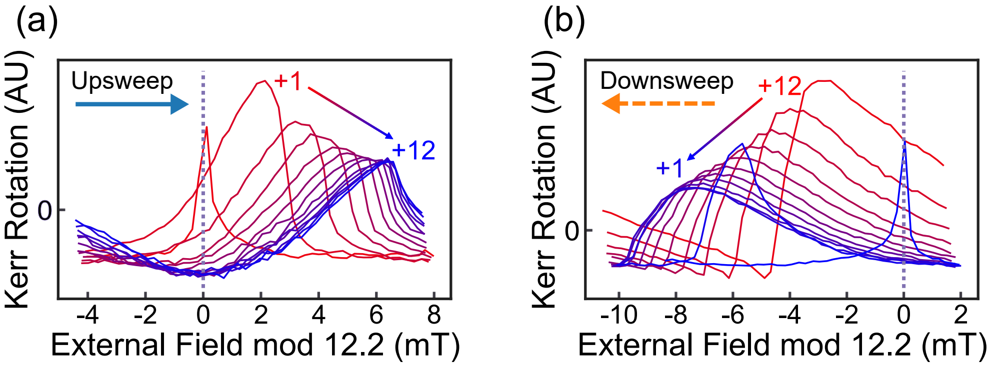

Figure 6.23: Peaks +1 through +12 from Fig. 6.19 superimposed as a function of external magnetic field, modulo the approximate RSA period 12.2 mT. The dotted purple line at 0 mT is provided for reference, as in Fig. 6.19. Peak color progresses from red to blue with the field sweep. Both (a) upsweep (+1 to +12) and (b) downsweep (+12 to +1) are shown. Successive peaks become increasingly warped and shifted. Peak positions calculated by Dr. Michael Macmahon. Figure adapted from panels originally prepared by Dr. Michael Macmahon and published in Ref. [10].

perspective. We superimpose the 12 peaks, plotted relative to the RSA period, in Fig. 6.23. Peak warping and shifting is made more salient in this view, with peak progression here a proxy for time. As the scan – and hence time – progresses, the warping and peak shifting become more and more pronounced. This is true for both upsweep and downsweep, so this effect is not tied to the external field itself.

It is difficult to disentangle time from the other aspects of the sweep in this case, so we turn our attention to a set of experiments that repeats the same field sweeps but with field steps of increasing duration (decreasing sweep rate). By waiting longer before incrementing the external field, we should observe a larger Overhauser field buildup. On one hand, at each external field value, we should observe an Overhauser field closer to the steady-state value. On the other hand, the Overhauser field depends on all of the previous field steps and how long the system was held at each. Thus, the history aspect of time becomes more important as field step time increases.

We present the class of field sweeps known as *rep tests*, named so because a longer duration at each field is achieved by repetition of the field steps with usual timing. For example, the

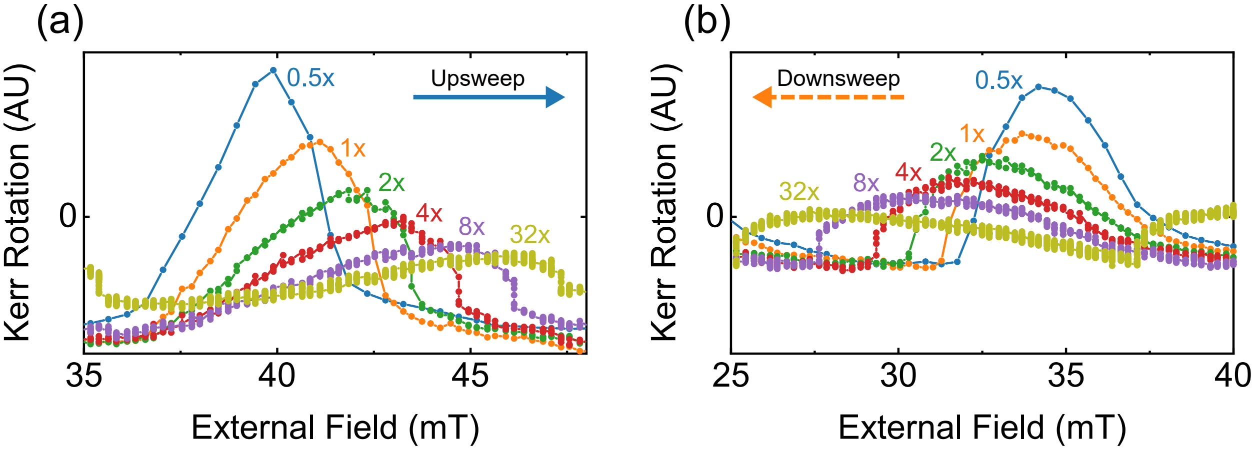

Figure 6.24: Rep tests centering on peak +3. Kerr rotation measured as a function of external magnetic field for a fixed pump-probe delay of 13 ns at laser wavelength 819.5 nm. The field range shown corresponds to peak +3 in Fig. 6.19. The labels indicate the number of measurements taken at each magnetic field step. Here, 1× corresponds to the field step timing and spacing used throughout this chapter. The exception is 0.5×, which utilized the same field step timing as 1× but skipped every other field step. Both (a) upsweep and (b) downsweep are shown. Data originally published in Ref. [10].

2× rep test corresponds to two measurement points taken at each field value, leading to half the effective magnetic field sweep rate. Low-field data corresponding to peak index +3 is shown in Fig. 6.24. Every data point is plotted as a circle to demonstrate the larger number of points taken for longer rep tests. As the number of reps increases, the peaks shift further in the direction of the sweep and warping becomes more pronounced. This implies that the Overhauser field is accumulating more for higher reps. The peak position shifts over 5 mT when comparing 32× to 1×, a significant increase considering the external field is in the range of 40 mT.

Rather than speculate about the magnitude of the Overhauser field, we can directly measure it with Snapshot TRKR. We consider a high-field upsweep for 818.2 nm (positive detuning) on the field range 120 to 180 mT in Fig. 6.25. Though we do not go all the way to 32×, we are able to see that the magnitude of the Overhauser field increases for increasing reps, from about 2 mT for 1× to 4 mT for 4×. The falling edges of the RSA peaks (vertically shifted for clarity) are increasingly prolonged as well. We simulate this experiment with our

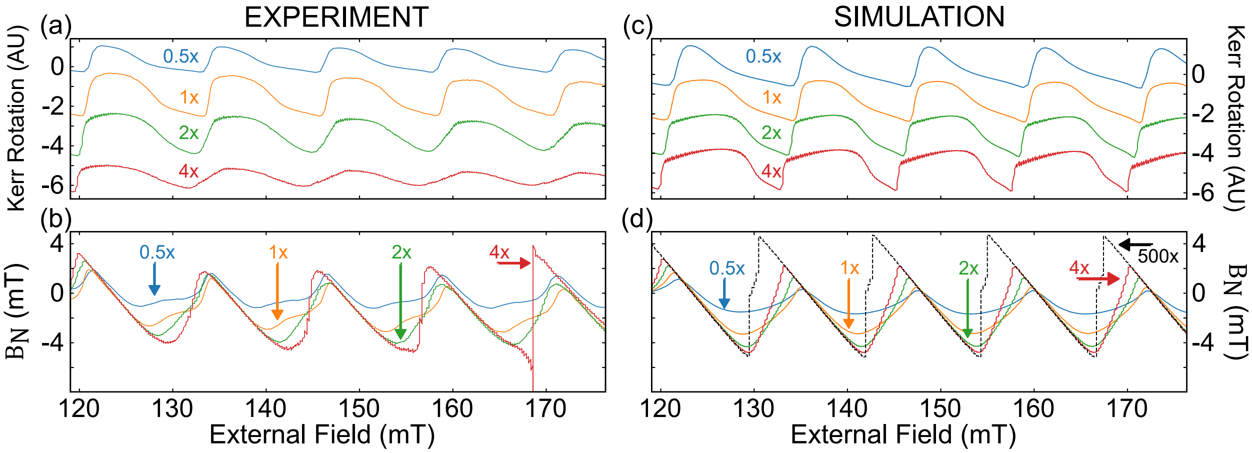

Figure 6.25: Comparison of measured and simulated rep tests. (a) Measured Kerr rotation as a function of external magnetic field for a fixed pump-probe delay of 13 ns at laser wavelength 818.2 nm. Snapshot TRKR was carried out on the external field range 120 to 180 mT, with pump-probe delay incremented from −1920 to +1920 ps in steps of 160 ps, though only the sweep at 13 ns is shown. The labels indicate the number of measurements taken at each magnetic field step. Here, 1× corresponds to the field step timing and spacing used throughout this chapter. The exception is 0.5×, which utilized the same field step timing as 1× but skipped every other field step. Field sweeps corresponding to a different number of reps are offset vertically for clarity. (b) Extracted Overhauser fields for the field sweeps shown in (a). (c) Simulated spin polarization S_z as a function of external magnetic field for a fixed pump-probe delay of 13 ns and positive detuning matching 818.2 nm. The simulations parallel the experiments shown in (a) and are similarly offset for clarity and comparison. (d) Simulated Overhauser fields corresponding to the simulated experiments in (c). The dashed black line represents a 500× rep test, nearly a steady-state measurement. Simulations assume $T_{1e} = 180$ s, $T_{1n} = 20$ s, spin lifetime $T_2^* = 30$ ns, pulse duration $\tau_p = 1$ ps, and pulse area $\theta = \pi/4$. Simulation and Overhauser fits provided by Michael Dominguez. Figure adapted from original prepared with Michael Dominguez and published in Ref. [11].

model, plotting both the spin polarization S_z and the Overhauser field. There is excellent agreement between the measured and simulated Overhauser fields. We also plot the simulated Overhauser field for a 500× rep test, which we expect to be close to the steady-state field. This gives us an idea of where subsequent rep tests will build to, though we currently have no plans to run a 500× rep test in our laboratory.

6.3.5 History Dependence

It could be argued that history dependence is a special case of time-dependence. However, it is more intimately related to the interplay between the nuclear and electron spin systems. Because our experiments take place on timescales shorter than the nuclear relaxation time, the nuclear polarization experienced at a given experimental instance will be due to contributions from electron spin polarizations long past. Those electrons experienced a nuclear field owing to electron spins before them, and so on. Though this history dependence does not appear explicitly in our model, it emerges from our modeling algorithm.

First, though, we present our own take on a famous quote often attributed to philosopher George Santayana: "Those who cannot learn from history are doomed to repeat it." Each of the field sweeps we have shown follow the same pattern of field steps. Whether ascending or descending, the field steps are always ordered. In some sense, they all follow the same kind of history. What might we observe if we followed a different set of field steps that were not ordered, doing away with field history as we know it? Our response to Santayana: "Those who are doomed to repeat history cannot learn."

We carried out a −40 to +40 zero-crossing with a twist: the field steps were randomized. The field step at +26.25 mT no longer needed to follow either +26.0 or +26.5 mT. We recorded Kerr rotation on this new series of field steps and then ordered the results. This data is shown as red circles in Fig. 6.26, with a non-randomized zero-crossing (dashed

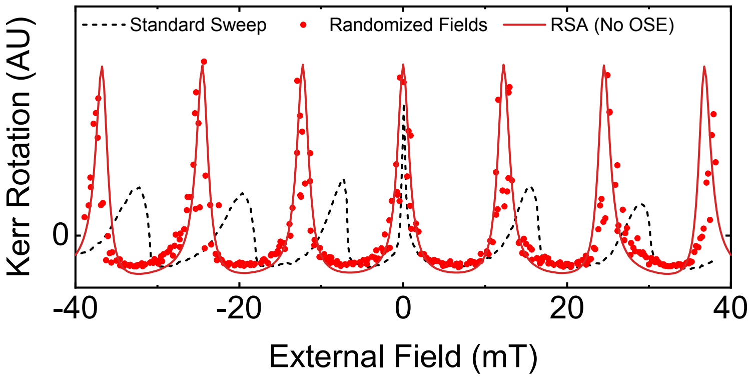

Figure 6.26: Comparison of randomized and ordered field sweep points on the low-field range. Kerr rotation measured as a function of external magnetic field for a fixed pump-probe delay of 13 ns at laser wavelength 819.5 nm. The external field range under consideration is -40 to $+40$ mT. Ordered field points (dashed black line) show peak shifting and warping consistent with the rest of the results in this chapter while the randomized field points (red circles) approach the expected shape for RSA in the absence of DNP (solid red line). The randomization of the field points has served to erase the field history of the system. The RSA model uses $g = -0.444$ and $T_2^* = 30$ ns.

black line) superimposed. We also include, as a guide to the eye, modeled S_z in the RSA regime, in the absence of both the OSE and DNP, using $g = -0.444$ and $T_2^* = 30$ ns (red line). The slight discrepancy in g factor shows better correspondence between the model and data. While the ordered field points yield warped, shifted peaks, the randomized field points instead appear to follow RSA in the absence of DNP. The amplitude of the peaks is significantly larger for the randomized peaks, with the non-zero-peaks matching the height of the zero-peak. This is a remarkable result. On one hand, randomizing the field steps was sufficient to "erase" history. On the other hand, the impact of DNP on Kerr rotation may be significantly reduced simply by taking the field steps out of order.

Previously, we stated that weak external fields can lead to nuclear depolarization. The randomization of field points may be concerning for this reason, as the erasure of field history could simply proceed from weak external fields encountered throughout the course of the scan. We were also concerned that switching the polarity of the external field too quickly could also depolarize the nuclei. As a result, we carried out these randomized field sweeps on other field ranges that do not involve crossing zero field, notably the high-field

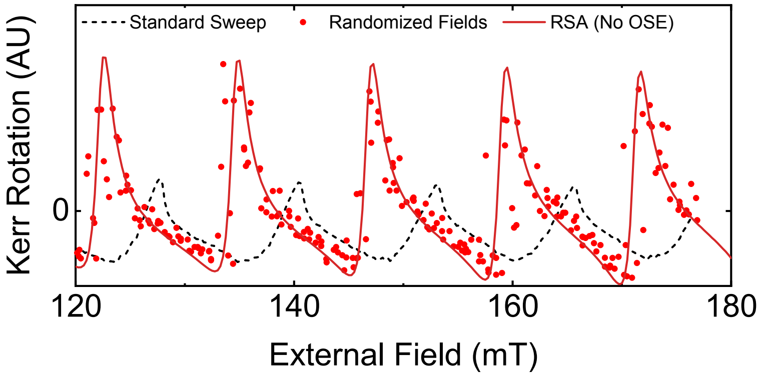

Figure 6.27: Comparison of randomized and ordered field sweep points on the high-field range. Kerr rotation measured as a function of external magnetic field for a fixed pump-probe delay of 13 ns at laser wavelength 819.5 nm. The external field range under consideration is 120 to 180 mT. Ordered field points (dashed black line) show peak shifting and warping consistent with the rest of the results in this chapter while the randomized field points (red circles) approach the expected shape for RSA in the absence of DNP (solid red line). The randomization of the field points has served to erase the field history of the system. The RSA model uses $g = -0.444$ and $T_2^* = 30$ ns.

range used for Snapshot TRKR. This data is shown in Fig. 6.27. In each case, we reach the same conclusion as above.

As a final check, we carried out these same experiments near resonance, where we expect to see minimal DNP. In Fig. 6.28, the randomized points (green circles) match the ordered sweep (dashed black line) fairly well. On the low-field range, these both follow the expected RSA. On the high-field range, this correspondence is not as clear, implying that one of our modeling choices is no longer accurate. Either way, randomization should serve to erase the field history of the system.

At last, we can address the mystery of the external-field-sweep-direction-dependence. We have already seen history- and direction-dependence emerge from the model, so we desire an intuitive reason why this must be. The following argument was formulated by Michael Dominguez for Ref. [11] and has been adapted here.

We return to the nuclear rate equation. This time, however, we will rewrite it not with a

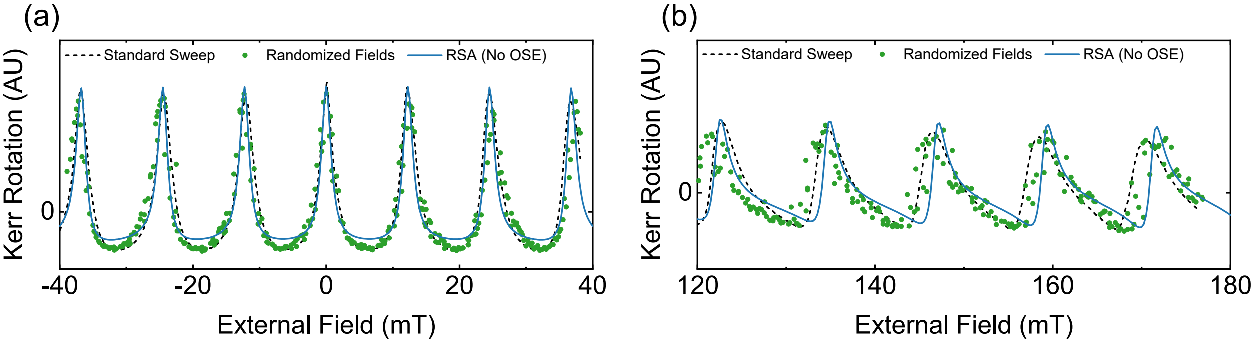

Figure 6.28: Comparison of randomized and ordered field sweep points for the resonance wavelength. Kerr rotation measured as a function of external magnetic field for a fixed pump-probe delay of 13 ns at laser wavelength 819.0 nm. The external field ranges under consideration match the (a) low-field and (b) high-field ranges shown in Fig. 6.26 and Fig. 6.27, respectively. Randomized field points (green circles) show fairly close correspondence to the ordered field points (dashed black line) at this wavelength. On the low-field range, these both match the expected shape for RSA in the absence of DNP (solid blue line). On the high-field range, this is not quite the case. The RSA model uses $g = -0.444$ and $T_2^* = 30$ ns.

focus on I_{av} but on $\langle S_x \rangle$:

$$\begin{aligned}\frac{dI_{\text{av}}}{dt} &= -\frac{1}{T_{1e}}\left(I_{\text{av}} - \frac{4}{3}I\left(I+1\right)\langle S_x \rangle\right) - \frac{I_{\text{av}}}{T_{1n}} \\ \frac{dI_{\text{av}}}{dt} + \left(\frac{1}{T_{1n}} + \frac{1}{T_{1e}}\right) I_{\text{av}} &= \frac{1}{T_{1e}}\frac{4}{3}I\left(I+1\right)\langle S_x \rangle.\end{aligned}$$

At the beginning of each experiment, we reset the external field to start with no DNP. So at time $t = 0$, $I_{\text{av}} = 0$. The rate of change of I_{av} is then directly proportional to $\langle S_x \rangle$. Already we have the opportunity for the sign of $\langle S_x \rangle$ to impact the buildup of DNP, and we will pursue this argument further in the next chapter. For now, we go one step further: if dI_{av}/dt follows $\langle S_x \rangle$, then I_{av} will follow the $\langle S_x \rangle$ integrated up to that point in the field sweep.

This can be shown via a series of simulations. High-field upsweeps and downsweeps on the range 120 to 180 mT are simulated in Fig. 6.29 for three integration times, corresponding to the time between 0.25 mT field steps. In Figs. 6.29a and 6.29b, the integration time is so brief that nuclear polarization cannot accumulate. While there is no Overhauser field (dotted green line), the integrated $\langle S_x \rangle$ (which is here multiplied by the nuclear-coupling

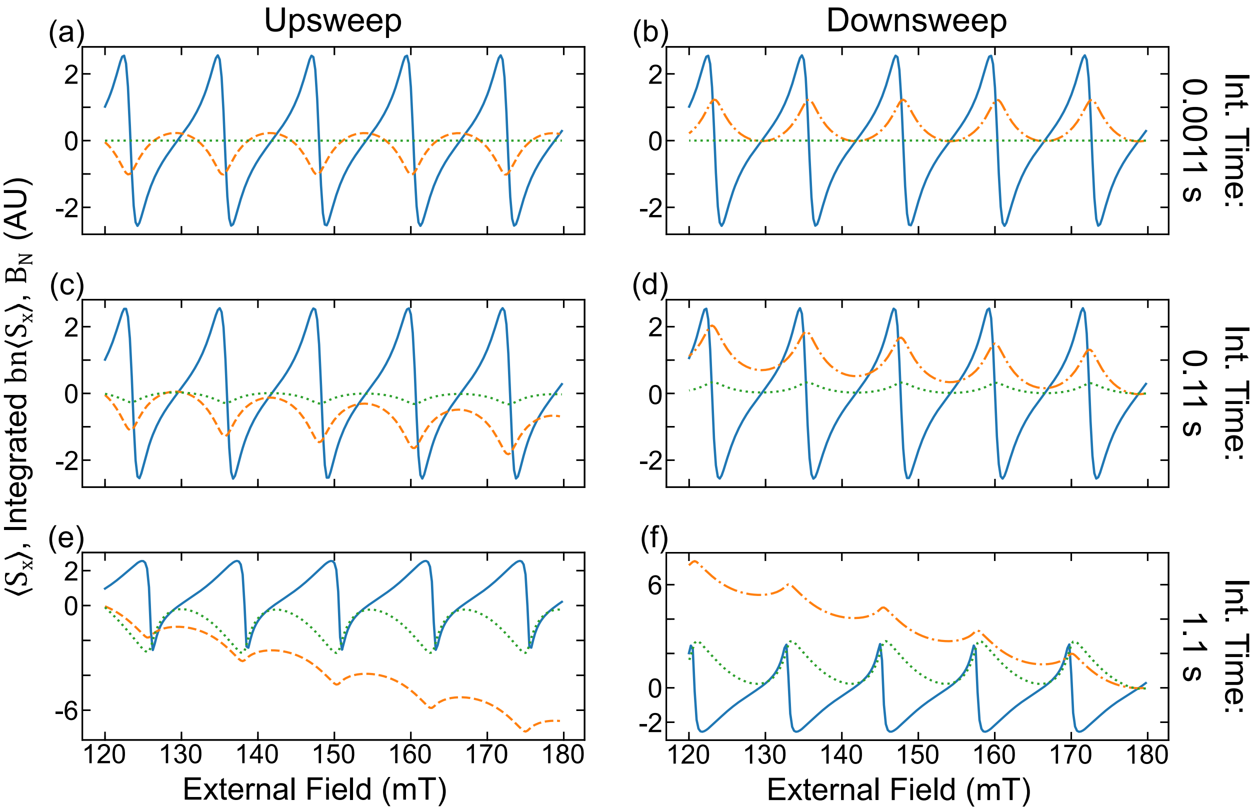

Figure 6.29: Integrated $\langle S_x \rangle$ and its connection to sweep-direction-dependence. Simulated $\langle S_x \rangle$ (solid blue line) as a function of external magnetic field for a fixed pump-probe delay of 13 ns at negative detuning, shown with $\langle S_x \rangle$ integrated over the course of the field sweep up to that point (dashed orange line). The integrated quantity is multiplied by bn and scaled 50× for comparison to the simulated Overhauser field (dotted green line). The left column corresponds to field upsweeps while the right column corresponds to field downsweeps. Integration time, the time between field steps, is listed along the right column. The longer this time interval, the more nuclear polarization can accumulate. This alters the total magnetic field experienced by the electron spin polarization and, by extension, the optical Stark rotation angle. This in turn alters $\langle S_x \rangle$, and thus integrated $\langle S_x \rangle$, in a feedback loop. Field-sweep-direction-dependence emerges from the opposite sign of integrated $\langle S_x \rangle$ for upsweeps and downsweeps. Simulations assume $T_{1e} = 180$ s, $T_{1n} = 20$ s, spin lifetime $T_2^* = 30$ ns, pulse duration $\tau_p = 1$ ps, and pulse area $\theta = \pi/4$. Simulation provided by Michael Dominguez. Figure adapted from panels originally prepared with Michael Dominguez and published in Ref. [11].

constant bn and multiplied by 50 times, dashed orange line) has opposite sign for upsweep and downsweep. This is not a detuning effect nor a DNP effect but solely depends on the field sweep direction. In Figs. 6.29c and 6.29d, the integration time is long enough for nuclear effects to appear. However, the time is still brief enough that $\langle S_x \rangle$ (solid blue line) is not appreciably warped by DNP. In this scenario, the sign of the Overhauser field still depends on the sign of the integrated $\langle S_x \rangle$. Finally, the experimental time steps in Figs. 6.29e and 6.29f match our experiments, confirming the relationship between the sign of the Overhauser field and the integrated $\langle S_x \rangle$.

6.3.6 Challenging the Model

We have presented a physical framework for understanding DNP in GaAs due to the OSE. This model reproduces our observed Kerr rotation (qualitatively) and extracted Overhauser field (quantitatively). In addition to the utility of this model for studies of DNP in GaAs, this chapter should provide sufficient characterization of the expected DNP effects that future researchers can reference it when encountering their own unexpected anomalies in spin polarization measurements.

The picture, while fairly representative of our data, is not yet complete. We have noted that the simulations fail to account for the amplitude variation in the zero-peak or the strong dependence of zero-peak width on detuning. These discrepancies may result from one of our assumptions. For example, we supposed a constant electron spin lifetime, while this quantity may in reality change appreciably with wavelength or magnetic field. However, we have in mind one further modification to the model, in the next chapter, which will be able to reproduce peak amplitude variation, in addition to another physical phenomenon we have not yet encountered in this chapter.

Now that we have a working model for the DNP observed in our GaAs sample, how can we dig deeper? How can we better understand and verify the nuclear timescales in our system? To start to answer these questions, we devised a new class of field sweeps that digs into timescales and introduces a unique take on history dependence. These *steep sweeps* also introduce a potentially useful and absolutely unexpected phenomenon: the steep echo.

CHAPTER 7

Nuclear-Induced Frequency Focusing and the Steep Echo

7.1 Motivation

In the previous chapter, we presented and verified a model for an OSE-generated DNP in GaAs that manifests for long nuclear polarization times. Our approach was interested in the inputs and outputs of the experiments without a regard for the underlying *why*. Yes, by pumping at an energy detuned from the donor-bound exciton resonance, we rotate spin polarization into the external field direction, and this spin polarization then transfers its spin to the nuclei. But this description may more properly be regarded as the *how*. Without the computational tool of simulations, would we have predicted the outcomes of our experiments?

In this chapter, we introduce a concept familiar to the DNP studies we cited previously: *nuclear-induced frequency focusing* (NIFF) [102]. Known alternatively as *spin mode-locking* [103], this concept provides a deeper insight into the DNP we observe. Rather than just the outcome of a set of equations, the behavior of the DNP can be characterized as the nuclei acting to focus the Larmor precession frequency of the electrons to match (or avoid) the phase synchronization condition (PSC) introduced with RSA. This ties our study even more closely to RSA, as it is not just the lens through which we observe the DNP but the very cause of the DNP itself. We adopt this teleological description of the DNP for the remainder of our discussion.

The last chapter concluded with a model that described well but not fully the behavior of our electron spin polarization. We employ a novel series of field scans, the *steep sweeps*, to further manipulate the time scales of polarization in our system. Combined with the insights granted by NIFF, we identify a key area of improvement for our model, allowing us to reproduce our experimental data more fully.

This chapter is partially based on work that has been previously published in Physical Review B (© American Physical Society) [10, 11] (see Chapter 6 for full citations). The remainder is currently in preparation for submission. Overhauser field fits are provided by Dr. Michael Macmahon, while simulations of spin polarization are provided by Michael Dominguez.

7.2 Nuclear-Induced Frequency Focusing

When we introduced the nuclear rate equation, Eq. 6.7, we stated that though our system would not be properly described as steady-state given the long timescales of nuclear polarization and relaxation expected in GaAs, many of the studies we have cited studied materials that meet this criteria. Specifically, the researchers at Dortmund have found the steady-state to describe their fluorine-doped ZnSe [76, 80]. Here, we consider this outcome to build intuition about the buildup of DNP.

To solve for the steady-state nuclear polarization, we set the time derivative of the nuclear rate equation to zero:

$$
\begin{aligned}
0 &= -\frac{1}{T_{1e}}\left(I_{\text{av}} - \frac{4}{3}I\left(I+1\right)\langle S_x\rangle\right) - \frac{I_{\text{av}}}{T_{1n}} \\
0 &= -\left(\frac{1}{T_{1n}} + \frac{1}{T_{1e}}\right) I_{\text{av}} + \frac{1}{T_{1e}}\frac{4}{3}I\left(I+1\right)\langle S_x\rangle \\
\left(\frac{1}{T_{1n}} + \frac{1}{T_{1e}}\right) I_{\text{av}} &= \frac{1}{T_{1e}}\frac{4}{3}I\left(I+1\right)\langle S_x\rangle \\
I_{\text{av}} &= \frac{1}{T_{1e}}\left(\frac{1}{T_{1n}} + \frac{1}{T_{1e}}\right)^{-1}\frac{4}{3}I\left(I+1\right)\langle S_x\rangle \\
I_{\text{av}} &= \frac{1}{T_{1e}}\left(\frac{T_{1e}+T_{1n}}{T_{1e}T_{1n}}\right)^{-1}\frac{4}{3}I\left(I+1\right)\langle S_x\rangle \\
I_{\text{av}} &= \frac{1}{T_{1e}}\left(\frac{T_{1e}T_{1n}}{T_{1e}+T_{1n}}\right)\frac{4}{3}I\left(I+1\right)\langle S_x\rangle \\
I_{\text{av}} &= \left(\frac{T_{1n}}{T_{1e}+T_{1n}}\right)\frac{4}{3}I\left(I+1\right)\langle S_x\rangle. \qquad (7.1)
\end{aligned}
$$

After some rearranging, we arrive at what looks like a simple dependence of I_{av} on $\langle S_x\rangle$. However, $\langle S_x\rangle$ is itself a function of the total magnetic field, which includes the Overhauser field, so I_{av} does depend on itself. To simplify matters, we will not consider any sorts of field scans here. For this thought experiment, we set an external field and let the system evolve in its due time.

When the system is just starting out, there will be no nuclear field and $\langle S_x\rangle$ will depend only on the external field. The initial action of I_{av} will be governed by the above equation. To understand this seeding of the nuclear field, we appeal back to the plots for $\langle S_x\rangle$ that we showed in the previous chapter. We have reproduced these as Fig. 7.1. Here, we will re-interpret external magnetic field as the total magnetic field experienced by the electron spin polarization.

Thanks to the OSE, we acquire an S_x component of spin polarization that follows the shape of S_y, with the periodicity of RSA. Whereas S_z has maxima at magnetic fields satisfying the PSC, S_y passes through zero at these fields. We also observe S_y to pass through zero at the midpoints between the PSC fields. These sign flips are passed on to S_x, which are

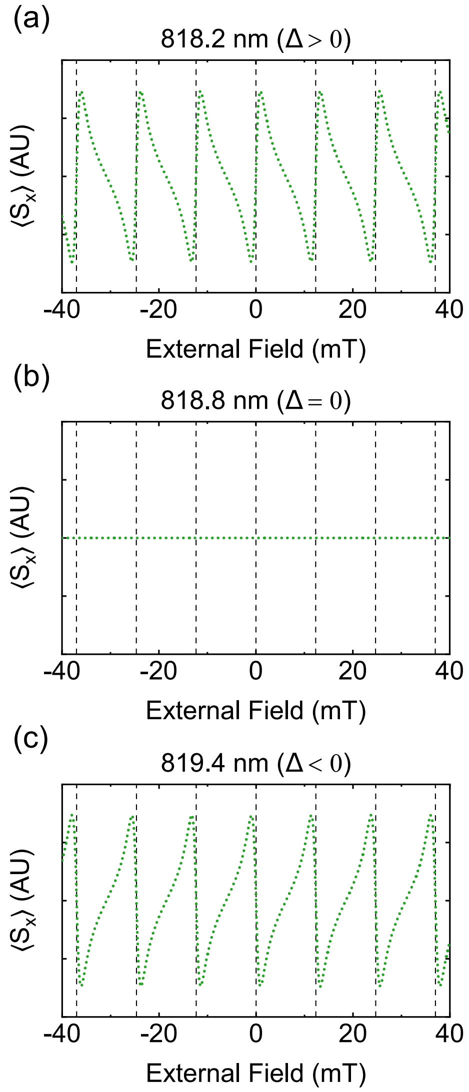

Figure 7.1: Calculated time-averaged component of electron spin polarization S_x under periodic optical excitation and the optical Stark effect in the absence of nuclear polarization, as a function of external magnetic field, for laser wavelengths (a) 818.2 nm (positive detuning), (b) 818.8 nm (resonance), and (c) 819.4 nm (negative detuning). Calculations assume pump-probe delay 13 ns, spin lifetime $T_2^* = 30$ ns, pulse duration $\tau_p = 1$ ps, and pulse area $\theta = \pi/4$. This figure represents the same calculations as Fig. 6.11, with dashed lines added at the PSC fields.

preserved in $\langle S_x \rangle$. The initial $I_{\rm av}$ at a given external field will essentially follow this shape. The resulting Overhauser field will be of opposite sign, since bn is proportional to the g factor, which is negative in GaAs.

We focus first on the positive detuning case, for which $\langle S_x \rangle$ has sign opposite of S_y. We select a starting external field value B_0 that is just a bit larger than the first PSC, about 12.3 mT for our system. This is identical to saying that the electron spins are precessing with a Larmor precession frequency that is a bit faster than the PSC frequency. Because $\langle S_x \rangle > 0$, the induced Overhauser field will be negative. The electron spin polarization will experience a total field less than B_0. We look back to Fig. 7.1 and observe that $\langle S_x \rangle > 0$ still holds so long as $B_0 + B_{\rm N} > 12.3$ mT, so the Overhauser field will continue to build up in opposition to the external field. When the nuclear field has accumulated such that $B_0 + B_{\rm N} = 12.3$ mT and the PSC has been reached, the electron spin polarization will lie along the optical axis at the end of the repetition period T_R. No spin polarization will be rotated into the external field direction, $\langle S_x \rangle = 0$, and the Overhauser field will not change. As time passes and the nuclear spins relax, the total field will approach back to B_0. No longer being at the PSC, the spin polarization will not fully lie along the optical axis when the next pump pulse arrives, and we will have a nonzero $\langle S_x \rangle$ yet again. The nuclear spins will follow $\langle S_x \rangle$ until the PSC is reached again. Should the Overhauser field overshoot, such that $B_0 + B_{\rm N} < 12.3$ mT, the rotated S_x will have the opposite sign. It will polarize the nuclei in this opposite direction, reducing the magnitude of the Overhauser field. This will serve to bring the total field back to 12.3 mT.

More succinctly, for magnetic fields on the more positive side of a PSC, $\langle S_x \rangle > 0$ and the Overhauser field will build in the more negative direction, back towards the PSC. For magnetic fields on the more negative side of the PSC, $\langle S_x \rangle < 0$ and so the Overhauser field should build in the more positive direction, back towards the PSC. In this way, for a

Larmor precession frequency not matching the PSC, the Overhauser field will work to pull the frequency to lock in with the PSC frequency. This is nuclear-induced frequency focusing [102, 103] and is shown schematically in Fig. 7.2.

For negative detuning, due to the reversed optical Stark rotation angle, $\langle S_x \rangle$ has the same sign as S_y. The frequency-focusing effect will reverse as well. For Larmor frequencies just a bit faster than the PSC, the nuclear field acts to speed up the precession, moving further away from the PSC. For Larmor frequencies just a bit slower than the PSC, the nuclear field tries to slow it down even further. The speeding and slowing will meet in the middle, with the nuclear polarization not satisfied until the electron spins are precessing at a frequency equal to a half-integer multiple of the PSC.

Based on detuning, our electron precession will be focused to ($\Delta > 0$) or away ($\Delta < 0$) from the PSC. We should note here that our assignment between focusing and detuning is the opposite of that established in Refs. [76] and [80] for fluorine-doped ZnSe and Ref. [89] for InAs quantum dots. The Dortmund studies note that reversing the sign of the g factor would reverse the behavior of positive and negative detuning, which is consistent with our results given that ZnSe has a positive g factor [80]. That said, our simulations do not reverse the focusing behavior when we implement a g factor with opposite sign, calling into question whether there is a deeper reason for the difference in detuning behavior.

Many of the DNP studies we cited in the previous chapter utilize the terminology of frequency focusing to understand the outcomes of their experiments. However, NIFF does not appear only in the context of the OSE. Refs. [104] and [105] explore the role of pump helicity modulation with frequency near the electron spin resonance. Ref. [92] is a theoretical study comparing NIFF to RSA in an inhomogeneous ensemble of quantum dots. Lastly, Ref. [106] considers how NIFF calculations change when each nuclear isotope is treated separately.

Now that we have a basis for understanding the end goal of the nuclear field, we can

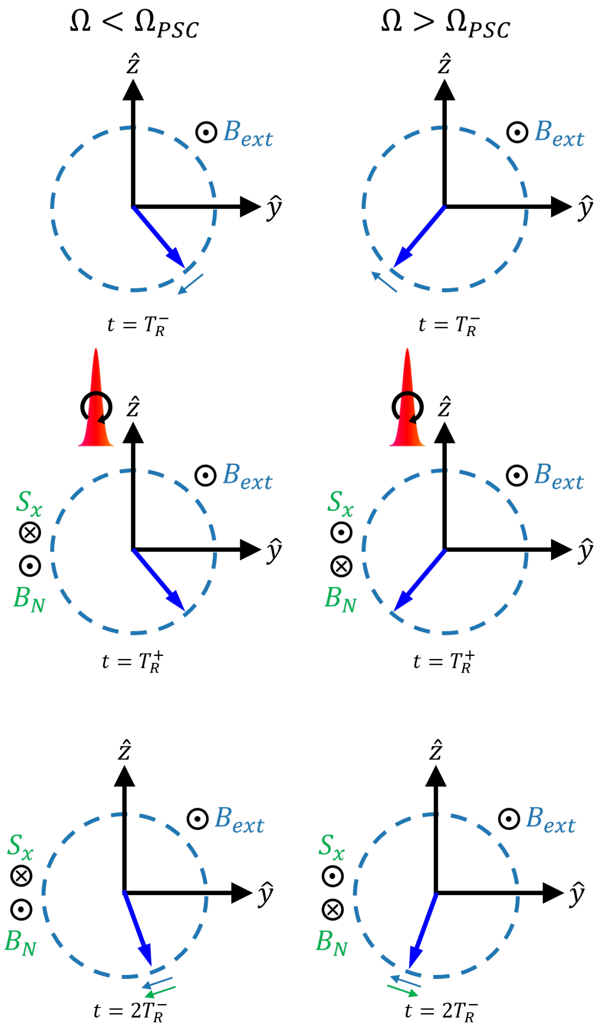

Figure 7.2: Schematic for nuclear-induced frequency focusing for positive detuning ($\Delta > 0$) in the GaAs system considered in this dissertation. This figure considers spin polarization generated along $-\hat{z}$ (blue arrow) and precessing in the clockwise direction ($g < 0$) about $\hat{x}$. The top row assumes no spin component S_x. The middle row represents the action of the pump pulse to rotate spin polarization into the x-direction. Because the OSE angle $\Phi < 0$ for positive detuning, S_x has opposite sign of S_y, and B_N has opposite sign of S_x. For clarity, the new spin polarization generated along $-\hat{z}$ is omitted. The bottom row shows the effect of the Overhauser field on the existing spin polarization. For precession frequencies slower than the nearest PSC (left), the nuclear field speeds up the precession. For precession frequencies faster than the nearest PSC (right), the nuclear field slows down the precession. In both cases, the precession frequency is focused to the nearest PSC, Ω_{PSC}. Under negative detuning, S_x has the same sign as S_y, so the Overhauser field will reverse, opposing precession and focusing away from the PSCs.

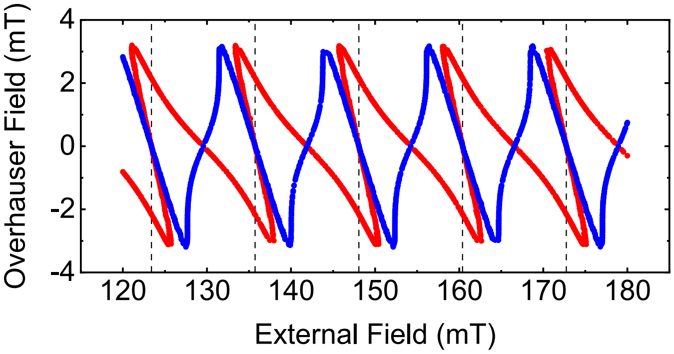

Figure 7.3: Calculated steady-state Overhauser field as a function of external magnetic field for material parameters matching the GaAs system considered in this dissertation. The blue (red) line indicates positive (negative) detuning. The two curves are similar in shape but differ in more than just a sign or phase shift. Black dashed lines indicate the fields satisfying the PSC. Calculations assume pulse duration $\tau_p = 1$ ps and pulse area $\theta = \pi/4$.

examine the steady-state solutions to the nuclear rate equation. We used the `FindRoot` function in *Mathematica* to obtain I_{av} on the high-field range 120 to 180 mT. The Overhauser field for positive (blue) and negative (red) detuning is displayed in Fig. 7.3.

It should be immediately apparent that the steady-state Overhauser field for negative detuning is not single-valued. There is nothing mathematically constraining the nuclear rate equation to a single solution. A physical system will choose one solution, allowing for hysteretic effects [76]. These effects are not the same as the history-dependence that leads to a reversal of the sign of the Overhauser field in our material. Interestingly, for this combination of parameters, positive detuning produces a single solution, providing an asymmetry to the detunings that has heretofore not been present.

Even so, for negative detuning, the Overhauser field is positive for external fields greater than the PSC and negative for external fields less than the PSC, pushing the electron precession frequency away from the PSC. Conversely, for positive detuning, the Overhauser field pushes the electron precession frequency towards the nearest PSC. This is precisely as expected from our discussion. It is even more apparent when considering the total magnetic field experienced by the electrons, shown in Fig. 7.4. Dashed lines corresponding to the PSC

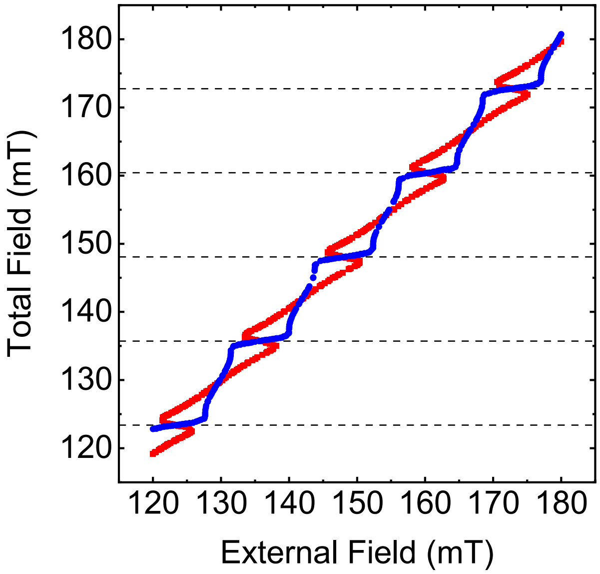

Figure 7.4: Calculated steady-state total magnetic field experienced by the electron spin polarization as a function of external magnetic field for material parameters matching the GaAs system considered in this dissertation. The blue (red) line indicates positive (negative) detuning. This figure is obtained by adding the Overhauser field shown in Fig. 7.3 to the external field. Black dashed lines indicate the fields satisfying the PSC. The positive-detuning total field focuses to the PSC while the negative-detuning total field focuses away from it. Calculations assume pulse duration $\tau_p = 1$ ps and pulse area $\theta = \pi/4$.

fields have been added to guide the eye.

The total field for positive detuning appears to be a series of steps or plateaus at the PSC fields. The jump between plateaus is nearly discontinuous, with only a small range of fields where the total field increases before leveling off again. This behavior has been referred to as discretizing the total magnetic field [76]. Negative detuning does not show such marked steps. Due to the degenerate solutions, it appears that there may be focusing around the PSCs, but this is just an artifact of including all of the solutions. In real experiments, the near-discontinuities appear here as well; see Ref. [76] for a presentation of such data.

We have been describing the steady-state behavior of the nuclear system, but we now apply these principles to the study of our material. Our discussion began with recognizing that I_{av} initially follows $\langle S_x \rangle$, which is the same fact we used to explain history-dependence. Thus, our starting point is the same. It should then follow that our system will also exhibit

NIFF. It does, and strikingly so.

While most of our DNP studies in the previous chapter relied on field scans, the evidence for NIFF will here come through delay scans. When comparing delay scans taken at different external fields, through the TRKR-RSA technique, we can see the Larmor precession frequency change by observing the number of oscillations in our delay range change. In the absence of DNP, we expect that a linearly-increasing external magnetic field would result in a linearly-increasing Larmor precession frequency. In the RSA regime, this is somewhat complicated by the field-dependent phase which flips sign at the PSC. Under the influence of NIFF, we may expect the precession frequency to stay constant for a range of external magnetic fields before changing nearly discontinuously.

In Fig. 7.5a, we show three delay scans at negative detuning for external fields 121, 130, and 139 mT. Once we have set the field, we increment our pump-probe delay from -2000 to $+5000$ ps, in steps of 100 ps with approximately 1.1 s between steps. Each of the three experimental traces shows a distinct Larmor precession frequency. Further, as we observed previously, the Kerr rotation at negative delays is of similar magnitude to the Kerr rotation at positive delays, implying a long spin lifetime.

These delay scans were part of a TRKR-RSA measurement, in which we carried out delay scans for external fields from 120 to 140 mT in steps of 1 mT. At the conclusion of each delay scan, we briefly reset the external field to zero to depolarize the accumulated nuclear polarization. In this way, nuclear polarization is only accumulated over the course of a single delay scan, which lasts on the order of 100 s, and we do not expect to reach steady-state. We aggregate the delay scans on a single 2D color plot, with the vertical axis representing increasing field, in Fig. 7.5c. The vertical bands are the peaks and troughs of the spin polarization oscillation. When we view the three example scans in the context of the entire external field range, we realize that these three precession frequencies are the only three

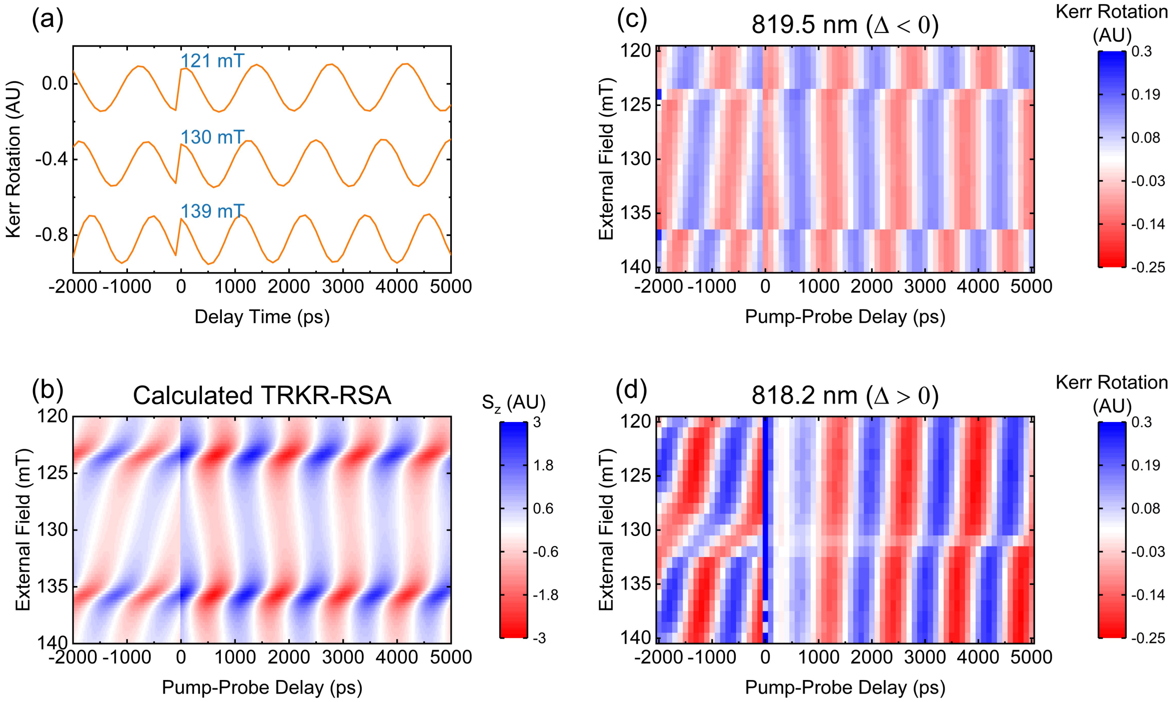

Figure 7.5: Nuclear-induced frequency focusing as observed through TRKR-RSA. (a) Kerr rotation measured as a function of pump-probe delay for pump power of approximately 5000 μW at laser wavelength 819.5 nm. (b) Calculated spin polarization S_z for the TRKR-RSA experiments shown in (c) and (d). Calculation assumes pump-probe delay 13 ns and spin lifetime $T_2^* = 30$ ns. (c), (d) Kerr rotation measured as a function of pump-probe delay and external magnetic field for pump power of approximately 5000 μW at laser wavelengths 819.5 nm (c, negative detuning) and 818.2 nm (d, positive detuning). The external field is held constant while the pump-probe delay is incremented from -2000 to $+5000$ ps. At the conclusion of each delay scan, the external field is briefly reset to zero to depolarize the nuclear spins before it is set to the next target external field, in steps of 1 mT. Nuclear-induced frequency focusing is observed for positive pump-probe delays, with sharp discontinuities occurring roughly every 12-13 mT, analogous to one RSA period. The negative-detuning case focuses away from the PSC while the positive-detuning case focuses to the PSC.

precession frequencies we could have measured.

Despite not being enough time to reach steady state, the nuclear buildup is sufficient for our system to show frequency focusing. The discontinuities between field regions with these precession frequencies are very clear and occur for fields fulfilling the PSC. This last point can be seen by comparing the data to the expected TRKR-RSA in the absence of DNP, as plotted in Fig. 7.5b. While the behavior of the negative detuning case may display some similarity to the non-DNP case when viewed as a 2D plot, the behavior for positive detuning in Fig. 7.5d is jarringly dissimilar. We observe a single discontinuity in precession frequency, which is not even as discontinuous as the negative-detuning case, but this plot would not be mistaken for Fig. 7.5b. The only difference between Fig. 7.5c and Fig. 7.5d is the laser detuning. All other parameters such as laboratory time elapsed and duration of delay steps remained the same.

Briefly, a few caveats about this data. To maximize the effect of DNP for demonstration purposes, we chose a pump power of approximately 5000 μW. Based on our power-dependent Kerr rotation presented in the previous chapter, this should have led to near-maximal buildup of nuclear spin polarization, thus accentuating the frequency focusing. Despite this, we do not achieve total frequency focusing for negative pump-probe delays. For these delays, the precession frequency still appears to increase with increasing external magnetic field, as we might expect in the absence of DNP. Each scan is building up DNP from zero, regardless of the delays considered. With a T_{1n} time of 20 s and a T_{1e} time of 180 s, the 20 s from -2000 to 0 ps delay is insufficient to build up the nuclear field to its steady-state value. Of course, the 100 s duration of a single scan is not sufficient. However, small differences in precession frequency are more salient at longer pump-probe delays due to more oscillations having passed. These two factors combined account for the different character of negative and positive delays. Finally, we must also note that the positive detuning case, at laser wavelength 818.2 nm, features the two-species behavior elaborated upon in the previous chapter. This beating reduces the amplitude of the first oscillation but does not stand in the way of frequency focusing.

Even on intermediate timescales, the nuclear polarization in our system acts to achieve NIFF. This principle has been at work in our material from our very first experiment. Consider again the presentation of wavelength-dependent Kerr rotation in Fig. 6.14 and how we described the effect of DNP on the RSA peaks. For negative detuning, the Overhauser field acted to prolong the rising edge of each non-zero-peak. That is, it was acting to slow down the precession of the electrons. Then, once we passed the RSA peak (due to the combination of external and nuclear field), the falling edge was sharp. Overall, the nuclear field pushed us away from the RSA peak, towards the half-integer PSC. For positive detuning, the rising edge was shortened in comparison to expected RSA because the nuclear field wanted to get to the PSC, the RSA peak. Once we passed the peak, the fall-off was noticeably prolonged.

Synthesizing the takeaway from this section with the conclusion of the previous chapter, we arrive at a general principle governing the DNP accumulation in our system. When detuning reverses, $\langle S_x \rangle$ reverses, which alters the focusing to or away from the PSC. When the external-field-sweep direction is reversed, $\langle S_x \rangle$ remains the same, but the sign of the integrated $\langle S_x \rangle$ reverses. This reverses the overall sign of the Overhauser field. For all DNP measurements, then, the sign of $\langle S_x \rangle$ matters. When not in steady-state, the sign of the integrated $\langle S_x \rangle$ matters as well.

7.3 Steep Sweeps

In the previous chapter, we pointed out time-dependence as a key aspect of the DNP we observed and the model meant to describe it. But we did not disentangle time from the act of sweeping the external field. We desired a means of building up DNP apart from sweeping. Though it is not a perfect solution, the *steep sweep* class of experiments is based on an incredibly simple concept: if we want DNP to build up, let it. Take a pause from sweeping the field to let the nuclear spin polarization accumulate. Because every data point in a field sweep reflects the history of all the points that came before it, we can observe the DNP buildup by how the remainder of the field sweep changes as a result.

Each steep sweep is a magnetic field sweep performed at a fixed pump-probe delay, with the field incremented 0.25 mT every 1.1 s, unless otherwise noted. At a chosen field within the sweep, the *steep field*, the external field is held constant for an appreciable amount of lab time, usually two minutes, before proceeding with the remainder of the field sweep. The Kerr rotation is measured throughout the steep and after, tracking how the electron spin polarization changes as the sweep is paused. From this we can infer the behavior of the nuclear spin system. The naming of this experiment, credited to Dr. Michael Macmahon, emerges from a comparison to soaking a tea bag in water to extract the flavor. Just as we steep the tea bag in a bath of water, so here we steep our electron spin polarization in a nuclear spin bath. This produces a type of field scan steeped in new information.

We carried out steep sweeps at both positive and negative detuning, but for simplicity we will primarily focus on negative detuning. We view the steep sweep from the perspective of both laboratory time elapsed and external field values in Fig. 7.6. Here, we have chosen negative detuning (819.3 nm) and sweep on the field range −80 to +25 mT. Only a portion of the field sweep is shown here for clarity, and the laboratory time has been indexed to the start of the data we show. In the left panels, we plot Kerr rotation as a function of laboratory

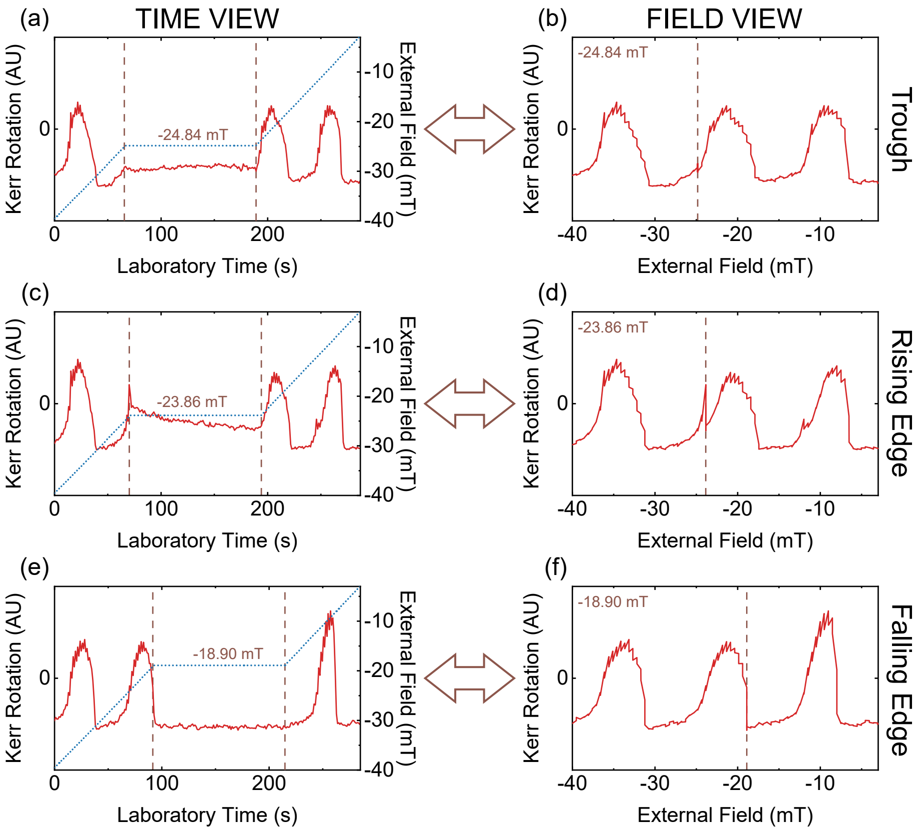

Figure 7.6: Steep sweeps viewed as both a measurement in time and a measurement in field. Kerr rotation measured for a fixed pump-probe delay of 13 ns at laser wavelength 819.3 nm. In the time view, the external magnetic field (dotted blue line) is swept up from −80 mT to the steep field (dashed brown line in the field view) and held constant for 2 min. The field is then swept up to +25 mT, though only the peaks before and after the steep field are shown. Here, the field is swept in steps of 0.5 mT with each step repeated twice, resulting in the same field sweep rate as elsewhere. The steep fields correspond to steeping (a), (b) in the trough between peaks; (c), (d) on the rising edge of a peak; and (e), (f) on the falling edge of a peak. Data originally published in Ref. [10]; figure inspired by Ref. [55].

time. The vertical brown lines indicate the two-minute period in which the external field was steeped, or held constant. An overlaid dotted blue line shows the external magnetic field corresponding to each laboratory time. Excepting the steep period, we increase the field linearly in time.

During the steep period, we expect the nuclear spins to push the electron Larmor precession frequency away from the PSC. By steeping close to the trough, the field range between RSA peaks, we expect the DNP to be satisfied and not appreciably change. This is what we see in Figs. 7.6a and 7.6b. When we instead steep on the rising edge of the peak, the DNP will build up to oppose the approach to the peak. This will effectively push the electron spins back down the peak, and we will observe a drop in Kerr rotation. This is precisely the case in Figs. 7.6c and 7.6d. Steeping on the falling edge accelerates the process of moving away from the peak, and we see in Figs. 7.6e and 7.6f a sharp, quick drop in Kerr rotation followed by a period of constant value.

When the steep is completed, the electron spins continue along in the field sweep as if nothing had happened. Looking at the Kerr rotation plotted as a function of external field in the right panels of Fig. 7.6, we might not even notice a change. Something has happened, though, and comparison between the steep sweep peak positions show that the peaks may now be shifted in field. This shift is one way for us to observe the action of the nuclear spins.

Of course, we can measure the change in Overhauser field directly by combining steep sweeps with Snapshot TRKR, though we must adapt to the high-field range. Since the accumulated Overhauser field is much smaller than the total field, we had some difficulty in identifying the proper steep fields for rising edge, falling edge, and trough behaviors. The behavior manifested in the individual steep sweeps is much less pronounced. Our procedure for choosing these steep fields consisted of trying single steep sweeps at 13 ns and selecting the steep fields that were closest to our desired behavior. Owing to the long runtime of a Snapshot TRKR experiment and adding in two minutes per steep sweep, we were limited in the number of data sets we could acquire in a single data run. Thus, the selected steep fields may not have been the optimal choices but were based on our best judgment.

We do not present the 2D Snapshot TRKR here; we do show the 13 ns steep sweep and the extracted Overhauser field in Fig. 7.7. We chose steep fields 134.8 mT (rising edge), 138.7 mT (falling edge), and 142.5 mT (trough). Because these are all upsweeps, the overall Overhauser field is negative. The steeps serve to shift the floor of the periodic B_{N}, shifting the subsequent peaks. In the case of the trough steep, the Overhauser field resumes its prior

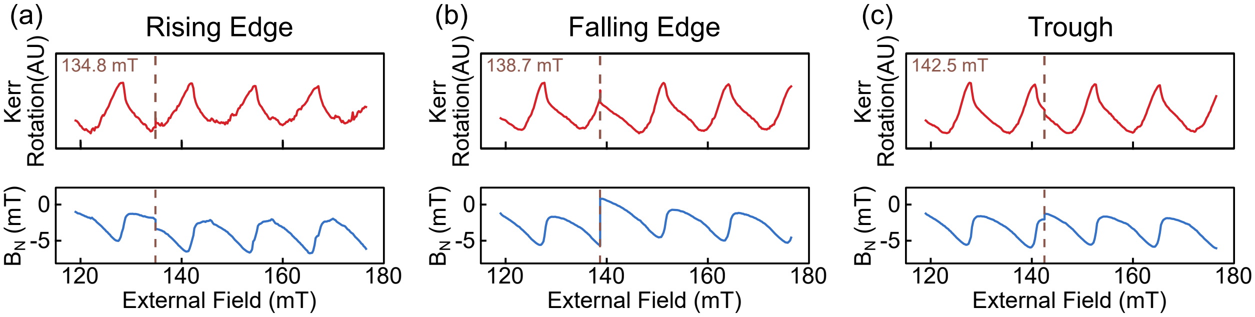

Figure 7.7: Steep sweeps and Overhauser field extracted from Snapshot TRKR on the high-field range. Kerr rotation measured as a function of external magnetic field for a pump-probe delay of 13 ns at laser wavelength 819.5 nm, for pump powers (a) 660 μW, (b) 620 μW, and (c) 640 μW, shown in the top panels. Snapshot TRKR was carried out on the external field range 120 to 180 mT, with pump-probe delay incremented from -1920 to -160 ps in steps of 160 ps, though only the sweep at 13 ns is shown. The external magnetic field is swept up from 120 mT to the steep field (dashed brown line) and held constant for 2 min. The field is then swept up to 180 mT. The extracted Overhauser field is shown in the bottom panels. The steep fields correspond to steeping (a) on the rising edge, (b) on the falling edge, and (c) in the trough. Data and fits reproduced from Ref. [10].

values fairly quickly after the steep has concluded.

The effect of steeping is much easier to see for low-field steep sweeps, so we focus on these for the remainder of the chapter. We will monitor the changes in Overhauser field through the shift in peaks after the steep field. This is a crude method for any quantitative analysis, but it more clearly demonstrates the B_{N} buildup.

7.4 The Steep Echo

We have addressed rising edge, falling edge, and trough, but this leaves out one more steep option: the peak itself. The Overhauser field wants to avoid the PSC at all costs. If we could steep exactly at this point, would the nuclear field try to push the total field to larger values? Or will it elect to oppose the external field to decrease the total field? Or will it do something else entirely?

We return to the field range -80 to $+25$ mT and present a wider array of steep fields in Fig. 7.8. In each plot, we mark the steep field with a dashed brown line. The concept of peak

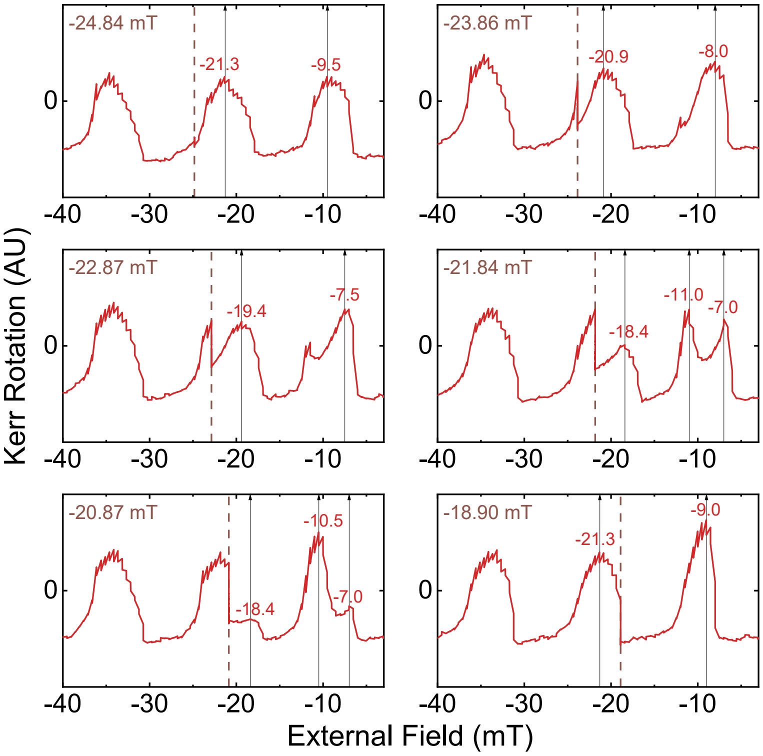

Figure 7.8: Steep sweeps at external fields near the steep echo. Kerr rotation measured as a function of external magnetic field for a fixed pump-probe delay of 13 ns at laser wavelength 819.3 nm. The external magnetic field is swept up from −80 mT to the steep field (dashed brown line) and held constant for 2 min. The field is then swept up to +25 mT, though only the peaks before and after the steep field are shown. Here, the field is swept in steps of 0.5 mT with each step repeated twice, resulting in the same field sweep rate as elsewhere. The post-steep peak positions are labeled and indicated with a thin black arrow. These positions vary with steep field, as steep fields closest to the peak result in the greatest shifts. For most of these steep fields, the following peak is deformed, "echoing" the effect of the steep on the shape of the steeped peak. Data originally published in Ref. [10].

position can no longer be applied in a straightforward way to these sweeps, so we mark the field (with a thin black line and red label) at which the maximum Kerr rotation occurs. We have specifically included steep fields near the expected peak position (approximately −21.3 mT for this peak). The closer we steep to the peak, the further the next peak is shifted away, as expected. But something strange happens when we steep too close. The steep significantly deforms the peak, appearing to split it into two parts as the sweep continues. This deformation is not limited to one peak, as it is mimicked by the subsequent peak. For steep sweeps that include more peaks, the strange deformation continues to echo, appearing, albeit less strikingly, on each peak that follows. For this reason, we call this observation the "steep echo." The electron-nuclear spin system appears to remember the steep as part of its field history, even minutes after the steep had concluded.

To be clear, the steep echo is not the same type of experiment as the spin echo. Whereas that experiment is meant to measure the homogeneous dephasing time T_2, this experiment is another manifestation of history-dependent DNP.

Of course, the steep sweep experiment is not limited to negative detuning, nor is the presence of the steep echo. We present a selection of steep fields for a new external field range, -5 to $+80$ mT, in Fig. 7.9. The steep field is indicated with a dashed brown line, while peak maxima are indicated with thin black lines and numerical labels. As before, only a selection of the field range is shown to highlight the region of interest. We have selected steep fields corresponding to the rising edge, peak, falling edge, and trough.

Positive detuning steeps follow the NIFF behavior we expect. The DNP wants to focus the Larmor precession frequency to the PSC, so subsequent peaks will be pushed closer (rising edge) or further (falling edge). Steeping near the peak results in very little Overhauser field buildup, while the steep echo now occurs in the trough. In our observations, the echo was less pronounced for positive detuning. This could be due to the small magnitude of Kerr rotation in the trough, so the changes aren't as apparent, or could be another aspect to the detuning asymmetry observed earlier. The expected steep behavior is summarized in Table 7.1.

Just like in the last chapter, we can simulate the steep sweeps with our numerical model.

Table 7.1: Effect of NIFF on the Overhauser field in different regions of the field sweep for positive and negative detuning.

	Rising Edge	Peak	Falling Edge	Trough
$\Delta < 0$	$\longleftarrow$	ECHO	$\longrightarrow$	0
$\Delta > 0$	$\longrightarrow$	0	$\longleftarrow$	ECHO

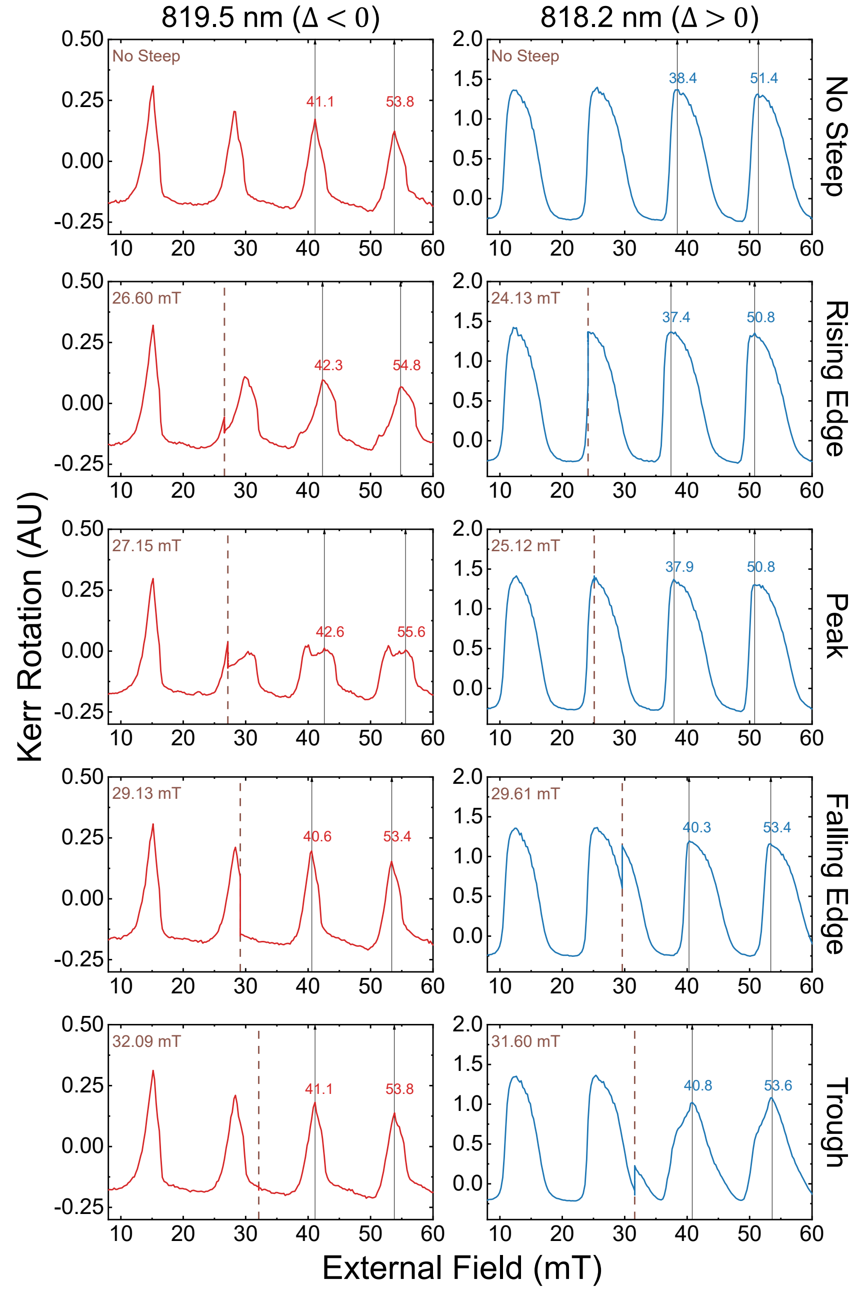

Figure 7.9: Steep sweeps for negative and positive detuning. Kerr rotation measured as a function of external magnetic field for a fixed pump-probe delay of 13 ns at laser wavelengths 819.5 nm (negative detuning, red, left column) and 818.2 nm (positive detuning, blue, right column). The external magnetic field is swept up from −5 mT to the steep field (dashed brown line) and held constant for 2 min. The field is then swept up to +80 mT, though only the peak before and two peaks immediately following the steep field are shown. The post-steep peak positions are labeled and indicated with a thin black arrow.

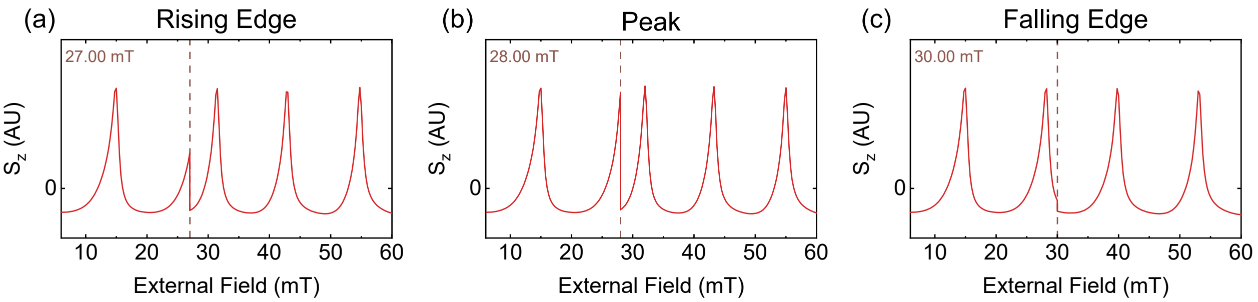

Figure 7.10: Simulated spin polarization S_z as a function of external magnetic field for a fixed pump-probe delay of 13 ns corresponding to the negative-detuning steep sweeps in Fig. 7.9. Rather than match the exact steep fields, the chosen steep fields correspond to steeping on the (a) rising edge, (b) peak, and (c) falling edge. For (a) and (c), the simulation reproduces the steep behavior observed previously. However, the peak steep does not show the steep echo effect in (b). Simulations assume $T_{1e} = 280$ s, $T_{1n} = 180$ s, spin lifetime $T_2^* = 30$ ns, pulse duration $\tau_p = 1$ ps, and pulse area $\theta = \pi/4$. Simulation provided by Michael Dominguez.

A simulated analog to the negative-detuning data in Fig. 7.9 is shown in Fig. 7.10. In contrast to the nuclear timescales presented in the previous chapter, we use $T_{1e} = 280$ s and $T_{1n} = 180$ s for the simulations in this chapter. For the falling and rising edges, the model reproduces the observed Kerr rotation. The steep echo, however, does not emerge from this model for the peak steep in Fig. 7.10b. The character of the steep peak is preserved, but the subsequent peaks do not share it. Something is missing.

We return to our observation that the steep echo appears to be a peak split in two. Figure 7.11 shows more finely spaced steep sweeps around the negative detuning steep echo from Fig. 7.9, along with a reference non-steep sweep. Vertical offset is added for clarity, as are dashed lines indicating the peak positions in the absence of steeping. For fields at the lower end of this range, we see a peak that has been shifted forward. For fields at the higher end of this range, we see a peak that has been pulled back. In the interim, the peak does not slowly shift to smaller fields. Instead, it doubles down on shifting forward, until it splits into two.

So we ask again. If we could steep exactly at the PSC, would the nuclear field try to push the total field to larger values? Or will it elect to oppose the external field to decrease the

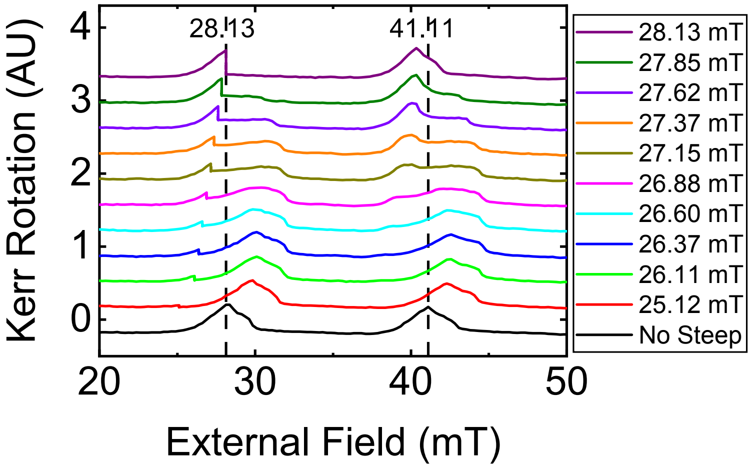

Figure 7.11: Steep sweeps at external fields finely spaced near the steep echo. Kerr rotation measured as a function of external magnetic field for a fixed pump-probe delay of 13 ns at laser wavelength 819.5 nm, for a selection of steep fields. The external magnetic field is swept up from −5 mT to the steep field and held constant for 2 min. The field is then swept up to +80 mT, though only the peak following the steep field is shown. The positions of the peaks for the no-steep case are labeled and marked with dashed black lines, and the steep sweeps are offset vertically for clarity. Steeping near a peak induces a steep echo, appearing to split the subsequent peak in two.

total field? The answer? **Yes.** The splitting of the RSA peak is explained by the nuclear spins choosing both options.

Well, perhaps it is not technically correct to say that the nuclei can make both choices simultaneously. After all, when we discussed the degenerate solutions to the steady-state nuclear rate equation, we maintained that the physical system must pick one of the solutions. Furthermore, it would be incredibly challenging to steep at exactly the PSC. More properly, then, we are seeing the effect of steeping on both sides of the PSC. The nuclear field both increases and decreases in line with NIFF. Our electron spin polarization simultaneously feels the effect of two (or more) Overhauser fields changing in opposite directions. We then see our RSA peaks ripped apart as the field steeps.

Thus the steep echo is a result of NIFF, but our conjecture only holds so far as we have some means of splitting either the electron or nuclear spin polarization into two or more subensembles. We discussed the two-species behavior in the last chapter, which may offer candidates to fit this description. However, only one of those species has a spin lifetime long enough to influence RSA.

Instead, we postulate that there is some distribution of electron-nuclear interactions. This distribution, whatever it may be, must be sufficiently wide such that when we steep near a PSC for negative detuning (or at the midpoint for positive detuning), some portion of this distribution will fall on either side and thus be pulled in both directions.

For the remainder of this chapter, we present three candidate distributions inspired by the literature and by our experimental setup. We show a preliminary simulation for one such distribution that replicates the steep echo, giving us confidence to pursue this question further.

7.5 Proposed Modifications to the Model

To capture the steep echo behavior present in our coupled electron-nuclear spin system, we must revise our model to incorporate a distribution. We propose three candidates:

1. Nuclear-coupling constants
2. Electron g factors
3. Laser wavelength

Each of these three candidates presents a different avenue through which the electron spin system interacts with the nuclei. In what follows, we briefly discuss how these distributions would factor into the model and the plausibility of each. To conclude, we present the output of a preliminary implementation of the laser wavelength distribution, showing that it can reproduce the steep echo as well as capture the peak amplitude variation previously unaccounted for by our model.

7.5.1 Candidate: Nuclear-Coupling Constants

The coupling constant bn converts the average nuclear polarization I_{av} into the Overhauser field B_{N} experienced by the electron spin polarization. A distribution of bn, based on a distribution of the hyperfine constant, would yield a spread of Overhauser fields. In this scenario, the nuclear polarization remains the same, but the way the electrons experience this polarization as a magnetic field varies. Studies in ensembles of quantum dots must take into account a distribution of hyperfine constants [107], inspiring us to propose this candidate distribution. That said, an ensemble of quantum dots is a very different physical system when compared to a bulk semiconductor, so we should not necessarily expect the same type of distribution of hyperfine constants to hold for both systems. Without a physical underpinning for such a distribution (some spatial or energy distribution, for example), it is difficult to determine how plausible this candidate is for our material.

7.5.2 Candidate: Electron g factors

The nuclear-coupling constants bn also depend on the electron g factor, so a spread in g factors would result in a spread of bn. Researchers at Dortmund have factored g factor distributions into their simulations of Faraday and Kerr rotation in materials like InGaAs/GaAs quantum wells [16], so our consideration is not without precedent. Their recent work on their OSE model mentions a possible extension to a system with a distribution of g factors [80]. Under the right conditions, they even expect that such a distribution could lead to "two ensembles" appearing in the spectrum of electron precession frequencies [80]. For this reason, we are emboldened to propose this second distribution.

The g factor describes how electrons in a crystal experience magnetic fields, both internal and external. On its face, this scenario is reminiscent of the first, just shifting the distributed quantity from the electron-nuclear interactions to the electrons themselves. This does not capture the whole picture, however. The g factor determines the precession frequency of the electron spin polarization. Changing the g factor changes the PSC itself, so the steep echoes are themselves, in a sense, distributed. We must model steeps from start to finish for each g factor and combine the resulting S_z.

While we have physical justification for this distribution, we do not have a good sense for how wide it should be. We know from the delay scans shown in the previous chapter that there cannot be too wide a spread in g factors, or else the TRKR would have been overwhelmed by beating. Apart from the wavelengths where we observe two-species behavior, this does not appear to be the case. Further, the work at Dortmund shows that RSA acquires an amplitude envelope for a g factor distribution. Unlike the dependence of peak amplitude on external field we observe, they see a reduction in amplitude that increases for increasing magnetic field. Our amplitude falls off as the sweep progresses, suggesting that this distribution will not be sufficient to totally describe our system.

7.5.3 Candidate: Laser Wavelength

The final distribution under consideration is not material-dependent. In Fig. 6.3, we compared the PL features of our material to the width of our laser. The full width at half maximum of the laser lies in the range of 0.5 to 0.7 nm. This makes the laser much narrower than the exciton features we are querying but still wide enough such that the OSE rotation angle Φ can change across its extent. Our model treats the laser as a single wavelength. Instead, we consider that the edges of the laser pulse's spectrum could lead to appreciably different values for Φ, and thus lead to appreciably different values for B_{N}. Unlike the nuclear-coupling constants, we do not need to guess at a shape and width of this distribution, or even a physical justification.

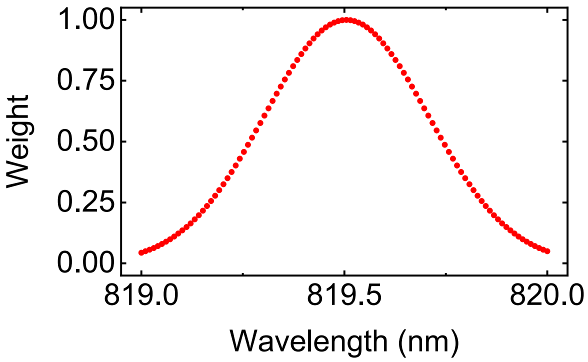

Figure 7.12: Gaussian distribution of wavelengths used for simulating the effect of a distribution of electron-nuclear interactions on measured spin polarization. One hundred evenly-spaced wavelengths are selected from the range 819.0 to 820.0 nm, weighted by a Gaussian shape with center amplitude 1. Weights provided by Michael Dominguez.

The laser wavelength, through the optical detuning Δ, affects every aspect of the system, from the OSE rotation angle Φ to the amplitude of the spin polarization components themselves. We can best think of this scenario as a composition of steep sweeps for every detuning, with the weighting of each sweep determined by the spectral profile of the laser. From the last chapter, we already know how individual field sweeps will change based on wavelength.

Because we know the width of our laser spectrum, we can test our model incorporating a distribution of detunings, employing the following method. First, we represent our laser pulse as a Gaussian centered at 819.5 nm with full-width at half-maximum of 0.6 nm. We discretize the Gaussian, selecting one hundred evenly-spaced detunings. This distribution is shown in Fig. 7.12, though at this juncture we do not normalize it. Then, we simulate the steep sweep for each detuning. The final sweep is a composite of the hundred individual steep sweeps, weighted by the Gaussian distribution. We can compare this resulting simulation to our experimental data to gauge the plausibility of our distribution. For now, we are interested in general qualitative correspondence; quantitative takeaways are left for future work.

Rather than try to match simulation wavelengths to the exact wavelengths used in our

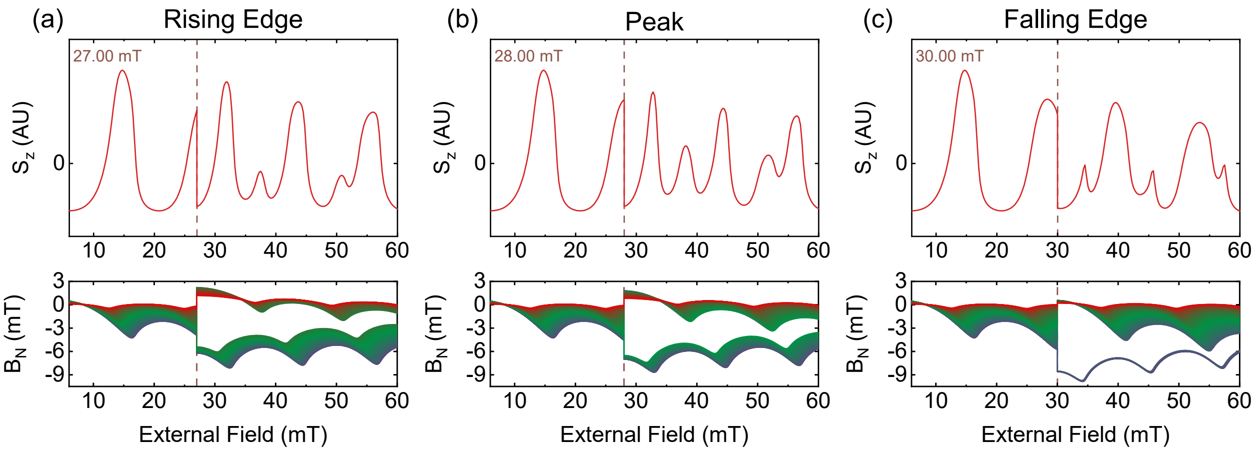

Figure 7.13: Simulated spin polarization S_z as a function of external magnetic field for a fixed pump-probe delay of 13 ns from Fig. 7.10 incorporating a wavelength distribution (Fig. 7.12). The distribution covers 100 discrete wavelengths, with the 100 corresponding Overhauser fields shown in the bottom panels. Each of the (a) rising edge, (b) peak, and (c) falling edge steeps show a steep echo effect, corresponding to a split in the set of Overhauser fields. Simulations assume $T_{1e} = 280$ s, $T_{1n} = 180$ s, spin lifetime $T_2^* = 30$ ns, pulse duration $\tau_p = 1$ ps, and pulse area $\theta = \pi/4$. Simulation provided by Michael Dominguez.

experiments, we again use the steep fields for rising edge, peak, and falling edge chosen for Fig. 7.10. These simulations are shown in Fig. 7.13.

The top panels of the figure show steep sweeps that, while not a perfect match to our data due to the RSA peak width, reproduce the general aspects of the steep echo. The bottom panels display the simulated Overhauser fields. At the steep, we see the splitting of B_N we had inferred from the steep echo data. This split occurs for each case considered here, with the echo effect more pronounced when the split is nearly even. As the steep continues, the two bands of Overhauser fields build back towards one another. Barring another steep, the echo will eventually fade away.

Both rising edge and falling edge cases (7.13a and 7.13c) show echoing, in contrast to our observations. Adjusting the nuclear timescales used in the simulation, which differ from the values used in the previous chapter, may resolve this discrepancy, as will using a Gaussian distribution of the appropriate width.

Despite its flaws, this distribution is very promising for describing our physical system.

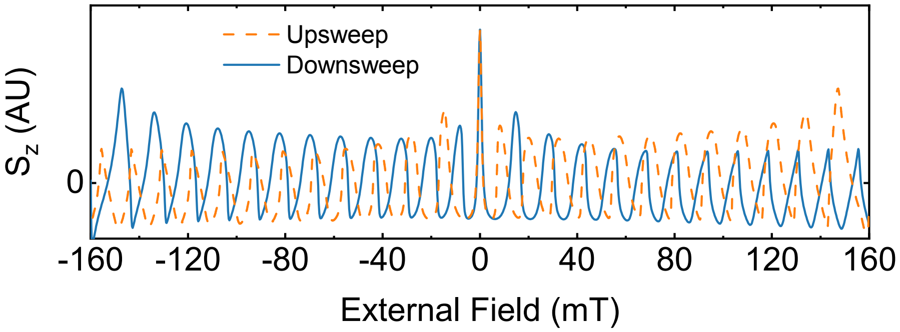

Figure 7.14: Simulated spin polarization S_z as a function of external magnetic field for a fixed pump-probe delay of 13 ns. The field range -160 to $+160$ mT matches the zero-crossing in Fig. 6.1. This simulation incorporates the wavelength distribution (Fig. 7.12) described in the text. Simulation assumes $T_{1e} = 280$ s, $T_{1n} = 180$ s, spin lifetime $T_2^* = 30$ ns, pulse duration $\tau_p = 1$ ps, and pulse area $\theta = \pi/4$. Simulation provided by Michael Dominguez.

Further in this distribution's favor is the simulated -160 to $+160$ mT zero-crossing shown in Fig. 7.14. Just like in our data, the amplitude of the RSA peaks decreases as the steep progresses, before seemingly resetting when crossing zero field. We also observe the peaks right before the zero-peak (-1 for upsweep and $+1$ for downsweep) pushed closer to the zero-peak, with reduced width compared to the preceding peaks. This seeming compaction of these peaks was present in the data but had not emerged from the previous iteration of the model. If this type of distribution is not a valid explanation for our experimental observations, it is at least a strong proof of principle.

7.6 Future Outlook

With three candidate distributions in hand, one thing is clear: the key to replicating the steep echo lies in the presence of some distributed quantity. Without intending to do so, our pursuit of the steep echo led us to address the amplitude-dependence lacking from the first iteration of our model. Thus, our model is now more accurately able to reproduce our history-dependent DNP.

So far, the steep echo has been presented as a curiosity that only emerged by the right

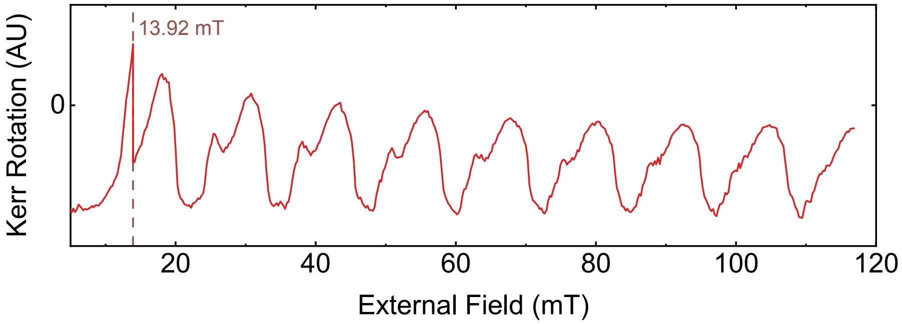

Figure 7.15: Steep sweep with steep echo on an extended field range. Kerr rotation measured as a function of external magnetic field for a fixed pump-probe delay of 13 ns at laser wavelength 819.3 nm. The external magnetic field is swept up from −5 mT to the steep field +13.92 mT (dashed brown line) and held constant for 2 min. The field is then swept up to +120 mT, though a portion of the sweep preceding the steep field is omitted. The extended field range post-steep shows the echo diminishing as the sweep progresses.

choice of steep field in a novel field scan. This characterization is certainly in line with the echo's first observation in Ref. [10]. However, we must not lose sight of the big picture. The steep echo is effectively a minutes-long memory of precise field history in the electron-nuclear spin system. While no memory architectures are currently built around RSA (that we know of), the steep echo hints at the potential the electron-nuclear spin system possesses for data processing and storage applications.

Even so, there is great utility in the steep echo for refining our DNP model. Consider the steep sweeps shown in Figs. 7.15 and 7.16. Unlike the sweeps shown so far in this chapter, these include many peaks following the steep. We observe the echo fading with each subsequent peak. As another point of difference, Fig. 7.16 features a ten-minute steep rather than the standard two minutes. Together, these experiments introduce additional measures of time into our system. The severity of the Overhauser field buildup and the time it takes for the distributed precession frequencies to coalesce again provide another window into the nuclear polarization timescales T_{1e} and T_{1n}. We can fine-tune the values used in our model through comparison and iteration. Perhaps we can even develop an approach to extract these values from real data. Such a goal is saved for future work.

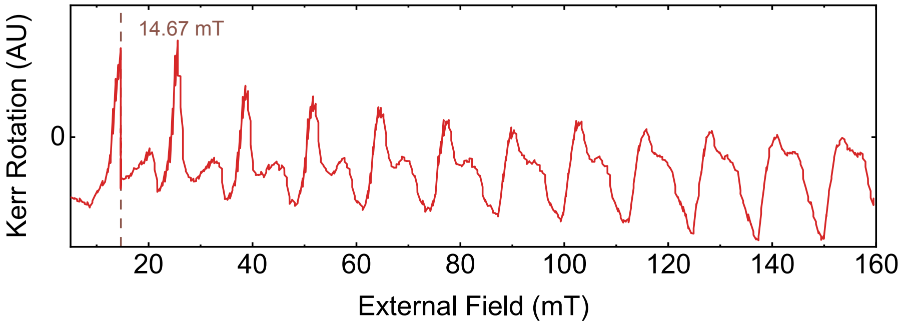

Figure 7.16: Long-time steep sweep with steep echo on an extended field range. Kerr rotation measured as a function of external magnetic field for a fixed pump-probe delay of 13 ns at laser wavelength 819.3 nm. The external magnetic field is swept up from −5 mT to the steep field +14.67 mT (dashed brown line) and held constant for 10 min. The field is then swept up to +160 mT, though a portion of the sweep preceding the steep field is omitted. Here, the field is swept in steps of 0.5 mT with each step repeated twice, resulting in the same field sweep rate as elsewhere. The prolonged steep time results in a pronounced deformation of the peak, while the extended field range post-steep shows the echo diminishing as the sweep progresses.

CHAPTER 8

Spintronics: Things are Looking Up (and Down)!

The spin of the electron holds great potential for the future of information processing and storage. To realize this promise, we must understand how to effectively generate, manipulate, and detect electron spin polarization in materials of interest. This dissertation is submitted in pursuit of that goal.

We have demonstrated a modified technique for measuring current-induced spin polarization in InGaAs. Applying a current to our material generates heat, and this heat can alter the optical properties of our sample. For the optical Faraday rotation measurements shown here, this becomes a barrier to reliable measurements of the CISP spin generation rate. Our technique is fairly straightforward: reduce the amount of time that the voltage is nonzero, reducing the amount of heat dissipated in the sample. Coupled with a simple data correction factor, we show that this technique preserves the measured generation rate at low applied voltages. Further, at high voltages, this reduction in heat increases the observed generation rate, bringing it into agreement with the expected linear behavior in voltage.

We have described at length the coupled electron-nuclear spin system in GaAs at 10 K. Spurred by the observation of a magnetic-field-sweep-direction-dependence in our Kerr rotation field scans, we laid out a model in which our optical pump pulses both generate spin polarization and rotate the existing spin polarization about the optical axis. We attribute this rotation to the optical Stark effect. This rotated spin polarization polarizes nuclear spins along the external field direction, accumulating an Overhauser field experienced by the electrons. When the nuclear polarization and relaxation timescales are much longer than our experimental timescale, field-history-dependent behavior emerges. We considered the various dependencies of our model on experimental parameters wavelength, pump power, elapsed time, and field history. The steep sweep class of experiments encapsulate this history dependence. We recast our discussion in terms of nuclear-induced frequency focusing, giving us insight into the mysterious steep echo. Finally, we proposed modifications to our model to fully capture the coupled electron-nuclear spin system.

Both of these projects share a common thread: in order to fully understand the outcomes of our experiments, we must be aware of any factors that could compromise the electron spin system. For CISP experiments, current heating has impacted our ability to reliably measure the spin generation rate at higher applied voltages. Our method greatly reduces heating, expanding the parameter space we can use for investigating the underlying physical mechanisms of CISP. For DNP experiments, the electron and nuclear spin systems are coupled in a nonlinear way. We did not attempt to remove these effects but rather to understand them. Our hope is that this interplay can be utilized in the future for spintronics applications. At the very least, our work can serve as a guide to future researchers, providing them insight on the nuclear effects to expect when working in GaAs.

8.1 Future Directions

With these improved techniques and understandings in hand, we turn our gaze to the future. The work in this dissertation lends itself to extensions in the study of both CISP and DNP.

8.1.1 Current-Induced Spin Polarization

Now that we have a technique for reducing heating in CISP measurements, we must put it to use. While much progress has been made in recent years in understanding the underlying mechanisms behind CISP, this is still an open question. Theoretical work has designated two-dimensional systems as the platform for this study [19], so we turn our attention there. One experimental technique not considered in this dissertation is the measurement of the spin Hall effect [62, 108, 109]. Implementing this measurement in our optical setup will give us another tool to explore the interaction between applied current and electron spin polarization.

8.1.2 Dynamic Nuclear Polarization

In some respects, we have solved the mystery of the history-dependent DNP, but there are still leads we have yet to follow. One such mystery is the appearance of two-species behavior in delay scans taken at certain wavelengths. While this behavior should not impact our field scans and hence the majority of our measurements, it is still a curiosity that demands further attention, far more than we have provided it here.

We concluded with a model that incorporates a distribution to explain the steep echo. Despite these encouraging preliminary results, we have not yet committed to the physical source of the distribution, though the optical bandwidth is a leading candidate. Ideally, we will devise experiments that allow us to distinguish further between the candidate distributions.

One potential aid to this end would be a direct measurement of the nuclear timescales. So far, we have proceeded with the expected values from the literature, refining them by correspondence between our simulations and our experimental data. Rather than a direct measurement, the steep echo may be the best tool for this job.

On the subject of experiments, our methods can be improved as well. Our current process for measuring the Overhauser field involves Snapshot TRKR. Individual field scans only take a few minutes, but when multiplying that by 20 or more delay steps, an individual run can surpass an hour. This is more severe when two-minute steeps are included. Any revision of our method that can reliably measure B_{N} in a shorter amount of time would be worth pursuing. Further, Ref. [55] discussed potential improvements for Snapshot TRKR in terms of the delay steps included and the fitting method utilized. These should be considered moving forward.

Finally, we can extend the scope of this study in two very different directions. First, we can carry out these same experiments in other materials, either GaAs with different dopant levels or another material altogether. We are especially interested in how ubiquitous this behavior is in the other GaAs samples we have in our laboratory. Second, we can extend the scope of our model down to the quantum level. Our current model is semiclassical in nature, but a full quantum treatment may give us further insight. There is no better way to get to the bottom of the mystery than to go as low in scale as possible!

8.2 Parting Thoughts

Spintronics offer an attractive alternative to modern electronics, with capability beyond what is possible with existing technology, but in order to realize this vision we must understand electron spin dynamics in semiconductors. This dissertation strives towards this goal by enabling investigations into CISP, a polarization generation mechanism, in InGaAs, and by focusing on understanding a DNP in GaAs that encodes minutes-long magnetic field history of the electron spin system. Through this work, we have contributed to the larger ongoing project of bringing spintronics one step closer to reality.

APPENDICES

APPENDIX A

Full Derivation for the RSA and OSE Matrix Equations

A.1 Motivation

In Chapter 2, we presented the Bloch equation to describe electron spin dynamics in our materials. We solved the equation in the case of optical orientation along $\hat{z}$ at time $t = 0$ and an external magnetic field $\vec{B} = B_{\mathrm{ext}}\hat{x}$:

$$S_x\left(t, B_{\mathrm{ext}}\right) = 0, \tag{A.1a}$$

$$S_y\left(t, B_{\mathrm{ext}}\right) = S_0\,\Theta\left(t\right)\,e^{-t/\tau}\sin\left(\Omega t\right), \tag{A.1b}$$

$$S_z\left(t, B_{\mathrm{ext}}\right) = S_0\,\Theta\left(t\right)\,e^{-t/\tau}\cos\left(\Omega t\right), \tag{A.1c}$$

where Ω is the Larmor precession frequency $g\mu_B B_{\mathrm{ext}}/\hbar$. Dephasing may be anisotropic, but we assume the same timescale for each direction for simplicity, and denote it with the lifetime τ. Spin polarization is precessing and decaying in the yz-plane. Were there any initial spin polarization along $\hat{x}$, S_x would just have decayed exponentially with the timescale τ. Note the Heaviside function $\Theta\left(t\right)$ added to ensure causality.

These equations specifically describe spin dynamics for an initial spin polarization $\vec{S} = S_0\hat{z}$ without any additional spin generation. This is not the case in our experiments, where we are periodically pumping our system with pump pulses. The pulse frequency is 76 MHz, corresponding to a pulse period $T_R = 13.16$ ns. In any system with spin dephasing time comparable to or exceeding T_R, we must consider the contribution from previous pulses in our analysis. This is as simple as adding up copies of Eq. A.1, each spaced in time by an integer multiple of T_R. This produces the equations

$$S_x\left(t, B_{\text{ext}}\right) = 0, \tag{A.2a}$$

$$S_y\left(t, B_{\text{ext}}\right) = S_0 \sum_{n=0}^{\infty} \Theta\left(t + nT_R\right)\, e^{-(t+nT_R)/\tau} \sin\left(\Omega\left(t + nT_R\right)\right), \tag{A.2b}$$

$$S_z\left(t, B_{\text{ext}}\right) = S_0 \sum_{n=0}^{\infty} \Theta\left(t + nT_R\right)\, e^{-(t+nT_R)/\tau} \cos\left(\Omega\left(t + nT_R\right)\right). \tag{A.2c}$$

The equation for S_x would simply be a sum of decaying exponentials, like S_y or S_z without the sinusoid. These equations are sometimes displayed without the Heaviside functions. Without them, we must restrict our attention to non-negative decay times only. Here, we can consider any time, indexed to the arrival of the most recent pulse (so for any time $t > 13.16$ ns, we must assume the train of pulses has stopped).

Some authors will leave the equations as is for their analysis. Fitting experimental data often requires only a few extra pulses, so most of the sum can be disregarded. Other authors, notably the authors of Ref. [36], will evaluate the sum. By restricting the domain to $(0, T_R]$, we can omit the Heaviside functions. Noticing that S_z and S_y are the real and imaginary parts, respectively, of a single complex exponential, the two sums can be reduced to one, a geometric series of an exponential function with a complex argument [36]. From there, we arrive at the single expressions

$$S_x\left(t, B_{\text{ext}}\right) = 0, \tag{A.3a}$$

$$S_y\left(t, B_{\text{ext}}\right) = -S_0\, r e^{-t/\tau} \sin\left(\Omega t - \gamma\right), \tag{A.3b}$$

$$S_z\left(t, B_{\text{ext}}\right) = S_0\, r e^{-t/\tau} \cos\left(\Omega t - \gamma\right). \tag{A.3c}$$

Here, r is a field-dependent effective amplitude

$$r = \left(1 - 2e^{-T_R/\tau} \cos\left(\Omega T_R\right) + e^{-2T_R/\tau}\right)^{-1/2} \tag{A.3d}$$

and γ a field-dependent effective phase

$$\gamma = -\arctan\left(\frac{e^{-T_R/\tau}\sin\left(\Omega T_R\right)}{1 - e^{-T_R/\tau}\cos\left(\Omega T_R\right)}\right). \tag{A.3e}$$

The influence of all previous pulses combines to modify the amplitude of the precessing spin polarization, an amplitude that is now dependent on the magnitude of the external magnetic field, and impart a field-dependent phase. When we make changes to the delay time or magnetic field on laboratory time scales, enough pulses are incident in that time interval that we can assume the system reaches the infinite pulse limit by the time we are taking data. This makes Eqs. A.3 valid for our experiments even during scans.

In this dissertation, we consider a different approach to evaluating the effect of an infinite number of pulses. We know from the Bloch equation that the spin polarization will precess, which is rotation about an axis. We can phenomenologically build up an expression for spin polarization after an infinite number of pulses in terms of rotation matrices. We will arrive at the same place as Ref. [36], but with the benefit of evaluating initial spin polarizations that do not lie along $\hat{z}$. Further, this formalism is extendable to applications involving the optical Stark effect, which we utilize in Chapter 6.

A.2 RSA: Constructing the Infinite Sum

We consider rotations in three dimensions. In our case, all of the rotations are about $\hat{x}$. A rotation through angle θ about $\hat{x}$ is given by

$$\hat{R}\left[\theta\right] = \begin{pmatrix} 1 & 0 & 0 \\ 0 & \cos\theta & -\sin\theta \\ 0 & \sin\theta & \cos\theta \end{pmatrix}. \tag{A.4}$$

To distinguish the rotation matrix from a function, and with the rotation operators of quantum mechanics in mind, we use "hat" notation and brackets for the argument. Rotations about $\hat{y}$ and $\hat{z}$ can be similarly defined, as can rotations about arbitrary unit vectors $\hat{u}$. We do not treat these here.

It can be shown that two subsequent rotations about the same axis are equivalent to a single rotation through an angle equal to the sum of the two angles of the individual rotations. In other words, $\hat{R}[\theta_1]\,\hat{R}[\theta_2] = \hat{R}[\theta_1 + \theta_2]$.

At every time interval T_R, a pulse is incident on our system. For now, we will assume that each pulse excites the same spin polarization $\vec{S}_0$ regardless of what else is going on in the system, though we do not have to define $\vec{S}_0$ at this point. If there is any component along $\hat{x}$, it will simply decay and not precess. A schematic of this process is shown in Fig. 2.10; the matrix expression for $\vec{S}$ is constructed in Table A.1.

Table A.1: Step-by-step construction of the RSA matrix equation.

$\vec{S}$ (matrix form)	Time t Since First Pulse
$\vec{S}_0$	$t = 0$ (first pulse)
$\hat{R}[\Omega t]\; e^{-t/\tau}\, \vec{S}_0$	$0 < t < T_R$
$\hat{R}[\Omega T_R]\; e^{-T_R/\tau}\, \vec{S}_0$	$t = T_R^-$ (pre-pulse)
$\vec{S}_0 + \hat{R}[\Omega T_R]\; e^{-T_R/\tau}\, \vec{S}_0$ $\left(\hat{I} + \hat{R}[\Omega T_R]\; e^{-T_R/\tau}\right) \vec{S}_0$	$t = T_R^+$ (post-pulse)
$\hat{R}[\Omega t]\; e^{-t/\tau} \left(\hat{I} + \hat{R}[\Omega T_R]\; e^{-T_R/\tau}\right) \vec{S}_0$ $\left(\hat{R}[\Omega t]\; e^{-t/\tau} + \hat{R}[\Omega t]\,\hat{R}[\Omega T_R]\; e^{-(t+T_R)/\tau}\right) \vec{S}_0$	$T_R < t < 2T_R$
$\left(\hat{R}[\Omega T_R]\; e^{-T_R/\tau} + \hat{R}^2[\Omega T_R]\; e^{-2T_R/\tau}\right) \vec{S}_0$	$t = 2T_R^-$ (pre-pulse)
$\vec{S}_0 + \left(\hat{R}[\Omega T_R]\; e^{-T_R/\tau} + \hat{R}^2[\Omega T_R]\; e^{-2T_R/\tau}\right) \vec{S}_0$ $\left(\hat{I} + \hat{R}[\Omega T_R]\; e^{-T_R/\tau} + \hat{R}^2[\Omega T_R]\; e^{-2T_R/\tau}\right) \vec{S}_0$	$t = 2T_R^+$ (post-pulse)
$\vdots$	$\vdots$
$\left(\hat{I} + \hat{R}[\Omega T_R]\; e^{-T_R/\tau} + \cdots + \hat{R}^N[\Omega T_R]\; e^{-NT_R/\tau}\right) \vec{S}_0$ $\left(\sum_{n=0}^{N} \hat{R}^n[\Omega T_R]\; e^{-nT_R/\tau}\right) \vec{S}_0$	$t = NT_R^+$ (post-pulse)
$\vdots$	$\vdots$
$\left(\sum_{n=0}^{\infty} \hat{R}^n[\Omega T_R]\; e^{-nT_R/\tau}\right) \vec{S}_0$	$t = \infty$

The spin polarization measured in our experiments can be thought of as having evolved for a time t following the final pulse considered. We apply a rotation and exponential decay (for time t) to the infinite-pulse expression constructed in the table, yielding an expression for $\vec{S}(t)$:

$$\begin{aligned}\vec{S} &= \hat{R}[\Omega t]\ e^{-t/\tau}\left(\sum_{n=0}^{\infty}\hat{R}^{n}[\Omega T_R]\ e^{-nT_R/\tau}\right)\vec{S}_0\\ &= \left(\sum_{n=0}^{\infty}\hat{R}[\Omega t]\,\hat{R}^{n}[\Omega T_R]\ e^{-(t+nT_R)/\tau}\right)\vec{S}_0\\ &= \left(\sum_{n=0}^{\infty}\hat{R}[\Omega t]\,\hat{R}[n\Omega T_R]\ e^{-(t+nT_R)/\tau}\right)\vec{S}_0\\ &= \left(\sum_{n=0}^{\infty}\hat{R}[\Omega(t+nT_R)]\ e^{-(t+nT_R)/\tau}\right)\vec{S}_0. \qquad (A.5)\end{aligned}$$

In the familiar case of $\vec{S}_0 = S_0\hat{z}$, we need only consider the z-column of the rotation matrix in the final expression. Familiarity ensues, as

$$\vec{S}(t) = S_0\sum_{n=0}^{\infty}\begin{pmatrix}0\\ -\sin(\Omega(t+nT_R))\\ \cos(\Omega(t+nT_R))\end{pmatrix}e^{-(t+nT_R)/\tau}. \qquad (A.6)$$

The only thing missing is the Heaviside function.

A.3 RSA: Evaluating the Infinite Sum

The rotation matrix approach has so far earned us nothing new. We generated an expression for the relation between the initial and final spin polarizations after an infinite number of pulses:

$$\vec{S}(t) = \left(\sum_{n=0}^{\infty}\hat{R}^{n}[\Omega T_R]\ e^{-nT_R/\tau}\right)\vec{S}_0. \qquad (A.7)$$

The sum in parentheses carries within it the fact that there have been infinitely many pulses incident on the system. However, it is independent of $\vec{S}_0$. Whether we orient spin polarization along $\hat{z}$, $\hat{x}$, or some arbitrary axis, this infinite sum of matrices carries the initial polarization through an infinite number of precessions about $\hat{x}$. We do not need to specify $\vec{S}_0$ to evaluate this sum.

The concept of geometric series extends to square matrices as well as scalars. For a matrix A with determinant less than 1,

$$\sum_{n=0}^{\infty} A^n = \left(\hat{I} - A\right)^{-1},$$

where the $^{-1}$ indicates the matrix inverse. Pure rotation matrices by definition have determinant 1. By incorporating the exponential factor $e^{-T_R/\tau}$, we ensure that our sum of matrices has determinant less than 1. We will label the resulting matrix as $\hat{R}^{\infty}$ even though it is not technically a rotation matrix. Then

$$\begin{aligned}
\hat{R}^{\infty} &= \sum_{n=0}^{\infty} \hat{R}^n \left[\Omega T_R\right] \, e^{-nT_R/\tau} \\
&= \sum_{n=0}^{\infty} \left(\hat{R}\left[\Omega T_R\right] \, e^{-T_R/\tau}\right)^n \\
&= \left(\hat{I} - \hat{R}\left[\Omega T_R\right] \, e^{-T_R/\tau}\right)^{-1} \\
&= \left(\begin{pmatrix} 1 & 0 & 0 \\ 0 & 1 & 0 \\ 0 & 0 & 1 \end{pmatrix} - \begin{pmatrix} 1 & 0 & 0 \\ 0 & \cos\left(\Omega T_R\right) & -\sin\left(\Omega T_R\right) \\ 0 & \sin\left(\Omega T_R\right) & \cos\left(\Omega T_R\right) \end{pmatrix} e^{-T_R/\tau}\right)^{-1} \\
&= \begin{pmatrix} 1 - e^{-T_R/\tau} & 0 & 0 \\ 0 & 1 - e^{-T_R/\tau}\cos\left(\Omega T_R\right) & e^{-T_R/\tau}\sin\left(\Omega T_R\right) \\ 0 & -e^{-T_R/\tau}\sin\left(\Omega T_R\right) & 1 - e^{-T_R/\tau}\cos\left(\Omega T_R\right) \end{pmatrix}^{-1} .
\end{aligned} \tag{A.8}$$

Square matrices are only invertible when their determinant is nonzero, so we calculate:

$$\begin{aligned}
\det\left[\left(\hat{R}^{\infty}\right)^{-1}\right] &= \left(1 - e^{-T_R/\tau}\right)\left(\left(1 - e^{-T_R/\tau}\cos\left(\Omega T_R\right)\right)^2 + \left(e^{-T_R/\tau}\sin\left(\Omega T_R\right)\right)^2\right) \\
&= \left(1 - e^{-T_R/\tau}\right)\left(1 - 2e^{-T_R/\tau}\cos\left(\Omega T_R\right) + \cdots\right. \\
&\qquad \left.\cdots + e^{-2T_R/\tau}\cos^2\left(\Omega T_R\right) + e^{-2T_R/\tau}\sin^2\left(\Omega T_R\right)\right) \\
&= \left(1 - e^{-T_R/\tau}\right)\left(1 - 2e^{-T_R/\tau}\cos\left(\Omega T_R\right) + e^{-2T_R/\tau}\right) \\
&\neq 0,
\end{aligned}$$

unless either $\tau \to \infty$ and the total spin polarization diverges or $T_R = 0$, in which case there was only ever one pulse anyways. Notice that the second term in parentheses is related to the r we defined earlier in Eq. A.3. That is,

$$\det\left[\left(\hat{R}^{\infty}\right)^{-1}\right] = \left(1 - e^{-T_R/\tau}\right) r^{-2}.$$

This identification is key for interpreting the inverted matrix.

Our matrix is invertible. Depending on the complexity of a 3×3 matrix, it may be easier to have *Mathematica* carry out the calculation. Be warned that the simplifications we prefer, based on the physical quantities we define, do not necessarily match the simplifications that *Mathematica*'s `FullSimplify` command will carry out. The resulting matrix is

$$\hat{R}^{\infty} = \begin{pmatrix} \frac{1}{1-e^{-T_R/\tau}} & 0 & 0 \\ 0 & \frac{1-e^{-T_R/\tau}\cos(\Omega T_R)}{1-2e^{-T_R/\tau}\cos(\Omega T_R)+e^{-2T_R/\tau}} & \frac{-e^{-T_R/\tau}\sin(\Omega T_R)}{1-2e^{-T_R/\tau}\cos(\Omega T_R)+e^{-2T_R/\tau}} \\ 0 & \frac{e^{-T_R/\tau}\sin(\Omega T_R)}{1-2e^{-T_R/\tau}\cos(\Omega T_R)+e^{-2T_R/\tau}} & \frac{1-e^{-T_R/\tau}\cos(\Omega T_R)}{1-2e^{-T_R/\tau}\cos(\Omega T_R)+e^{-2T_R/\tau}} \end{pmatrix}. \tag{A.9}$$

Careful comparison to Eqs. A.3 allows us to interpret the elements of our matrix in a way that simplifies it greatly and gives us insight:

$$\hat{R}^{\infty} = \begin{pmatrix} \frac{1}{1-e^{-T_R/\tau}} & 0 & 0 \\ 0 & r\cos\gamma & r\sin\gamma \\ 0 & -r\sin\gamma & r\cos\gamma \end{pmatrix}. \tag{A.10}$$

Any spin polarization along $\hat{x}$ will simply decay, with the decay amplitude just being evaluation of an infinite sum of exponential decays. Meanwhile, S_y and S_z are coupled. Infinitely many pulses have the effect of modifying by an amplitude r and rotating by an angle γ. As with all rotations, this can be thought of as a phase shift. This was our earlier conclusion, but here the effect of previous pulses are isolated to a single matrix with a ready interpretation. Furthermore, we did not need to assume the form of the initial spin polarization.

The functional forms of $\sin\gamma$ and $\cos\gamma$ may not have been clear from Eqs. A.3. Consider that if

$$\tan\gamma = -\left(\frac{e^{-T_R/\tau}\sin\left(\Omega T_R\right)}{1-e^{-T_R/\tau}\cos\left(\Omega T_R\right)}\right),$$

then the sides of a triangle defined by the angle γ are given by $a = 1 - e^{-T_R/\tau}\cos\left(\Omega T_R\right)$ and $b = -e^{-T_R/\tau}\sin\left(\Omega T_R\right)$. This yields a hypotenuse length c, given by

$$\begin{aligned} c^2 &= a^2 + b^2 \\ c^2 &= \left(1 - e^{-T_R/\tau}\cos\left(\Omega T_R\right)\right)^2 + \left(-e^{-T_R/\tau}\sin\left(\Omega T_R\right)\right)^2 \\ &= 1 - 2e^{-T_R/\tau}\cos\left(\Omega T_R\right) + e^{-2T_R/\tau} \\ c &= \left(1 - 2e^{-T_R/\tau}\cos\left(\Omega T_R\right) + e^{-2T_R/\tau}\right)^{1/2}. \end{aligned}$$

See that $c = r^{-1}$, so the lower matrix entries are essentially a/c^2 or b/c^2, and we arrive at Eq. A.10.

Taken together, we can rewrite the total spin polarization at a time t after the final pulse as

$$\vec{S}\left(t\right) = \hat{R}\left[\Omega t\right]\, e^{-t/\tau}\hat{R}^{\infty}\vec{S}_0. \tag{A.11}$$

There are two approaches to move forward. Either treat $\hat{R}^{\infty}\vec{S}_0$ as the initial spin polarization for a single-pulse precession and decay or multiply the matrices together to get the new effective rotation matrix (including the exponential decay of course). The former approach is straightforward, especially with a simple initial spin polarization along a single axis. Instead, we will calculate the final matrix to describe the entirety of the experiment on the initial spin polarization. For clarity, we will leave the exponential factor out of the calculations and restore it at the end.

The desired matrix product is given by

$$\hat{R}\left[\Omega t\right]\hat{R}^{\infty} = \begin{pmatrix} 1 & 0 & 0 \\ 0 & \cos\left(\Omega t\right) & -\sin\left(\Omega t\right) \\ 0 & \sin\left(\Omega t\right) & \cos\left(\Omega t\right) \end{pmatrix} \begin{pmatrix} \frac{1}{1-e^{-T_R/\tau}} & 0 & 0 \\ 0 & r\cos\gamma & r\sin\gamma \\ 0 & -r\sin\gamma & r\cos\gamma \end{pmatrix}$$

$$= \begin{pmatrix} \frac{1}{1-e^{-T_R/\tau}} & 0 & 0 \\ 0 & r\begin{pmatrix} \cos(\Omega t)\cos\gamma + \\ \sin(\Omega t)\sin\gamma \end{pmatrix} & -r\begin{pmatrix} \sin(\Omega t)\cos\gamma - \\ \cos(\Omega t)\sin\gamma \end{pmatrix} \\ 0 & r\begin{pmatrix} \sin(\Omega t)\cos\gamma - \\ \cos(\Omega t)\sin\gamma \end{pmatrix} & r\begin{pmatrix} \cos(\Omega t)\cos\gamma + \\ \sin(\Omega t)\sin\gamma \end{pmatrix} \end{pmatrix}$$

$$= \begin{pmatrix} \frac{1}{1-e^{-T_R/\tau}} & 0 & 0 \\ 0 & r\cos\left(\Omega t-\gamma\right) & -r\sin\left(\Omega t-\gamma\right) \\ 0 & r\sin\left(\Omega t-\gamma\right) & r\cos\left(\Omega t-\gamma\right) \end{pmatrix}. \tag{A.12}$$

Reading off the right-most column, we recognize the expressions derived previously for initial polarization along $\hat{z}$. Viewing the whole matrix, we see that any spin polarization along $\hat{x}$ will simply decay while S_y and S_z are mixed, with amplitude modified by r and rotation angle modified by γ.

We write again $\vec{S}$ in terms of $\vec{S}_0$ with the matrix product evaluated:

$$\vec{S}\left(t\right) = e^{-t/\tau} \begin{pmatrix} \frac{1}{1-e^{-T_R/\tau}} & 0 & 0 \\ 0 & r\cos\left(\Omega t-\gamma\right) & -r\sin\left(\Omega t-\gamma\right) \\ 0 & r\sin\left(\Omega t-\gamma\right) & r\cos\left(\Omega t-\gamma\right) \end{pmatrix} \vec{S}_0. \tag{A.13}$$

This matrix equation holds for any initial spin polarization, so long as the external field is applied along $\hat{x}$. In the case of optical orientation for spin polarization along $\hat{z}$:

$$\vec{S}\left(t\right) = S_0 r\ e^{-t/\tau} \begin{pmatrix} 0 \\ -\sin\left(\Omega t-\gamma\right) \\ \cos\left(\Omega t-\gamma\right) \end{pmatrix}. \tag{A.14}$$

Thus, the matrix approach reproduces the alternative approach of Ref. [36] with perhaps more flexibility and more obvious physical interpretation.

A.4 Rotation via Optical Pulses (the Optical Stark Effect)

In Chapter 6, we introduced the optical Stark effect (OSE) as a means by which our ultrafast pump pulses can rotate exisitng spin polarization in our material. Thus, we can describe it with a rotation matrix of sorts. Integrating this approach into the above derivation for RSA will yield an expression for $\vec{S}\,(t)$ that will be applicable to our GaAs system.

The relationship between the spin polarization components pre $(-)$ and post $(+)$ -pulse are given by the equations [15]

$$S_x^+ = Q\cos\Phi S_x^- + Q\sin\Phi S_y^-, \tag{A.15a}$$

$$S_y^+ = Q\cos\Phi S_y^- - Q\sin\Phi S_x^-, \tag{A.15b}$$

$$S_z^+ = \frac{Q^2-1}{4} + \frac{Q^2+1}{2} S_z^-. \tag{A.15c}$$

Forming these together into matrix form, we arrive at something resembling a rotation matrix:

$$\hat{R}_{\mathrm{OSE}} = \begin{pmatrix} Q\cos\Phi & Q\sin\Phi & 0 \\ -Q\sin\Phi & Q\cos\Phi & 0 \\ 0 & 0 & \delta \end{pmatrix}, \tag{A.16}$$

where we use δ as shorthand for the modified amplitude of S_z following the action of a pump pulse, $\left(Q^2+1\right)/2$. Note that the direction of rotation is opposite to that considered above for spin precession. This is not a proper rotation matrix (like spin precession) due to the amplitude modification Q and the action on S_z. Thus we will write it as a special term $\hat{R}_{\mathrm{OSE}}$ without an argument.

Constructing the infinite sum is similar to before, but now the OSE also acts at every multiple of T_R. We proceed under the assumption that the pulse acts to simultaneously rotate the existing spin polarization along $\hat{x}$ and $\hat{y}$ while generating a new spin polarization S_0. Above, we did not presume the direction of the generated spin polarization. Since the OSE rotation is about the optical axis, we must declare S_0 up front. Therefore, we calculate the entire rotation matrix only to be able to use the z-column. Construction is analogous to that for the RSA equation and is shown in Table A.2. That said, this result could potentially find use in a case with very small spin polarization along another axis (as a perturbation). Spin generation along another axis will require a different optical Stark matrix, with the precession matrix tied to the direction of the external magnetic field. Finally, the Eqs. A.15 give a value for S_0 as well: $\left(Q^2-1\right)/4$. We will make use of this expression near the end of our derivation.

Table A.2: Step-by-step construction of the RSA matrix equation incorporating the OSE.

$\vec{S}$ (matrix form)	Time t Since First Pulse
$\vec{S}_0$	$t = 0$ (first pulse)
$\hat{R}\left[\Omega t\right]\, e^{-t/\tau}\, \vec{S}_0$	$0 < t < T_R$
$\hat{R}\left[\Omega T_R\right]\, e^{-T_R/\tau}\, \vec{S}_0$	$t = T_R^-$ (pre-pulse)
$\vec{S}_0 + \hat{R}_{\text{OSE}}\hat{R}\left[\Omega T_R\right]\, e^{-T_R/\tau}\, \vec{S}_0$ $\left(\hat{I} + \hat{R}_{\text{OSE}}\hat{R}\left[\Omega T_R\right]\, e^{-T_R/\tau}\right) \vec{S}_0$	$t = T_R^+$ (post-pulse)
$\hat{R}\left[\Omega t\right]\, e^{-t/\tau} \left(\hat{I} + \hat{R}_{\text{OSE}}\hat{R}\left[\Omega T_R\right]\, e^{-T_R/\tau}\right) \vec{S}_0$ $\left(\hat{R}\left[\Omega t\right]\, e^{-t/\tau} + \hat{R}\left[\Omega t\right] \hat{R}_{\text{OSE}}\hat{R}\left[\Omega T_R\right]\, e^{-(t+T_R)/\tau}\right) \vec{S}_0$	$T_R < t < 2T_R$
$\left(\hat{R}\left[\Omega T_R\right]\, e^{-T_R/\tau} + \hat{R}\left[\Omega T_R\right] \hat{R}_{\text{OSE}}\hat{R}\left[\Omega T_R\right]\, e^{-2T_R/\tau}\right) \vec{S}_0$	$t = 2T_R^-$ (pre-pulse)
$\vec{S}_0 + \hat{R}_{\text{OSE}} \left(\hat{R}\left[\Omega T_R\right]\, e^{-T_R/\tau} + \hat{R}\left[\Omega T_R\right] \hat{R}_{\text{OSE}}\hat{R}\left[\Omega T_R\right]\, e^{-2T_R/\tau}\right) \vec{S}_0$ $\left(\hat{I} + \hat{R}_{\text{OSE}}\hat{R}\left[\Omega T_R\right]\, e^{-T_R/\tau} + \left(\hat{R}_{\text{OSE}}\hat{R}\left[\Omega T_R\right]\right)^2 e^{-2T_R/\tau}\right) \vec{S}_0$	$t = 2T_R^+$ (post-pulse)
$\vdots$	$\vdots$
$\left(\hat{I} + \hat{R}_{\text{OSE}}\hat{R}\left[\Omega T_R\right]\, e^{-T_R/\tau} + \cdots + \left(\hat{R}_{\text{OSE}}\hat{R}\left[\Omega T_R\right]\right)^N e^{-NT_R/\tau}\right) \vec{S}_0$ $\left(\sum_{n=0}^{N} \left(\hat{R}_{\text{OSE}}\hat{R}\left[\Omega T_R\right]\right)^n e^{-nT_R/\tau}\right) \vec{S}_0$	$t = NT_R^+$ (post-pulse)
$\vdots$	$\vdots$
$\left(\sum_{n=0}^{\infty} \left(\hat{R}_{\text{OSE}}\hat{R}\left[\Omega T_R\right]\right)^n e^{-nT_R/\tau}\right) \vec{S}_0$	$t = \infty$

As before, we will evaluate the infinite sum, now with a different matrix raised to the nth power. Then, we can apply a rotation and decay through experiment time t.

First off, we calculate the matrix $\hat{R}_{\text{rot}}$:

$$\begin{aligned}
\hat{R}_{\text{rot}} &= \hat{R}_{\text{OSE}}\hat{R}\left[\Omega T_R\right] \\
&= \begin{pmatrix} Q\cos\Phi & Q\sin\Phi & 0 \\ -Q\sin\Phi & Q\cos\Phi & 0 \\ 0 & 0 & \delta \end{pmatrix} \begin{pmatrix} 1 & 0 & 0 \\ 0 & \cos\left(\Omega T_R\right) & -\sin\left(\Omega T_R\right) \\ 0 & \sin\left(\Omega T_R\right) & \cos\left(\Omega T_R\right) \end{pmatrix} \\
&= \begin{pmatrix} Q\cos\Phi & Q\sin\Phi\cos\left(\Omega T_R\right) & -Q\sin\Phi\sin\left(\Omega T_R\right) \\ -Q\sin\Phi & Q\cos\Phi\cos\left(\Omega T_R\right) & -Q\cos\Phi\sin\left(\Omega T_R\right) \\ 0 & \delta\sin\left(\Omega T_R\right) & \delta\cos\left(\Omega T_R\right) \end{pmatrix}. \qquad \text{(A.17)}
\end{aligned}$$

The desired matrix, which we will designate as $\hat{R}_{\text{OSE}}^{\infty}$ despite not being a proper rotation matrix, is given by

$$
\begin{aligned}
\hat{R}_{\mathrm{OSE}}^{\infty} &= \sum_{n=0}^{\infty} \left(\hat{R}_{\mathrm{OSE}} \hat{R}\left[\Omega T_R\right]\right)^n e^{-nT_R/\tau} \\
&= \sum_{n=0}^{\infty} \left(\hat{R}_{\mathrm{OSE}} \hat{R}\left[\Omega T_R\right]\, e^{-T_R/\tau}\right)^n \\
&= \left(\hat{I} - \hat{R}_{\mathrm{OSE}} \hat{R}\left[\Omega T_R\right]\, e^{-T_R/\tau}\right)^{-1} \\
&= \left(\begin{pmatrix} 1 & 0 & 0 \\ 0 & 1 & 0 \\ 0 & 0 & 1 \end{pmatrix} - \cdots \right. \\
&\qquad \left. \cdots - \begin{pmatrix} Q\cos\Phi & Q\sin\Phi\cos\left(\Omega T_R\right) & -Q\sin\Phi\sin\left(\Omega T_R\right) \\ -Q\sin\Phi & Q\cos\Phi\cos\left(\Omega T_R\right) & -Q\cos\Phi\sin\left(\Omega T_R\right) \\ 0 & \delta\sin\left(\Omega T_R\right) & \delta\cos\left(\Omega T_R\right) \end{pmatrix} e^{-T_R/\tau} \right)^{-1} \\
&= \begin{pmatrix} 1- Qe^{-T_R/\tau}\cos\Phi & -Qe^{-T_R/\tau}\sin\Phi\cos\left(\Omega T_R\right) & Qe^{-T_R/\tau}\sin\Phi\sin\left(\Omega T_R\right) \\ Qe^{-T_R/\tau}\sin\Phi & 1- Qe^{-T_R/\tau}\cos\Phi\cos\left(\Omega T_R\right) & Qe^{-T_R/\tau}\cos\Phi\sin\left(\Omega T_R\right) \\ 0 & -\delta e^{-T_R/\tau}\sin\left(\Omega T_R\right) & 1-\delta e^{-T_R/\tau}\cos\left(\Omega T_R\right) \end{pmatrix}^{-1} . \qquad \text{(A.18)}
\end{aligned}
$$

There is resemblance to the analogous matrix in absence of the OSE, but there is a lack of symmetry here that makes the inversion much more difficult. There is some merit in calculating the determinant of this matrix. When we did so previously, it had a value proportional to r^{-2}.

$$
\begin{aligned}
\det\left[\left(\hat{R}^{\infty}_{\mathrm{OSE}}\right)^{-1}\right] &= \left(1 - Qe^{-T_R/\tau}\cos\Phi\right) \times \\
&\quad \left[\left(1 - Qe^{-T_R/\tau}\cos\Phi\cos\left(\Omega T_R\right)\right)\left(1 - \delta e^{-T_R/\tau}\cos\left(\Omega T_R\right)\right) - \cdots \right. \\
&\quad \left. \cdots - \left(-\delta e^{-T_R/\tau}\sin\left(\Omega T_R\right)\right)\left(Qe^{-T_R/\tau}\cos\Phi\sin\left(\Omega T_R\right)\right)\right] - \cdots \\
&\quad \cdots - \left(Qe^{-T_R/\tau}\sin\Phi\right) \times \\
&\quad \left[\left(-Qe^{-T_R/\tau}\sin\Phi\cos\left(\Omega T_R\right)\right)\left(1 - \delta e^{-T_R/\tau}\cos\left(\Omega T_R\right)\right) - \cdots \right. \\
&\quad \left. \cdots - \left(-\delta e^{-T_R/\tau}\sin\left(\Omega T_R\right)\right)\left(Qe^{-T_R/\tau}\sin\Phi\sin\left(\Omega T_R\right)\right)\right] \\
&= \left(1 - Qe^{-T_R/\tau}\cos\Phi\right) \times \\
&\quad \left[\left(1 - Qe^{-T_R/\tau}\cos\Phi\cos\left(\Omega T_R\right)\right)\left(1 - \delta e^{-T_R/\tau}\cos\left(\Omega T_R\right)\right) + \cdots \right. \\
&\quad \left. \cdots + Q\delta e^{-2T_R/\tau}\cos\Phi\sin^2\left(\Omega T_R\right)\right] + \cdots \\
&\quad \cdots + \left(Qe^{-T_R/\tau}\sin\Phi\right) \times \\
&\quad \left[\left(Qe^{-T_R/\tau}\sin\Phi\cos\left(\Omega T_R\right)\right)\left(1 - \delta e^{-T_R/\tau}\cos\left(\Omega T_R\right)\right) - \cdots \right. \\
&\quad \left. \cdots - Q\delta e^{-2T_R/\tau}\sin\Phi\sin^2\left(\Omega T_R\right)\right] \\
&= \left(1 - Qe^{-T_R/\tau}\cos\Phi\right) \times \\
&\quad \left(\left[\left(1 - Qe^{-T_R/\tau}\cos\Phi\cos\left(\Omega T_R\right)\right)\left(1 - \delta e^{-T_R/\tau}\cos\left(\Omega T_R\right)\right) + \cdots \right.\right. \\
&\quad \left. \cdots + Q\delta e^{-2T_R/\tau}\cos\Phi\sin^2\left(\Omega T_R\right)\right] + \cdots \\
&\quad \cdots + K\left[\left(Qe^{-T_R/\tau}\sin\Phi\cos\left(\Omega T_R\right)\right)\left(1 - \delta e^{-T_R/\tau}\cos\left(\Omega T_R\right)\right) - \cdots \right. \\
&\quad \left.\left. \cdots - Q\delta e^{-2T_R/\tau}\sin\Phi\sin^2\left(\Omega T_R\right)\right]\right).
\end{aligned}
$$

We have pulled out the term $\left(1 - Qe^{-T_R/\tau}\cos\Phi\right)$ in order to define the quantity

$$
K = \frac{Qe^{-T_R/\tau}\sin\Phi}{1 - Qe^{-T_R/\tau}\cos\Phi}, \tag{A.19}
$$

the relative amplitude between the rotated S_x and S_y components immediately following the action of a pump pulse.

We can further simplify the portion of the determinant in the large parentheses:

$$
\begin{aligned}
&= \left[\left(1 - Qe^{-T_R/\tau}\cos\Phi\cos\left(\Omega T_R\right)\right)\left(1 - \delta e^{-T_R/\tau}\cos\left(\Omega T_R\right)\right) + \cdots\right.\\
&\quad \left.\cdots + Q\delta e^{-2T_R/\tau}\cos\Phi\sin^2\left(\Omega T_R\right)\right] + K\times\\
&\quad \left[\left(Qe^{-T_R/\tau}\sin\Phi\cos\left(\Omega T_R\right)\right)\left(1 - \delta e^{-T_R/\tau}\cos\left(\Omega T_R\right)\right) - Q\delta e^{-2T_R/\tau}\sin\Phi\sin^2\left(\Omega T_R\right)\right]\\
&= \left[1 - \delta e^{-T_R/\tau}\cos\left(\Omega T_R\right) - Qe^{-T_R/\tau}\cos\Phi\cos\left(\Omega T_R\right) + \cdots\right.\\
&\quad \left.\cdots Q\delta e^{-2T_R/\tau}\cos\Phi\cos^2\left(\Omega T_R\right) + Q\delta e^{-2T_R/\tau}\cos\Phi\sin^2\left(\Omega T_R\right)\right] + \cdots\\
&\quad \cdots + K\left[Qe^{-T_R/\tau}\sin\Phi\cos\left(\Omega T_R\right) - Q\delta e^{-2T_R/\tau}\sin\Phi\cos^2\left(\Omega T_R\right) - \cdots\right.\\
&\quad \left.\cdots - Q\delta e^{-2T_R/\tau}\sin\Phi\sin^2\left(\Omega T_R\right)\right]\\
&= \left[1 - \delta e^{-T_R/\tau}\cos\left(\Omega T_R\right) - Qe^{-T_R/\tau}\cos\Phi\cos\left(\Omega T_R\right) + Q\delta e^{-2T_R/\tau}\cos\Phi\right] + \cdots\\
&\quad \cdots + K\left[Qe^{-T_R/\tau}\sin\Phi\cos\left(\Omega T_R\right) - Q\delta e^{-2T_R/\tau}\sin\Phi\right]\\
&= 1 - \delta e^{-T_R/\tau}\cos\left(\Omega T_R\right) - e^{-T_R/\tau}\cos\left(\Omega T_R\right)\left(Q\cos\Phi - KQ\sin\Phi\right) + \cdots\\
&\quad \cdots + \delta e^{-2T_R/\tau}\left(Q\cos\Phi - KQ\sin\Phi\right) \qquad \text{(A.20)}\\
&= 1 - \delta e^{-T_R/\tau}\cos\left(\Omega T_R\right) - \alpha e^{-T_R/\tau}\cos\left(\Omega T_R\right) + \alpha\delta e^{-2T_R/\tau}\\
&= 1 - \left(\alpha + \delta\right)e^{-T_R/\tau}\cos\left(\Omega T_R\right) + \alpha\delta e^{-2T_R/\tau}, \qquad \text{(A.21)}
\end{aligned}
$$

where we have defined

$$\alpha = Q\cos\Phi - KQ\sin\Phi, \qquad \text{(A.22)}$$

the amplitude change in S_y due to the pump pulse.

Equation A.21 resembles the magnetic-field-dependent amplitude r^{-2} from RSA as well as the r^{-2} previously derived for the OSE in Ref. [11]. As it turns out, we will still encounter this latter term. In fact, we will effectively have two amplitude terms factor into our final expression (and we will choose to define a third). We label this quantity as ρ^{-2} in analogy to r. Thus,

$$\det\left[\left(\hat{R}_{\mathrm{OSE}}^{\infty}\right)^{-1}\right] = \left(1 - Qe^{-T_R/\tau}\cos\Phi\right)\rho^{-2}. \tag{A.23}$$

Inverting the matrix by hand is far more difficult than the RSA case, so we enlist *Mathematica.* Assuming our simplifications are correct, the matrix of interest is too large to print on this page. Instead, we list the matrix elements, omitting the common factor of $\left(\det\left[\left(\hat{R}_{\mathrm{OSE}}^{\infty}\right)^{-1}\right]\right)^{-1}$:

$$R_{xx} \propto 1 - \delta e^{-T_R/\tau}\cos(\Omega T_R) - Qe^{-T_R/\tau}\cos\Phi\cos(\Omega T_R) + Q\delta e^{-2T_R/\tau}\cos\Phi$$

$$R_{xy} \propto \left(Qe^{-T_R/\tau}\sin\Phi\right)\left(\cos(\Omega T_R) - \delta e^{-T_R/\tau}\right)$$

$$R_{xz} \propto -\left(Qe^{-T_R/\tau}\sin\Phi\right)\sin(\Omega T_R)$$

$$R_{yx} \propto -\left(Qe^{-T_R/\tau}\sin\Phi\right)\left(1 - \delta e^{-T_R/\tau}\cos(\Omega T_R)\right)$$

$$R_{yy} \propto \left(1 - Qe^{-T_R/\tau}\cos\Phi\right)\left(1 - \delta e^{-T_R/\tau}\cos(\Omega T_R)\right)$$

$$R_{yz} \propto -\left(\cos\Phi - Qe^{-T_R/\tau}\right)Qe^{-T_R/\tau}\sin(\Omega T_R)$$

$$R_{zx} \propto -\left(Qe^{-T_R/\tau}\sin\Phi\right)\delta e^{-T_R/\tau}\sin(\Omega T_R)$$

$$R_{zy} \propto \left(1 - Qe^{-T_R/\tau}\cos\Phi\right)\delta e^{-T_R/\tau}\sin(\Omega T_R)$$

$$R_{zz} \propto 1 - Qe^{-T_R/\tau}\cos\Phi - Qe^{-T_R/\tau}\cos\Phi\cos(\Omega T_R) + Q^2 e^{-2T_R/\tau}\cos(\Omega T_R).$$

Each matrix element has been factored to pull out any factors of $Qe^{-T_R/\tau}\sin\Phi$ or $\left(1 - Qe^{-T_R/\tau}\cos\Phi\right)$, if possible. We will divide each element by Eq. A.23, the $\left(1 - Qe^{-T_R/\tau}\cos\Phi\right)$ terms will cancel, and the $Qe^{-T_R/\tau}\sin\Phi$ terms will become K terms. Of the three elements that do not immediately present one of these terms – R_{xx}, R_{yz}, and R_{zz}

– two of them can be manipulated further to reveal hidden structure:

$$\begin{aligned}
R_{yz} &\propto -\left(\cos\Phi - Qe^{-T_R/\tau}\right) Qe^{-T_R/\tau}\sin\left(\Omega T_R\right)\\
&\propto -\left(Q\left(\cos\Phi - Qe^{-T_R/\tau}\right)\right) e^{-T_R/\tau}\sin\left(\Omega T_R\right)\\
&\propto -\left(\alpha\left(1 - Qe^{-T_R/\tau}\cos\Phi\right)\right) e^{-T_R/\tau}\sin\left(\Omega T_R\right)\\
&\propto -\left(1 - Qe^{-T_R/\tau}\cos\Phi\right) \alpha e^{-T_R/\tau}\sin\left(\Omega T_R\right)\\
R_{zz} &\propto 1 - Qe^{-T_R/\tau}\cos\Phi - Qe^{-T_R/\tau}\cos\Phi\cos\left(\Omega T_R\right) + Q^2e^{-2T_R/\tau}\cos\left(\Omega T_R\right)\\
&\propto 1 - Qe^{-T_R/\tau}\cos\Phi - e^{-T_R/\tau}\cos\left(\Omega T_R\right)\left(Q\left(\cos\Phi - Qe^{-T_R/\tau}\right)\right)\\
&\propto 1 - Qe^{-T_R/\tau}\cos\Phi - e^{-T_R/\tau}\cos\left(\Omega T_R\right)\left(\alpha\left(1 - Qe^{-T_R/\tau}\cos\Phi\right)\right)\\
&\propto 1 - Qe^{-T_R/\tau}\cos\Phi - \alpha e^{-T_R/\tau}\cos\left(\Omega T_R\right)\left(1 - Qe^{-T_R/\tau}\cos\Phi\right)\\
&\propto \left(1 - Qe^{-T_R/\tau}\cos\Phi\right)\left(1 - \alpha e^{-T_R/\tau}\cos\left(\Omega T_R\right)\right).
\end{aligned}$$

Were we to proceed with analogous identifications for $\sin\gamma$ and $\cos\gamma$ as in the absence of the OSE, we would have, for a suitable definition of r:

$$\begin{aligned}
\sin\gamma &= -r\alpha e^{-T_R/\tau}\sin\left(\Omega T_R\right),\\
\cos\gamma &= r\left(1 - \alpha e^{-T_R/\tau}\cos\left(\Omega T_R\right)\right),
\end{aligned}$$

based on the definition for γ:

$$\gamma = -\arctan\left(\frac{\alpha e^{-T_R/\tau}\sin\left(\Omega T_R\right)}{1 - \alpha e^{-T_R/\tau}\cos\left(\Omega T_R\right)}\right), \tag{A.24}$$

the phase shift due to both external magnetic field and the actions of the pump pulse.

We would then identify R_{yz} with $\sin\gamma$ and R_{zz} with $\cos\gamma$, which would complete the analogy and get us towards the desired final matrix. However, ρ is not r. Thus, we will manually insert factors of r, which now has the definition

$$r = \left(1 - 2\alpha e^{-T_R/\tau}\cos\left(\Omega T_R\right) + \alpha^2 e^{-2T_R/\tau}\right)^{-1/2}, \tag{A.25}$$

as previously defined in Ref. [11].

Applying the common multiplicative factor Eq. A.23, we can simplify the elements of $\hat{R}^{\infty}_{\mathrm{OSE}}$:

$$\begin{aligned}
R_{xx} &= \frac{\rho^2}{1 - Qe^{-T_R/\tau}\cos\Phi}\times \\
&\qquad \left(1 - \delta e^{-T_R/\tau}\cos\left(\Omega T_R\right) - Qe^{-T_R/\tau}\cos\Phi\cos\left(\Omega T_R\right) + Q\delta e^{-2T_R/\tau}\cos\Phi\right) \\
R_{xy} &= \rho^2 K\left(\cos\left(\Omega T_R\right) - \delta e^{-T_R/\tau}\right) \\
R_{xz} &= -\rho^2 K\sin\left(\Omega T_R\right) \\
R_{yx} &= -\rho^2 K\left(1 - \delta e^{-T_R/\tau}\cos\left(\Omega T_R\right)\right) \\
R_{yy} &= \rho^2\left(1 - \delta e^{-T_R/\tau}\cos\left(\Omega T_R\right)\right) \\
R_{yz} &= -\rho^2\alpha e^{-T_R/\tau}\sin\left(\Omega T_R\right) \\
R_{zx} &= -\rho^2 K\delta e^{-T_R/\tau}\sin\left(\Omega T_R\right) \\
R_{zy} &= \rho^2\delta e^{-T_R/\tau}\sin\left(\Omega T_R\right) \\
R_{zz} &= \rho^2\left(1 - \alpha e^{-T_R/\tau}\cos\left(\Omega T_R\right)\right).
\end{aligned}$$

Other than R_{xx}, the interpretation of this matrix is much cleaner. We can proceed to achieving our final result, the spin polarization at a time t after an infinite series of pulses:

$$\vec{S} = \hat{R}\left[\Omega t\right]\, e^{-t/\tau}\hat{R}^{\infty}_{\mathrm{OSE}}\vec{S}_0. \tag{A.26}$$

As before, we can evaluate the effect of the pulses on the initial spin polarization and then apply the additional rotation. However, we will again follow the second approach and evaluate the matrix product $\hat{R}\left[\Omega t\right]\hat{R}^{\infty}_{\mathrm{OSE}}$. We use the matrix element notation R_{ij} for clarity.

$$\begin{aligned}\hat{R}\left[\Omega t\right]\hat{R}^{\infty}_{\mathrm{OSE}} &= \begin{pmatrix} 1 & 0 & 0 \\ 0 & \cos\left(\Omega t\right) & -\sin\left(\Omega t\right) \\ 0 & \sin\left(\Omega t\right) & \cos\left(\Omega t\right) \end{pmatrix} \begin{pmatrix} R_{xx} & R_{xy} & R_{xz} \\ R_{yx} & R_{yy} & R_{yz} \\ R_{zx} & R_{zy} & R_{zz} \end{pmatrix} \\ &= \begin{pmatrix} R_{xx} & R_{xy} & R_{xz} \\ \begin{matrix} R_{yx}\cos(\Omega t)- \\ R_{zx}\sin(\Omega t) \end{matrix} & \begin{matrix} R_{yy}\cos(\Omega t)- \\ R_{zy}\sin(\Omega t) \end{matrix} & \begin{matrix} R_{yz}\cos(\Omega t)- \\ R_{zz}\sin(\Omega t) \end{matrix} \\ \begin{matrix} R_{zx}\cos(\Omega t)+ \\ R_{yx}\sin(\Omega t) \end{matrix} & \begin{matrix} R_{zy}\cos(\Omega t)+ \\ R_{yy}\sin(\Omega t) \end{matrix} & \begin{matrix} R_{zz}\cos(\Omega t)+ \\ R_{yz}\sin(\Omega t) \end{matrix} \end{pmatrix}. \end{aligned}$$

The spin polarization at time t is then

$$\vec{S} = S_0 \begin{pmatrix} R_{xz} \\ R_{yz}\cos\left(\Omega t\right) - R_{zz}\sin\left(\Omega t\right) \\ R_{zz}\cos\left(\Omega t\right) + R_{yz}\sin\left(\Omega t\right) \end{pmatrix} e^{-t/\tau}, \tag{A.27}$$

which can be further simplified:

$$\begin{aligned}
S_x(t) &\propto R_{xz} \\
&= -\rho^2 K \sin(\Omega T_R) \\
&= -\rho^2 K \times \\
&\quad \big(\sin(\Omega T_R) - \alpha e^{-T_R/\tau} \sin(\Omega T_R)\cos(\Omega T_R) + \alpha e^{-T_R/\tau} \sin(\Omega T_R)\cos(\Omega T_R)\big) \\
&= -\rho^2 K \left(\sin(\Omega T_R)\big(1 - \alpha e^{-T_R/\tau}\cos(\Omega T_R)\big) + \alpha e^{-T_R/\tau}\sin(\Omega T_R)\cos(\Omega T_R)\right) \\
&= -\rho^2 K \left(\sin(\Omega T_R)\frac{1}{r}\cos\gamma - \frac{1}{r}\sin\gamma\cos(\Omega T_R)\right) \\
&= -\frac{\rho^2}{r} K \left(\sin(\Omega T_R)\cos\gamma - \sin\gamma\cos(\Omega T_R)\right) \\
&= -\frac{\rho^2}{r} K \sin(\Omega T_R - \gamma), \qquad \text{(A.28)} \\
S_y(t) &\propto R_{yz}\cos(\Omega t) - R_{zz}\sin(\Omega t) \\
&= \big(-\rho^2 \alpha e^{-T_R/\tau}\sin(\Omega T_R)\big)\cos(\Omega t) - \big(\rho^2\big(1 - \alpha e^{-T_R/\tau}\cos(\Omega T_R)\big)\big)\sin(\Omega t) \\
&= \rho^2\left(-\alpha e^{-T_R/\tau}\sin(\Omega T_R)\cos(\Omega t) - \big(1 - \alpha e^{-T_R/\tau}\cos(\Omega T_R)\big)\sin(\Omega t)\right) \\
&= \rho^2\left(\frac{1}{r}\sin\gamma\cos(\Omega t) - \frac{1}{r}\cos\gamma\sin(\Omega t)\right) \\
&= -\frac{\rho^2}{r}\left(\sin(\Omega t)\cos\gamma - \cos(\Omega t)\sin\gamma\right) \\
&= -\frac{\rho^2}{r}\sin(\Omega t - \gamma), \qquad \text{(A.29)} \\
S_z(t) &\propto R_{zz}\cos(\Omega t) + R_{yz}\sin(\Omega t) \\
&= \big(\rho^2\big(1 - \alpha e^{-T_R/\tau}\cos(\Omega T_R)\big)\big)\cos(\Omega t) + \big(-\rho^2\alpha e^{-T_R/\tau}\sin(\Omega T_R)\big)\sin(\Omega t) \\
&= \rho^2\left(\big(1 - \alpha e^{-T_R/\tau}\cos(\Omega T_R)\big)\cos(\Omega t) - \big(\alpha e^{-T_R/\tau}\sin(\Omega T_R)\big)\sin(\Omega t)\right) \\
&= \rho^2\left(\frac{1}{r}\cos\gamma\cos(\Omega t) + \frac{1}{r}\sin\gamma\sin(\Omega t)\right) \\
&= \frac{\rho^2}{r}\left(\cos(\Omega t)\cos\gamma + \sin(\Omega t)\sin\gamma\right) \\
&= \frac{\rho^2}{r}\cos(\Omega t - \gamma). \qquad \text{(A.30)}
\end{aligned}$$

At last, we have

$$\vec{S} = S_0 \frac{\rho^2}{r} e^{-t/\tau} \begin{pmatrix} -K \sin\left(\Omega T_R - \gamma\right) \\ -\sin\left(\Omega t - \gamma\right) \\ \cos\left(\Omega t - \gamma\right) \end{pmatrix}. \tag{A.31}$$

The insertion of factors of r allows us to recast the matrix elements as $\sin\gamma$ and $\cos\gamma$ terms, resulting in a final expression strongly reminiscent of RSA in the absence of the OSE. The only difference would be the presence of a nonzero S_x. Notice that δ does not explicitly show up at all in this final expression, as it is absent from matrix elements R_{xz}, R_{yz}, and R_{zz}.

This form would be sufficient for numerical calculations. However, we can make the resemblance to the RSA expression even stronger by re-defining the pre-factor ρ^2/r as a new effective amplitude r'. Using the definition for ρ, we have

$$
\begin{aligned}
r' \equiv \frac{\rho^2}{r} &= \frac{\left(1-(\alpha+\delta)\,e^{-T_R/\tau}\cos(\Omega T_R)+\alpha\delta e^{-2T_R/\tau}\right)^{-1}}{r} \\
&= r^{-1}\left(1-(\alpha+\delta)\,e^{-T_R/\tau}\cos(\Omega T_R)+\alpha\delta e^{-2T_R/\tau}\right)^{-1} \\
&= r^{-1}\times \\
&\quad \left(1-(\alpha+\delta)\,e^{-T_R/\tau}\cos(\Omega T_R)+\alpha\delta e^{-2T_R/\tau}\left(\cos^2(\Omega T_R)+\sin^2(\Omega T_R)\right)\right)^{-1} \\
&= r^{-1}\left(1-\alpha e^{-T_R/\tau}\cos(\Omega T_R)-\delta e^{-T_R/\tau}\cos(\Omega T_R)+\alpha\delta e^{-2T_R/\tau}\cos^2(\Omega T_R)\right. \\
&\left. +\,\alpha\delta e^{-2T_R/\tau}\sin^2(\Omega T_R)\right)^{-1} \\
&= r^{-1}\left(\left(1-\alpha e^{-T_R/\tau}\cos(\Omega T_R)\right)\left(1-\delta e^{-T_R/\tau}\cos(\Omega T_R)\right)\right. \\
&\left. -\,\delta e^{-T_R/\tau}\sin(\Omega T_R)\left(-\alpha e^{-T_R/\tau}\sin(\Omega T_R)\right)\right)^{-1} \\
&= \left(r\left(1-\alpha e^{-T_R/\tau}\cos(\Omega T_R)\right)\left(1-\delta e^{-T_R/\tau}\cos(\Omega T_R)\right)\right. \\
&\left. -\,\delta e^{-T_R/\tau}\sin(\Omega T_R)\left(-r\alpha e^{-T_R/\tau}\sin(\Omega T_R)\right)\right)^{-1} \\
&= \left(\cos\gamma\left(1-\delta e^{-T_R/\tau}\cos(\Omega T_R)\right)-\delta e^{-T_R/\tau}\sin(\Omega T_R)\sin\gamma\right)^{-1} \\
&= \left(\cos\gamma-\delta e^{-T_R/\tau}\cos(\Omega T_R)\cos\gamma-\delta e^{-T_R/\tau}\sin(\Omega T_R)\sin\gamma\right)^{-1} \\
&= \left(\cos\gamma-\delta e^{-T_R/\tau}\left(\cos(\Omega T_R)\cos\gamma-\sin(\Omega T_R)\sin\gamma\right)\right)^{-1} \\
&= \left(\cos\gamma-\delta e^{-T_R/\tau}\cos(\Omega T_R-\gamma)\right)^{-1}.
\end{aligned}
$$

This yields the final expression

$$
\vec{S} = \left(\frac{Q^2-1}{4}\right)\frac{1}{\cos\gamma-\left(\frac{Q^2+1}{2}\right)e^{-T_R/\tau}\cos(\Omega T_R-\gamma)}e^{-t/\tau}\begin{pmatrix} -K\sin(\Omega T_R-\gamma) \\ -\sin(\Omega t-\gamma) \\ \cos(\Omega t-\gamma)\end{pmatrix} \tag{A.32}
$$

$$
= S_0 r' e^{-t/\tau}\begin{pmatrix} -K\sin(\Omega T_R-\gamma) \\ -\sin(\Omega t-\gamma) \\ \cos(\Omega t-\gamma)\end{pmatrix}. \tag{A.33}
$$

While the notation is slightly different, this matrix method reproduces the results derived in Ref. [11].

APPENDIX B

Faraday and Kerr Rotation

B.1 Motivation

In Chapter 3, we hinted at a difference in the spectral dependence of Faraday and Kerr rotation. To show this difference, we present a full derivation of Faraday rotation in terms of the complex index of refraction.

B.2 Deriving Faraday Rotation

For experimental reasons, we prefer to work with s-polarization, which is vertical with respect to our lab frame. Based on the coordinate axes used throughout this dissertation, this vertical direction is also labeled as $\hat{y}$. Vertical linear polarization can be rewritten as a superposition of σ^+ and σ^-:

$$\begin{aligned}\hat{y} &= \begin{pmatrix} 0 \\ 1 \end{pmatrix} \\ &= \frac{1}{2i}\left[\begin{pmatrix} 1 \\ i \end{pmatrix} - \begin{pmatrix} 1 \\ -i \end{pmatrix}\right] \\ &= \frac{1}{\sqrt{2}i}\left[\hat{\sigma}^+ - \hat{\sigma}^-\right].\end{aligned}$$

The (complex) transmission coefficient for a wave of frequency ω moving from a material with complex index $\tilde{n}_1$ to a material with complex index $\tilde{n}_2$ is given by

$$t = \frac{2\tilde{n}_1}{\tilde{n}_1 + \tilde{n}_2}.$$

In real systems, there may be additional layers of other materials. For example, our InGaAs epilayer was grown on a GaAs epilayer. When the layers have sufficiently different energy band gaps, we can choose the incident field frequency in such a way that the additional layers are effectively transparent with respect to that frequency. Therefore, we maintain the simplicity of this exercise by ignoring any further layers. The transmission coefficients t_{in} from the air to the material and t_{out} from the material to the air are given by

$$\begin{aligned} t_{\text{in}}^{\pm} &= \frac{2}{1+\tilde{n}^{\pm}} = \frac{2}{1+n^{\pm}+i\kappa^{\pm}}, \\ t_{\text{out}}^{\pm} &= \frac{2\tilde{n}^{\pm}}{\tilde{n}^{\pm}+1} = \frac{2\left(n^{\pm}+i\kappa^{\pm}\right)}{1+n^{\pm}+i\kappa^{\pm}}, \end{aligned}$$

where the complex index depends on which polarization (σ^+ or σ^-) we are considering. It behooves us to rewrite these coefficients in phasor notation. That is, it will be physically more relevant to write

$$t_{\text{in}}^{\pm} = \left|t_{\text{in}}^{\pm}\right| e^{i\phi_{\text{in}}^{\pm}}, \tag{B.1}$$

$$t_{\text{out}}^{\pm} = \left|t_{\text{out}}^{\pm}\right| e^{i\phi_{\text{out}}^{\pm}}, \tag{B.2}$$

with most of our attention on the phase component.

That said, our real interest lies in the phase that the light acquires upon transversing the material. This phase will also differ based on polarization. Due to the complex index of refraction, this term is both a phase and an attenuation term:

$$\begin{aligned} e^{i\tilde{n}^{\pm}\frac{\omega}{c}d} &= e^{i\left(n^{\pm}+i\kappa^{\pm}\right)\frac{\omega}{c}d} \\ &= e^{in^{\pm}\frac{\omega}{c}d}e^{-\kappa^{\pm}\frac{\omega}{c}d}. \end{aligned}$$

There will be absorption due to the imaginary part of the complex index, as is seen clearly here.

Putting this all together, the electric field $\vec{E}_{\text{out}}$ transmitted through a magnetized material of depth d for an incident field $\vec{E}_{\text{in}}$ is given by

$$\begin{aligned}
\vec{E}_{\text{in}} &= E_0 \hat{y} \\
&= \frac{E_0}{\sqrt{2}i}\left(\hat{\sigma}^+ - \hat{\sigma}^-\right) \\
&\Rightarrow \qquad \qquad \text{(B.3)} \\
\vec{E}_{\text{out}} &= \frac{E_0}{\sqrt{2}i}\left(t^+_{\text{out}} e^{i\tilde{n}^+ \frac{\omega}{c} d} t^+_{\text{in}} \hat{\sigma}^+ - t^-_{\text{out}} e^{i\tilde{n}^- \frac{\omega}{c} d} t^-_{\text{in}} \hat{\sigma}^-\right) \\
&= \frac{E_0}{\sqrt{2}i}\left(t^+_{\text{out}} e^{-\kappa^+ \frac{\omega}{c} d} e^{in^+ \frac{\omega}{c} d} t^+_{\text{in}} \hat{\sigma}^+ - t^-_{\text{out}} e^{-\kappa^- \frac{\omega}{c} d} e^{in^- \frac{\omega}{c} d} t^-_{\text{in}} \hat{\sigma}^-\right) \\
&= \frac{E_0}{\sqrt{2}i}\Bigg(\left|t^+_{\text{out}}\right| e^{i\phi^+_{\text{out}}} e^{-\kappa^+ \frac{\omega}{c} d} e^{in^+ \frac{\omega}{c} d} \left|t^+_{\text{in}}\right| e^{i\phi^+_{\text{in}}} \hat{\sigma}^+ - \cdots \\
&\quad \cdots - \left|t^-_{\text{out}}\right| e^{i\phi^-_{\text{out}}} e^{-\kappa^- \frac{\omega}{c} d} e^{in^- \frac{\omega}{c} d} \left|t^-_{\text{in}}\right| e^{i\phi^-_{\text{in}}} \hat{\sigma}^-\Bigg) \\
&= \frac{E_0}{\sqrt{2}i}\Bigg(\left|t^+_{\text{out}}\right| e^{-\kappa^+ \frac{\omega}{c} d} \left|t^+_{\text{in}}\right| e^{i\left(n^+ \frac{\omega}{c} d + \phi^+_{\text{out}} + \phi^+_{\text{in}}\right)} \hat{\sigma}^+ - \cdots \\
&\quad \cdots - \left|t^-_{\text{out}}\right| e^{-\kappa^- \frac{\omega}{c} d} \left|t^-_{\text{in}}\right| e^{i\left(n^- \frac{\omega}{c} d + \phi^-_{\text{out}} + \phi^-_{\text{in}}\right)} \hat{\sigma}^-\Bigg) \\
&= \frac{E_0}{\sqrt{2}i}\left(\tau^+ e^{i\theta^+} \hat{\sigma}^+ - \tau^- e^{i\theta^-} \hat{\sigma}^-\right), \qquad \text{(B.4)}
\end{aligned}$$

where $\tau^\pm$ is a real quantity describing the amplitude modification due to the combined effect of the transmission coefficients and the attenuation due to propagation:

$$\tau^\pm = \left|t^\pm_{\text{out}}\right| e^{-\kappa^\pm \frac{\omega}{c} d} \left|t^\pm_{\text{in}}\right|, \tag{B.5}$$

and $\theta^\pm$ is a real quantity that consolidates the total phase acquired due to transmission and propagation:

$$\theta^\pm = \left(n^\pm \frac{\omega}{c} d + \phi^\pm_{\text{out}} + \phi^\pm_{\text{in}}\right). \tag{B.6}$$

Now that we have re-expressed the transmission and propagation in phasor form, we can proceed in deriving the Faraday rotation. We will hold off on making approximations as long as possible.

$$\begin{aligned}
\vec{E}_{\text{out}} &= \frac{E_0}{\sqrt{2}i}\left(\tau^+ e^{i\theta^+}\hat{\sigma}^+ - \tau^- e^{i\theta^-}\hat{\sigma}^-\right) \\
&= \frac{E_0}{\sqrt{2}i}\left(\tau^+ e^{i\theta^+}\frac{1}{\sqrt{2}}\begin{pmatrix}1\\ i\end{pmatrix} - \tau^- e^{i\theta^-}\frac{1}{\sqrt{2}}\begin{pmatrix}1\\ -i\end{pmatrix}\right) \\
&= \frac{E_0}{2i}\begin{pmatrix}\tau^+ e^{i\theta^+} - \tau^- e^{i\theta^-} \\ i\left(\tau^+ e^{i\theta^+} + \tau^- e^{i\theta^-}\right)\end{pmatrix} \\
&= \frac{E_0}{2i}e^{i\left(\frac{\theta^+ + \theta^-}{2}\right)}\begin{pmatrix}\tau^+ e^{i\left(\frac{\theta^+ - \theta^-}{2}\right)} - \tau^- e^{-i\left(\frac{\theta^+ - \theta^-}{2}\right)} \\ i\left(\tau^+ e^{i\left(\frac{\theta^+ - \theta^-}{2}\right)} + \tau^- e^{-i\left(\frac{\theta^+ - \theta^-}{2}\right)}\right)\end{pmatrix} \\
&= \frac{E_0}{2i}e^{i\left(\frac{\theta^+ + \theta^-}{2}\right)}\begin{pmatrix}\left(\tau + \Delta\tau\right)e^{i\theta} - \left(\tau - \Delta\tau\right)e^{-i\theta} \\ i\left(\left(\tau + \Delta\tau\right)e^{i\theta} + \left(\tau - \Delta\tau\right)e^{-i\theta}\right)\end{pmatrix}. \qquad \text{(B.7)}
\end{aligned}$$

See that

$$\begin{aligned}
\tau^{\pm} &= \frac{\tau^{\pm} + \tau^{\pm}}{2} \\
&= \frac{\tau^{\pm} + \tau^{\pm}}{2} + \frac{\tau^{\mp} - \tau^{\mp}}{2} \\
&= \frac{\tau^{\pm} + \tau^{\mp}}{2} + \frac{\tau^{\pm} - \tau^{\mp}}{2} \\
&\equiv \tau \pm \Delta\tau, \qquad \text{(B.8)}
\end{aligned}$$

where τ is defined as the average of τ^+ and τ^-, and $\Delta\tau$ is defined as half the difference. We also define

$$\begin{aligned}
\theta &= \frac{\theta^+ - \theta^-}{2} \\
&= \left(\frac{n^+ - n^-}{2}\right)\frac{\omega}{c}d + \frac{\phi^+_{\text{out}} - \phi^-_{\text{out}}}{2} + \frac{\phi^+_{\text{in}} - \phi^-_{\text{in}}}{2}. \qquad \text{(B.9)}
\end{aligned}$$

This θ will end up being our Faraday rotation.

At this juncture, we have simplified to the greatest extent possible without knowing more about the nature of our complex index of refraction. Once we know that, we can proceed numerically. However, if we expect the difference in light absorption between handedness of light to be very small with respect to the incident amplitude, we can proceed with the assumption that $\tau \pm \Delta\tau \approx \tau$. This opens the door to further analysis:

$$
\begin{aligned}
\vec{E}_{\text{out}} &\approx \frac{E_0}{2i} e^{i\left(\frac{\theta^+ + \theta^-}{2}\right)} \begin{pmatrix} \tau e^{i\theta} - \tau e^{-i\theta} \\ i\left(\tau e^{i\theta} + \tau e^{-i\theta}\right) \end{pmatrix} \\
&= \frac{E_0 \tau}{2i} e^{i\left(\frac{\theta^+ + \theta^-}{2}\right)} \begin{pmatrix} e^{i\theta} - e^{-i\theta} \\ i\left(e^{i\theta} + e^{-i\theta}\right) \end{pmatrix} \\
&= \frac{E_0 \tau}{2i} e^{i\left(\frac{\theta^+ + \theta^-}{2}\right)} \begin{pmatrix} 2i\sin\theta \\ i\left(2\cos\theta\right) \end{pmatrix} \\
&= E_0 \tau e^{i\left(\frac{\theta^+ + \theta^-}{2}\right)} \begin{pmatrix} \sin\theta \\ \cos\theta \end{pmatrix} &\text{(B.10)} \\
&= E_0 \tau e^{i\left(\frac{\theta^+ + \theta^-}{2}\right)} \begin{pmatrix} \cos\theta & \sin\theta \\ -\sin\theta & \cos\theta \end{pmatrix} \begin{pmatrix} 0 \\ 1 \end{pmatrix}. &\text{(B.11)}
\end{aligned}
$$

We receive back our initial polarization, rotated by an angle θ. This rotation of the initial polarization is the Faraday rotation. The overall effective transmission coefficient $\tau e^{i\left(\frac{\theta^+ + \theta^-}{2}\right)}$ does not factor into the rotation itself.

Without diving any deeper into the character of the system under study, can we learn anything more about the Faraday rotation angle? We know that it is a function of the distance propagated d as well as the frequency of the propagating light ω. It also depends in a nonlinear way on the complex index of refraction.

We argue that we can ignore the phase terms resulting from transmission and focus solely on the propagation term in θ. Based on the definitions above, we can calculate these phases:

$$\tan\phi_{\text{in}}^{\pm} = -\frac{\kappa^{\pm}}{n^{\pm} + 1}, \tag{B.12}$$

$$\tan\phi_{\text{out}}^{\pm} = \frac{\kappa^{\pm}}{n^{\pm}\left(n^{\pm} + 1\right)}. \tag{B.13}$$

Away from the absorption resonances, we expect these terms to be negligible. That does not describe our situation. Even so, we expect these terms to be small such that we can ignore the tangent. Note that we are taking the differences of the + and − terms. That means that

$$\begin{aligned}
\theta &= \left(\frac{n^+ - n^-}{2}\right)\frac{\omega}{c}d + \frac{\phi^+_{\text{out}} - \phi^-_{\text{out}}}{2} + \frac{\phi^+_{\text{in}} - \phi^-_{\text{in}}}{2} \\
&\approx \left(\frac{n^+ - n^-}{2}\right)\frac{\omega}{c}d + \frac{1}{2}\left(\frac{\kappa^+}{n^+\left(n^+ + 1\right)} - \frac{\kappa^-}{n^-\left(n^- + 1\right)}\right) + \frac{1}{2}\left(-\frac{\kappa^+}{n^+ + 1} + \frac{\kappa^-}{n^- + 1}\right) \\
&= \left(\frac{n^+ - n^-}{2}\right)\frac{\omega}{c}d + \cdots \\
&\quad \cdots + \frac{1}{2}\left(\frac{\kappa^+}{n^+\left(n^+ + 1\right)} - \frac{\kappa^-}{n^-\left(n^- + 1\right)} - \frac{n^+\kappa^+}{n^+\left(n^+ + 1\right)} + \frac{n^-\kappa^-}{n^-\left(n^- + 1\right)}\right) \\
&= \left(\frac{n^+ - n^-}{2}\right)\frac{\omega}{c}d - \frac{1}{2}\left(\frac{\left(n^+ - 1\right)\kappa^+}{n^+\left(n^+ + 1\right)} - \frac{\left(n^- - 1\right)\kappa^-}{n^-\left(n^- + 1\right)}\right).
\end{aligned} \tag{B.14}$$

Interestingly, two terms emerge. The first, due to propagation, is proportional to the difference in index of refraction for the two circular polarizations. The second is due to interface transmission effects and, while incorporating n and κ in a nonlinear way, is effectively proportional to the difference in extinction coefficients for the two circular polarizations.

For the optical frequencies under consideration, the quantity ω/c will be in the range of $5 - 20$ μm^{-1}. For usual sample depths on the order of a micron, this gives us a term that is multiple times the difference of the indices. Compare that to the additional phase terms, which collectively are a difference of already small terms. We expect, then, that the propagation will win out and dominate for most values of d. Numerical calculations bear out this conclusion. Thus, we are usually justified in neglecting the additional terms and defining Faraday rotation θ as

$$\theta = \left(\frac{n^+ - n^-}{2}\right)\frac{\omega}{c}d. \tag{B.15}$$

This is the expression given in the main text.

B.3 Deriving Kerr Rotation

We can repeat the earlier calculation for Faraday rotation in the reflection geometry instead. We will end up with a surprisingly different result. We need only a single reflection coefficient for a single surface (between the material and air):

$$r = \frac{\tilde{n} - 1}{\tilde{n} + 1}.$$

As before, we must consider polarization in our definition. We again write these coefficients in phasor notation:

$$r^{\pm} = \left| r^{\pm} \right| e^{i\phi^{\pm}}, \tag{B.16}$$

where we recycle the notation ϕ for a similarly defined physical quantity that will have a different functional form.

There is no propagation in the reflection geometry (ignoring any sort of skin depth effects), which greatly simplifies the calculation. The electric field $\vec{E}_{\text{out}}$ reflected off a magnetized material for an incident field $\vec{E}_{\text{in}}$ is given by

$$\begin{aligned}
\vec{E}_{\text{in}} &= E_0\hat{y} \\
&= \frac{E_0}{\sqrt{2}i}\left(\hat{\sigma}^+ - \hat{\sigma}^-\right) \\
&\Rightarrow \qquad\qquad\qquad\qquad\qquad\qquad\qquad\qquad\qquad\qquad\qquad\qquad\qquad\qquad\qquad\qquad\qquad\qquad \text{(B.17)} \\
\vec{E}_{\text{out}} &= \frac{E_0}{\sqrt{2}i}\left(r^+\hat{\sigma}^+ - r^-\hat{\sigma}^-\right) \\
&= \frac{E_0}{\sqrt{2}i}\left(\left|r^+\right|e^{i\phi^+}\hat{\sigma}^+ - \left|r^-\right|e^{i\phi^-}\hat{\sigma}^-\right) \\
&= \frac{E_0}{\sqrt{2}i}\left(\left|r^+\right|e^{i\phi^+}\frac{1}{\sqrt{2}}\begin{pmatrix}1\\ i\end{pmatrix} - \left|r^-\right|e^{i\phi^-}\frac{1}{\sqrt{2}}\begin{pmatrix}1\\ -i\end{pmatrix}\right) \\
&= \frac{E_0}{2i}\begin{pmatrix}\left|r^+\right|e^{i\phi^+} - \left|r^-\right|e^{i\phi^-}\\ i\left(\left|r^+\right|e^{i\phi^+} + \left|r^-\right|e^{i\phi^-}\right)\end{pmatrix} \\
&= \frac{E_0}{2i}e^{i\left(\frac{\phi^+ + \phi^-}{2}\right)}\begin{pmatrix}\left|r^+\right|e^{i\left(\frac{\phi^+ - \phi^-}{2}\right)} - \left|r^-\right|e^{-i\left(\frac{\phi^+ - \phi^-}{2}\right)}\\ i\left(\left|r^+\right|e^{i\left(\frac{\phi^+ - \phi^-}{2}\right)} + \left|r^-\right|e^{-i\left(\frac{\phi^+ - \phi^-}{2}\right)}\right)\end{pmatrix} \\
&= \frac{E_0}{2i}e^{i\left(\frac{\phi^+ + \phi^-}{2}\right)}\begin{pmatrix}\left(r + \Delta r\right)e^{i\phi} - \left(r - \Delta r\right)e^{-i\phi}\\ i\left(\left(r + \Delta r\right)e^{i\phi} + \left(r - \Delta r\right)e^{-i\phi}\right)\end{pmatrix}, \qquad \text{(B.18)}
\end{aligned}$$

with definitions for r and Δr analogous to the transmission definitions for τ and $\Delta\tau$. Here is a form suited for numerical calculations. However, we will again assume that $\Delta r \ll r$ so that we can write

$$\begin{aligned}
\vec{E}_{\text{out}} &\approx \frac{E_0}{2i} e^{i\left(\frac{\phi^+ + \phi^-}{2}\right)} \begin{pmatrix} re^{i\phi} - re^{-i\phi} \\ i\left(re^{i\phi} + re^{-i\phi}\right) \end{pmatrix} \\
&= \frac{E_0 r}{2i} e^{i\left(\frac{\phi^+ + \phi^-}{2}\right)} \begin{pmatrix} e^{i\phi} - e^{-i\phi} \\ i\left(e^{i\phi} + e^{-i\phi}\right) \end{pmatrix} \\
&= \frac{E_0 r}{2i} e^{i\left(\frac{\phi^+ + \phi^-}{2}\right)} \begin{pmatrix} 2i \sin\phi \\ i\left(2\cos\phi\right) \end{pmatrix} \\
&= E_0 r e^{i\left(\frac{\phi^+ + \phi^-}{2}\right)} \begin{pmatrix} \sin\phi \\ \cos\phi \end{pmatrix} \qquad \text{(B.19)} \\
&= E_0 r e^{i\left(\frac{\phi^+ + \phi^-}{2}\right)} \begin{pmatrix} \cos\phi & \sin\phi \\ -\sin\phi & \cos\phi \end{pmatrix} \begin{pmatrix} 0 \\ 1 \end{pmatrix}, \qquad \text{(B.20)}
\end{aligned}$$

where now ϕ is our Kerr rotation angle. This form for the reflected light looks nearly identical to that derived for transmitted light. However, the difference lies in the definition of ϕ. For now, we have at least verified that reflection also rotates the polarization.

We cannot argue away the phase terms due to reflection here or else we will have no Kerr rotation. We only have a single reflection term (as opposed to two transmission terms), with clear phase:

$$\tan\phi^{\pm} = \frac{2\kappa^{\pm}}{n^{\pm 2} - 1 + \kappa^{\pm 2}}. \qquad \text{(B.21)}$$

We again assume that $\phi^{\pm}$ is small enough for the small angle approximation. Then

$$\begin{aligned}
\phi &= \frac{\phi^+ - \phi^-}{2} \\
&\approx \frac{1}{2}\left(\frac{2\kappa^+}{n^{+2} - 1 + \kappa^{+2}} - \frac{2\kappa^-}{n^{-2} - 1 + \kappa^{-2}}\right) \\
&\approx \frac{1}{n^{\pm 2} - 1 + \kappa^{\pm 2}}\left(\kappa^+ - \kappa^-\right). \qquad \text{(B.22)}
\end{aligned}$$

In the last line, we make the further assumption that the index and extinction coefficient are close enough in value that we can pull out the denominators as a common term. This makes it even clearer that ϕ is effectively proportional to the difference in extinction coefficients, just like the additional (but neglected) phase term in Faraday rotation. This means that Kerr rotation depends on absorption more directly than Faraday rotation. We expect Kerr rotation to be smaller than Faraday rotation on the same material given the Faraday rotation propagation term, which is proportional also to the material thickness d. However, we note that Kerr rotation ϕ is the difference in small quantities over a small quantity, which could become large. Numerical calculations do confirm that Kerr rotation follows the difference in extinction coefficient for the most part.

To summarize, then, in the limit of small absorption difference, transmission through and reflection from a magnetized surface both rotate the polarization of a linearly polarized laser pulse. For transmission, this rotation angle should roughly have the spectral character of $n^+ - n^-$. For reflection, this reflection angle should roughly have the spectral character of $\kappa^+ - \kappa^-$. This conclusion matches the sentiment expressed in the literature that Faraday and Kerr rotation emerge from the real and imaginary parts of the dielectric function [42].

BIBLIOGRAPHY

BIBLIOGRAPHY

[1] G. M. Moore, Cramming more components onto integrated circuits, Electronics **38**, 114-117 (1965).

[2] S. A. Wolf, D. D. Awschalom, R. A. Buhrman, J. M. Daughton, S. von Molnár, M. L. Roukes, A. Y. Chtchelkanova, and D. M. Treger, Spintronics: A Spin-Based Electronics Vision for the Future, Science **294**, 1488-1495 (2001).

[3] C. Chappert, A. Fert, and F. N. V. Dau, The emergence of spin electronics in data storage, Nature Materials **6**, 813-823 (2007).

[4] W. P. McCray, How spintronics went from the lab to the iPod, Nature Nanotechnology **4**, 2-4 (2009).

[5] J. S. Townsend, *A Modern Approach to Quantum Mechanics*, 2nd ed. (University Science Books, Mill Valley, 2012).

[6] D. D. Awschalom and N. Samarth, Spintronics without magnetism, Physics **2**, 50 (2009).

[7] D. D. Awschalom and M. E. Flatté, Challenges for semiconductor spintronics, Nature Physics **3**, 153-159 (2007).

[8] I. Žutić, J. Fabian, and S. Das Sarma, Spintronics: Fundamentals and applications, Reviews of Modern Physics **76**, 323-410 (2004).

[9] J. R. Iafrate, S. Huang, D. Del Gaudio, R. S. Goldman, and V. Sih, Effect of modified periodic waveforms on current-induced spin polarization measurements, AIP Advances **8**, 065113 (2018).

[10] M. Macmahon, J. R. Iafrate, M. J. Dominguez, and V. Sih, Observation of magnetic field sweep direction dependent dynamic nuclear polarization under periodic optical electron spin pumping, Physical Review B **99**, 075201 (2019).

[11] M. J. Dominguez, J. R. Iafrate, and V. Sih, Dynamic nuclear polarization by optical Stark effect in periodically pumped gallium arsenide, Physical Review B **101**, 205203 (2020).

[12] N. W. Ashcroft and N. D. Mermin, *Solid State Physics*, (Brooks/Cole, Belmont, 1976).

[13] *Optical Orientation*, edited by F. Meier and B. P. Zakharchenya (Elsevier, Amsterdam, 1984).

[14] R. I. Dzhioev, K. V. Kavokin, V. L. Korenev, M. V. Lazarev, B. Ya. Meltser, M. N. Stepanova, B. P. Zakharchenya, D. Gammon, and D. S. Katzer, Low-temperature spin relaxation in n-type GaAs, Physical Review B **66**, 245204 (2002).

[15] I. A. Yugova, M. M. Glazov, E. L. Ivchenko, and Al. L. Efros, Pump-probe Faraday rotation and ellipticity in an ensemble of singly charged quantum dots, Physical Review B **80**, 104436 (2009).

[16] L. V. Fokina, I. A. Yugova, D. R. Yakovlev, M. M. Glazov, I. A. Akimov, A. Greilich, D. Reuter, A. D. Wieck, and M. Bayer, Spin dynamics of electrons and holes in InGaAs/GaAs quantum wells at millikelvin temperatures, Physical Review B **81**, 195304 (2010).

[17] M. M. Glazov, *Electron & Nuclear Spin Dynamics in Semiconductor Nanostructures*, edited by R. J. Nicholas and H. Kamimura (Oxford University Press, Oxford, 2018).

[18] C. J. Trowbridge, B. M. Norman, Y. K. Kato, D. D. Awschalom, and V. Sih, Dynamic nuclear polarization from current-induced electron spin polarization, Physical Review B **90**, 085122 (2014).

[19] C. Gorini, A. M. Sheikhabadi, K. Shen, I. V. Tokatly, G. Vignale, and R. Raimondi, Theory of current-induced spin polarization in an electron gas, Physical Review B **95**, 205424 (2017).

[20] M. Luengo-Kovac, S. Huang, D. Del Gaudio, J. Occena, R.S. Goldman, R. Raimondi, and V. Sih, Current-induced spin polarization in InGaAs and GaAs epilayers with varying doping densities, Physical Review B **96**, 195206 (2017).

[21] F. Bloch, Nuclear induction, Physical Review **70**, 460-474 (1946).

[22] B. M. Norman, *Electrical generation of spin polarization in strained III-V semiconductors*, PhD thesis, University of Michigan (2014).

[23] H. C. Torrey, Bloch Equations with Diffusion Terms, Physical Review **104**, 563-565 (1956).

[24] J. D. Jackson, *Classical Electrodynamics*, 3rd ed. (John Wiley & Sons, Inc., New York, 1998).

[25] G. Dresselhaus, Spin-Orbit Coupling Effects in Zinc Blende Structures, Physical Review **100**, 580-586 (1955).

[26] Yu. A. Bychkov and É. I. Rashba, Oscillatory effects and the magnetic susceptibility of carriers in inversion layers, Journal of Physics C: Solid State Physics **17**, 6039-6045 (1984).

[27] Yu. A. Bychkov and É. I. Rashba, Properties of a 2D electron gas with lifted spectral degeneracy, Pis'ma Zh. Eksp. Teor. Fiz. **39**, 66-69 (1984) [JETP Letters **39**, 78-81 (1984)].

[28] M. Luengo-Kovac, *Investigation of Current Induced Spin Polarization in III-V Semiconductor Epilayers*, PhD thesis, University of Michigan (2017).

[29] E. L. Hahn, Spin echoes, Physical Review **80**, 580-594 (1950).

[30] H. Y. Carr and E. M. Purcell, Effects of Diffusion on Free Precession in Nuclear Magnetic Resonance Experiments, Physical Review **94**, 630-638 (1954).

[31] J. Fabian and S. Das Sarma, Spin relaxation of conduction electrons, Journal of Vacuum Science & Technology B **17**, 1708-1715 (1999).

[32] M. I. D'yakonov and V. I. Perel', Spin Orientation of Electrons Associated with the Interband Absorption of Light in Semiconductors, Zh. Eksp. Teor. Fiz, **60**, 1954-1965 (1971) [Soviet Physics JETP **33**, 1053-1059 (1971)].

[33] R. J. Elliott, Theory of the Effect of Spin-Orbit Coupling on Magnetic Resonance in Some Semiconductors, Physical Review **96**, 266-279 (1954).

[34] Y. Yafet, g Factors and Spin-Lattice Relaxation of Conduction Electrons, in *Solid State Physics, Volume 14*, edited by F. Seitz and D. Turnbull (Academic Press, New York, 1963).

[35] J. M. Kikkawa and D. D. Awschalom, Resonant Spin Amplification in n-Type GaAs, Physical Review Letters **80**, 4313-4316 (1998).

[36] C. J. Trowbridge and V. Sih, Phase effects due to previous pulses in time-resolved Faraday rotation measurements, Journal of Applied Physics **117**, 063906 (2015).

[37] A. W. Overhauser, Polarization of Nuclei in Metals, Physical Review **92**, 411-415 (1953).

[38] W. D. Knight, Nuclear Magnetic Resonance Shift in Metals, Physical Review **76**, 1259-1260 (1949).

[39] J. M. Kikkawa and D. D. Awschalom, All-Optical Magnetic Resonance in Semiconductors, Science **287**, 473-476 (2000).

[40] E. A. Zhukov, A. Greilich, D. R. Yakovlev, K. V. Kavokin, I. A. Yugova, O. A. Yugov, D. Suter, G. Karczewski, T. Wojtowicz, J. Kossut, V. V. Petrov, Yu. K. Dolgikh, A. Pawlis, and M. Bayer, All-optical NMR in semiconductors provided by resonant cooling of nuclear spins interacting with electrons in the resonant spin amplification regime, Physical Review B **90**, 085311 (2014).

[41] M. Faraday, *Faraday's Diary of Experimental Investigation, 1820-1862, Vol. IV.*, 2nd ed. (HR Direct, Riverton, 2008).

[42] J. F. Dillon, Jr., Magneto-Optical Properties of Magnetic Garnets, in *Physics of Magnetic Garnets*, edited by A. Paoletti (North-Holland Publishing Company, Amsterdam, 1978).

[43] A. Kanno, *Study of Spin Dynamics in III-V Quantum Dots by Time Resolved Kerr Rotation*, PhD thesis, University of Tsukuba (2005).

[44] P. R. Berman, Optical Faraday rotation, American Journal of Physics **78**, 270-276 (2010).

[45] P. Bhattacharya, *Semiconductor Optoelectronic Devices*, 2nd ed. (Prentice Hall, Upper Saddle River, 1997).

[46] M. A. Noyan and J. M. Kikkawa, Accuracy and form of off-resonance time-resolved Kerr rotation spectroscopy, Applied Physics Letters **115**, 142401 (2019).

[47] F. Urbach, The Long-Wavelength Edge of Photographic Sensitivity and of the Electronic Absorption of Solids, Physical Review **92**, 1324 (1953).

[48] C. W. Greeff and H. R. Glyde, Anomalous Urbach tail in GaAs, Physical Review B **51**, 1778-1783 (1995).

[49] S. John, C. Soukoulis, M. H. Cohen, and E. N. Economou, Theory of Electron Band Tails and the Urbach Optical-Absorption Edge, Physical Review Letters **57**, 1777-1780 (1986).

[50] T. Moss, Optical Absorption Edge in GaAs and Its Dependence on Electric Field, Journal of Applied Physics **32**, 2136-2139 (1961).

[51] Y. Kato, *Electrical Manipulation of Electron Spin Coherence in Nonmagnetic Semiconductors*, PhD thesis, University of California, Santa Barbara (2005).

[52] J. Lee, A. Venugopal, and V. Sih, Anisotropic spin dephasing of impurity-bound electron spins in ZnO, Applied Physics Letters **106**, 012403 (2015).

[53] B. C. Pursley, *Resonant and Time Resolved Spin Noise Spectroscopy of Electron Spin Dynamics in Semiconductors*, PhD thesis, University of Michigan (2015).

[54] F. C. D. Moraes, S. Ullah, M. A. G. Balanta, F. Iikawa, Y. A. Danilov, M. V. Dorokhin, O. V. Vikhrova, B. N. Zvonkov, and F. G. G. Hernandez, Acceleration of the precession frequency for optically-oriented electron spins in ferromagnetic/semiconductor hybrids, Scientific Reports **9**, 7294 (2019).

[55] M. Macmahon, *Investigation of the Coupled Electron-Nuclear Spin System in GaAs Under Periodic Optical Electron Spin Pumping*, PhD thesis, University of Michigan (2019).

[56] X. Song, S. Xie, K. Kang, J. Park, and V. Sih, Long-Lived Hole Spin/Valley Polarization Probed by Kerr Rotation in Monolayer WSe_2, Nano Letters **16**, 5010-5014 (2016).

[57] I. Stepanov, S. Kuhlen, M. Ersfeld, M. Lepsa, and B. Beschoten, All-electrical time-resolved spin generation and spin manipulation in n-InGaAs, Applied Physics Letters **104**, 062406 (2014).

[58] A. Banerjee, F. Doğan, J. Heo, A. Manchon, W. Guo, and P. Bhattacharya, Spin Relaxation in InGaN Quantum Disks in GaN Nanowires, Nano Letters **11**, 5396-5400 (2011).

[59] M. Fox, *Optical Properties of Solids*, 2nd ed. (Oxford University Press, Oxford, 2010).

[60] Y. K. Kato, R. C. Myers, A. C. Gossard, and D. D. Awschalom, Current-Induced Spin Polarization in Strained Semiconductors, Physical Review Letters **93**, 176601 (2004).

[61] A. Yu. Silov, P. A. Blajnov, J. H. Wolter, R. Hey, K. H. Ploog, and N. S. Averkiev, Current-induced spin polarization at a single heterojunction, Applied Physics Letters **85**, 5929-5931 (2004).

[62] V. Sih, R. C. Myers, Y. K. Kato, W. H. Lau, A. C. Gossard, and D. D. Awschalom, Spatial imaging of the spin Hall effect and current-induced polarization in two-dimensional electron gases, Nature Physics **1**, 31-35 (2005).

[63] C. L. Yang, H. T. He, L. Ding, L. J. Cui, Y. P. Zeng, J. N. Wang, and W. K. Ge, Spectral Dependence of Spin Photocurrent and Current-Induced Spin Polarization in an InGaAs/InAlAs Two-Dimensional Electron Gas, Physical Review Letters **96**, 186605 (2006).

[64] N. P. Stern, S. Ghosh, G. Xiang, M. Zhu, N. Samarth, and D. D. Awschalom, Current-Induced Polarization and the Spin Hall Effect at Room Temperature, Physical Review Letters **97**, 126603 (2006).

[65] A. Chernyshov, M. Overby, X. Liu, J. K. Furdyna, Y. Lyanda-Geller, and L. P. Rokhinson, Evidence for reversible control of magnetization in a ferromagnetic material by means of spin-orbit magnetic field, Nature Physics **5**, 656-659 (2009).

[66] W. F. Koehl, M. H. Wong, C. Poblenz, B. Swenson, U. K. Mishra, J. S. Speck, and D. D. Awschalom, Current-induced spin polarization in gallium nitride, Applied Physics Letters **95**, 072110 (2009).

[67] B. M. Norman, C. J. Trowbridge, D. D. Awschalom, and V. Sih, Current-Induced Spin Polarization in Anisotropic Spin-Orbit Fields, Physical Review Letters **112**, 056601 (2014).

[68] F. G. G. Hernandez, G. M. Gusev, and A. K. Bakarov, Resonant optical control of the electrically induced spin polarization by periodic excitation, Physical Review B **90**, 041302(R) (2014).

[69] P. Horowitz and W. Hill, *The Art of Electronics*, 2nd ed. (Cambridge University Press, New York, 1990).

[70] B. Urbaszek, X. Marie, T. Amand, O. Krebs, P. Voisin, P. Maletinsky, A. Högele, and A. Imamoglu, Nuclear spin physics in quantum dots: An optical investigation, Reviews of Modern Physics **85**, 79-133 (2013).

[71] R. J. Warburton, Single spins in self-assembled quantum dots, Nature Materials **12**, 483-493 (2013).

[72] E. A. Chekhovich, M. N. Makhonin, A. I. Tartakovskii, A. Yacoby, H. Bluhm, K. C. Nowack, and L. M. K. Vandersypen, Nuclear spin effects in semiconductor quantum dots, Nature Materials **12**, 494-504 (2013).

[73] J. A. Reimer, Nuclear hyperpolarization in solids and the prospects for nuclear spintronics, Solid State Nuclear Magnetic Resonance **37**, 3-12 (2010).

[74] G. Lampel, Nuclear Dynamic Polarization by Optical Electronic Saturation and Optical Pumping in Semiconductors, Physical Review Letters **20**, 491-493 (1968).

[75] F. Heisterkamp, A. Greilich, E. A. Zhukov, E. Kirstein, T. Kazimierczuk, V. L. Korenev, I. A. Yugova, D. R. Yakovlev, A. Pawlis, and M. Bayer, Inhomogeneous nuclear spin polarization induced by helicity-modulated optical excitation of fluorine-bound electron spins in ZnSe, Physical Review B **92**, 245441 (2015).

[76] E. A. Zhukov, E. Kirstein, N. E. Kopteva, F. Heisterkamp, I. A. Yugova, V. L. Korenev, D. R. Yakovlev, A. Pawlis, M. Bayer, and A. Greilich, Discretization of the total magnetic field by the nuclear spin bath in fluorine-doped ZnSe, Nature Communications **9**, 1941 (2018).

[77] G. Salis, D. T. Fuchs, J. M. Kikkawa, D. D. Awschalom, Y. Ohno, and H. Ohno, Optical Manipulation of Nuclear Spin by a Two-Dimensional Electron Gas, Physical Review Letters **86**, 2677-2680 (2001).

[78] D. Gammon, Al. L. Efros, T. A. Kennedy, M. Rosen, D. S. Katzer, D. Park, S. W. Brown, V. L. Korenev, and I. A. Merkulov, Electron and Nuclear Spin Interactions in the Optical Spectra of Single GaAs Quantum Dots, Physical Review Letters **86**, 5176-5179 (2001).

[79] S. Markmann, C. Reichl, W. Wegscheider, and G. Salis, Universal nuclear focusing of confined electron spins, Nature Communications **10**, 1097 (2019).

[80] N. E. Kopteva, I. A. Yugova, E. A. Zhukov, E. Kirstein, E. Evers, V. V. Belykh, V. L. Korenev, D. R. Yakovlev, M. Bayer, and A. Greilich, Theoretical Modeling of the Nuclear-Field Induced Tuning of the Electron Spin Precession for Localized Spins, Physica Status Solidi (B) **256**, 1800534 (2019).

[81] M. D. Sturge, Optical Absorption of Gallium Arsenide between 0.6 and 2.75 eV, Physical Review **127**, 768-773 (1962).

[82] E. A. Zhukov, D. R. Yakovlev, M. Bayer, M. M. Glazov, E. L. Ivchenko, G. Karczewski, T. Wojtowicz, and J. Kossut, Spin coherence of a two-dimensional electron gas induced by resonant excitation of trions and excitons in CdTe/(Cd,Mg)Te quantum wells, Physical Review B **76**, 205310 (2007).

[83] E. H. Bogardus and H. B. Bebb, Bound-Exciton, Free-Exciton, Band-Acceptor, Donor-Acceptor,and Auger Recombination in GaAs, Physical Review **176**, 993-1002 (1968).

[84] A. Mysyrowicz, D. Hulin, A. Antonetti, A. Migus, W. T. Masselink, and H. Morkoç, "Dressed Excitons" in a Multiple-Quantum-Well Structure: Evidence for an Optical Stark Effect with Femtosecond Response Time, Physical Review Letters **56**, 2748-2751 (1986).

[85] M. Combescot and R. Combescot, Excitonic Stark Shift: A Coupling to "Semivirtual" Biexcitons, Physical Review Letters **61**, 117-120 (1988).

[86] J. A. Gupta, R. Knobel, N. Samarth, and D. D. Awschalom, Ultrafast Manipulation of Electron Spin Coherence, Science **292**, 2458-2461 (2001).

[87] T. A. Wilkinson, D. J. Cottrill, J. M. Cramlet, C. E. Maurer, C. J. Flood, A. S. Bracker, M. Yakes, D. Gammon, and E. B. Flagg, Spin-selective AC Stark shifts in a charged quantum dot, Applied Physics Letters **114**, 133104 (2019).

[88] S. E. Economou, L. J. Sham, Y. Wu, and D. G. Steel, Proposal for optical U(1) rotations of electron spin trapped in a quantum dot, Physical Review B **74**, 205415 (2006).

[89] S. G. Carter, A. Shabaev, S. E. Economou, T. A. Kennedy, A. S. Bracker, and T. L. Reinecke, Directing Nuclear Spin Flips in InAs Quantum Dots Using Detuned Optical Pulse Trains, Physical Review Letters **102**, 167403 (2009).

[90] A. Greilich, S. E. Economou, S. Spatzek, D. R. Yakovlev, D. Reuter, A. D. Wieck, T. L. Reinecke, and M. Bayer, Ultrafast optical rotations of electron spins in quantum dots, Nature Physics **5**, 262-266 (2009).

[91] P. S. Pershan, J. P. van der Ziel, and L. D. Malmstrom, Theoretical Discussion of the Inverse Faraday Effect, Raman Scattering, and Related Phenomena, Physical Review **143**, 574-583 (1966).

[92] I. A. Yugova, M. M. Glazov, D. R. Yakovlev, A. A. Sokolova, and M. Bayer, Coherent spin dynamics of electrons and holes in semiconductor quantum wells and quantum dots under periodical optical excitation: Resonant spin amplification versus spin mode locking, Physical Review B **85**, 125304 (2012).

[93] A. Abragam, *The Principles of Nuclear Magnetism* (Clarendon Press, Oxford, 1961).

[94] M. I. D'yakonov and V. I. Perel', Optical orientation in a system of electrons and lattice nuclei in semiconductors. Theory, Zh. Eksp. Teor. Fiz **65**, 362-375 (1973) [Soviet Physics JETP **38**, 177-183 (1974)].

[95] D. Paget, G. Lampel, B. Sapoval, and V. I. Safarov, Low field electron-nuclear spin coupling in gallium arsenide under optical pumping conditions, Physical Review B **15**, 5780-5796 (1977).

[96] J. M. Lu, M. J. R. Hoch, P. L. Kuhns, W. G. Moulton, Z. Gan, and A. P. Reyes, Nuclear spin-lattice relaxation in n-type insulating and metallic GaAs single crystals, Physical Review B **74**, 125208 (2006).

[97] G. Kaur and G. Denninger, Dynamic Nuclear Polarization in III-V Semiconductors, Applied Magnetic Resonance **39**, 185-204 (2010).

[98] D. Kölbl, D. M. Zumbühl, A. Fuhrer, G. Salis, and S. F. Alvarado, Breakdown of the Korringa Law of Nuclear Spin Relaxation in Metallic GaAs, Physical Review Letters **109**, 086601 (2012).

[99] L.A. Machlan, J. W. Gramlich, L. J. Powell, and G. M. Lambert, Absolute Isotopic Abundance Ratio And Atomic Weight of a Reference Sample of Gallium, Journal of Research of the National Bureau of Standards **91**, 323-331 (1986).

[100] V. M. Litvyak, R. V. Cherbunin, K. V. Kavokin, and V. K. Kalevich, Determination of the local field in the nuclear spin system of n-type GaAs, Journal of Physics: Conference Series **951**, 012006 (2018).

[101] F. Heisterkamp, E. Kirstein, A. Greilich, E. A. Zhukov, T. Kazimierczuk, D. R. Yakovlev, A. Pawlis, and M. Bayer, Dynamics of nuclear spin polarization induced and detected by coherently precessing electron spins in fluorine-doped ZnSe, Physical Review B **93**, 081409(R) (2016).

[102] A. Greilich, A. Shabaev, D. R. Yakovlev, Al. L. Efros, I. A. Yugova, D. Reuter, A. D. Wieck, and M. Bayer, Nuclei-Induced Frequency Focusing of Electron Spin Coherence, Science **317**, 1896-1899 (2007).

[103] A. Greilich, D. R. Yakovlev, A. Shabaev, Al. L. Efros, I. A. Yugova, R. Oulton, V. Stavarache, D. Reuter, A. Wieck, and M. Bayer, Mode Locking of Electron Spin Coherences in Singly Charged Quantum Dots, Science **313**, 341-345 (2006).

[104] V. L. Korenev, Multiple stable states of a periodically driven electron spin in a quantum dot using circularly polarized light, Physical Review B **83**, 235429 (2011).

[105] M. M. Glazov, I. A. Yugova, and Al. L. Efros, Electron spin synchronization induced by optical nuclear magnetic resonance feedback, Physical Review B **85**, 041303(R) (2012).

[106] W. Beugeling, G. S. Uhrig, and F. B. Anders, Influence of the nuclear Zeeman effect on mode locking in pulsed semiconductor quantum dots, Physical Review B **96**, 115303 (2017).

[107] J. Hackmann and F. B. Anders, Spin noise in the anisotropic central spin model, Physical Review B **89**, 045317 (2014).

[108] Y. K. Kato, R. C. Myers, A. C. Gossard, and D. D. Awschalom, Observation of the Spin Hall Effect in Semiconductors, Science **306**, 1910-1913 (2004).

[109] V. Sih, W. H. Lau, R. C. Myers, V. R. Horowitz, A. C. Gossard, and D. D. Awschalom, Generating Spin Currents in Semiconductors with the Spin Hall Effect, Physical Review Letters **97**, 096605 (2006).